

# Probing the micromechanical strength of oxide ceramic composite reinforcements

THÈSE N° 8065 (2017)

PRÉSENTÉE LE 27 OCTOBRE 2017  
À LA FACULTÉ DES SCIENCES ET TECHNIQUES DE L'INGÉNIEUR  
LABORATOIRE DE MÉTALLURGIE MÉCANIQUE  
PROGRAMME DOCTORAL EN SCIENCE ET GÉNIE DES MATÉRIAUX

ÉCOLE POLYTECHNIQUE FÉDÉRALE DE LAUSANNE

POUR L'OBTENTION DU GRADE DE DOCTEUR ÈS SCIENCES

PAR

Václav PEJCHAL

acceptée sur proposition du jury:

Prof. A. Fontcuberta i Morral, présidente du jury  
Prof. A. Mortensen, directeur de thèse  
Prof. J. Chevalier, rapporteur  
Prof. R. Todd, rapporteur  
Prof. J. Botsis, rapporteur



ÉCOLE POLYTECHNIQUE  
FÉDÉRALE DE LAUSANNE

Suisse  
2017





# Acknowledgements

I would like to express my sincere gratitude to all who supported me throughout the last five years to help to make this thesis a reality.

Firstly, a special thanks to my supervisor Prof. Andreas Mortensen; the mastermind of this thesis and of our project “*PhaseNanoCracker*” which received advanced grant funding from the European Research Council (ERC Advanced Grant Agreement No. 291085) for which I am grateful. Thank you, Andreas, for giving me the opportunity to be a part of this great group at LMM, and for your guidance and trust. Your passion and enthusiasm for science is inspirational and I have learned so much from you over the years.

I would also like to thank the members of my thesis examination jury Prof. Anna Fontcuberta i Morral, Prof. John Botsis, who followed my progress for five years, Prof. Jérôme Chevalier, and Prof. Richard Todd for their careful examination of my thesis, insightful comments, and fruitful discussion on the subject matter of this thesis.

I would like to express my sincere gratitude to EPFL, with a special thanks to the Doctoral School and EDMX’s personnel for the great care with which they treat doctoral candidates. I would like to thank the personnel of the Microscopy Centre (CIME), particularly Dr. Marco Cantoni and Fabienne Bobard for their time and valuable help, and to Pierre André Despont’s team in the ATMX workshop. I would also like to thank Prof. Miroslav Karlik for his support in my application to EPFL as a doctoral candidate. At various stages of my PhD I also received support from Prof. Craig Carter, Prof. Nina Orlovskaya and Prof. Bhaskar Majumdar, to whom I am grateful.

I am indebted to my dear ERC teammates Martin Mueller, Goran Žagar, Lionel Michelet, and Marta Fornabaio, who all significantly contributed to the present work and with whom I spent countless hours — or rather days — discussing, designing, and performing experiments. We shared the pain of failure, the joy of success, and often spent good times together travelling to conferences. Thank you very much, you were not only the best colleagues, but great friends as well.

It has been a pleasure to work with everyone, both past and present colleagues, at LMM who created an enjoyable atmosphere and with whom I share many memorable memories. Thank you Maïté, Christian, and Cyrill for being great office-mates, Gionata for being thorough in arranging “café à 10h,” Gabriella for being a great travel companion on the train from Geneva during the first few months, Hamed for jokes, Alex for anecdotes, Suzanne for her care of our wonderful group by arranging gifts and wish cards, Roberto and José Miguel for their Mediterranean temperaments, Alain and Jérôme for providing their wisdom as PhD seniors, Léa, Ana, Aparna, Arda, and Florian for

sharing enjoyable moments, Andreas Rossoll and Ludger for their knowledge, Madame Zanetta, Fabienne, Willy, Raphael, and Cyril for ensuring that the lab worked like a well-tuned Swiss clock, and last but not least “mon chéri” Amaël for being a great colleague and friend. Thank you all for the laughs and nice moments.

I would like to thank to all the undergraduate students I supervised, namely Chatchai Hirunlabh, Yarmille Gaviña Sanchez, Adrien Mazuryk, Dennis, Lang, Charlotte Bondaz, Melanie Adams, Grégory Riesen, and Romain Martin. Your work was valuable contribution to the project.

I would also like to express my deepest gratitude to my whole family, especially my supportive parents Václav and Magdaléna. Ďakujem za vašu podporu, lásku, starostlivosť, a za život ktorý ste mi dali.

And finally, thank you to my darling Vierka. I could not have completed this milestone without your everyday support and care. You are the home to which I return every day from work, you are my best friend, my beloved wife, and the person with whom I share all the joys life has to offer.

# Abstract

This work shows how one can probe the micromechanical strength of ceramic reinforcements used in metal matrix composites, which greatly influences the mechanical performance of the composite material yet has seldom been quantified with precision. More specifically, this study presents two methods by means of which one can measure the statistical strength distribution of microscopic, low-aspect-ratio, ceramic particles. Additionally, the study reveals the nature of specific defects that weaken such ceramic reinforcements and shows that, when those defects are absent, one can produce particles of near-theoretical strength, which have the potential to produce remarkably strong and tough metal matrix composites.

In one developed method called here the Meridian Crack Test, individual spherical particles are compressed uniaxially between a pair of parallel elasto-plastic platens. It is shown that, by tailoring the platen hardness one can control the relative area of particle-to-platen contact during the test, thereby eliminating the initiation of contact microcracks that are often found to influence particle fracture when hard platens are used. It is shown how this method, coupled with the mathematics of statistical survival-analysis, can give unambiguous access to the particle statistical tensile strength as governed by surface flaws.

The method is first demonstrated using microscopic fused quartz spheres  $40\pm 20\mu\text{m}$  in diameter and is then used to measure the strength controlled by surface and subsurface flaws in plasma-sprayed spherical amorphous and nanocrystalline near-eutectic "Eucor" alumina-zirconia-silica ceramic particles of diameter near  $30\mu\text{m}$ . Results show that nanocrystalline Eucor particles exhibit a characteristic Weibull strength of 1490 MPa, which is approximately 30% higher than in corresponding amorphous particles.

The second developed method, called here the C-shaped sample test, combines focused ion beam milling, loading using a nanoindentation device, and bespoke finite element simulations to measure the local strength of ceramic reinforcements free of artifacts commonly present in micromachined specimens. The method is first demonstrated on Nextel 610<sup>TM</sup> nanocrystalline alumina fibres embedded in aluminium. Results reveal a size effect that does not follow, across size scales, the Weibull statistical strength distribution that is measured by tensile testing macroscopic samples of the fibres. This indicates that, in micromechanical analysis of multiphase materials, highly localized events such as the propagation of internal damage require input data that are measured at the same, local, micro-scale as the event.

Finally, we implement the C-shaped sample test method with additional micro-cantilever beam testing to measure the local strength of vapour-grown  $\alpha$ -alumina Sumicorundum<sup>®</sup> particles 15 to  $30\mu\text{m}$  in diameter, known to be attractive reinforcing particles for aluminium. Results show that, provided

the particle surface is free of readily observable defects such as pores, twins or grain boundary grooves, the particles can achieve local strength values that approach those of high-perfection single-crystal alumina whiskers, on the order of 10 GPa. It is also shown that by far the most harmful defects are grain boundaries, leading to the general conclusion that alumina particles must be single-crystalline or alternatively nanocrystalline to fully develop their potential as a strong reinforcing phase in composite materials.

## Keywords

Micromechanical testing, local strength, uniaxial compression, survival-analysis, ceramic particles, alumina, focused ion beam (FIB), nanoindentation, micro-cantilever, nano-ceramic, glass-ceramic, Weibull statistics, alumina-zirconia-silica.

# Résumé

Ce travail présente deux nouvelles méthodes d'essai de la résistance mécanique de renforts céramique utilisés dans les composites à matrice métallique. En outre, l'étude révèle quels sont les défauts qui limitent la résistance de tels renforts et contribue à notre compréhension de la façon dont on peut produire des particules plus résistantes pouvant mener à des composites à matrice métallique remarquablement résistants et isotropes.

Dans la première des méthodes développées ici, appelée le « Meridian Crack Test », les particules sont comprimées individuellement entre deux plateaux élasto-plastiques parallèles. En adaptant la dureté des plateaux on peut contrôler la surface relative de contact particule-plateau pendant l'essai. Ceci élimine le développement de microfissures créées par l'essai et généralement responsables de la fracture des particules lorsque des plateaux rigides sont utilisés. Nous montrons comment cette modification de la méthode donne accès à la résistance mécanique des particules telle qu'elle est contrôlée par les défauts de surface et mettons en œuvre la méthode avec des sphères en verre de diamètre  $40 \pm 20 \mu\text{m}$ .

La méthode est utilisée pour mesurer la résistance mécanique de particules amorphes et nanocristallines sphériques ayant une composition proche de l'eutectique alumine-zircone-silice, préparées par pulvérisation thermique avec une torche à plasma. Les résultats montrent que les particules nanocristallines sont environ 30% plus résistantes que les particules amorphes, avec une résistance caractéristique de Weibull égale à 1490 MPa.

La deuxième méthode développée ici, baptisée le « C-shape sample test », est basée sur la mise en œuvre de la sonde ionique focalisée (FIB), d'un appareil de nanoindentation et de l'analyse par éléments finis et mesure la résistance locale de renforts en céramique sans les artefacts habituellement présents dans des échantillons micro-usinés. La méthode est d'abord démontrée en mesurant la résistance locale des fibres nanocristallines Nextel 610<sup>TM</sup> intégrées dans une matrice d'aluminium. Les résultats mettent en lumière un effet de taille: la statistique de rupture ne suit pas, à échelle micro-métrique, la loi de Weibull mesurée par le biais d'essais de traction menés sur les fibres. Ceci implique que, dans la micromécanique de matériaux biphasés, l'analyse de phénomènes fortement localisés tels que la propagation localisée de l'endommagement nécessitent des données d'entrée qui doivent être mesurées à la même échelle, locale, à laquelle l'événement se déroule.

Finalement, cette méthode est utilisée pour mesurer la résistance locale de particules d'alumine Sumicorundum<sup>®</sup> ayant un diamètre de 15 – 30  $\mu\text{m}$ , connues pour être les particules de renforcement attrayantes pour l'aluminium. Les résultats montrent que, si la surface des particules ne contient pas des imperfections tels que les pores, macles, ou les rainures formées à l'intersection de joints de grain avec la surface libre de la céramique, les particules peuvent atteindre une résistance locale de l'ordre

de ce qui est habituellement mesuré pour les trichites d'alumine, proche de 10 GPa. Il est aussi montré que les défauts de loin plus délétères sont les joints de grains, menant à conclure que les particules d'alumine doivent être monocristallines ou alternativement nanocristallines pour développer pleinement le potentiel de cette céramique en tant que phase de renfort de matériaux composites.

## Mots-clés

Essais micromécaniques, résistance locale, compression uniaxiale, analyse de survie, particules céramique, alumine, sonde ionique focalisée (FIB), nanoindentation, poutre en porte-à-faux microscopique, nanocéramique, vitrocéramique, statistique de Weibull, alumine-zircone-silice.

# Contents

<b>Acknowledgements</b> .....	<b>i</b>
<b>Abstract</b> .....	<b>iii</b>
<b>Résumé</b> .....	<b>v</b>
<b>List of Figures</b> .....	<b>xii</b>
<b>List of Tables</b> .....	<b>xxviii</b>
<b>Introduction</b> .....	<b>29</b>
<b>Chapter 1 Literature review</b> .....	<b>33</b>
1.1 Metal matrix composites: an overview .....	33
1.2 Alumina as a reinforcement .....	35
1.2.1 Overview of alumina as material .....	35
1.2.2 Alumina whiskers and fibres .....	39
1.2.3 Alumina particles.....	42
1.3 The role of particle strength in PRMMCs: theory and experiments .....	43
1.3.1 Particle fracture .....	43
1.3.2 Tensile properties .....	46
1.3.3 Fracture toughness .....	49
1.4 Deducing the particle strength from the macroscopic composite behaviour .....	51
1.5 Probing the strength of hard and brittle particles directly.....	53
1.5.1 Uniaxial compression .....	54
1.5.2 C-shaped particle test .....	60
1.6 Micro- and nano-mechanical testing for strength .....	62
1.6.1 Introduction .....	62
1.6.2 Uniaxial compression at the microscale .....	64
1.6.3 Micropillar compression.....	65

1.6.4	Microtensile testing .....	66
1.6.5	Microbend testing .....	67
1.6.6	FIB damage .....	69
1.7	Concluding remarks .....	70
<b>Chapter 2</b>	<b>Compression testing spherical particles for strength: Theory of the meridian crack test and implementation for microscopic fused quartz .....</b>	<b>71</b>
2.1	Disclaimer .....	71
2.2	Introduction .....	71
2.3	Theory .....	72
2.4	Materials and methods .....	77
2.5	Results .....	80
2.6	Discussion .....	84
2.6.1	Survival analysis for data points known to be measure of the surface strength .....	84
2.6.2	Interpreting data for competing centre and surface failure .....	88
2.6.3	Effect of slow-crack-growth .....	90
2.7	Conclusion .....	93
2.8	Appendix 2.A .....	94
2.9	Appendix 2.B .....	96
2.10	Appendix 2.C .....	97
2.11	Appendix 2.D .....	98
2.12	Appendix 2.E: Supplementary information .....	101
2.12.1	Finite element analysis of a spherical particle crushing test .....	101
2.12.2	Elastic contact with a particle representing an inhomogeneity along the platen-particle contact area .....	103
<b>Chapter 3</b>	<b>Meridian crack test strength of plasma-sprayed amorphous and nanocrystalline ceramic microparticles.....</b>	<b>107</b>
3.1	Disclaimer .....	107
3.2	Introduction .....	107
3.3	Materials and methods .....	108
3.3.1	Amorphous Eucor powder .....	108
3.3.2	Nanostructured Eucor powder .....	108
3.3.3	The meridian crack test .....	109
3.4	Results .....	110



3.4.1	Eucor particles microstructure.....	110
3.4.2	Uniaxial compression .....	111
3.4.3	Fractography.....	112
3.5	Discussion .....	114
3.5.1	The meridian crack test evaluation.....	114
3.5.2	Surface strength distribution.....	119
3.5.3	Strength limiting defects.....	121
3.5.4	Data for competing centre and surface failure – Domain II.....	121
3.5.5	Comparison with other microscopic ceramic fibre/particle strength data..	122
3.6	Conclusion .....	123
3.7	Supplementary information .....	123
3.7.1	Particle Poisson’s ratio and platen-particle friction.....	123
3.7.2	Effect of the particle Poisson’s ratio and platen-particle friction coefficient on results.....	124
3.7.3	Fracture stress vs. defect size and estimation of the particle fracture toughness	125
3.7.4	The precision of Weibull parameter estimation .....	127
3.7.5	Comparison of the particle strength with Nextel fibres.....	128
<b>Chapter 4</b>	<b>The local strength of microscopic alumina reinforcements.....</b>	<b>129</b>
4.1	Disclaimer .....	129
4.2	Introduction.....	129
4.3	Methods.....	130
4.3.1	Notched sample preparation .....	130
4.3.2	Mechanical testing.....	132
4.4	Results.....	133
4.4.1	General response of a notched micro-specimen.....	133
4.4.2	Role of friction .....	135
4.4.3	Strengths measurements and fractography .....	137
4.5	Discussion .....	139
4.5.1	Critical flaws .....	139
4.5.2	Statistical strength analysis.....	140
4.6	Conclusion .....	143
4.7	Supplementary information .....	144

4.7.1	Notched specimen FE model with explicit contact friction .....	144
4.7.2	First principal stress distribution at the moment of ligament fracture.....	145
4.7.3	Sensitivity and error analysis.....	149
4.7.4	Statistical strength analysis.....	151
<b>Chapter 5</b>	<b>The local strength of individual alumina particles .....</b>	<b>155</b>
5.1	Disclaimer .....	155
5.2	Introduction.....	155
5.3	Materials and Methods.....	156
5.3.1	Material.....	156
5.3.2	Micromechanical testing .....	156
5.3.3	Finite Element (FE) simulation .....	158
5.4	Results.....	159
5.4.1	Mechanical testing.....	159
5.4.2	FEM analysis.....	165
5.4.3	Strength measurement results.....	167
5.5	Discussion.....	168
5.5.1	Precision of data .....	168
5.5.2	Near-theoretical strength in pristine particle regions .....	169
5.5.3	Strength-limiting defects .....	170
5.6	Conclusion .....	172
5.7	Appendix: Details of specimen preparation and testing .....	173
5.7.1	Carbon coating.....	173
5.7.2	C-shaped particle FIB machining.....	173
5.7.3	Micrometric bend beams .....	175
5.8	Appendix: Supplementary information.....	175
5.8.1	Polymer matrix – alumina particles sample preparation .....	175
5.8.2	Experimental data of tested particles.....	176
5.8.3	Supplementary figures.....	177
5.8.4	Sensitivity analysis .....	179
5.8.5	Investigation of the etching effect by means of nanoindentation.....	179
<b>Chapter 6</b>	<b>Conclusions .....</b>	<b>183</b>
6.1	Achieved results.....	183

6.2 Future developments.....	186
<b>References.....</b>	<b>189</b>
<b>Curriculum vitae.....</b>	<b>211</b>

## List of Figures

- Figure 1.1 – Illustration of three types of MMCs with (grey) different form of reinforcement: (a) particles, (b) whiskers and short fibres, and (c) continuous fibres. Figure reproduced from Ref. [15] with permission of Cambridge University Press. ....34
- Figure 1.2 – Specific modulus  $E/\rho$  vs. specific strength  $\sigma_f/\rho$  of different classes of materials according to [17]. The typical specific properties of fibre reinforced metal matrix composites (FRMMCs) in the longitudinal (fibre) direction and that of particle reinforced metal matrix composites (PRMMCs) are indicated with cyan boxes. A theoretical estimate of what can be achieved in PRMMCs provided that ceramic particles as strong as today engineering fibres are used as reinforcement is shown in red box. Figure reproduced from Ref. [17] with permission of Elsevier. Overlaid data from [5,16,18–21]. ....35
- Figure 1.3 – Alumina whisker strength as a function of its diameter and effect of chemical polishing with hot orthophosphoric acid on the whisker strength. Data from [84]. ....40
- Figure 1.4 – Selection of four different types of microscopic alumina particles produced by different methods, which have been used to produce PRMMCs. (a) Comminuted fused alumina containing visible cracks (reproduced from Ref. [116] with permission of Elsevier). (b) Vapour-grown Sumicorundum<sup>®</sup> alumina showing facets and grain-boundary grooves (reproduced from Ref. [116] with permission of Elsevier). (c) Atomized alumina prepared by a thermal spray technique with dendritic microstructure forming grain-boundary grooves and micropores (reproduced from Ref. [111] with permission of Springer). (d) Alumina platelets prepared by a proprietary mechanochemical process with notch-like asperities (image source: Merck KGaA (CC-by-ca 3.0)). ....43
- Figure 1.5 – 3D finite element simulation of a representative volume (RV) element of aluminium metal matrix composite reinforced with stiff (400 GPa) ceramic particles occupying 40 vol%. The RV element is deformed in the direction of the arrow (top right corner) with the applied strain 5%. Particles exhibit high tensile stresses in the direction of the applied strain with the peak value several times higher than the yield strength of the aluminium matrix. Figure reproduced from Ref. [117] with permission of Elsevier. ....44
- Figure 1.6 – An example of damage accumulation by particle fracture in an aluminium metal matrix composite reinforced with spherical ceramic particles investigated by 3D synchrotron X-ray tomography. Cracks in particles appear

perpendicular to the applied tensile stress. Reproduced and adapted from Ref. [118] with permission of Elsevier. ....45

Figure 1.7 – The effect of particle fracture on tensile properties of high-volume fraction (>40%) alumina particle reinforced aluminium MMC. (a) Larger reinforcement particles lead to a higher rate of damage accumulation by particle fracture, which in turn leads to higher loss of composite stiffness. (b) Composite reinforced with high quality vapour-grown alumina particles has a lower rate of damage accumulation by particle fracture than a composite produced with comminuted alumina particles, which (c) leads to enhanced tensile ductility in comparison with composite reinforced with comminuted alumina powder exhibiting a high density of surface cracks. Plots in panels (a) and (b) and particle pictures are reproduced and adapted from Ref. [116] with permission of Elsevier. Data in panel (c) is replotted from Ref. [116]. ....47

Figure 1.8 – Stress-strain curves of a ceramic particle reinforced metal matrix composite predicted using the local load sharing model of [16] with matrix hardening following the classical power law,  $\sigma = c \cdot \epsilon^{n_h}$ , with the strength coefficient  $c = 300$  MPa, hardening coefficient  $n_h = 0.2$ , and  $10^7$  ceramic particles occupying 50 vol% of the composite volume. (a) The role of the characteristic strength,  $\sigma_0$ , of ceramic particles on the resulting composite strength with particles' Weibull modulus fixed ( $m = 3$ ). (b) The role of the particles' Weibull modulus on the resulting composite strength with particles' characteristic strength fixed ( $\sigma_0 = 700$  MPa). Plots in the figure are reproduced from Ref. [16] with permission of Elsevier. ....49

Figure 1.9 – 2D finite element simulation of a single-edge notched aluminium metal matrix composite reinforced with 15 vol% SiC particles specimen containing a crack. (a) The effect of particle fracture on the Von Mises stress distribution. Notice that when particle fracture is operational particles fracture relatively far away from the crack tip which would lead to crack coalescence by particle fracture ahead of the primary crack. (b) Particle fracture reduces the degree of shielding from the particles, attracting the crack and decreasing the crack deflection. Figure reproduced from Ref. [188] with permission of Annual Reviews.....50

Figure 1.10 – The influence of the alumina particle intrinsic strength on fracture toughness of an aluminium alloy metal matrix composite. (a) The fracture toughness of the composite can be almost two times higher when the matrix is reinforced with higher quality vapour grown particles and comparable with aerospace grade engineering aluminium alloys. (b) The proportion of the cracked particles along the crack path is higher when low quality comminuted alumina particles are used. Plots in panels (a) and (b) reproduced from Ref. [19] with permission of Elsevier. Particle pictures reproduced from Ref. [116] with permission of Elsevier. ....51

Figure 1.11 – Weibull strength distribution of (a) comminuted white fused alumina from Hauert et al. [135] (reproduced with permission of Elsevier) and (b) presumably comminuted white fused alumina from Mochida et al. [164] (reproduced with permission of the Japan Institute of Metals and Materials) inferred from macroscopic composite testing using two different micromechanical models. (c) Comparison of the two strength distributions shows considerable difference in the predicted strength.....52

Figure 1.12 – Schematic representation of a sphere of radius  $R$  in uniaxial compression with the geometry definition. When the particle is compressed uniaxially by a pair of uniformly distributed loads  $F$  over a spherical cap represented by the contact radius  $a < (0.1 \times R)$ , a region of high tensile stress develops in the central portion of the particle with its peak located along the compression axis according to Hiramatsu and Oka [212]. The images in the figure are reproduced and adapted from Ref. [212] with permission of Elsevier...55

Figure 1.13 – Overview of Weibull statistic characteristic strength values from uniaxial compression of different pure engineering alumina particles prepared by different methods: (circles) comminuted fused alumina, (rectangle) comminuted sintered alumina and (triangle) vapor-grown alumina. Dashed lines represent extrapolation of the reported Weibull distribution results for different particle size. Data from [106,107,226,228,233]. .....58

Figure 1.14 – Uniaxial compression of a relatively equiaxed vapor-grown Sumitomo alumina particle between a pair of hard platens (diamond and glass). The particle broke into two pieces one of which was left on the glass bottom platen, such that fractography could be performed. The fracture initiated from the heavily damaged region where the particle contacted the diamond upper platen during the test, rather than from the centre of the particle, where one can observe large flaws in the form of pores. SEM image from unpublished work performed by the candidate. ....59

Figure 1.15 – Overview of the C-shaped test conducted on a 1mm silicon nitride sphere. The notch in the particle (a) was machined using a diamond-grinding wheel and tested in compression measuring the fracture load  $P$ . (b) Finite element simulation of the tested C-shape specimen shows that a state of high tensile stress is present along the surface just opposite to the root of the notch. (c-e) Fractographic analysis of SEM micrographs of one of the tested spheres reveals a surface scratch as the strength-limiting flaw located near the peak of the first principal stress (indicated by an arrow). The images in the figure are reproduced and adapted from Ref. [252] with permission of Elsevier.....62

Figure 1.16 – A schematic representation of a modern dual beam SEM/FIB instrument, which can micromachine various materials into specimens that can be tested for strength. The ion bombardment of material results in collision cascade of

- the primary ion with atoms of the sample, which in turn leads to a number of different processes including atom sputtering, irradiation damage of the sample and ion implantation. Images in the figure are reproduced from [260] with permission of Cambridge University Press.....64
- Figure 1.17 – Single crystal  $\alpha$ -alumina micropillar compression in the  $\langle 0001 \rangle$  direction. The crystal after compression exhibits apparent step formation and gliding along the  $\{01\bar{1}2\}1/3\langle 01\bar{1}1 \rangle$  slip system. Its activation was identified at a critical uniaxial compression stress near 23.7 GPa and critical resolved shear stress equal to 10.7 GPa. The figure is reproduced from Ref. [75] with permission of Elsevier. ....66
- Figure 1.18 – *In-situ* SEM microtensile test of a FIB milled copper dog-bone specimen protruding from a copper needle. The specimen is pulled using FIB machined tungsten microgripper fitted in a *in-situ* microindenter apparatus. The figure is reproduced from Ref. [295] with permission of Elsevier.....67
- Figure 1.19 – Microscopic three-point bending test of (a) a plate-like Si particle leached out of an Al-Si alloy. (b) The FIB milled bend beam features a trapezoidal cross-section and (c and d) is loaded with a wedge-shaped diamond probe. (e) The trapezoidal geometry of the beam results in a stress distribution such that the peak stress along the FIB unaffected surface subject to tension is 10% to 20% higher than the stress along one of the FIB milled beam edges. Images in the figure are reproduced from Ref. [300] available under the terms of the Creative Commons Attribution License (CC BY).....68
- Figure 1.20 – TEM micrographs of  $\alpha$ -alumina surface irradiated by 30 kV  $\text{Ga}^+$ . (a) A microcantilever specimen with FIB milled notch exhibits  $\approx 20$  nm thick Ga implanted layer, which appears as a dark film on the surface of the specimen and is indicated by the arrow. (b) High resolution TEM showing that FIB milling did not cause surface amorphization. The minute  $\approx 2$ nm thick amorphous layer was reported as a result of redeposition. (c) Nanobeam diffraction pattern from the implanted layer, confirming crystallinity. Images in the figure are reproduced from Ref. [315] with permission of Elsevier.....70
- Figure 2.1 - (a) Sketch of a spherical particle of radius  $R$  compressed between two elasto-plastic platens under load  $F$ . (b) Simplified boundary value problem associated with the sketch in (a). Pressure distribution in the region of contact, i.e. over the area of the spherical cap defined by the contact radius  $a$  and contact depth  $h$ , is assumed to be uniform: shear contact forces arising from friction and variations in normal stress are neglected. Possible pile-up of the platen material due to indentation is assumed comprised via the contact radius definition.....72
- Figure 2.2 – Distribution of the positive (tensile) normalized first principal stress,  $\sigma_1 = \sigma_1 \pi R^2 / F$ , calculated by solving Eq. (2.2), for relative contact radius values

$(a/R) = 0.1$  (a),  $0.5$  (b) and  $0.7$  (c). Regions of the sphere where  $\sigma_1$  is negative (*i.e.*, compressive) are shown in white. Poisson's ratio of the sphere is taken as  $\nu = 0.17$ , typical of glass. Given spherical symmetry only one quarter of the  $\{r, \theta\}$ -plane is considered. The axes represent normalized radial distance  $r/R$ . .....73

Figure 2.3 – Normalized first principal stress  $\sigma_1 = \sigma_1 \pi R^2 / F$  vs. the relative contact radius  $a/R$ , obtained by solving Eq. (2.2), in the centre of the sphere  $\sigma_{1c} = \sigma_1(r = 0, \theta = 0)$  (dashed line) and on the surface equator  $\sigma_{1s} = \sigma_1(r = R, \theta = \pi/2)$  (dotted line). The value of the global maximum,  $\max \sigma_1$ , is shown with the solid line. Poisson's ratio of the sphere is taken as  $\nu = 0.17$ , typical of glass. ....74

Figure 2.4 – (a) Evolution of the normalized first principal stress  $\sigma_1/k$  in the sphere center (dashed line) and along the surface equator (dotted line) versus the relative contact radius  $a/R$ , as obtained from Eq. (2.5). The global maximum of the field is shown with the solid line. The exponent of Meyer's law,  $n$ , used in calculations is 2 (blue) and 2.5 (red). In (b) and (c) grey areas show regions within the particle where the maximum tensile principal stress is increasing; (b):  $(a/R) = 0.5$ ; (c):  $(a/R) = 0.7$ ; for both, the platen Meyer index,  $n$  equals 2. Poisson's ratio of the sphere is  $\nu = 0.17$ . .....75

Figure 2.5 – Required platen Meyer hardness to test particles of given strength, assuming platen material with  $n = 2$  and relative contact radius at the moment of failure  $(a/R) = 0.7$ . The three lines represent the relationship for three values of the particle Poisson ratio  $\nu$ . Hardness values of the four materials indicated on the left are conversions to SI units of Brinell or Vickers hardness values from the literature (close although not exactly equal to Meyer hardness values). .....77

Figure 2.6 – Custom-built instrumented compression apparatus. (a)  $x$ -,  $y$ - and  $z$ -axis linear motion stages, (b) monochromatic camera, (c) piezo actuator, (d) high-stiffness load cell, (e) objective, (f) flat-end conical tip, (g) two-axis goniometric tilt stage, (h) active vibration-isolation system. ....78

Figure 2.7 – Typical uniaxial compression test of a fused quartz particle: (a) force-displacement curve. Initial non-linear part of the response represents the embedding of the particle in the soft colloidal graphite layer. Contact between the particle and the steel platen is marked by a significant increase of the response slope; (b) and (d) scanning electron microscopy images of the particle before and after the test; (c) optical image of the upper platen surface showing the indent left by the particle after the test. ....81

Figure 2.8 – (a) Experimentally measured values of the critical force divided by the particle cross-sectional area,  $F_{max}/\pi R^2$ , versus the relative contact radius  $a/R$ . (b) The data align on a master curve when normalized by the Vicker's hardness  $HV$  in SI units. The dashed line represents the least squares fit of Meyer's law giving  $k = kHV = 1.2$  and  $n = 2.2$ . ....81



Figure 2.9 – First principal stress versus the relative contact radius  $a/R$ : (a) in the centre of the compressed particle,  $\sigma_{1c}$  and (b) along the surface equator,  $\sigma_{1s}$ . Symbols represent calculated stress values using the HO-SH analysis, Eq. (2.2), based on measurements of the critical load at failure  $F_{max}$  and corresponding relative contact radius  $a/R$ . Dashed lines give predictions for  $\sigma_{1c}$  and  $\sigma_{1s}$  based on the HO-SH solution and Meyer’s law (Figure 2.8 and Eq. (2.5)). Symbol shape and colour indicate the platens used: HV450 (circle, orange), HV600 (triangle, red), HV750 (diamond, green) and HV950 (square, blue). Vertical lines separate different failure domains, as discussed in the Theory section. ....82

Figure 2.10 – SEM images of particles after uniaxial compression testing. (a) Particle that failed at  $(a/R) < 0.65$  (in Domain II), shattered into many pieces but leaving a central column roughly extending from the lower surface to the particle centre, along which river markings suggest crack growth from the particle centre to a point of load application. (b) and (c) show two particles that failed at relatively mild surface peak stress values, namely 610 and 450 MPa, respectively. The particle in (b) failed at  $(a/R) > 0.65$  (Domain III): several meridian cracks are visible, consistent with the predicted stress distribution at that moment. The particle in (c) failed at  $(a/R) < 0.65$  (Domain II); a subsurface pore can be observed along the path of one meridian crack, with river markings suggesting crack growth away from the pore. ....83

Figure 2.11 – Estimated particle surface strength distribution computed using only data for which  $(a/R) \geq 0.65$  (Domains III and IV), using left-truncation and right-censoring according to the non-parametric Product-limit estimator, plotted together with 95% point-wise confidence intervals, or alternatively assuming Weibull statistics coupled with a maximum likelihood estimation of parameters. ....88

Figure 2.12 – (a) Product-limit estimation of particle surface strength for particle populations from (black) Domains III and IV (left-truncated/right-censored data), together with (black dotted) corresponding 95% point-wise confidence intervals, (dark-grey) data from Domain II (right-truncated data), and (light-grey) ensemble of all data points (right-censored) except for four particles containing evident large pores, which failed at low stress. (b) The same three data sets with their maximum likelihood estimation of two-parameter Weibull distribution parameters: (black)  $m = 6.3$  and  $\sigma_0 = 890$  MPa, (dark-grey)  $m = 6.5$  and  $\sigma_0 = 920$  MPa, (light-grey)  $m = 6.6$  and  $\sigma_0 = 910$  MPa. ....89

Figure 2.13 – Evolution of the normalized first principal stress for a fused quartz particle with 15  $\mu\text{m}$  radius loaded with upper platen displacement rate 1  $\mu\text{m/s}$  and Mayer’s law index of the platen  $n = 2.2$ . ....92

Figure 2.14 – Comparison of the peak surface strength distribution of the (black) original data (influenced by SCG) and (grey) same after correction for the effect of SCG. Smooth solid curves represent the estimated Weibull distributions using a

maximum likelihood method; corresponding parameters are  $m = 6.3$ ,  $\sigma_0 = 890$  MPa and  $m = 5.6$ ,  $\sigma_0 = 1540$  MPa for the original and SCG corrected data, respectively. The solid stepped curves represent the Product-limit estimator, together with corresponding dotted curves representing 95% point-wise confidence intervals of the Product-limit estimator. ....93

Figure 2.15 – The uniaxial compression test done in the same conditions as the other test in this work except that loading was deliberately interrupted before failure and particle was left under the static load of roughly 2.5 N with the relative contact radius of  $\sim 0.87$  resulting in roughly 600 MPa peak surface stress for approximately 60 s after which the particle failure occurred accompanied by a sharp drop in load. The particle failed in shattering mode into many pieces as was typical for the majority of particles tested in the study. This experiment shows that particle may fail even after the maximum attainable peak tensile surface stress was applied when SCG operates. ....97

Figure 2.16 – Particles with apparent internal pores that were not considered in the surface failure statistics. (a), (b), (c), (d) optical images before the test of particles HV600-#1-2, HV600-#1-4, HV600-#1-7 and HV450-#5-5, respectively. (e) SEM image made at  $33^\circ$  tilt after the test of the particle A564-AH-450-#5-5 with two big pores present on the fracture surface that match the two distinct dark spots on the optical image.....97

Figure 2.17 – (a) Product-limit estimator of the left-truncated and right-censored data from the Table 2.4 obtained from hypothetical three sets of 30 duplets representing particles tested in the Meridian crack test along with the Maximum likelihood estimation of two parameter Weibull distribution ( $m = 7.2$ ,  $s = 910$ ). (b) Product-limit estimator of the left-truncated and right-censored obtained from hypothetical three sets of 10,000 duplets representing particles tested in the Meridian crack test along with the Maximum likelihood estimation of two-parameter Weibull distribution ( $m = 7.01$ ,  $s = 902$ ). In both cases the original Weibull distribution of surface strength was with parameters  $m = 7$ ,  $s = 900$ .101

Figure 2.18 – (a) Sketch of an axisymmetric finite element mesh used for modelling the crushing test of spherical particles by elastic-perfectly-plastic platen. Prescribed vertical boundary displacement  $u_y$  along the top platen surface was used to load the system. (b) Stress field contour map for particle compressed up to contact radius  $a/R \approx 0.85$  for case of frictionless contact between the sphere and the platen.102

Figure 2.19 – (a) Normalized first principal stress  $\sigma_1 = \sigma_1 \pi R^2 / F$  as a function of the relative contact radius  $a/R$  in the center of the sphere (dashed lines) and on the surface equator (solid lines). Solution by Hiramatsu and Oka (Eqs. (2.1a-d), main text) is shown with black lines and results of FEM calculations with coloured lines. FEM calculations are carried out for three values of the contact friction coefficient: 0 (red), 0.1 (green) and 0.3 (blue). (b) Distribution of the contact pressure at contact

radii  $a/R = 0.2, 0.4, 0.6$  and  $0.8$  and for the case of contact friction  $\mu = 0$  (red) and  $0.3$  (blue).....103

Figure 2.20 – (a) Sketch of a spherical particle of radius  $R$  compressed between two elasto-plastic platens under load  $F$  with a far smaller debris particle present in-between the compressed particle and platen at Spot  $A$ . The contact perimeter between the compressed particle and steel platen is indicated by the letter  $B$ . (b) The debris particle of Young’s modulus  $E'$ , Poisson’s ratio  $\nu'$  and radius  $\rho$  (red) indents the larger tested particle (grey) under uniaxial compression with a force  $P$ , creating a local elastic contact of radius  $b$ . The local cylindrical coordinate system  $x, z, \alpha$  is at the debris particle plane of symmetry taken to be homothetic with the compressed sphere coordinate system  $\theta, r, \varphi$ . .....104

Figure 2.21 – Distribution of the normalized stress  $\sigma/\theta$  along the surface of a compressed fused quartz particle due to (black) uniaxial compression with relative contact radius  $(a/R)=0.7$  and platen with Meyer’s constants representing HV600 steel platen, (green) a Hertzian indentation stress along the surface of fused quartz particle by a debris particle with relative radius  $\rho = 0.2\mu\text{m}$ , elastic modulus of 72 GPa and Poisson’s ratio 0.17, (red) a Hertzian indentation stress along the surface of fused quartz particle by a debris particle with relative radius  $\rho = 1\mu\text{m}$ , elastic modulus of 400 GPa and Poisson’s ratio 0.25 and (blue) a Hertzian indentation stress along the surface of fused quartz particle by a debris particle with relative radius  $\rho = 1\mu\text{m}$ , elastic modulus of 72 GPa and Poisson’s ratio 0.17. The dashed vertical line represents the contact perimeter defined by the compressed particle-platen contact radius  $a$ . .....106

Figure 3.1 – (a) Overview of as-sprayed Eucor particles after sieving through  $45\mu\text{m}$  sieve. (b) XRD pattern of (black) as-sprayed and (red) annealed powder.  $t =$  tetragonal,  $m =$  monoclinic. ....110

Figure 3.2 – (a) SEM micrograph of polished cross-section of as-sprayed amorphous Eucor particles. Panel (a) shows an amorphous particle. Panels (b) and (c) are micrographs of nanocrystalline Eucor particles obtained after 1h annealing at  $1300^\circ\text{C}$  revealing nanostructured grains of (gray) mullite and (light) tetragonal and monoclinic zirconia. A micropore is evident in the cross-section of the amorphous particle (a). .....111

Figure 3.3 – Experimentally measured values of the critical force at failure normalized by the cross-sectional area of the tested particle,  $F_{\text{max}}/(\pi R^2)$  for (triangles) amorphous and (circles) nanocrystalline Eucor particles tested with (blue) HV700, (red) HV600, and (cyan) HV450 platens, respectively. Solid lines represent best fit with the power-law function  $f(a/R) = k(a/R)^n$  representing the platen material Meyer’s law. Values of the fitted parameters were (blue)  $k = 8150$ ,  $n = 2$  for HV700 platens, (red)  $k = 5900$  and  $n = 1.8$  for HV600 platens, and (cyan)  $k = 3990$ ,  $n = 1.7$  for HV450 platens. ....112

Figure 3.4 – SEM images of amorphous Eucor particles after uniaxial compression, illustrating particles for which distinct flaws were observed at one of the meridional cracks. (a) One meridional crack was observed for this particle, which broke at relatively low load. A pore of diameter  $\approx 1 \mu\text{m}$  was observed just below the surface on the meridional crack surface. (b) The mirror-mist and hackle fractographical features point to a subsurface pore as the origin of failure. (c) shows the only particle fracture surface along which a flaw other than a pore was identified as the origin of the failure, this being a surface inclusion. The fracture surface of amorphous Eucor particles is typically very smooth and featureless in the “mirror” region close to the origin of failure. ....113

Figure 3.5 – SEM images of nanocrystalline Eucor particles after uniaxial compression. Panels (a), (b), and (c) illustrate three different particles for which mirror-mist-hackle patterns surrounding a pore present at one of the meridional crack fracture surfaces can be observed. In each case a surface pore was identified as the origin of failure. The fracture surface exhibits greater roughness compared to amorphous particles (Fig. 3.4). The grain structure is revealed on fracture surfaces, showing transgranular fracture of mullite grains (gray) and intergranular decohesion of zirconia grains (bright) close to the fracture initiation point (panel (c)). ....114

Figure 3.6 – Average (tensile) stress trajectories during uniaxial compression of spherical particles with Poisson’s ratio 0.28, particle-platen friction coefficient 0.28 and tested with (blue) HV700, (red) HV600, and (cyan) HV450 platens calculated using Eqs. (3.5)-(3.6). The stress trajectories are plotted for (dotted) the center of the particle and (dashed) the particle surface equator versus the relative contact radius. Arrows indicate maxima for each stress trajectory and as such represent boundaries (in terms of  $a/R$ ) between different Domains. ....116

Figure 3.7 – Surface equatorial stress at the moment of failure for tested particles versus the relative contact radius  $a/R$  for (a) amorphous and (b) nanocrystalline Eucor particles. Dashed lines represent the average stress trajectories and solid vertical lines represent predicted boundaries between Domains III and IV for given platens. Symbols at the far right represent particles that survived until platens contacted. ....118

Figure 3.8 – Survival probability of (red) amorphous and (blue) nanocrystalline Eucor particles with respect to the surface equatorial stress evaluated from Domain III and IV events. (continuous solid lines) two parameter Weibull distribution, (stepped lines) Kaplan-Meier product-limit estimator, (dashed stepped lines) 95% confidence intervals for the Kaplan-Meier estimation. ....120

Figure 3.9 – Comparison of the surface equatorial stress survival distribution of (a) amorphous and (b) nanocrystalline Eucor particles obtained using events from Domains III and IV and Domains II, III and IV where failure events from Domain

II are considered all to be due to the surface stress. Two optical microscopy pictures represent amorphous and nanocrystalline particles observed before testing and which failed at relatively low loads in Domain II: one notices the presence of micrometric pores near the particle center. These (a) amorphous and (b) nanocrystalline particles failed for central stress values  $\sigma_{1c} = 580$  MPa and  $\sigma_{1c} = 660$  MPa, respectively. ....122

Figure 3.10 – FIB machined cantilever beam at the top of an amorphous Eucor particle partially embedded in a polymer matrix. ....124

Figure 3.11 – The measured equatorial fracture stress versus the observed mirror diameter surrounding pores identified as failure origin for (circles) 5 particles that failed in Domain III and (triangle) 2 particle that failed in Domain II. Straight lines represent different slopes of different values of  $k_m \cdot K_{IC}$ . ....126

Figure 3.12 – (a) The measured equatorial fracture stress versus the observed radius  $r_p$  of surface or subsurface pores identified as the failure origin and assimilated to sharp penny-shape cracks with a geometry factor  $Y = 1.13$ , for (circles) 3 particles that failed in Domain III and (triangles) 5 particles that failed in Domain II. Straight lines represent different slopes for different values of the (Mode I) fracture toughness  $K_{IC}$ . (b) SEM micro-fractograph of a nanocrystalline particle with a surface pore that was visibly the origin of failure, exhibiting a relatively rough fracture surface giving a relatively high deduced fracture toughness  $\approx 2.2$  MPa.m<sup>1/2</sup>. (c) SEM micro-fractograph of a particle that exhibits a very fine microstructure with equiaxed grains a few tens of nanometer in diameter and a small (relative to the previous case) pore as the failure origin. This particle exhibits a relatively low deduced fracture toughness  $\approx 1.1$  MPa.m<sup>1/2</sup>. ....127

Figure 3.13 – Comparison of the strength distribution of nanocrystalline Eucor from this study with (cyan) chemically and microstructurally similar 3M Nextel™ 720 fibres and (orange) 3M Nextel™ 610 nanocrystalline alumina fibres both tested along 25 mm gauge length in tension in [335]. In red is the estimated local strength distribution of the Nextel™ 610 fibres for the effective volume 10  $\mu\text{m}^3$  tested using the micromechanical C-shaped sample test in [324]. ....128

Figure 4.1 – Notched micro-strength test specimen prepared in an alumina fibre embedded within an aluminium matrix composite. (a) Composite wire polished in two planes with a  $\sim 90^\circ$  edge passing roughly through the wire diameter. (b) Alumina fibres exposed by deep etching the Al matrix. (c) Typical notched sample prepared by FIB milling. (d) Sketch of the one half of a notched specimen (left) with dimensions defined within the specimen plane of symmetry (right)..131

Figure 4.2 - Notched specimen with ligament outer surface that is shielded by other fibres from being directly exposed to the FIB. (a) Perspective and (b) view along

the FIB machining direction of the same notched fibre sample (indicated by an arrow).....132

Figure 4.3 – Notched specimen response to load-unload cycle. (a) Vertical force, (b) lateral force, and (c) apparent friction coefficient as a function of vertical displacement. The experimentally measured response is shown in light grey. The response obtained by finite element calculations from non-optimized models and for a friction coefficient  $\mu = 0.08$  is shown with (magenta) inverted triangles and for  $\mu = 0.15$  with (green) circles. The corresponding responses after optimization of models are indicated with solid line. ....135

Figure 4.4 – Effect of friction on the first principal stress distribution,  $\sigma_1$ , at vertical displacement  $0.25 \mu\text{m}$ . (a)  $\sigma_1$  distribution map on the surface of the specimen for  $\mu = 0.08$ . (b)  $\sigma_1$  distributions along the Line PQ for non-optimized ( $H$ ) and optimized ( $H+H_m$ ) notched specimen length as a function of  $\mu$ . Line colouring in graph is the same as in Figure 4.3.  $\sigma_1$  maps in plane of axial symmetry for the case  $\mu=0.15$  are shown to the right. (c)  $\sigma_1$  distribution along the Line PQ and in the plane of axial symmetry for the case  $\mu \rightarrow \infty$ . Data for the non-optimized and optimized specimen length are indicated with symbols and dash-dotted line, respectively. The colour scheme for  $\sigma_1$  maps in panels (c) is the same as that indicated in panel (b). Arrows denote additional regions of elevated stress in non-optimized models that may develop under certain circumstances; see the main text for discussion.137

Figure 4.5 – Fracture of a notched specimen. Specimen before (a) and after (b) fracture. (c) Fractured surface of the ligament sample shown in panel (b) investigated by high resolution SEM. (d) High magnification image of the critical flaw region from panel (c). (e)–(h) Representative examples of the mirror region encompassing the zone of debonded grains indicating the critical defect (outlined in red) as observed on the fracture surfaces of other broken ligaments. ....138

Figure 4.6 – Strength as a function of surface defect size for alumina fibre. Triangles represent strength data obtained by macroscopic tensile tests in samples for which the critical defect was identified as a surface flaw. Circles represent data obtained from the present work (peak stress  $\sigma_{1cp}$  and critical flaw size  $c$  reported in Table 4.1 in Supplementary information, Section 4.7.2). The solid line is a linear fit of Eq. (4.1) to the data points with  $K_{Ic} = 2.34 \text{ MPam}$  and a geometrical factor  $Y=1.04$  (treated as a fitting parameter). ....140

Figure 4.7 – Alumina fibre size effect. Weibull scaling from literature data measured by macroscopic tensile tests on alumina fibres of gauge length  $L = 25 \text{ mm}$  (triangles),  $125 \text{ mm}$  (squares) and  $254 \text{ mm}$  (diamonds) [99,100,335]. The slope of the dashed line is  $-1/m$  with  $m = 9.7$ . The strength data obtained from present notched microspecimen tests are indicated by circles. Weibull scaling based on microscopic strength statistics is indicated by the dotted line with slope of  $-1/7.2$ . Open symbols represent results obtained for individual tests indicating the range of



- effective volumes. Solid symbols represent the characteristic strength values corresponding to representative effective volumes of the tests. ....142
- Figure 4.8 – Example of 3D FE mesh used in modelling notched specimen.144
- Figure 4.9 – Vertical response of two notched specimens up to the moment of fracture and corresponding tensile first principal stress distribution,  $\sigma_{1c}$ , at the critical point C indicated with the square symbol. The experimentally measured response is plotted in black. Corresponding response obtained from FE calculations is indicated in colour. The predicted response assuming fully constrained lateral motion of the rooftop is shown in red. The two-step calculations used to obtain the stress distribution at the critical point are: (1) frictionless sliding up to the critical vertical displacement  $U_{zc}$  (blue) and (2) lateral pullback deflection at constant vertical displacement  $U_{zc}$  up to the critical load  $F_{zc}$  (green). The response of the model in panel (b) assuming constant, back-calculated friction coefficient (see text for details) is shown with magenta crosses. The scale bar for the stress map in panel (b) is the same as in panel (a). The tensile first principal stress field contained within the volume outlined in pink is used for the statistical strength analysis. ....146
- Figure 4.10 – Distribution of normalized first principal stress  $\sigma_{1c}$  at the moment of ligament fracture on the surface of a ligament in the plane of axial symmetry along the relative ligament height (Line PQ) for all 26 tested specimens. The first principal stress  $\sigma_{1c}$  is normalized by the corresponding peak stress  $\sigma_{1cp}$  in the ligament. The ligament length is  $l$ , while the beginning of the ligament is measured by  $z$ -coordinate of point Q, *e.g.*  $z_Q$  (see also main text, Figure 4.4). ....148
- Figure 4.11 – The Weibull failure probability distribution for nano-crystalline alumina fiber obtained from the 26 notched specimens is characterized by the Weibull modulus  $m = 7.2$  and the scaling constant  $S_0 = 6.88 \text{ GPa} \cdot \mu\text{m}^{3/7.2}$ . ....153
- Figure 5.1 – Schematic representation of a C-shaped particle test. (a) A polyhedral Sumicorundum particle partially embedded in a polymer matrix is (b) FIB machined into a C-shape configuration, and then tested in compression to bend a ligament of rectangular cross-section. The back surface of the ligament is left unaffected by the FIB milling operation, by design of the machining process and by coating the particle surface with a layer of weak carbon  $\approx 40 \text{ nm}$  thick. The roof machined at the top of the particle defines the load application line. (c) Sketch of a notched specimen with dimensions defined. (d) As a result of the machining process, the roof and notch side are oriented at a shallow angle ( $< 5^\circ$ ) with respect to the matrix free surface normal (see Appendix, Section 5.7), such that the roof-edge and indenter can be aligned using a tilt stage so as to be parallel in the nanoindentation apparatus prior to testing. (e) Once the notched specimen is loaded by applying a vertical displacement (along the  $z$ -axis), the roof slides laterally along

- the flat indenter surface, introducing a measurable friction force in the lateral direction (along the x-axis).....157
- Figure 5.2 – (a) A partially embedded Sumicorundum particle containing a grain boundary is (b) FIB milled to form a micro-cantilever that contains the grain boundary. The top surface of the micro-cantilever subject to tension during mechanical testing is left in its pristine condition, meaning unaffected by FIB. (c) Sketch of a cantilever beam geometry used in the work with definition of relevant dimensions. The edge defined by angle  $\delta$  is formed where two particle facets meet. The dashed line represents the simplified beam geometry in which the geometry-related stress concentration is eliminated. ....158
- Figure 5.3 – C-shaped particle test of a typical single-crystalline Sumicorundum AA-18 particle with the ligament back-surface in *pristine* condition, free of FIB damage and apparent defects (Category I, Specimen I-4). (a) SEM image of a polymer-matrix composite sample with particles partially embedded in the matrix after deep-etching. SEM images of the selected particle (b) before and (c) after FIB machining. (d) Vertical and lateral force vs. vertical-displacement response of the notched particle during the test. (e) SEM image of the particle after the test and (f) close-up of the fracture surface with an arrow indicating the apparent failure initiation location suggested by river-markings observed on the fracture surface. ....161
- Figure 5.4 – Summary of cantilever beam testing of a Sumicorundum AA-18 particle containing a grain-boundary groove (Category VI, specimen VI-3). SEM micrographs of (a) selected particle before and (b) after FIB machining. (c) Three frames during the in-situ SEM test using nanomechanical testing instrument equipped with sharp tungsten needle. (d) Close-up of the fracture surface of the beam after the test with arrows indicating two observed pores in the fracture surface. ....162
- Figure 5.5 – Overview of tested representative specimens from (a) Category II (II-1), (b) Category III (III-1), and (c) Category IV (IV-1). (a1-2) A few hundred nanometers of pristine ligament back-surface were milled away with the focused ion beam parallel to the original surface. (a3) Radial ridges observed on the fracture surface suggest fracture initiation (arrow). (b1) A pore  $\approx 800\text{nm}$  in diameter (arrow) was revealed while machining the sides. (b2) The outer ligament surface was also FIB machined in order to locate the pore close to the ligament surface where the tensile stress peaks during the consequent mechanical test. (b3) Close-up of the fracture surface after the test with fractographical features suggesting that the pore was indeed the origin of the failure. (c1) Twinned surface specimen before and (c2) after FIB machining with visible re-deposition of material on the ligament back-surface. (c3) The same specimen after the test with its fracture surface: re-deposited material has delaminated during the mechanical testing. ....163



Figure 5.6 – Overview of tested representative specimens from (a) Category V (V-3) and (b) Category VI (VI-1). (a1) A specimen with a grain-boundary oriented roughly horizontal to the free-surface of the polymer matrix and (a2) contained in the ligament with all four sides machined by FIB and therefore a flat ligament back surface (without grain-boundary groove). (b1) The only C-shape specimen from the Category VI with a grain boundary groove. (b2) Specimen contained the grain boundary within its ligament after FIB machining. Compared to the other two specimens from Category VI tested in the cantilever beam configuration, the grain boundary extends only through a portion of the ligament cross-section; see (b3).  
 .....165

Figure 5.7 – FEM simulation of a C-shaped specimen test with representative particle dimensions (I-2). (a) Simplified 2D plane strain FEM model of the particle with dimensions visible by imaging from its side and with encastre boundary condition at its bottom. (b) The full 3D FEM model of the same particle takes into account the portion of the particle embedded in the polymer matrix. (c) The load-displacement curves from (blue) experiment, (dashed-green) the 3D FEM model including the polymer matrix, (dotted-red) the 2D plane-strain FEM model, and (dashed-yellow) 3D model with the same boundary conditions as for the 2D model. A loop in the experimental curve represents one load-unload cycle conducted before the displacement was ramped-up all the way to failure. (d) Comparison of the distribution of the maximum (tensile) principal stress along the ligament outer surface of the full 3D and 2D FEM model loaded with the pair of vertical and lateral force ( $F_x$ ,  $F_z$ ) measured at the moment of failure in the experiment. ....166

Figure 5.8 – FEM model of the cantilever beam from Figure 5.4 with visible grain-boundary groove. (a) Dimensions used to produce (b) the 3D FEM model. Note that the simplified beam geometry was used with the beam’s top surface flat as outlined in Section 5.3.3 (Figure 5.2). The strength of the specimen evaluated as the first principal stress at the position of the grain-boundary groove was 2.3 GPa.167

Figure 5.9 – Summary of results obtained by testing C-shape and micro-cantilever beam specimens of Sumicorundum alumina particles. The vertical axis of the plot represents the first principal stress present in the vicinity of the observed fracture initiation at the moment of failure. Specimens are sorted along the horizontal axis by category. Two fully black circles for Category I represent specimens for which the fracture surface could be observed and for which the stress in the vicinity of the observed failure is reported, while the three grey circles represent specimens for which the fracture surface was likely not apparent; for these three specimens, the reported failure stress value is the peak first principal stress in the ligament at the moment of failure. ....168

Figure 5.10 – Strength values for Categories III, IV and VI corrected for the corresponding stress concentration factor, namely  $k_t = 2$  for spherical pores,  $k_t \approx 2.5$

for a jagged surface calculated from separate FEM simulation and approximately  $k_t \approx 2-3$  for realistic geometry of the present grain boundary grooves from [389]. Measured values for Categories I, II and V with no visible defects are plotted along as partially transparent symbols. Note that the correction for the jagged surface sample is the value of maximum principal stress in the root of the twinned jagged surface notch; however, the exact location of failure (at the scale of the strong stress gradient around the notch root) is unknown, thus the value presented is an upper bound. In the case of grain boundary grooves, symbols represent correction with the average estimated stress concentration of 2.5 and the uncertainty in this factor (which can be between 2 and 3) translates into bigger error bars. ....172

Figure 5.11 – Two ways to FIB machine a notched specimen from a polyhedral particle (a) partially embedded in a matrix to test in C-shape configuration, by bending a ligament of rectangular cross-section. The particle sides are first machined either (i) with a FIB beam roughly perpendicular to the free surface of the matrix (i-b) or (ii) sideways with the FIB beam at a shallow angle ( $26^\circ$ ) (ii-b). The last step of a notched specimen preparation involves machining of the wide rectangular notch and single-edge roof, again using the FIB beam, oriented at a very shallow angle ( $2-5^\circ$ ) roughly perpendicular to the previously machined sides which is identical for both milling strategies (i-c and ii-c). ....174

Figure 5.12 – Panels (a) and (b) represent a particle from Category I (I-5) for which the observed fracture surface appears somewhat below the original ligament in the region that experienced significantly lower tensile stress than along the ligament surface. Panels (c) and (d) show a particle from Category II (II-2) that also broke for relatively high stress along the ligament surface and exhibit secondary microcrack (arrows) propagating from the bottom corner of the ligament towards the opposite end below the ligament. ....178

Figure 5.13 – (a) Specimen of Category III (III-2) with an elliptical pore within the ligament, which was revealed only after the test by observing the (b) lower and (c) upper part of the fracture surface. Although all four sides of the ligament were FIB milled, failure initiated from the pore below the ligament surface, and hence from material unaffected by FIB machining. ....178

Figure 5.14 – Representative nanoindentation curves of alumina particles before (black lines) and after (red lines) the etching exposure .....180

Figure 6.1 – (a1-a3) A C-shaped sample test conducted on one comminuted “F-series” white fused alumina particle with the ligament machined along a particle flat facet. The strength evaluated using finite element analysis according to Chapter 5 was found to be  $(11 \pm 2)$  GPa. Fracture apparently initiated close to the location of peak maximum principal stress, situated roughly in the centre of the ligament width; the fracture surface presents very clear mirror-mist-hackle features indicating the failure origin, which was associated with one of the shallow surface

cracks (white arrow) running along the ligament surface parallel to the tensile stress.  
Panels (b-d) show deep cracks (white arrows) that are readily observed in other  
comminuted alumina particles of this type.....187

## List of Tables

Table 1.1 – Properties of selected alumina and alumina-based polycrystalline fibres. .....	41
Table 2.1 – The four platen materials. ....	80
Table 2.2 – Results used for surface strength survival analysis. ....	87
Table 2.3 – Experimental and numerical data of tested particles. ....	96
Table 2.4 – Data from a hypothetical test. ....	100
Table 3.1 – Values of the relative contact radius $a/R$ at the beginning and end of Domain III for tested amorphous and nanocrystalline Eucor particles ( $\nu = 0.28$ , $\mu = 0.28$ ) and the tensile stress values identified as the left-truncation, $\sigma_T$ , and right-censoring, $\sigma_C$ values. ....	117
Table 3.2 – Ensemble of the Domain III and IV results used to calculate the surface stress survival probability. ....	119
Table 3.3 – The effect of different Poisson’s ratio on results of surface Weibull strength distribution of Eucor particles. Particle-platen friction fixed at 0.28.	125
Table 3.4 – The effect of different platen-particle friction coefficient on results of surface Weibull strength distribution of Eucor particles. Particle Poisson’s ratio fixed at 0.28. ....	125
Table 4.1 – Experimental and numerical data of tested notched fiber specimens. .....	147
Table 4.2 – Sensitivity of the ligament peak stress on notched sample geometry perturbations. ....	149
Table 5.1 – Dimensions and experimental data of tested C-shaped particle specimens. ....	177
Table 5.2 – Dimensions and experimental data of tested micro-cantilever specimens. ....	177
Table 5.3 – Average and standard deviation values of reduced modulus of Sumicorundum alumina particles before and after etching exposure. ....	180

# Introduction

The emergence of advanced engineering fibres with extremely high strength and modulus of elasticity such as boron, carbon, silicon carbide, and alumina fibres was the answer of materials scientists and engineers to the great demand for stronger, stiffer and yet lighter materials in fields such as aerospace, energy, and civil engineering. Composites reinforced with such strong fibres and with a metallic, ceramic or polymer matrix have since become omnipresent. Most composites nowadays have a polymeric matrix; however, metals are attractive as a matrix material in composites because they combine high strength with high toughness and can maintain these properties well above room-temperature.

In all such composites, the strength of the composite reinforcement is crucial as the stiff hard second phase carries a higher proportion of the applied load and as damage accumulation by reinforcement fracture is generally the critical composite failure mechanism. Advanced engineering fibres are made strong by controlling their microstructure and keeping their size only a few tens of micrometres in diameter, which significantly decreases the chance of finding a gross defect along the fibre. Advanced composite fibres therefore provide one of the clearest manifestations of the *smaller is stronger* phenomenon.

While the strength of the reinforcing fibres used in composites has been the subject of intensive research without which the emergence of strong fibres and advanced composites would not have been possible, the strength of their particulate counterparts, also of microscopic size and used in composites but also found as coarse precipitates in alloys, have received far less attention. In general, comminuted ceramic powder particles ( $\text{Al}_2\text{O}_3$ , SiC), originally produced for use as abrasives and typically containing a high density of large defects, have commonly been used in the development, realization, use and study of particle-reinforced metal matrix composites (PRMMCs). As a consequence, the properties of today's PRMMCs remain well below those of fibre-reinforced metals or advanced metallic materials. The composite becomes in general more brittle with higher volume fraction of ceramic particles while rather high ceramic contents are necessary for an effective increase of the composite stiffness. The importance of the particulate reinforcement intrinsic strength on the overall composite mechanical performance can be illustrated using today's attractive class of composites inspired by nature – brick-and-mortar “nacre-like” composites. The substitution of relatively weak and fragile polycrystalline aragonite ( $\text{CaCO}_3$ ) reinforcing platelets present in naturally occurring nacre, with inherently stronger synthetic alumina platelets, leads to a substantial increase of both strength and fracture toughness of the composite [1–4].

Particulate reinforcements compared to their fibrous counterparts are attractive as a reinforcement for metals because they offer in general (i) potentially lower cost of the reinforcement production, (ii) simpler and thus lower cost composite production processes, (iii) isotropic composite properties, (iv) in certain conditions compatibility with conventional metalworking (machining, welding etc.), and (v) in certain conditions superior ductility [5]. In prior research within the Laboratory of Mechanical Metallurgy at EPFL it has been shown that (i) the particle intrinsic strength has pronounced effects on tensile properties of MMCs [6], (ii) even high-volume fraction ( $\approx 50\%$ ) PRMMCs may exhibit toughness comparable to engineering aluminium alloys [7], and (iii) if particles with strengths of advanced engineering fibres were produced and used as reinforcement, remarkably strong and tough PRMMCs should result [8].

One of the main reasons why the strength of microscopic reinforcing particles has received little attention in research is that it is difficult to measure. There are several reasons for this. The most obvious is that any near-spherical object is difficult to grip, making the application of tensile stress a challenge. Another reason is that particles typically used in composites are both irregularly shaped and small. Detecting the fracture of such second phases and estimating their strength is therefore generally conducted using indirect methods, based on more or less elaborate and realistic micromechanical models of two-phase composite material behaviour. Such models generally assume second phase particles of strongly simplified shape (e.g. spherical) and lead to little if any knowledge of the flaws that determine the particle strength.

One aim of this work is thus to develop new methods by which one can probe the local strength of individual microscopic hard and brittle particles, and at the same time to identify the strength-limiting defects within such particles. Novel methods of probing the strength of particles at the microscopic scale can furthermore be transferred and have significant impact also in other fields; notably for testing hard and brittle precipitates in alloys, fillers, or reinforcing particles in ceramic matrix composites, or as another example, to test microscopic particles used in the pharmaceutical industry. The second goal of the thesis is to implement these methods towards testing specific microscopic ceramic particles of potential interest for metal matrix composites, and finding what limits their strength, aiming to understand how one could produce stronger ceramic particles, this being a pathway towards strong, tough and lightweight isotropic metal matrix composites. We focus our work on alumina and alumina-based particles because (i) alumina itself is stiff, relatively lightweight and can be potentially very strong as was long ago demonstrated on microscopic alumina whiskers, (ii) it is an abundant ( $\approx 8\%$  of the earth's crust) compound that can economically be produced in large quantities and by different methods, and (iii) it is also very often used as a model reinforcement material in the development of metal matrix composites.

This thesis starts with a comprehensive literature review (Chapter 1) and is then followed by four Chapters, each based on a published and/or submitted scientific article. Two of these chapters deal with the development of new tensile strength measurement strategies at the microscopic scale. One is based on the uniaxial compression of individual particles between a pair of platens; this is presented in Chapter 2. This approach, developed using spherical fused quartz particles as a testbench material, introduces a departure from usual practice in that, instead of using hard (generally diamond) platens,

we implement softer elasto-plastic platens that plastically deform when in contact with the comparatively hard particles, leaving a deep indent in the platens. This significantly reduces the stress concentration along and around the platen-particle contact, which with hard platens often leads to the nucleation of extraneous cracks, which strongly reduce the validity of data. We confirm, as was shown by Shipway and Hutchings [9,10] that with softer platens one sees the emergence of a domain of particle loading where it is unambiguously known that, if a particle fails abruptly, it does so because of a surface flaw forming a meridional crack – hence the name given to the test: *the Meridian Crack Test*. The method is then implemented to measure the strength of amorphous and nanocrystalline alumina-zirconia-silica based spherical particles prepared using a plasma spraying technique in collaboration with the Institute of Plasma Physics of the Czech Academy of Sciences; this is presented in Chapter 3.

The second strategy developed here to measure the strength of microscopic particles is presented in Chapter 4. This method combines focused ion beam (FIB) micromilling, nanotesting, and bespoke finite element (FE) simulations in a way that yields local strength data free of artefacts brought by ion-beam damage; this method is baptised the *C-shape test*. The main idea behind the method is to create a deep and wide notch within the particle, which then makes it possible to create states of high tensile stress along an external surface of the particle that is not affected by ion milling, when applying a compressive load normal to the plane of the notch. This strategy was developed using nanocrystalline Nextel™ 610 alumina fibres of known strength distribution as the testbench material. Then, in Chapter 5, we implement the C-shape test to measure the local strength of irregularly shaped vapour-grown alumina particles that were shown in earlier work to be highly performant as a particulate reinforcement in PRMMCs. We show that single-crystalline vapour-grown alumina particles can exhibit strength values comparable to those of high-perfection alumina whiskers; however, their strength is significantly reduced due to presence of pores, shape irregularities, and most critically grain boundaries along with their associated grain boundary grooves.





# Chapter 1 Literature review

## 1.1 Metal matrix composites: an overview

A metal matrix composite (MMC) is a material that intimately combines a continuous metallic matrix with a second phase generally called the reinforcement, with a goal to create a new material with properties unavailable using either of the individual constituents. The composite physical and mechanical properties can be tailored by the appropriate choice of the matrix/reinforcement combination and the geometry and volume fraction of phases present within the composite. Metals that are commonly used as the matrix are aluminium, copper, or magnesium, as these cannot be reinforced with a significant amount of hard ceramic particles by conventional metallurgical alloying. Iron, titanium and nickel are sometimes also used as they can provide a very strong matrix; however, their high density and the fact that carbides and oxides are easily produced in iron makes them somewhat less interesting.

As illustrated in Figure 1.1 the reinforcement phase comes typically in three different forms: (i) particles, (ii) whiskers and short fibres, and (iii) continuous fibres. It can be made of various materials that include but are not limited to oxides, borides, carbides, nitrides, carbon or boron. The volume fraction of the reinforcement in MMCs can vary based on the processing method, from a few percent up to roughly 64 %. In some specific cases reinforcement volume fractions above 80vol.% can be achieved, as in the case of aligned platelets [2].

There are many MMC processing routes; these can be divided into two main classes: (i) solid-state processes and (ii) liquid state processes. In each of these classes there are several subcategories [5,11,12]. Powder metallurgy is a well-established solid-state processing route, which is relatively cost-effective and provides freedom in selection of metal and reinforcement. The reinforcement can be of almost any shape, size or volume fraction provided this last parameter is on the low side ( $\approx 40\%$  for particles; more for fibres). The metal and reinforcement are first blended to obtain a homogeneous reinforcement distribution, then the mixture is cold pressed and consolidated at high temperature using hot isotactic processing (HIP) or the field assisted sintering technique (FAST). The final product is generally nearly fully dense if produced competently, and can be further processed by extrusion or forging if the reinforcement volume fraction is sufficiently low. One of the main drawbacks of the powder metallurgy method is that bonding between metallic and ceramic powder particles can be weak, the reason being that many metallic powder particles are often covered with an oxide skin along their surface [13,14].

One way to produce fully dense bulk MMCs with a strong matrix-reinforcement interface is via liquid metal processing routes such as infiltration or stir-casting. Liquid metal infiltration consists of the injection of molten metal into a porous preform of the reinforcement. Typically this is conducted under vacuum or is assisted with a high pressure to overcome (generally adverse) capillary forces and fill with metal the narrow space between individual reinforcing particles or fibres. In stir-casting the reinforcement is mechanically stirred into the molten metal, often under vacuum to avoid metal oxidation. In both cases a strong metallurgical bond between the matrix and reinforcement can be achieved; however, liquid metal routes are in general not suitable for matrix-reinforcement combinations that react chemically at temperatures of the molten matrix. A typical example is the reaction between carbon based reinforcements with molten aluminium forming aluminium carbide,  $Al_4C_3$  at the interface; this has documented detrimental effects on the mechanical and corrosion properties of resulting composites [5].

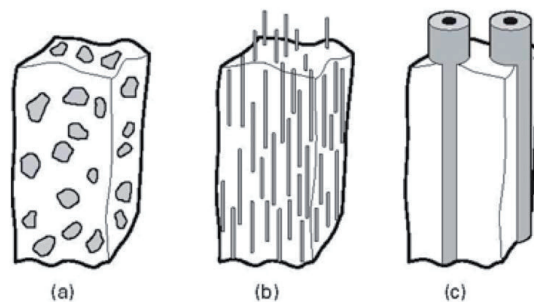


**Figure 1.1 – Illustration of three types of MMCs with (grey) different form of reinforcement: (a) particles, (b) whiskers and short fibres, and (c) continuous fibres. Figure reproduced from Ref. [15] with permission of Cambridge University Press.**

One of the characteristic features of MMCs is that the reinforcement bears a significant fraction of the applied load; this is a difference with dispersion-strengthened alloys where the secondary « reinforcing » phase, present at the nanometre scale but at very low volume fractions, mostly act as an obstacle to dislocation motion. Metal matrix composites can thus offer enhancements in strength and stiffness simultaneously, while retaining relatively high toughness and maintaining these properties at elevated temperatures. Combination of light metals such as aluminium, magnesium or titanium with stiff and potentially strong ceramics was one of the main driving forces in the development of MMCs [5,11]. Figure 1.2 shows that today's MMCs (cyan boxes) push the envelope of available specific properties for both metals and ceramics, providing attractive materials for applications where strong, stiff and lightweight materials are needed. Fibre reinforced metal matrix composites (FRMMCs) exhibit comparable specific properties to those of carbon fibre reinforced plastics (CFRP) while offering advantages typical for metals (e.g. higher service temperatures, electrical and thermal conductivity, no moisture absorption, etc.). Particle reinforced metal matrix composites (PRMMCs) with slightly lower specific properties, provide on the other hand isotropic behaviour. Estimations based on micromechanical modelling by Hauert et al. [16] show that PRMMCs with specific properties approaching those of fibre-reinforced metals could be achieved provided that strongly bonded particles with strength characteristics of today's high-strength engineering ceramic fibres are used as reinforcement (red box in Figure 1.2).

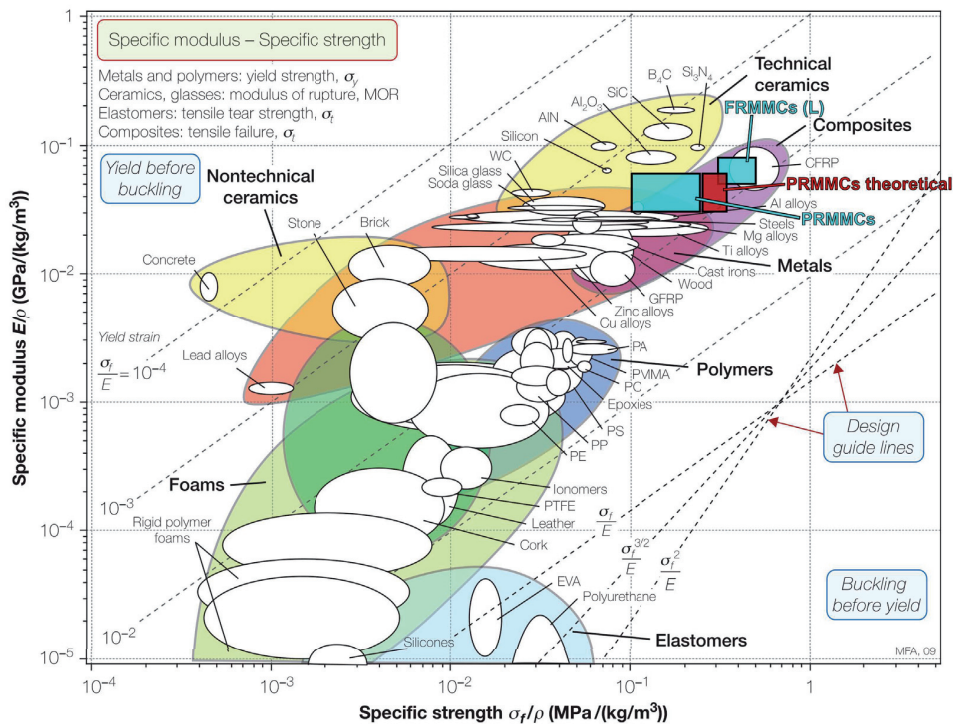


**Figure 1.2 – Specific modulus  $E/\rho$  vs. specific strength  $\sigma_f/\rho$  of different classes of materials according to [17]. The typical specific properties of fibre reinforced metal matrix composites (FRMMCs) in the longitudinal (fibre) direction and that of particle reinforced metal matrix composites (PRMMCs) are indicated with cyan boxes. A theoretical estimate of what can be achieved in PRMMCs provided that ceramic particles as strong as today engineering fibres are used as reinforcement is shown in red box. Figure reproduced from Ref. [17] with permission of Elsevier. Overlaid data from [5,16,18–21].**

Reinforcing metals, particularly aluminium and its alloys, with alumina has demonstrated that composites with attractive specific mechanical properties can be produced. Alumina is furthermore often used as a model material for the reinforcement in experimental explorations of this class of composite materials. The reason why alumina has received much attention as a reinforcement material in MMCs is that it is relatively lightweight, stiff and it can be potentially very strong especially in form of microscopic fibres or particles. It does not react with aluminium at elevated temperatures and can form a strong interface with aluminium. Moreover, it is an abundant compound that can be produced in large quantities and by different methods. The following paragraphs summarize different types of alumina reinforcements used in MMCs and their properties with particular emphasis on their strength (in both theory and practice).

## 1.2 Alumina as a reinforcement

### 1.2.1 Overview of alumina as material

Given the widespread utilization and its frequent use as a typical representative of the group of structural ceramics, strength and fracture mechanisms have been extensively studied, in both single- and poly-crystalline forms of alumina. Its stable crystalline form at room temperature is  $\alpha$  (alpha) phase, also called corundum or, in its single-crystalline form, sapphire [22]. For simplicity the term *alumina*

will hereafter refer to its polymorphic phase  $\alpha$ -Al<sub>2</sub>O<sub>3</sub>. The mechanical properties of alumina with all its details is an interesting topic by itself; below is given a brief review of its properties relevant to the testing of alumina reinforcements.

The crystallographic structure of alumina consists of close packed planes of oxygen anions and aluminium cations forming a hexagonal unit cell. The description of the elastic properties of alumina needs therefore a total of six elastic constants. These constants were determined by Watchman et al. using a resonance technique [23]. The extreme values of Young's modulus  $E$  are 461 GPa and 336 GPa determined for  $\langle 0001 \rangle$  and  $\langle 10\bar{1}1 \rangle$  directions, respectively. For polycrystalline alumina, the orientation-dependent variations of the elastic constants balance each-other resulting (for a texture-free material) in an isotropic behaviour on the macroscopic scale with an average Young's modulus 403 GPa and Shear modulus 163 GPa [23]. The theoretical strength of alumina was estimated by Wiederhorn et al. [24]. Using elastic properties of the  $\{10\bar{1}0\}$  plane and formulae derived from the Born potential the theoretical strength limit of sapphire is 31 GPa. In MacMillan's approach [25] the theoretical strength increases with increasing Young's modulus and surface energy, giving a theoretical strength estimate for alumina equal to 46 GPa. Engineering alumina, however, contains flaws that act as stress concentrators. Due to the lack of plastic deformation, furthermore, stresses often cannot relax and in the vicinity of the most severe flaws stresses may reach the theoretical cohesive strength causing premature failure and diminishing the load-bearing capacity of the material.

The strength of alumina, and more broadly of brittle materials, can be understood in the light of fracture mechanics [26]. The strength,  $\sigma_f$ , of a brittle body containing a sharp flaw of size,  $c$ , is equal to

$$\sigma_f = \frac{1}{Y} \sqrt{\frac{2\gamma E}{c}} \quad (1.1)$$

where  $E$  is Young's modulus,  $Y$  a geometric factor and  $\gamma$  is the fracture surface energy, which represents the brittle material's resistance to unstable crack growth; this is related to the fracture toughness via  $\gamma = K_{IC}^2/2E$ , where  $K_{IC}$  is the (mode I) fracture toughness of the (perfectly brittle) material.

A first evaluation of the fracture energy of single crystal alumina,  $\gamma_{SC}$ , was done by Wiederhorn [24], who reported  $\gamma_{SC}$  values ( $K_{IC}$  equivalents in brackets) at room temperature in a dry gaseous nitrogen atmosphere equal to 6 J/m<sup>2</sup> (2.15 MPa.m<sup>1/2</sup>), 7.3 J/m<sup>2</sup> (2.4 MPa.m<sup>1/2</sup>) and > 40 J/m<sup>2</sup> (> 5.6 MPa.m<sup>1/2</sup>) for the rhombohedral plane  $\{10\bar{1}2\}$ , the prismatic plane  $\{10\bar{1}0\}$  and the basal plane  $\{0001\}$ , respectively. In polycrystalline alumina the fracture mode can be transgranular or intergranular. For transgranular fracture, it may be expected that the fracture process is controlled by  $\gamma_{SC}$ , while in the latter case the fracture is likely to be controlled by the grain-boundary fracture energy,  $\gamma_{GB}$ . Very little is known about the experimental value of  $\gamma_{GB}$ . It has been repeatedly assumed to be  $\approx 1/2$  of the surface energy of single crystalline alumina [27,28]. So far the best estimation of the grain boundary fracture toughness was provided in the work of Chantikul et al. [29]. In that work, extrapolation of a model for the fracture toughness dependence on grain size and crack length considering the grain-bridging

effect, yields a grain-boundary fracture toughness of  $2.75 \text{ MPa}\cdot\text{m}^{1/2}$ . The fracture of a polycrystalline body is, however, a complicated process and most experimental values of fracture energy of alumina polycrystals,  $\gamma_{\text{PC}}$  exceed  $\gamma_{\text{SC}}$  characteristic of single crystals, by a factor of 3 to 10 [27,30–36]. Translated into fracture toughness, values vary from  $3 \text{ MPa}\cdot\text{m}^{1/2}$  to  $6.5 \text{ MPa}\cdot\text{m}^{1/2}$ . This relatively high scatter in polycrystal toughness values is caused by several factors. Among those reported, main parameters are the manufacturing process and treatment, purity and grain size of the alumina sample.

Various inherent mechanisms explaining the relatively high fracture toughness of polycrystalline alumina, and ceramics in general, compared to their single crystal values, have been suggested [29,37–40]. A central consideration of each mechanism is the micro-scale heterogeneity of the polycrystal. Crack deflection could be considered as one of the toughening mechanisms as the fracture surface of a polycrystal is larger than the projected surface used in calculating the fracture energy per unit area. Microcracking ahead of the crack front as a possible toughening mechanism was proposed by Rice and Freiman [39] after extensive study of the grain-size dependence of steady-state fracture toughness in non-cubic ceramics. The idea behind the mechanism of micro-crack toughening is that stable grain boundary micro-cracks are nucleated in the vicinity of the macroscopic crack tip. These micro-cracks then lower the stress experienced by the crack tip. The model has not been supported by direct observations or by ultrasound investigation [40,41] and has been abandoned mostly due to the experimental evidence of grain bridging and crack wake effects as more important toughening mechanisms. Macrocrack bridging appears as the toughening mechanism with clear experimental evidence in single-phase alumina in Refs. [40,42]. The operating mode of this mechanism was identified as frictional interlocking of grain-scale bridging ligaments across the newly formed crack surfaces, stretching as far as several tens of grain diameters behind the crack tip, in turn producing *R*-curve behaviour. It was shown by Vekinis et al. [42] as well as Chantikul et al. [29] that the bridging mechanism is more effective for coarser-grained alumina resulting in a rising *R*-curve (fracture resistance) behaviour as opposed to a flat *R*-curve for  $2.5 \mu\text{m}$  fine-grained alumina. Improvements in the fracture toughness of alumina can be achieved by reinforcing with second phase particles. The most commonly and widely used particulate reinforcement in alumina is tetragonal zirconia. The effect of zirconia particles on fracture toughness is two-fold. First, second-phase zirconia particles act as obstacle to the propagating crack and secondly transformation of the tetragonal zirconia to its monoclinic phase accompanied with  $\approx 4\%$  expansion in volume can be induced in the highly stressed region in front of the crack, thus effectively shielding the crack from experiencing stress that would otherwise lead to failure [43].

The strength of alumina is also controlled by the size of flaws that it contains and by its environment. It is a well-documented phenomenon that environments such as water or moist air promote subcritical growth of sharp flaws initially present in the microstructure of both single and polycrystalline alumina [44–52]. As a consequence, original flaws increase in size over time when under load. Slower loading rates and longer time under loading conditions allow for an increase in flaw size by subcritical crack growth and hence lower the strength of alumina. This phenomenon is also often referred to as slow-crack-growth (SCG) and takes place at stress intensity factor values well below those causing failure.



SCG is typical of many ceramics and has its parallel in the stress corrosion cracking of metals. For engineering purposes SCG kinetics are typically described by a power law [48]

$$v = AK^r \quad (1.2)$$

where  $v$  is the velocity of the propagating crack,  $K$  is the stress intensity factor, and  $A$  and  $r$  are experimentally determined crack growth parameters. The  $v - K$  relation typically consists of three regions, I, II and III, and therefore can be described with three sets of parameters  $A$  and  $r$  [46,53,54]. During loading a flaw subject to slow crack growth typically spends most of its time in Region I, which is the region most often investigated in the literature. Typical values of the crack growth exponent,  $r$  for polycrystalline alumina in Region I have been reported to be in the range 16-110. Often a negative dependence of  $r$  on grain size for conventional commercial purities of alumina is reported [28,46,51,55]. Ebrahimi et al. [56] have shown that, when in given purity alumina the grain bridging toughening mechanism is taken into account, SCG of alumina of three different grain sizes 1.9  $\mu\text{m}$ , 4.8  $\mu\text{m}$  and 12.7  $\mu\text{m}$  is characterized by a single value of  $r$  equal to 75. Values of the parameter  $A$  are rarely presented in the literature. Theoretically,  $A$  depends on the concentration of active species in the environment [28]. Evaluating published  $v - K$  relations in the literature [46,52,56,57], values of  $A$  for moist air of approximately 50% relative humidity in Region I vary considerably, from  $2 \times 10^{-22}$  to  $6 \times 10^{-41}$  (in SI units) depending mainly on the purity of the alumina grade investigated.

SCG in alumina is almost exclusively associated with intergranular crack growth followed by catastrophic failure in the transgranular regime [28,29,48,52,58]. Although Kirchner and Gruver attributed cleavage regions on fracture surfaces surrounding original flaws in hot-pressed and 96% alumina to SCG [44,49], Rice later pointed out [59] that Kirchner's observations are consistent with cleavage regions showing an "inner mirror" analogous to glass fracture surface characteristic [48,60]. The micromechanism underlying SCG was investigated by Michalske and Freiman [61]. Their study led to conclude that the dominant mechanism at low and intermediate temperatures is the breaking of chemical bonds at the crack tip as a result of stress-assisted reaction with polar molecules present in the environment. In a study of high-purity alumina grades Krell et al. [52] suggested that water promotes SCG preferentially in microstructural regions with segregated impurities along grain boundaries thus promoting intergranular fracture. Rice supports this statement in a review where he claims that SCG often occurs due to boundary phases that are particularly susceptible to the environment [28].

Kirchner and Gruver reported that delayed fracture in polycrystalline alumina can also originate from pores that do not appear to be directly connected to the atmosphere [49]. Wiederhorn et al. observed in a study of crack propagation in single crystal alumina that metastable slow crack growth can occur at low homologous temperatures in vacuum [62]. While at high temperatures ( $> 400^\circ\text{C}$ ) alumina exhibits twinning and plastic flow, TEM observations did not suggest the occurrence of plastic flow at lower temperatures [63–65]. Wiederhorn et al. also reported a temperature dependence of fracture. The observation of slow crack growth in vacuum and a strong temperature dependence of strength

and fracture toughness contradict the classical theory of brittle fracture, which assumes that the surface free energy is the main barrier for fracture (if this simple theory were true, it would follow that fracture would be a nearly temperature-independent process and slow crack growth would not occur [62]). Several theories have been developed to describe brittle fracture as a thermally activated process considering fracture as a diffusion process [66,67] or based on atomic bond fluctuations at the crack tip [68–70].

In contrast to TEM observations, Lankford and co-workers [71–74] identified microplastic flow and twinning as active mechanisms in coarse-grained alumina at low homologous temperatures including room temperature, in both compression and tension. Their acoustic emission experiments indicate that twinning starts at stresses as low as 130 MPa in tension. They attributed the temperature-dependent strength of alumina to deformation twinning as a microcrack initiation mechanism. Stresses associated with dislocation pileups blocked by grain boundaries may also relax by the nucleation of micro or intergranular cracks. Deformation twins may serve as active flaws, causing microcrack initiation and extension. Plasticity in single crystalline alumina at room temperature has been reported by Montagne et al. [75] using FIB milled micropillar compression tests, with plasticity occurring above 11 GPa in uniaxial compression stress, and critical resolved shear stress values between 4 and 11 GPa depending on the crystal orientation. Therefore it would seem possible that, for high purity single crystal or polycrystalline alumina with strong grain boundaries and sufficiently free of pre-existing flaws, plastic yielding and associated phenomena might control the ultimate attainable strength of alumina even at room temperature.

### 1.2.2 Alumina whiskers and fibres

As exposed earlier a perfect, defect-free alumina crystal can theoretically achieve strengths on the order of 30–40 GPa. First attempts to produce high-perfection and thus strong alumina crystals in the form of whiskers date back to 1950s. Methods developed to produce alumina whiskers include a vapour-phase growth technique in which a stream of moist hydrogen is passed over aluminium powder at high temperature [76], the Edge-defined, Film-fed growth method developed by LaBelle [77], the laser-heated pedestal-growth (LHPG) method [78] or vapor-liquid-solid (VLS) deposition [79,80].

A pioneer of the mechanical characterization of alumina whiskers, and whiskers in general, was Brenner [81]. Brenner reported maximum elastic strains achieved in single-crystal alumina whiskers of up to 3 %; this translates to strength value on the order of 12 GPa. Other authors reported similar values: for whiskers and needles a few micrometres in diameter measured strength values typically lie between 7 to 14 GPa [82–86]. Reported alumina strength values are strongly dependent on the size of the whiskers (see Figure 1.3), with whiskers 50  $\mu\text{m}$  in diameter having reported strength values as low as 1 GPa [82]. No prominent dependence of the alumina microcrystal strength on crystal orientation has been reported in the literature [87], although in one study somewhat higher strength values for A-type ( $\langle\text{hk}0\rangle$ ) whiskers were reported compared to C-type ( $\langle 0001\rangle$ ) whiskers [85]. Experimental data on alumina whiskers with strength values consistent with the theoretical strength of alumina were achieved testing nanoscale alumina whiskers [65].

The high strength of alumina whisker crystals is linked to the absence of gross imperfections. The evidence shows very clearly that flaws along the crystal surface control its strength. Polishing of alumina whiskers surface in hot orthophosphoric acid improved the strength of larger less strong whiskers (<8 GPa of strength) [84,88] (see Figure 1.3). Similarly, flame-polishing of millimetre-scale high-perfection alumina crystals led to improvement of the strength [87]. Bayer et al. in [88], based on the observation that whiskers with chemically polished and unpolished surface behave in qualitatively similar manner when their fracture stress exceeds 8-10 GPa, suggested that such strong crystals may fail by crack nucleation induced by dislocation motion (pile-up or dislocation interaction) regardless of the whisker orientation. Observations consistent with those of Bayer et al. were reported by Grenier and Kelly [84] (see Figure 1.3).

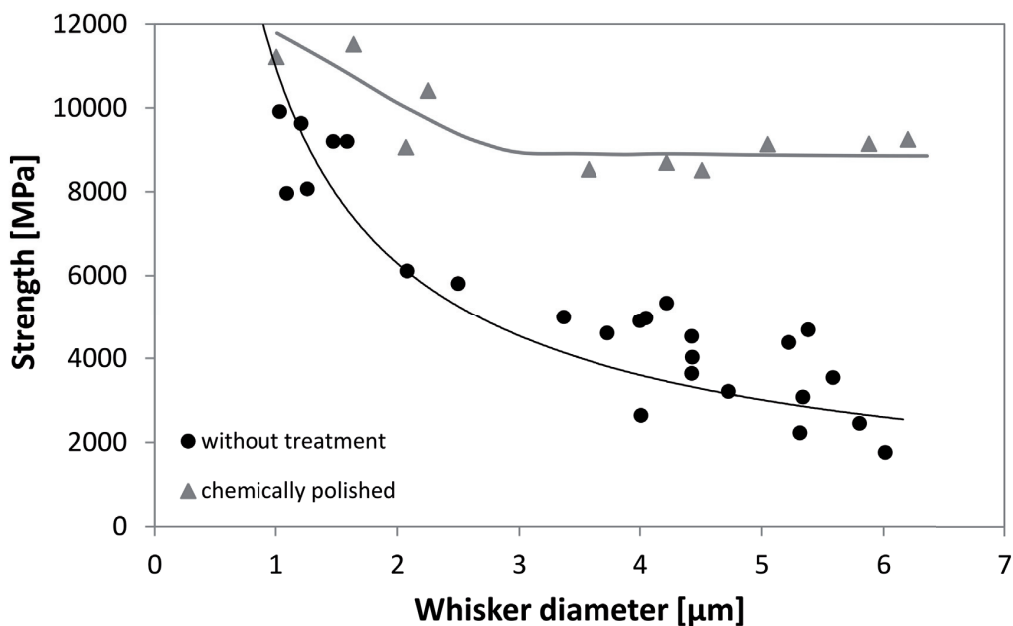


**Figure 1.3 – Alumina whisker strength as a function of its diameter and effect of chemical polishing with hot orthophosphoric acid on the whisker strength. Data from [84].**

It has been demonstrated that the reinforcement of materials with strong whiskers has potential from the perspective of materials properties (but is restricted by the high price of whiskers) [89,90]. At room temperature peak fracture strengths of 1.6 GPa were reported for a silver matrix composite reinforced with alumina whiskers of 7.7 GPa average strength. The use of such composites at elevated temperatures ( $> 1000\text{ }^{\circ}\text{C}$ ) was found to be limited due to the disruption of whisker-matrix bonds observed for a nickel matrix composite [91]. Additionally, high strength whiskers as reported above are achieved only when great care is taken during their production and selection. In the case of whiskers and single crystalline fibres produced on an industrial scale, individual whisker/fibre strengths seldom reach values above  $\approx 6\text{ GPa}$  [91–93].

Long (up to 250 mm) monocrystalline alumina fibres can be produced via the internal crystallization method (ICM) developed by Mileiko et al. [94–98]. The method is essentially based on crystallization of an oxide fibre from the melt in the channels of a molybdenum preform formed by alternating layers



of foils and wires made of molybdenum. The channels are filled with the oxide melt by capillary forces and fibres are crystallized by cooling down the preform, directionally by pulling it out from the melt. Resulting fibres exhibit non-circular cross-sections with a characteristic transverse width in the range 50-500  $\mu\text{m}$ . The main advantage of the method is its relative simplicity and (comparative) low cost, since fibres are produced from the melt. The effective strength of alumina fibres prepared by the ICM method was reported to be near 2 GPa for 1 mm long fibre and few hundred MPa for fibre lengths between 10-20 mm. The fibre strength was significantly improved by coating their surface with silicon oxy-carbide using a CVD process; strength values near 7 GPa for 1 mm fibre length and approximately 1 GPa for 20 mm fibre lengths are then reported, suggesting that the fibre strength is mainly limited by surface defects (although fractography revealed that pores were often the strength-limiting defects) [98].

Continuous polycrystalline alumina fibres can also achieve relatively high strengths ( $>3$  GPa) when they are defect-free and nanocrystalline [99,100]. Polycrystalline alumina fibres can be produced via a sol-gel method, in which a viscous aqueous solution of aluminium salts (sol) is spun to produce a gel fibre that is subsequently thermally treated [11]. Table 1.1 summarizes properties of some of the available polycrystalline alumina and alumina based fibres used as reinforcements. Aluminium and aluminium alloys reinforced with Nextel<sup>TM</sup> fibres reach tensile strengths of nearly 1600 MPa and a modulus of elasticity around 240 GPa along the fibre direction; these represent a showcase MMC material. The strength-limiting defects of polycrystalline alumina fibres are typically larger pores, surface defects (e.g. blisters, cracks, weld-lines) [99], grain boundary grooves [101], and abnormally large grains [102].

Table 1.1 – Properties of selected alumina and alumina-based polycrystalline fibres.

Fibre	Composition (wt%)	Diameter ( $\mu\text{m}$ )	Density ( $\text{g}\cdot\text{cm}^{-3}$ )	Young's modulus (GPa)	Average tensile strength (GPa)
Nextel <sup>TM</sup> 610 [100]	$>99\text{Al}_2\text{O}_3$	10-12	3.9	373	3.3 <sup>a</sup>
Nextel <sup>TM</sup> 650 [100]	$89\text{Al}_2\text{O}_3$ , $10\text{ZrO}_2$ , $1\text{Y}_2\text{O}_3$	10-10	4.1	358	2.5 <sup>a</sup>
Nextel <sup>TM</sup> 720 [100]	$85\text{Al}_2\text{O}_3$ , $15\text{SiO}_2$	10-12	3.4	260	2.1 <sup>a</sup>
Altex [103]	$85\text{Al}_2\text{O}_3$ , $15\text{SiO}_2$	17	3.2	210	1.8 <sup>b</sup>
Almax [103,104]	$>99\text{Al}_2\text{O}_3$	10	3.6	340	1.3 <sup>b</sup>
Saffil [11]	$96\text{Al}_2\text{O}_3$ , $4\text{SiO}_2$	3	2.3	100	1.5 <sup>c</sup>

<sup>a</sup> 25mm gauge length, <sup>b</sup> 10mm gauge length, <sup>c</sup> manufacturer's data

### 1.2.3 Alumina particles

Most of the alumina powder produced commercially is obtained from bauxite ore via the calcination of aluminium hydroxides – a step in the so-called Bayer process. Alternatively it is produced from transition aluminas and calcium salts. There exist several different grades of alumina powder originating from the Bayer process, of different purity, shape and properties. For example, *white fused* grade alumina, which is probably the most widely used type of alumina particles in producing PRMMCs, is made by melting calcined alumina, which is an agglomerate of microscopic alumina grains from the Bayer process, in electric arc furnaces by passing an electrical current between carbon electrodes. Resulting fused bulk alumina is typically very pure except that it contains residual sodium oxide, which volatilizes during melting giving rise to relatively large internal pores [105]. *Brown fused* alumina is another kind of fused alumina, which has roughly 96 wt% of  $\text{Al}_2\text{O}_3$  and contains residual titanium dioxide. It is in general considered stronger than white fused alumina, the latter also having a higher friability [105,106]. Fused alumina can be additionally modified by small amounts of alloying elements such as chromium or vanadium oxide [105]. Calcined alumina from the Bayer process can also be sintered. This typically results in alumina with fine grains, a few micrometres in diameter, and containing a finite fraction of regular microporosity [107]. Sintered alumina is sometimes also called *tabular* alumina owing to its microstructure, which is often made of small plate-like “tabular” grains [108]. Either fused or sintered, the bulk alumina is then crushed and sieved in order to obtain fine powder. Because fused or sintered alumina powders are typically comminuted, they tend to contain a high density of microcracks, which weakens them. This is something that is not necessarily unwanted in an abrasive powder (the main use of this type of powder) as high friability and the ability for particle self-sharpening are sought [105]. Other methods of alumina powder production exist and to list all of them is far beyond the scope of this thesis. Comprehensive surveys on the topic of alumina powder production are provided in [22,108,109].

Methods that do not require size reduction (e.g., comminution) processes are attractive if one wishes to avoid the formation of strength-limiting microcracks typical of comminuted powder. At Sumitomo, an *in-situ* vapour-phase transition method is used to produce nearly-monodispersed high-purity polyhedral alumina particles [110]. Atomization of comminuted powder by a thermal spraying technique can alternatively be used to prepare amorphous and/or nanocrystalline powder particles in which original comminution defects are eliminated [111,112]. A proprietary mechanochemical crystal growth process from an aqueous solution has also been used to produce microscopic alumina platelets [113,114].

Figure 1.4 shows alumina particles prepared by four different methods, namely (a) comminuted fused alumina, (b) *in-situ* vapour-phase formation, (c) atomization using a thermal spraying technique and (d) mechanochemical crystal growth, all of which have been successfully used as reinforcement in a metallic matrix [2,115,116]. All four types of alumina particle shown in Figure 1.4 contain defects, however; namely: microcracks, grain boundaries and grain-boundary grooves, micropores, and irregular surface forming local stress concentrators. These defects are expected to have a detrimental effect on individual particle strength. Yet, not much is known about the strength of these particles or the quantitative effect of these observed defects on the particle strength and its distribution. There are

only few studies in which the authors attempted to measure the strength of ceramic particles similar to those used in composites; these are reviewed together with the used testing methods in Subchapters 1.5.1 and 1.6.5. The particle intrinsic strength, however, has pronounced effects on the composite mechanical properties such as strength, ductility, and fracture toughness, as will be explained in the next section.

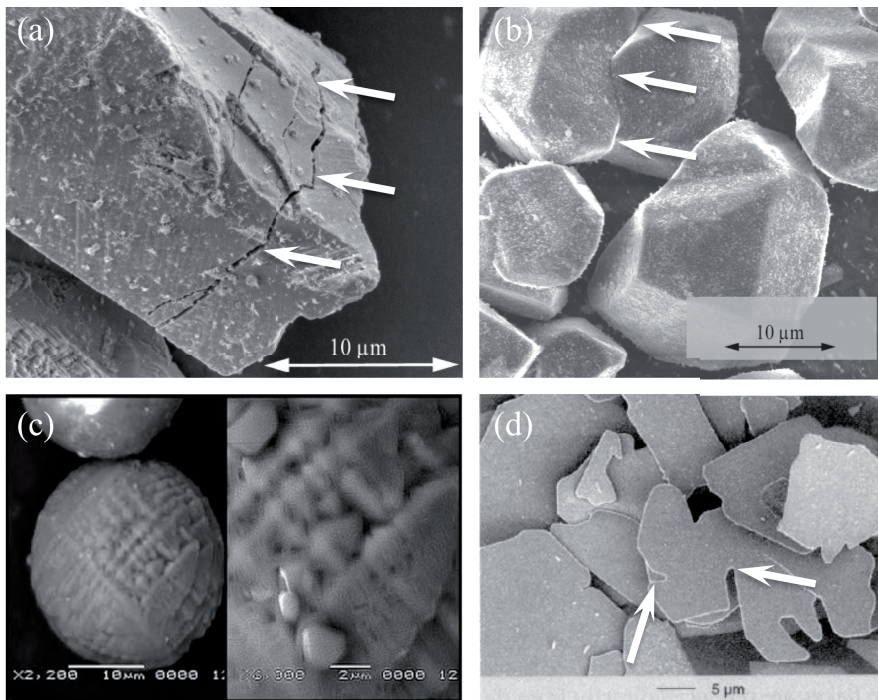


**Figure 1.4 – Selection of four different types of microscopic alumina particles produced by different methods, which have been used to produce PRMMCs. (a) Comminuted fused alumina containing visible cracks (reproduced from Ref. [116] with permission of Elsevier). (b) Vapour-grown Sumicorundum<sup>®</sup> alumina showing facets and grain-boundary grooves (reproduced from Ref. [116] with permission of Elsevier). (c) Atomized alumina prepared by a thermal spray technique with dendritic microstructure forming grain-boundary grooves and micropores (reproduced from Ref. [111] with permission of Springer). (d) Alumina platelets prepared by a proprietary mechanochemical process with notch-like asperities (image source: Merck KGaA (CC-by-ca 3.0)).**

### 1.3 The role of particle strength in PRMMCs: theory and experiments

#### 1.3.1 Particle fracture

As particle reinforced metal matrix composites deform, the matrix undergoes plastic deformation while the much stiffer ceramic particles remain elastic and take up a disproportionate portion of the applied stress. A three-dimensional finite element simulation of a representative volume element (RVE) of stiff spherical ceramic particles occupying 40 vol % embedded in aluminium matrix from the work of Segurado and LLorca [117] shown in Figure 1.5 demonstrates that particles carry high tensile stress oriented along the loading axis, particularly when they are close to each other. The peak stress found in particles can be several times higher than the yield stress of the matrix and, as can be observed from the figure, the stress distribution within each particle can be very inhomogeneous.

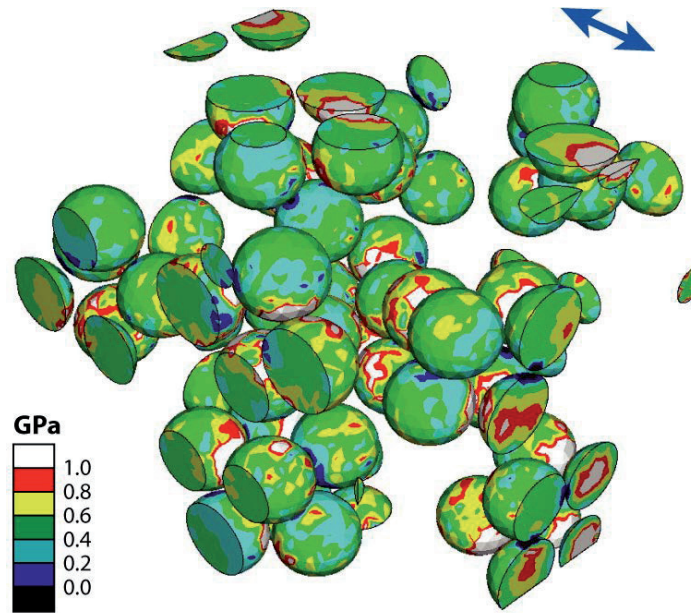


**Figure 1.5 – 3D finite element simulation of a representative volume (RV) element of aluminium metal matrix composite reinforced with stiff (400 GPa) ceramic particles occupying 40 vol%. The RV element is deformed in the direction of the arrow (top right corner) with the applied strain 5%. Particles exhibit high tensile stresses in the direction of the applied strain with the peak value several times higher than the yield strength of the aluminium matrix. Figure reproduced from Ref. [117] with permission of Elsevier.**

It is well documented that the high stresses that particles are subjected to during deformation of the composite under external loading lead to stochastic particle fracture [116,118–133]. Hard equiaxed particles in metal have been found to fracture normal to the direction of applied uniaxial stress when it is tensile [118,122,134–136] or parallel to it when it is compressive [137]. The fracture of particles within two-phase materials has been probed by various means, including microscopic examination of surfaces during *in-situ* testing [130], *ex-situ* metallography of strained or fractured samples [123,131] or serial sectioning [138], acoustic emission [139], neutron diffraction [128,140], and 3D synchrotron X-ray tomography [118,134,141,142].

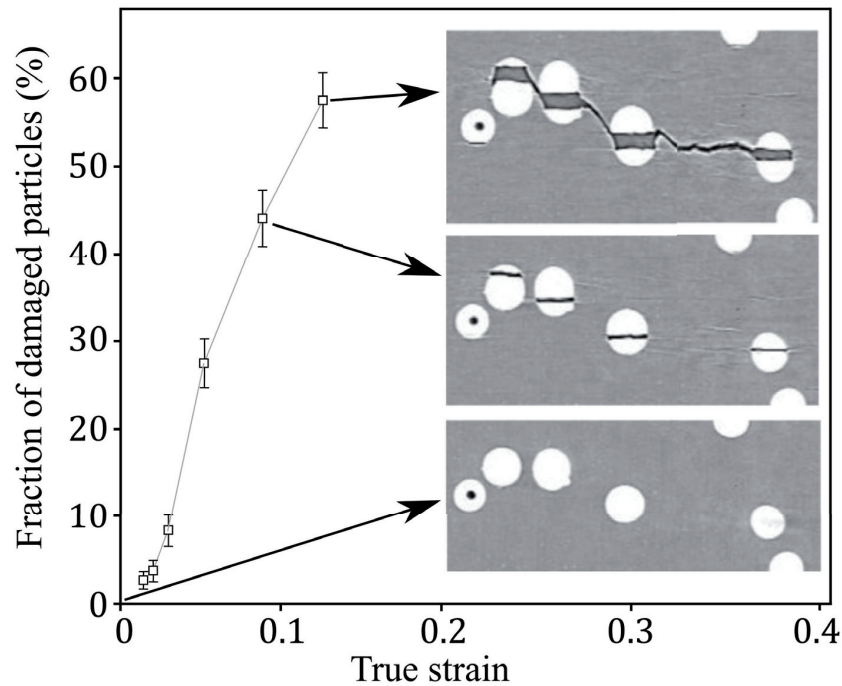


**Figure 1.6** – An example of damage accumulation by particle fracture in an aluminium metal matrix composite reinforced with spherical ceramic particles investigated by 3D synchrotron X-ray tomography. Cracks in particles appear perpendicular to the applied tensile stress. Reproduced and adapted from Ref. [118] with permission of Elsevier.

Fracture of the particles causes the two-phase material to accumulate damage over the course of deformation, reducing in turn its load-bearing capacity and also its rate of work hardening. Studies have clearly shown that the proportion of broken particles is directly linked to the applied tensile stress and/or tensile strain [123,125,143–146]. Figure 1.6 displays a demonstration of this phenomenon revealed by three-dimensional *in-situ* synchrotron X-ray microtomography experiments performed by Maire et al. [118,141]. It has been repeatedly observed that the propensity for particle failure is higher for larger particles and increases with increasing volume fraction of the reinforcement [119,123,130,146–149]. A direct link of the particle shape with the propensity for particle fracture is on the other hand less clear. While some studies found that particles with prominent angularity are more prone to fracture [150,151], Li et al. reported only an insignificant effect [147]. Indeed, sharp angles in particles can act as stress concentrators either as geometric irregularity sites within individual particles [152,153] or in case of high-volume fraction particle-reinforced composites at particle-particle contact points [123].

The flaw-controlled intrinsic strength of particles was found to be the key parameter controlling the rate of damage accumulation in PRMMCs [116,154–157]. The effect of particle size on the propensity for particle fracture can be explained by the fact that bigger particles are more likely to contain large defects and thus are weaker, as is characteristic for any brittle ceramic [89]. It is often reasoned that particle strength distributions should follow the Weibull distribution, which is hence often used to describe the failure probability of ceramics, including particles in composites [125,158,159]. The



probability of fracture,  $P_f$ , of a particle of volume,  $V$ , following the two-parametric Weibull distribution is given by:

$$P_f = 1 - e^{-\frac{V}{V_0} \left(\frac{\sigma_p}{\sigma_0}\right)^m} \quad (1.3)$$

where  $V_0$  is the reference volume,  $\sigma_p$  is the stress experienced by the particle,  $\sigma_0$  is the Weibull scale parameter, itself related to the particle characteristic strength for which the probability of particle failure equals 63.2 %. The exponent  $m$  is the Weibull shape parameter, also called Weibull modulus, and describes the dispersion of the particles' strength.

The accumulation of damage during loading by particle fracture has pronounced effects on the composite physical and mechanical properties. In the next two sections we focus on the effect of particle fracture on tensile and fracture properties of the composite, respectively.

### 1.3.2 Tensile properties

One of the effects of particle fracture and thus of the particle strength on the tensile properties of a particle-reinforced metal matrix composite is a degradation of the composite Young's modulus under increasing applied load and/or strain [116,123,125,146,158,160–167]. As soon as the composite yield stress is reached, a noticeable decrease in elastic modulus is typically measured. The rate of particle fracture and thus the rate of the ensuing Young's modulus degradation depends on the particle statistical strength distribution. The decrease of the elastic modulus can reach more than 20% compared to the initial value; clear experimental evidence for this can be found in Kouzeli et al. [116], results of which are here summarized in Figure 1.7. In this study the Young's modulus evolution of high-volume fraction (>40%) pure aluminium reinforced with two different types of alumina particles of different sizes was monitored by a series of load-unload cycles over the course of a tensile test. The results show that, if all else is equal, a composite with larger and thus weaker particles loses stiffness at a higher rate relative to strain (Figure 1.7a). The observed trend cannot be explained by other damage accumulation mechanism such as matrix voiding: if matrix voiding were stress controlled, composites with smaller particles would accumulate damage at a higher rate since the matrix stress is higher in the case of smaller particles. For strain-controlled matrix voiding, no size dependence is expected. A different damage accumulation rate was also observed when two composites were reinforced with particles of the same size but of different quality. The observed rate of damage accumulation was higher for composite reinforced with comminuted powder compared to composite reinforced with high-quality and intrinsically stronger vapour-grown particles (Figure 1.7b). Similar observations were made in copper alloy matrix composites reinforced with comminuted and high-quality vapour-grown alumina powders [154].

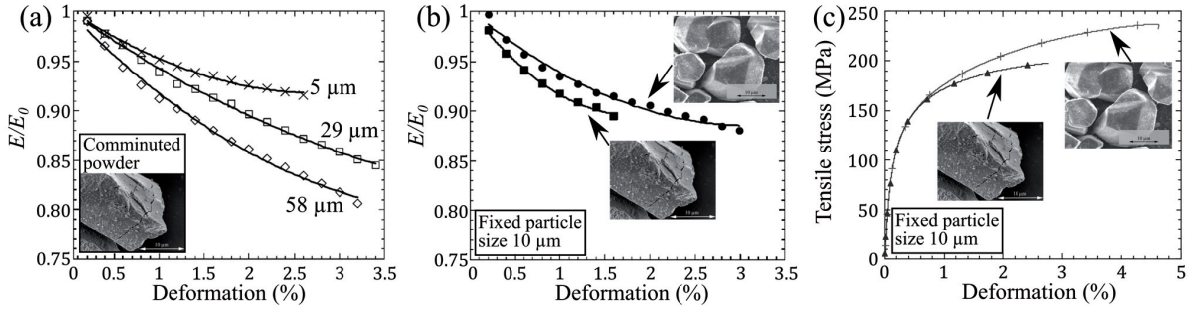


**Figure 1.7 – The effect of particle fracture on tensile properties of high-volume fraction (>40%) alumina particle reinforced aluminium MMC. (a) Larger reinforcement particles lead to a higher rate of damage accumulation by particle fracture, which in turn leads to higher loss of composite stiffness. (b) Composite reinforced with high quality vapour-grown alumina particles has a lower rate of damage accumulation by particle fracture than a composite produced with comminuted alumina particles, which (c) leads to enhanced tensile ductility in comparison with composite reinforced with comminuted alumina powder exhibiting a high density of surface cracks. Plots in panels (a) and (b) and particle pictures are reproduced and adapted from Ref. [116] with permission of Elsevier. Data in panel (c) is replotted from Ref. [116].**

The particle intrinsic strength and the related rate of damage accumulation by particle fracture have a significant effect on the composite flow curve as well, as shown in Figure 1.7c from [116]. As particles break the “effective” load-bearing average cross-sectional area of the composite decreases; the differences in the flow curve can be explained with the principles of Continuum Damage Mechanics making the hypothesis of strain equivalence [168]. Assuming that the contribution to the composite strain due to strain hardening of the matrix is unchanged by particle fracture, the stress of the undamaged composite follows  $\tilde{\sigma} \propto E_0$  and that of damaged composite,  $\sigma \propto E$ , where  $E_0$  and  $E$  are the initial and actual elastic modulus of the composite, respectively. One can back-calculate the flow curve of the tested composite reinforced with hypothetical ideally strong particles (in the absence of other internal damage mechanisms) as

$$\tilde{\sigma} = \sigma \frac{E_0}{E} \quad (1.4)$$

Thus in this simple (approximate) analysis scheme, a 20% decrease of the Young’s modulus due to particle fracture decreases the flow stress of the composite by 20%. Equation (1.4) was found to be adequate in [116] giving the same “effective” composite flow curve in case of two microstructurally identical composites reinforced with qualitatively different particles and exhibiting different rates of damage accumulation by particle fracture.

Another rather important property that is significantly influenced by the particle intrinsic strength is the tensile ductility, as depicted in Figure 1.7c. Specifically, the *rate* of particle fracture was reported to significantly affect the composite failure strain [116,122,150,166,169,170]. In MMCs failing due to the onset of tensile instability, combining the Considere criterion with the expression for the effective stress Eq. (1.4) with a constitutive law for the undamaged material and neglecting the change in volume in the composite due to particle fracture, Kouzeli et al. [116] derived a simple expression for the failure strain, which reads

$$\varepsilon_f = \frac{n_h}{1 + \frac{d \ln(E_0/E)}{d\varepsilon}} \quad (1.5)$$

with  $n_h$  being the strain-hardening exponent of the undamaged effective composite flow curve, and predicts that a higher rate of stiffness loss due to particle fracture hastens tensile instability. The expression (1.5) was found to be in good agreement with experimental data of various MMCs [116,162,171].

In the previous paragraphs we discussed the role of the particle strength on the tensile properties of particle-reinforced composites that fail progressively, by essentially ductile failure. Additionally, PRMMCs often break in brittle manner, suddenly and well before the onset of tensile instability [7,172,173]. Tekoglu and Pardoen [174] developed an “Integrated Mori-Tanaka-Damage” model which predicts that, if the reinforcing particle (and matrix-particle interface) strength is several times higher than the yield stress of the matrix, then the ductility and ultimate tensile strength improve. The composite ultimate tensile strength is predicted to be up to 4 times higher than the yield stress of the matrix when the critical stress for particle fracture is more than 12 times the matrix yield stress.

To address the observed ductile-to-brittle transition in the composite failure mode and to assess the role of the particle strength quantitatively, Hauert et al. [16] developed a mean-field analytical micromechanical model that integrates both failure modes, namely ductile and brittle. The model combines tensile flow curve prediction via the Torquato Identical Hard Spheres model and the simplified variational estimate of Ref. [175] with the effect of damage accumulation by particle fracture following the Weibull distribution (Eq. (1.3)). The latter is governed by a local load sharing rule, which assumes that only the nearest neighbouring particles take part in local stress redistribution after particle failure. This forms clusters of several neighbouring broken particles, which can reach a critical size that causes sudden, brittle failure of the entire composite. This abrupt brittle failure mode is modelled using an adaptation of Batdorf’s local load-sharing model for fibre-reinforced composites [176] giving the stress at which an avalanche-like propagation of damage via the creation and unstable growth of ever bigger clusters of broken particles commences. Figure 1.8 illustrates stress strain curves predicted using this model for a composite reinforced with particles with different realistic statistical strength distribution. The model predicts that an increase in characteristic particle strength,  $\sigma_0$  at fixed Weibull modulus leads to an increase in the composite tensile strength and ductility (Figure 1.8a). For the strongest modelled particles, composite failure occurs instead by the onset of tensile instability. The model also shows that the effect of the Weibull modulus of the particles’ statistical strength distribution is almost as important as their characteristic strength; this is a manifestation of the important role played by the weakest particles in composite failure (Figure 1.8b). Hauert et al. went further in their estimates by answering the question of what could be achieved if particles having the statistical strength of today’s engineering ceramic fibres (see Table 1.1) were used as reinforcement of a strong metallic matrix. Although there are several limitations in the model, one of which is the assumption that only particle fracture contributes to damage accumulation, this approach provides a theoretical limit for what could be achieved in PRMMCs. Its predictions were already presented in



Figure 1.2, showing that isotropic PRMMCs with specific properties approaching those of fibre-reinforced composites along the fibre direction are achievable in particulate reinforced metals.

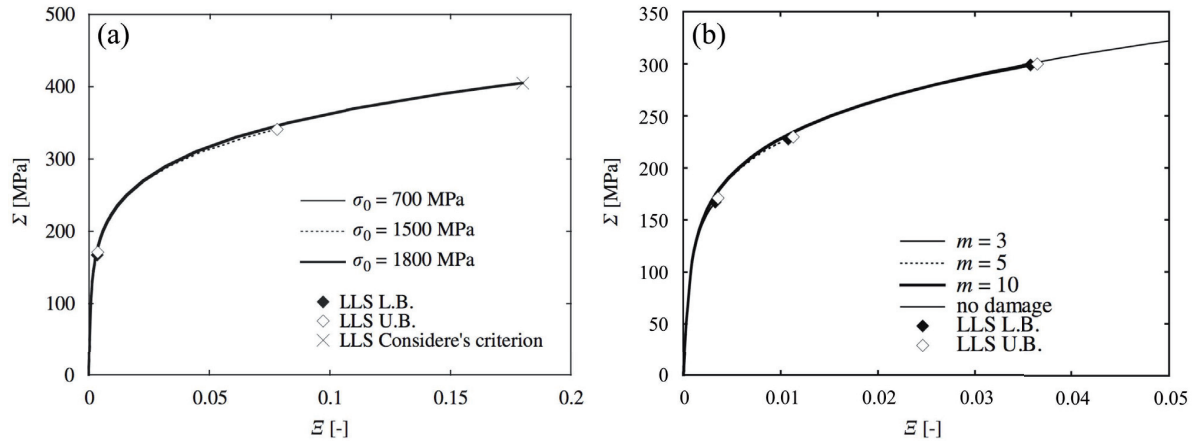


**Figure 1.8 – Stress-strain curves of a ceramic particle reinforced metal matrix composite predicted using the local load sharing model of [16] with matrix hardening following the classical power law,  $\sigma = c \cdot \epsilon^{n_h}$ , with the strength coefficient  $c = 300$  MPa, hardening coefficient  $n_h = 0.2$ , and  $10^7$  ceramic particles occupying 50 vol% of the composite volume. (a) The role of the characteristic strength,  $\sigma_0$ , of ceramic particles on the resulting composite strength with particles' Weibull modulus fixed ( $m = 3$ ). (b) The role of the particles' Weibull modulus on the resulting composite strength with particles' characteristic strength fixed ( $\sigma_0 = 700$  MPa). Plots in the figure are reproduced from Ref. [16] with permission of Elsevier.**

### 1.3.3 Fracture toughness

Although crack growth in PRMMCs is in general a complex problem, which depends on the interplay of a multitude of factors including the particle size and volume fraction, the interface strength or the matrix strength, particle fracture and thus the particle intrinsic strength is one of the most important among parameters controlling the composite crack growth resistance [7,19,127,155,163,177–182]. This appears as intuitively evident (obviously weaker particles will ease crack growth); however, there is only scant experimental data documenting quantitatively the influence of the particle strength on composite fracture toughness, for the obvious reason that particle strength has seldom been studied. Additionally, complicating factors exist that obscure trends; for example, increasing the particle size and in proportion (at fixed particle volume fraction) the interparticle distance has mixed influences, in that increasing the microstructural scale increases per se the composite toughness, while it also tends to decrease the intrinsic strength of brittle particles [180,183,184].

It has been shown using FEM and other methods of micromechanical modelling that broken particles and also particles with a flaw both tend to attract a crack, leading to a substantial increase in the crack driving force, while simultaneously easing crack propagation and embrittling the composite [177,181,185–187]. Figure 1.9 summarizes the qualitative effect on the stress state ahead of the crack tip and the crack path in the case when particles do not fracture (the case of ideally strong particles) and when particle fracture occurs at a critical particle stress of 1 GPa obtained via two-dimensional FE simulations by Ayyar and Chawla [160]. Simulations show that particles bear a significant portion of the load even far away from the crack-tip, which leads to their failure and formation of microcracks

ahead of the crack tip (Figure 1.9a). Although the model could not capture the formation and growth of multiple cracks, this would lead to crack coalescence ahead of the primary crack. Simulation of the crack path (Figure 1.9b) showed that when particles fracture ahead of the crack tip their crack shielding capacity is significantly weakened, attracting the crack and reducing the level of crack deflection.

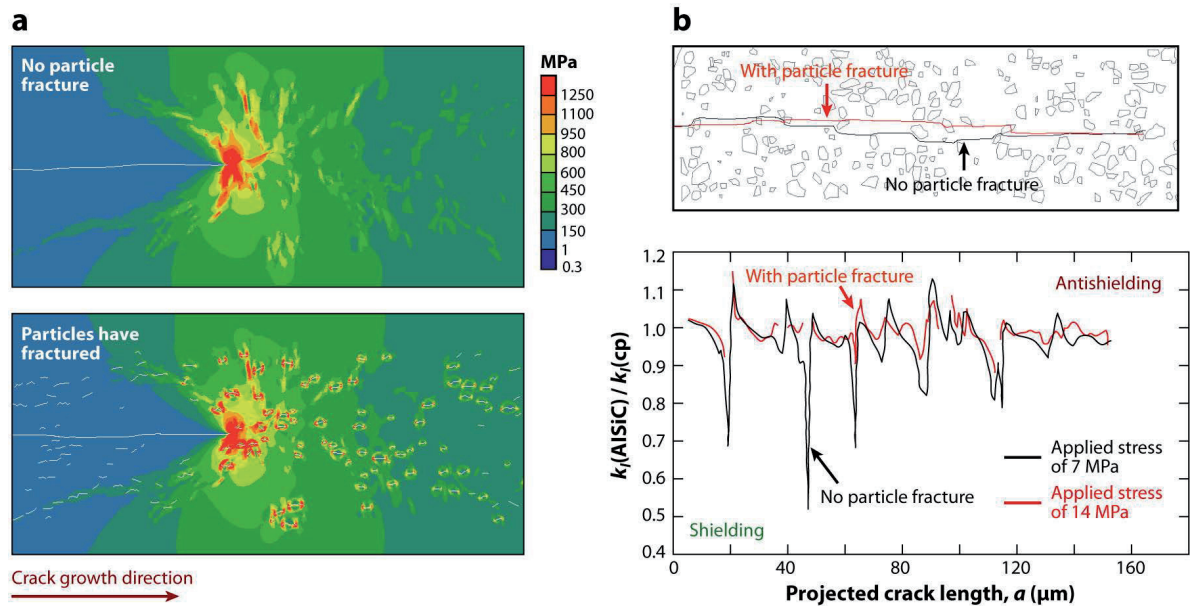


**Figure 1.9 – 2D finite element simulation of a single-edge notched aluminium metal matrix composite reinforced with 15 vol% SiC particles specimen containing a crack. (a) The effect of particle fracture on the Von Mises stress distribution. Notice that when particle fracture is operational particles fracture relatively far away from the crack tip which would lead to crack coalescence by particle fracture ahead of the primary crack. (b) Particle fracture reduces the degree of shielding from the particles, attracting the crack and decreasing the crack deflection. Figure reproduced from Ref. [188] with permission of Annual Reviews.**

Clear experimental evidence of the importance of the particle intrinsic strength on the composite fracture toughness was provided by Miserez et al. [19,155–157]. In their experiments, microstructurally simple aluminium and aluminium-copper alloy matrix composites reinforced with  $\approx 50\text{vol}\%$  alumina particles of different quality and intrinsic strength were studied with other parameters such as the particle size and volume fraction, matrix-particle interface quality and matrix strength kept at a fixed value. Experimental results summarized in Figure 1.10 show that the composite fracture toughness is almost two times higher when reinforced with high-quality vapour grown alumina particles compared to the composite reinforced with comminuted particles containing high density of surface defects (Figure 1.10a). Investigation of the crack profiles from arrested chevron-notched specimens showed that, with all else equal, the composite reinforced with comminuted powder exhibited a higher portion of broken particles along the crack path compared to the composite with vapour-grown particles (Figure 1.10b). The level of crack-deflection for the composite reinforced with high-quality vapour-grown particles was also more pronounced, consistent with the afore mentioned FE simulations (Figure 1.9b).

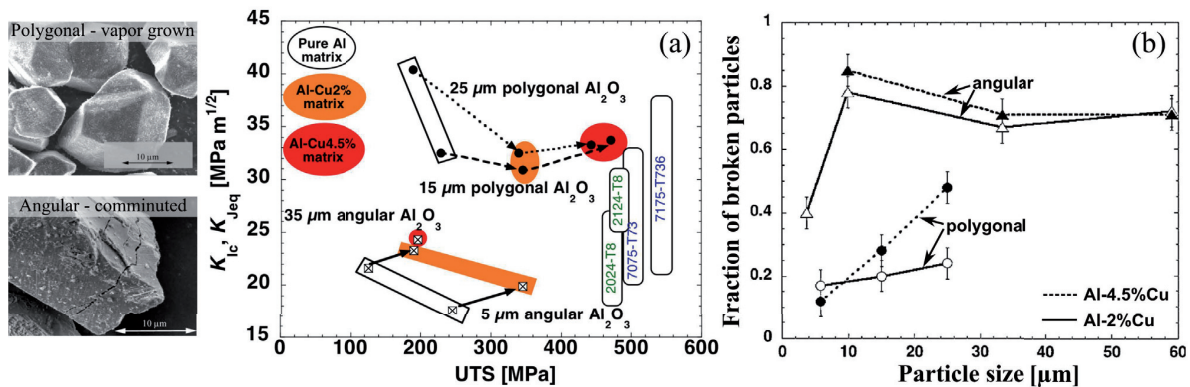


Figure 1.10 – The influence of the alumina particle intrinsic strength on fracture toughness of an aluminium alloy metal matrix composite. (a) The fracture toughness of the composite can be almost two times higher when the matrix is reinforced with higher quality vapour grown particles and comparable with aerospace grade engineering aluminium alloys. (b) The proportion of the cracked particles along the crack path is higher when low quality comminuted alumina particles are used. Plots in panels (a) and (b) reproduced from Ref. [19] with permission of Elsevier. Particle pictures reproduced from Ref. [116] with permission of Elsevier.

#### 1.4 Deducing the particle strength from the macroscopic composite behaviour

To date, the strength distribution of particulate reinforcements has mainly been estimated indirectly, by employing more or less elaborate micromechanical models of two-phase composite material behaviour to estimate the stress borne by particles from measured composite stress and strain states, coupled with direct or indirect observations of particle fracture and Weibull statistics. Wallin et al. [189] were among the first to estimate the statistical strength of reinforcing particles by adopting a simple fibre loading model in which the stress in particles is proportional to the matrix flow stress. Some researchers estimated the average stress in particles considering dispersion hardening models [190]. Most other works rely on adaptations of models derived by Eshelby and/or Mori and Tanaka to estimate the stresses borne by particles [135,158,191]. In his work Eshelby [192] derived a tensor that links the far-field strain of a linear elastic matrix with the strain in the isolated elastic inclusion. In the Mori and Tanaka approach [193] the authors take into account the interaction among inclusions by also considering an isolated inclusion but subject to an effective strain field equal to the average matrix internal strain.

Mochida et al. [164] considered that the stress induced in particles is a sum of the thermal residual stress due to CTE mismatch strain and the stress induced by the matrix plastic strain during tensile loading. The residual stress was estimated using a model based on dislocation punching by Taya et al. [194]. The stress in particles due to the matrix plastic strain was analysed using the Eshelby model [192] considering that the matrix contains unbroken as well as broken particles with the latter assimilated to voids. This approach led to predict that the particle stress scales linearly with the plastic strain, with the scale parameter a function of elastic constants of the matrix and the particle, and of the volume fraction of particles and voids. Hauert et al. used their model [16], already mentioned earlier in Subchapter 1.3.2 and developed to model the tensile properties of a PRMMC considering

the local load-sharing and gradual growth of clusters of broken particles, to back-calculate the strength distribution of comminuted alumina reinforcement particles [135].

Numerical modelling using finite element analysis was also employed to calculate the stress borne by particles during composite loading. Llorca et al. [125] modelled the composite as an array of unit cells with a particle represented as a cylinder of length equal to the size of the particle embedded in a matrix. A similar approach was adopted by Babout et al. [118] who assumed a spherical particle to reinforce the unit cell. Majumdar and Pandey [127] used the results of Llorca et al. [125] to estimate average stresses in SiC particle reinforcements. In their simplified procedure the stress in the composite is shared between particles and matrix with the constraint factor increasing the portion of the load borne by particles. FE calculations were also used in the development of micromechanical models and estimations of particle stress by Zok et al. [122,172,195]. These authors expressed the particle stress as the matrix flow stress scaled with a stress amplification factor that arises from elastic/plastic mismatch between the particles and matrix obtained from FE simulation.

It is difficult to compare results of the “back-calculated” particle strengths from the literature because results depend strongly on the model used, and because basic parameters such as the particle size and type (comminuted, sintered, atomized, etc.) are seldom reported in the description of experimental procedures. Hauert et al. [135] studied the strength distribution of  $\approx 50\text{vol}\%$  comminuted white fused alumina  $\approx 33 \mu\text{m}$  in diameter reinforcing an aluminum-copper alloy, reporting back-calculated Weibull characteristic strength  $\sigma_0 = 850 \text{ MPa}$  and Weibull modulus  $m = 3$  (Figure 1.11a). These authors also inferred the strength of the same particles when embedded in a softer pure aluminium matrix. In that case the inferred strength of particles was significantly different ( $\sigma_0 = 445 \text{ MPa}$ ,  $m = 3.5$ ), the reason invoked being extensive particle-particle interaction due to significantly higher achieved strains during composite loading compared to stronger alloyed matrix composites, which do not deform as extensively. As a comparison, Mochida et al. reported estimated particles strengths of  $15\text{vol}\%$  alumina particles  $\approx 25 \mu\text{m}$  in diameter of (presumably) similar type reinforcing a 6061 aluminium alloy (Figure 1.11b). Using their approach, the reported particle strength distribution had the characteristic strength  $\sigma_0 = 1990 \text{ MPa}$  and Weibull modulus  $m = 1.43$ . Extrapolating the two distributions from one particle size to the other shows a marked difference between the two estimations (Figure 1.11c).

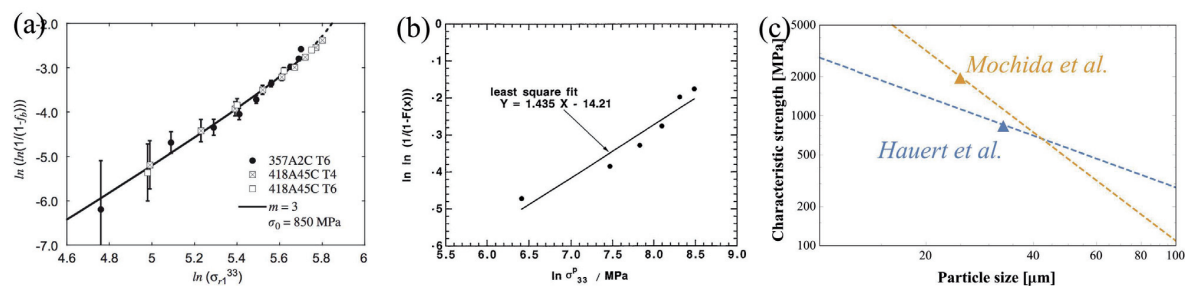


**Figure 1.11 – Weibull strength distribution of (a) comminuted white fused alumina from Hauert et al. [135] (reproduced with permission of Elsevier) and (b) presumably comminuted white fused alumina from Mochida et al. [164] (reproduced with permission of the Japan Institute of Metals and Materials) inferred from macroscopic composite testing using two different micromechanical models. (c) Comparison of the two strength distributions shows considerable difference in the predicted strength.**

A common feature of studies described above is that they focus on the average stress exerted on the particles during the (measured) deformation history of the composite, which may differ strongly from the stress at which a given individual particle fractures. The approach also provides little information on the relation between the structure and the properties of the particles themselves. All micromechanical models furthermore rest on strong simplifications; for example, particles are often considered to be monodispersed spheres subject to an average stress homogeneously distributed in their volume perfectly bonded to the matrix and with no physical interaction between particles. Analytical models used are furthermore often ad-hoc adaptations of linear elastic models, the legitimacy of which is often open to question. The stress redistribution after particle failure is also a complex problem that is difficult to model [135]. Lewis and Withers in Ref. [158] reanalysed data from Llorca et al. [125] using four different micromechanical composite models to derive the average particle stress evolution including (i) a simple relationship of the particle stress being proportional to the particle aspect ratio, (ii) an elastic Eshelby inclusion based model, (iii) the Eshelby model including the effect of matrix-particle plastic deformation modelled as a misfit strain, and (iv) the previous approach (iii) adding the effect of plastic relaxation. The authors' analysis shows that the choice of the model has a considerable effect on the resulting particle strength Weibull distribution. In addition, the distribution parameters appeared to depend on the strain at which the data were measured and analysed, regardless of the model used. The authors admit that this can be a manifestation of the incapacity of the models to accurately predict the evolution of the particle stress in the deforming composite.

Quantification of particle fracture is also commonly assessed indirectly. Most such work relies on various measurements of the fraction of broken particles using quantitative metallography. This has limitations as some broken particles may go unnoticed [196] when only 2D surfaces are studied [197] or when damage close to, or along, a free-surface is evaluated [198]. Also, great care must be taken when preparing samples in order not to introduce artefacts such as particles broken in grinding or polishing. Monitoring of a damage parameter, such as Young's modulus, to assess the fraction of broken particles rests on idealizations, notably as concerns the particle stress estimation [135]. Although the use of modern tomographic methods (X-ray or neutron) enables the *in-situ* tracking, within the material while it is strained, of the progression of particle fracture in two-phase materials, these do not in general make it possible to detect the underlying cause for their failure.

In short, the collective behaviour of a large number of hard brittle second phase particles within an elasto-plastic matrix, the *in-situ* behaviour of which is furthermore not known *a priori* (being potentially influenced by the particles and the plasticity size effect), remains a sufficiently complex problem. This makes the back-calculation of particle strength from that of a composite subject to question, such that this approach has seldom given access to a clear quantification of the local *in-situ* fracture stress of the particles themselves.

## 1.5 Probing the strength of hard and brittle particles directly

If one broadens the scope of a literature search to go beyond the micromechanics of metal matrix composites, one finds that the mechanical testing of particles and grains of various materials in general is a relatively wide and self-standing area of research, the topic having relevance in many



branches of engineering besides metallurgy. The strength of rock and mineral particles dictates the energy consumed in mining processes [199]. Particle strength also governs the mechanical behaviour of many soils [200–202] and is an important parameter in processes of powder granulation and compaction, which are present across a wide range of industries (including for example food and pharmaceutical industries) [203–207]. In materials processing the strength of particles governs grinding [208] and comminution processes, and also the processing of ceramics [209]. Testing for strength is of interest in various oxide, nitride or carbide microspheres with a potential use as nuclear fuels [210] or in pebble beds of nuclear fusion reactors [211]. This has motivated a sustained level of research, spanning decades, into the behaviour of small particles, and also of macroscopic grains and coupons of rocks and minerals. Typically, these are tested by compression between a pair of platens – the so-called uniaxial compression test, which is reviewed in what follows. A recent and elegant approach demonstrated on small millimetre-scale ceramic ball-bearings, which involves introducing a wide straight-through notch into the particle, which results in a state of elevated hoop tensile stress along the surface opposite to the notch root when the particle is compressed normal to the notch plane, is then reviewed in turn.

### 1.5.1 Uniaxial compression

#### *Introduction*

Compressing a spherical or irregular test piece, recording the load at which it breaks to measure its strength, has a long tradition. An important contribution to the question dates back to the mid-1960s, when Hiramatsu and Oka [212] analysed the stress state within an isotropic linear elastic sphere of radius  $R$  compressed by a pair of uniformly distributed radial loads acting symmetrically over two equal spherical caps centred along the compression axis and of outer circle defining the *contact radius*,  $a$  (see Figure 1.12). These authors showed that when a sphere is compressed over such a small spherical cap of relative contact radius ( $a/R$ ) lower than  $\approx 0.1$ , a state of high tensile stress is present within the compressed sphere with its peak uniformly distributed along the compression axis stretching from the sphere centre towards the two opposite ends just below the stress application points. This peak stress is roughly equal to  $\sim 0.7$  times the *nominal stress*, defined as  $F/\pi R^2$ , where  $F$  is the load acting on each spherical cap (see Figure 1.12). Using the frozen-stress photoelastic technique on an irregular test coupon made of epoxy resin, these authors also showed that the stress state in the centre of a similar irregular test piece under compression with concentrated loads does not differ significantly from that of a spherical test piece, suggesting that the strength formula derived for sphere compression can be in principle used for any irregular test piece.

The approach consisting in computing the particle strength as 0.7 times the nominal stress has, however, been debated, notably because, depending on the precise value of  $a/R$ , the peak value of the tensile stress along the compression axis can deviate significantly from 0.7 [213–216]. Following Hiramatsu and Oka’s analysis, the “tensile strength” of particles tested in uniaxial compression is therefore often computed as:

$$\sigma_f = \kappa \frac{F_f}{\pi R^2} \quad (1.6)$$

where  $F_f$  is the peak (failure) load and  $\kappa$  is a constant near unity. Experimental data of Jaeger [217] and analyses by several authors suggest that  $0.7 \leq \kappa \leq 1.4$ . Many experimental studies have used this expression to evaluate the strength of spherical or irregular particles tested in uniaxial compression [201,202,206,207,211,218–226] and its analogue can be found in the standardized Brazilian disc test [227].

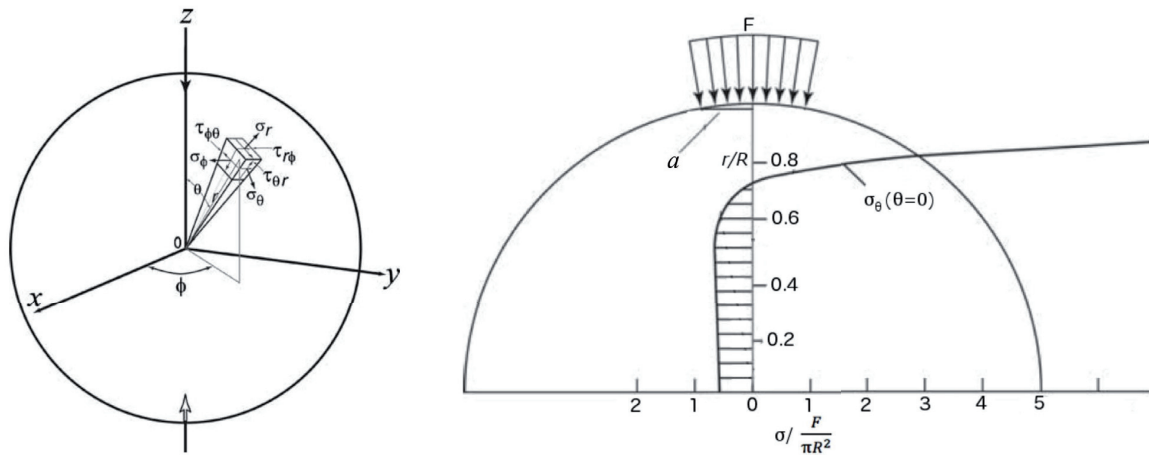


**Figure 1.12 – Schematic representation of a sphere of radius  $R$  in uniaxial compression with the geometry definition. When the particle is compressed uniaxially by a pair of uniformly distributed loads  $F$  over a spherical cap represented by the contact radius  $a < (0.1 \times R)$ , a region of high tensile stress develops in the central portion of the particle with its peak located along the compression axis according to Hiramatsu and Oka [212]. The images in the figure are reproduced and adapted from Ref. [212] with permission of Elsevier.**

*Review of the uniaxial compression of alumina particles: from millimetres to nanometres*

Methods of uniaxial compression were used to investigate the strength of individual ceramic particles, some of them being very similar to those that are used as the reinforcement in metal matrix composites. Alumina abrasive grains several tens to several hundred micrometres in size produced by different methods followed by comminution were tested in compression between two hard (relative to the particle strength) surfaces, resulting in small particle-platen contacts, and evaluated according to Eq. (1.6) and then statistically analysed using the Weibull distribution [106,226,228–233]. In general, a strong strength size-effect has been reported, with smaller particles giving higher strengths, in line with flaw statistics mentioned earlier (Eq. (1.3)). Very low Weibull moduli, in the range 1-4, of the crushing strengths were reported, and strength varied significantly depending on the particle type and processing, ranging from a few hundred to a few thousand MPa (see Figure 1.13).

Interestingly, in all of the cited studies, a weak dependence of the Weibull modulus on the size of the tested particles was reported. With smaller particles higher Weibull modulus values tend to be observed, suggesting that the flaw distribution is more uniform in smaller particles [107]. In two studies [228,231] it was also reported that a critical particle size exists past which an increase in the particle

size has a negligible effect on the particle strength. It was speculated in [228] that there is a ductile to brittle transition for alumina particles of size around 0.7  $\mu\text{m}$  which, however, does not have support in the literature. A ductile-to-brittle transition is expected in particles at most below a few micrometres in size; this was experimentally observed in particles below 100 nm in size [234,235].

Comparing results for silicon carbide and alumina, comminuted black silicon carbide (97-99% purity) particles were reported to have roughly 25% higher crushing strengths than unspecified « regular » comminuted alumina particles [231]. The strongest silicon carbide particles from the study exhibited average crushing strength  $\approx 2$  GPa for 125  $\mu\text{m}$  average particle size tested in ambient conditions. The strength was even higher when tested in dry (0% relative humidity) conditions  $\approx 2.5$  GPa. In an earlier study, Becker [228] reported black silicon carbide particles crushing strength values to be somewhat lower than for « regular » alumina particles, while the higher purity green silicon carbide was almost two times weaker than black silicon carbide particles, consistent with another study in which green silicon carbide was found to be weaker than alumina [106].

The strengths of several different types of alumina particles were reported in the literature. For instance, the crushing strength of brown fused alumina, which is processed in the same way as white fused alumina except for the presence of a larger amount of impurities including notably  $\text{TiO}_2$ , exhibited somewhat higher strength values than did white fused alumina [106,107]. The strongest tested brown alumina particles exhibited average crushing strength  $\approx 200$  MPa for an average particle size 780  $\mu\text{m}$ . The estimated characteristic strength for strong brown fused alumina was 140 MPa/ $\text{mm}^3$  with a Weibull modulus  $m = 5$  [106,230]. This would translate to characteristic particle strength near 2000 MPa for particles around 30  $\mu\text{m}$  in diameter. It was observed from SEM micrographs that the white fused alumina particles exhibited a “weaker”, less dense, microstructure containing a higher density of microcracks compared to the brown alumina. Sintered tabular-type alumina particles were repeatedly reported to exhibit superior strengths and Weibull modulus to that of fused aluminas [106,107,228]. Here again the microstructural differences were reported to be the main source of the strength difference. While fused alumina contained fewer but larger voids, sintered alumina exhibited finer uniformly distributed pores and less sharp corners than fused alumina, of more angular shape [106,107]. The sintered alumina also consisted of comparably smaller crystallites than fused alumina. The size reduction during the comminution process of sintered alumina may take place predominantly by cracking through weak and smaller grain boundaries, thus leaving less sharp corners.

It was demonstrated that it is possible to change the strength distribution of alumina particles by low-energy ball-milling, which results in more rounded particles by elimination of the weak particles with large defects and low crushing strengths [106]. Comparison of the crushing strength distribution of ball-milled particles to raw particles showed increased average crushing strength and Weibull modulus values after ball-milling. By removing the weakest particles from the dataset of the raw particles the strength distribution became comparable to that of stronger ball-milled particles, consistent with the assumption that weak particles were eliminated (by fracture) during the low-energy ball milling process.



Rosenflanz et al. [236] performed uniaxial compression on amorphous and nanocrystalline rare-earth aluminate microspheres 70-100  $\mu\text{m}$  in diameter prepared by a thermal spraying technique. Results show that the particle strength is significantly influenced by the particle microstructure. While fully amorphous particles exhibited crushing strengths near 1000 MPa, by annealing them to make them nanocrystalline, the strength increased almost two-fold reaching 1800 MPa for particles annealed at 1250°C. Further annealing at higher temperatures promoted grain coarsening and led to a decrease in crushing strengths. A strong correlation of the crushing strength with the particle hardness was also observed.

Vapour-grown Sumicorundum particles with a mean diameter near 1 $\mu\text{m}$  similar to those in Figure 1.4b were tested in compression by Yoshida, Ogiso et al. [220,226]. These authors used a nanoindentation apparatus equipped with a flat diamond tip to crush individual particles spread on a diamond substrate. The resulting crushing strengths according to Eq. (1.6) with  $\kappa = 0.7$  ranged from 1 to 8 GPa and followed a Weibull distribution with a characteristic strength value of 3.2 GPa and a Weibull modulus equal to 1.8.

The so far smallest alumina particle compression tests were to the author's knowledge performed by Calvié et al. [234,237] on 40 to 120 nm in diameter transition  $\gamma+\delta$ -alumina nanospheres made by physical vapour synthesis. These authors tested particles inside a TEM microscope between a flat diamond tip and a sapphire substrate. The maximum tensile stress that these particles could sustain, calculated by FE simulation using material properties of  $\alpha$ -alumina, were estimated to be near 3.4 GPa. The smallest, 40 nm diameter, particles exhibited plastic deformation without brittle failure, suggesting the presence of a brittle-ductile transition in the tested transition alumina at that scale. This is consistent with the comminution limit of  $\alpha$ -alumina, expected to occur with particles around 20 nm in size.

Figure 1.13 summarizes crushing strength results for pure engineering grade alumina particles from the studies cited above. The particle strength values from Figure 1.13 were reported to follow the Weibull distribution and extrapolation (dashed lines in the figure) of the hard data (symbols in the figure) is given according to Weibull scaling across different particle sizes. From the figure it appears that (i) the strength of particles with a size in the range between 1 and 50  $\mu\text{m}$  (sizes of interest in MMC reinforcements) is mostly an unexplored territory and (ii) the Weibull statistics obtained from the crushing experiments with one particle size range cannot in general be used to predict the strength across a wider range of different particle sizes, or to a different type of alumina particle.

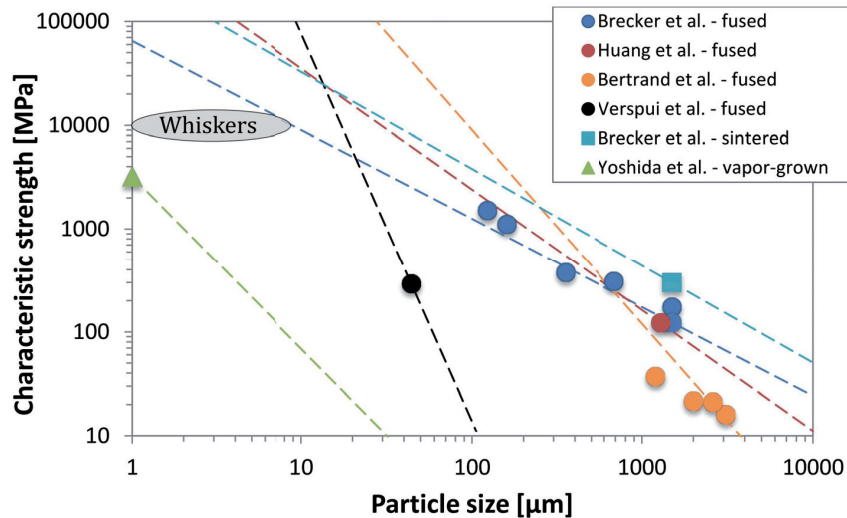


**Figure 1.13 – Overview of Weibull statistic characteristic strength values from uniaxial compression of different pure engineering alumina particles prepared by different methods: (circles) comminuted fused alumina, (rectangle) comminuted sintered alumina and (triangle) vapor-grown alumina. Dashed lines represent extrapolation of the reported Weibull distribution results for different particle size. Data from [106,107,226,228,233].**

#### *Limitations*

Although qualitatively the results presented in previous paragraphs provide reasonable insights into ceramic particle strength, and although the quantitative data are of the right order of magnitude, there are several limitations to the uniaxial compression test method that make those results subject to caution. First of all, the assumed value of the constant  $\kappa$  in Eq. (1.6) used in the interpretation of the measured crushing force, can change the calculated fracture stress by a factor of up to 2. Additionally, except for perfectly spherical particles, uncertainty in the particle size term used in Eq. (1.6) is another source of imprecision. While Hiramatsu and Oka [212] suggested to take the interplaten distance at the moment of failure as  $2R$ , Brecker [228] proposed that the average particle size be used, and yet another method using the particle projected area can be found cited in Verspui et al. Ref. [229]. This inconsistency in the parameters used in Eq. (1.6) was recognized by Verspui et al. [229,232], which led to a reevaluation of the data using crushing loads rather than stress; this is a common practice in evaluating the uniaxial compression data [221,222,224,238].

More worrisome is the reported dependence of the uniaxial compression results on the particle-platen contact properties including the particle morphology near the contact and the hardness of the platens relative to that of the particle. Brecker [228] performed crushing tests on various alumina particles with their opposite surfaces ground flat. The strength of such particles was found to be up to 8 times higher than that of the same “as-received” particles exhibiting sharp corners. Verspui et al. [229,233] observed that higher force was required to crush alumina particles when compressed between glass platens compared to the case where diamond platens were used. The same authors also observed that the vast majority (72%) of the tested angular alumina particles broke in the chipping mode of failure, in which small pieces of particle detach during the test; this is a rather common mode of failure observed in uniaxial compression of irregular particles [223,239,240]. This observation is in stark

contrast with the assumption that particle failure occurs due to tensile stress near its centre made in deriving Eq. (1.6).

There are several studies that cast considerable doubt on whether the uniaxial compression test using concentrated loads can at all be used to measure the tensile strength of particles [205,213,240–244]. The main concern is that when a particle (whether irregularly shaped or spherical) is compressed between two platens much harder than itself, the high stress concentration that develops at and near the small area of contact between the platens and the particle can cause the nucleation of extraneous cracks that may then govern the measured particle fracture stress, obscuring the detection of intrinsic particle flaws. An example from unpublished internal research is given in Figure 1.14. High-speed camera imaging of transparent particles and of coupons of material under uniaxial compression was used to show this in Refs. [240,242,244]. Acknowledging this, some authors attempted to estimate the stress near the periphery of the region of direct load application by means of Hertzian contact theory [200,231] or using a more simplistic average of a mean contact pressure [245]. In the case of angular particles this approach was found to be inapplicable, as the contact stress depends strongly on the size of the contact [231], which is *a priori* unknown unless it is carefully measured for each test using microscopy techniques. Such careful estimation of the contact size was done in the study of Brzesowsky et al. [200] testing relatively round sand particles between ceramic platens. This approach led, however, to back-calculated flaw sizes that were 1 to 3 orders of magnitude smaller than the flaws observed by microscopy. Moreover, in many strong brittle solids, the largest defects are located not within the particle, but along its surface [246], which is at best poorly sampled when the site of peak tensile stress is located deep within the particle, as it is predicted to be in the Hiramatsu and Oka approach.

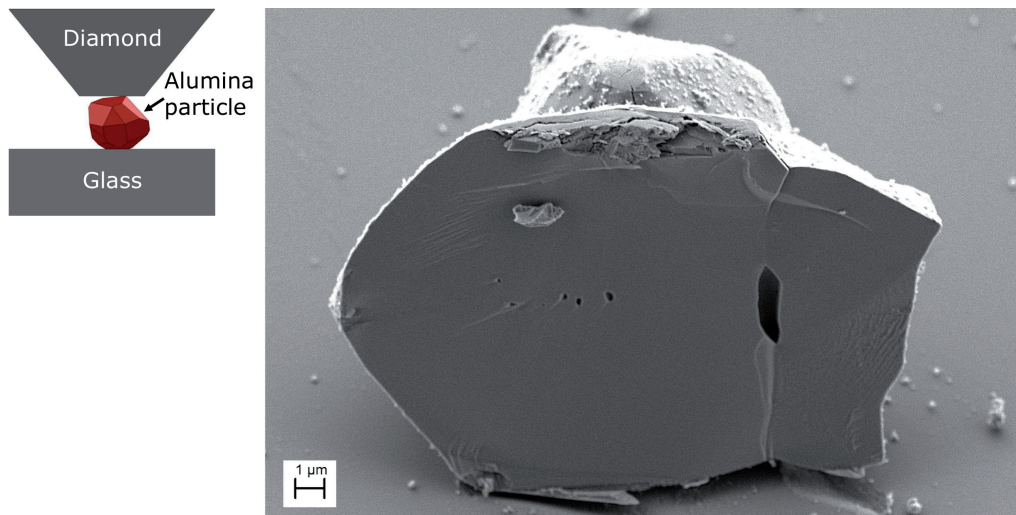


**Figure 1.14 – Uniaxial compression of a relatively equiaxed vapor-grown Sumitomo alumina particle between a pair of hard platens (diamond and glass). The particle broke into two pieces one of which was left on the glass bottom platen, such that fractography could be performed. The fracture initiated from the heavily damaged region where the particle contacted the diamond upper platen during the test, rather than from the centre of the particle, where one can observe large flaws in the form of pores. SEM image from unpublished work performed by the candidate.**

*Addressing the limitations of the classical uniaxial compression test*

The previously mentioned limitations, and a solution thereto, were identified by Shipway and Hutchings in a 1993 contribution that is a significant, but so far underexploited, advance in the state of the art of particle testing [9,10]. These authors reanalysed the particle stress field solution for the problem of compression of a linearly elastic sphere compressed by symmetric pressure uniformly distributed over the surface of the spherical caps at either end of a diameter. They pointed out that distributing the compressive load over a larger area would decrease the high stress concentration near the particle-platen contact, and secondly, that there can be a significant tensile hoop stress,  $\sigma_\phi$ , acting along the equatorial belt of the particle surface and due to which the particle could fail. Over the range  $0 \leq (a/R) \leq 0.8$  this tensile hoop stress remains (very) roughly equal to

$$\sigma_\phi \approx 0.4 \frac{F}{\pi R^2} \quad (1.7)$$

In addition, Shipway and Hutchings showed that as the ratio  $a/R$  increases, *i.e.*, if the particle is allowed to sink more deeply into the platen material, then the location of the peak tensile stress shifts from the compression axis to the equatorial belt region. For a particle material of Poisson's ratio  $\nu = 0.25$ , this transition happens when  $(a/R) \approx 0.6$ . Past that point, the hoop tensile stress  $\sigma_\phi$  in the equatorial belt exceeds the tensile stress anywhere else within the spherical particle.

Shipway and Hutchings also put their conclusions to practice, testing spheres roughly 700-800  $\mu\text{m}$  in diameter, of lead glass or of sapphire, using a variety of platen materials, some of them being made of a metallic material which deformed plastically where it contacted hard particles. Particle-platen relative contact areas of value approaching 0.6 were thus produced. Shipway and Hutchings showed that more consistent particle strength values are obtained using Eq. (1.7) than with Eq. (1.6), implying that fracture was more likely initiated from the particle surface rather than from its interior.

### 1.5.2 C-shaped particle test

Testing small ceramic ball bearings for strength poses difficulties that are very similar to those that are associated with testing of microscopic ceramic particle reinforcements. Spherical ball-bearings are, as their composite reinforcing counterparts, nearly impossible to grip for loading in tension or bending. To test ceramic ball-bearings, an ingenious approach that was recently developed is to compress the spheres after machining a wide and deep notch across an equatorial plane normal to the loading axis (Figure 1.15a). When the notched spheres are then tested in direct compression between two platens with the notch aligned parallel to the platen surfaces, the region of the sphere situated along its outer surface opposite to the root of the notch is placed under elevated tensile stress, peaking along the surface, with one principal stress component much larger than the remaining two (Figure 1.15b). This approach was named the "C-sphere test" by its inventors Wereszczak et al. [247,248] or "notched-ball test" in a more recent version [249] or the "notched roller test" for cylindrical specimens [250]. Its analogy can be found in the "C-ring" test which is a standardized test method to measure ultimate tensile strength of advanced ceramics of tubular form [251].

This test has several advantages over the uniaxial compression of a bulk test piece between hard platens. First, the stresses at and near the contact between the test piece and platens are significantly lower than what is attained further away along the surface on the opposite side of the notch: this makes the site of failure better defined and hence the failure stress better known. These peak stress distributions are also simpler and less sensitive to details of load application. Secondly, the applied loads are far smaller than in direct compression of a bulk sphere, such that the particles do not shatter into many pieces upon fracture. This, in turn, makes fractography and the identification of fracture-inducing flaws easier than in many other micromechanical fracture tests (Figure 1.15c-e). Thirdly, and this is an important consideration with brittle materials, the sample breaks in a region, the surface of which has not been machined (on the other hand the machining of the notch may introduce extrinsic flaws along the surface of the notch that is under compression), Figure 1.15b. So far the smallest particles tested by the C-shaped method were  $\approx 1$ mm diameter silicon nitride spheres studied by Wereszczak et al. [247]. The notch in the sphere was machined using a  $\approx 300\mu\text{m}$  wide diamond-grinding wheel while the ball was fixed in a specially made jig. The spheres exhibited  $\approx 940\text{MPa}$  characteristic Weibull strength with very narrow strength distribution characterised by a Weibull modulus  $m = 28$ . Microscopic scratches (Figure 1.15e) and agglomerates containing glassy regions were identified as strength-limiting defects.



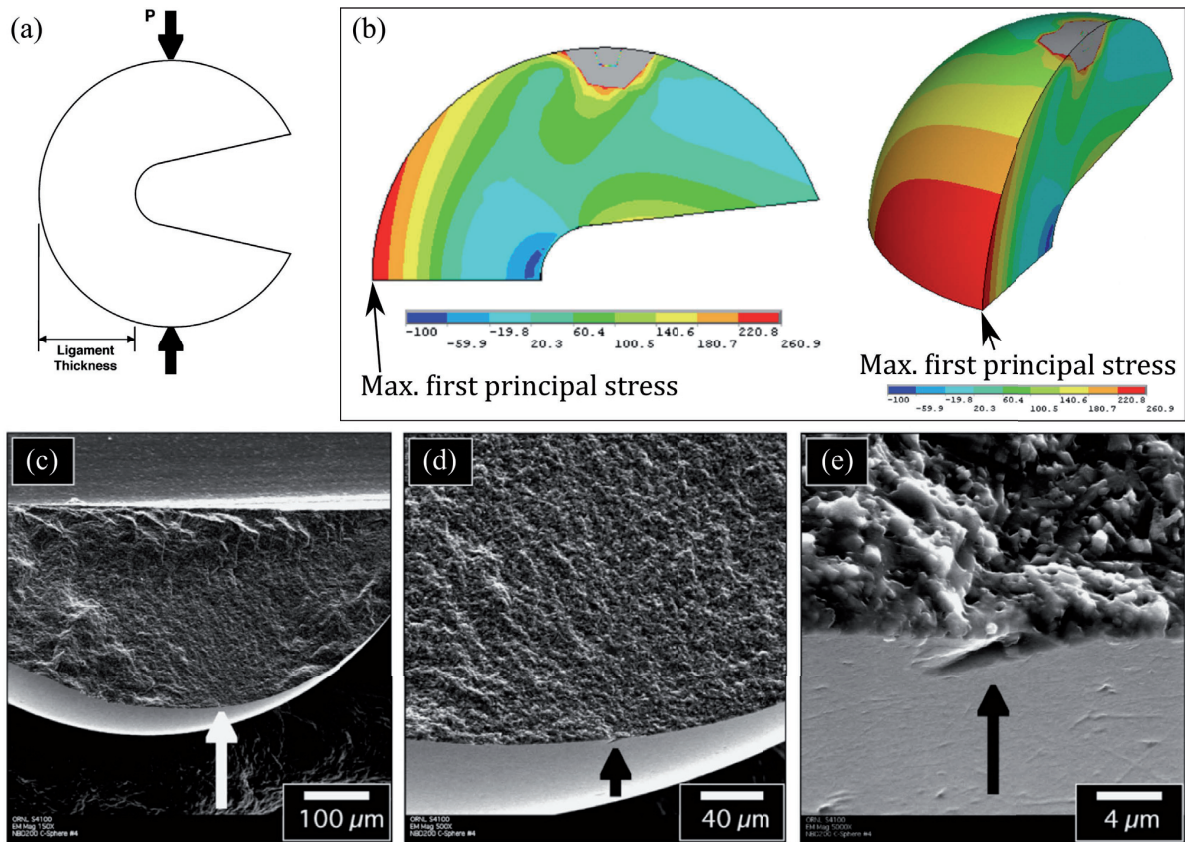


**Figure 1.15** – Overview of the C-shaped test conducted on a 1mm silicon nitride sphere. The notch in the particle (a) was machined using a diamond-grinding wheel and tested in compression measuring the fracture load  $P$ . (b) Finite element simulation of the tested C-shape specimen shows that a state of high tensile stress is present along the surface just opposite to the root of the notch. (c-e) Fractographic analysis of SEM micrographs of one of the tested spheres reveals a surface scratch as the strength-limiting flaw located near the peak of the first principal stress (indicated by an arrow). The images in the figure are reproduced and adapted from Ref. [252] with permission of Elsevier.

## 1.6 Micro- and nano-mechanical testing for strength

### 1.6.1 Introduction

The testing for strength at microscale dates back to 1950s, when first strength measurements of microscopic whisker crystals were performed by Herring and Galt, and Brenner [253,254], mostly on metal single crystals. These first attempts to measure microscopic strengths relied either on the measurement of failure strains from the deformation of the high-aspect ratio crystals by photography, or alternatively were conducted using ingenious, highly-skilled laboratory rigs built to measure small loads. Pioneers in the subject matter of the present thesis were Webb and Forgeng [86] who tested individual vapour-grown alumina needles and individual hard and brittle reinforcing plate-like particles isolated from alloys adopting the strain measurement method from [254], suggesting that such microcrystals approach the theoretical strength limits for the given materials. Studies of other groups and researchers followed what resulted in the extensive mechanical characterization of various mi-

crocrystals including alumina whiskers reviewed in Section 1.2.2; however, the mechanical characterization was mostly limited to rather long whisker-like specimens that can be relatively easily gripped and pulled on in tension.

A key development that is behind the explosive growth of scientific contributions in the past 30 years on mechanical properties of materials at the microscopic scale has been the advent of the instrumented nanoindentation apparatus, capable of locally applying and resolving forces as small as a few micro-newtons and displacements in the nanometre range; this development dates back to the mid-1980s and the beginning of the 1990s [255–258]. Nanoindentation makes it possible to sample the modulus and hardness of materials in areas only a few tens of nanometres wide. In a broader picture, a modern nanoindenter can be considered as a general-purpose microscale load-application apparatus, which can today be used in combination with electron microscopy when performing *in-situ* testing [259].

A second important development has been the advent of Focused Ion Beam (FIB) machining [260]. The FIB is similar to a scanning electron microscope (SEM), except that a beam of tightly focused and accelerated ions is used to raster the surface of a sample rather than electrons. A typically used source of ions in the FIB instrument is gallium, owing to its low melting temperature (30°C), low volatility, and low vapour pressure. Systems using He<sup>+</sup> or Xe<sup>+</sup> ions also exist. Modern FIB instruments are equipped with an additional SEM column so that SEM imaging can be used in parallel with FIB machining (see Figure 1.16). When an accelerated ion impinges the surface of a solid, the ion kinetic energy and momentum are transferred to the solid, which results in a collision cascade and sputtering of the solid atoms (see Figure 1.16). This results in a local removal of material that makes it possible to carve microscopic specimens out of almost any solid. Besides the atomic sputtering, a number of other processes take place during the ion-solid interaction that have to be considered during FIB micromachining: (i) emission of secondary electrons, (ii) primary ion reflection and backscattering, (iii) sample damage, (iv) sample heating, (v) electromagnetic radiation, and (v) primary ion implantation in the sample surface. The substantial sample damage caused by cascade collisions with primary ions and ion implantation in turn raise concerns about the validity of data from tests conducted using microscopic specimens that contain such FIB artefacts; this is discussed below in Subchapter 1.6.5.

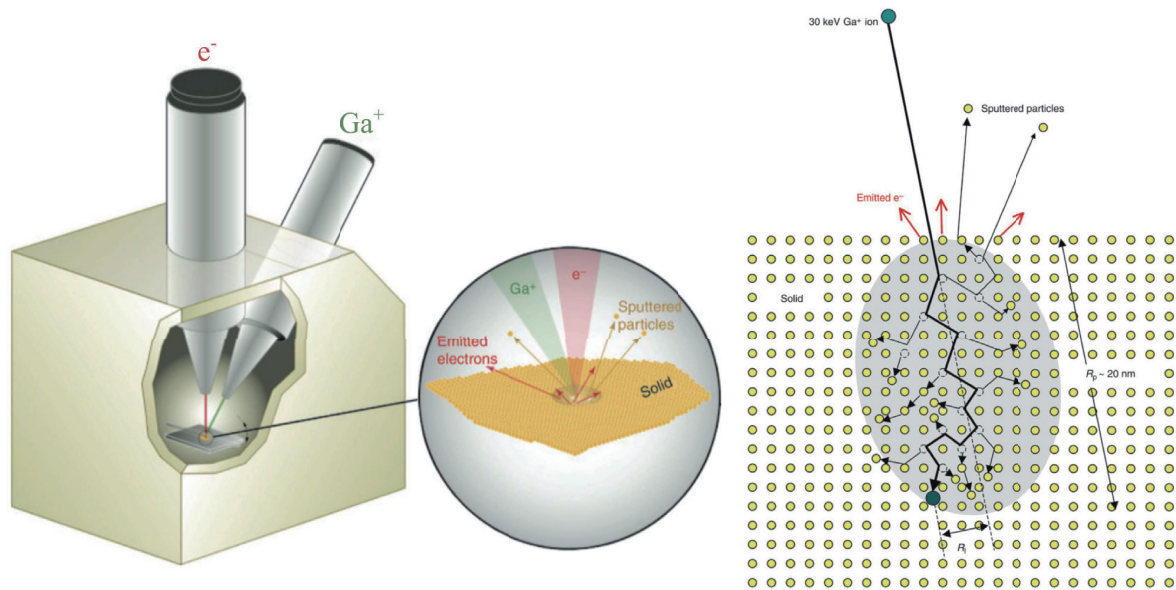


**Figure 1.16 – A schematic representation of a modern dual beam SEM/FIB instrument, which can micro-machine various materials into specimens that can be tested for strength. The ion bombardment of material results in collision cascade of the primary ion with atoms of the sample, which in turn leads to a number of different processes including atom sputtering, irradiation damage of the sample and ion implantation. Images in the figure are reproduced from [260] with permission of Cambridge University Press.**

### 1.6.2 Uniaxial compression at the microscale

To measure microscopic strength data, a nanoindentation apparatus can be adapted to perform the uniaxial compression test reviewed in Section 1.5.1. This was demonstrated by Yoshida, Ogiso et al. [220,226] testing in compression the strength of submicrometric vapour-grown Semicorundum particles. These authors used a nanoindentation apparatus equipped with a Focused Ion Beam (FIB) milled flat diamond tip of diameter comparable to the size of particles in order to facilitate compression of individual particles by avoiding contact with neighbouring particles during compression. A high-precision stage with a motion accuracy near  $0.1 \mu\text{m}$  was used for positioning of the particles under the flat tip. The used nanoindentation tester was, however, a soft machine (as is the case for most standard nanoindentation machines). Once abrupt failure of a particle occurred, release of the stored elastic energy drove the indenter downwards, crushing the particle fragments into (micro) rubble, in turn rendering fractography impossible, thus inhibiting the identification of strength-flaw size relationships.

Compressing micro- and nanosized particles *in situ* in a scanning electron microscope or transmission electron microscope has in recent years attracted significant attention as it enables the direct observation of particles during the test. The main motivation for such tests was a desire to shed light on plasticity size effects and elucidate mechanisms of plastic deformation of various metal particles [261–264], but also of ceramic particles: when sufficiently small they too may deform plastically at room temperature [234,237,265–269]. Comparatively, probing the strength of micro- and nano-particles has attracted much less attraction. One body of work in this vein that stands out is the work of



Gerberich et al. [245,270–272]. These authors probed plasma-deposited spherical Si particles by compressing them with a rounded diamond tip, including tests conducted *in-situ* in the TEM, studying their deformation and fracture. Fracture loads were used to derive strength using somewhat simplified effective contact stress calculation, which assumed failure initiation at or near the contact periphery. Additionally, these authors derived size-dependent fracture toughness values, calculated by assuming that the strength-limiting flaw is as wide as the outer oxide layer is thick, and that cracks grow from the periphery of the region of direct load application. While the work cited above embodies today's state-of-the art in uniaxial compression testing, its main limitations, described previously in Section 1.5.1, were at micro- and nano-scales not addressed yet.

### 1.6.3 Micropillar compression

Recent advances in FIB micromilling have led to the development of a relatively simple micromechanical test method in which a portion of material along a polished surface (e.g. a single phase, crystal, or particle) is carved into the form of a micron- or submicron-scale pillar by digging a deep trench around its periphery. The pillar is typically of cylindrical shape and is then compressed uniaxially using a nanoindenter fitted with a flat punch tip of diameter slightly higher than that of the pillar. Compared to the uniaxial compression of whole particles, the micropillar compression test offers in principle a simple uniaxial compression stress state within the compressed specimen.

Early applications of the micropillar compression test focused on identification of the pillar deformation mode with interest in the study of size effects in crystal plasticity within metals [273]. Owing to its relative simplicity and the possibility to couple the mechanical testing *in situ* with electron microscopy techniques (SEM, TEM, EBSD) [274–277], or X-ray diffraction [278,279], the FIB-machined micropillar compression test has become one of the most widely used and powerful techniques to study elastic modulus, yield stress, plastic deformation, failure mechanisms and compressive strength in pure metals [280–285], alloys [286], bulk metallic glasses [287,288], nanocomposites [289,290] or complex hierarchical composites such as bone [291]. Micropillar compression was also used to investigate the fracture mode and measure the shear strength and effect of temperature on plastic deformation of brittle crystals such as  $\text{MgAl}_2\text{O}_4$ , Si, InAs, MgO [292,293]. Wheeler et al. [294] tested diamond micropillars, reporting so far highest experimental uniaxial compression strength values, near 250 GPa, in  $\langle 111 \rangle$  oriented diamond pillars and shear strengths near 75 GPa in  $\{111\}$  planes, corresponding to  $\approx G/7$  and thus approaching the theoretical shear strength estimate for diamond. In the same group, Montagne et al. [75] performed micropillar compression tests on single crystalline  $\alpha$ -alumina in four different orientations namely, compressing  $\{0001\}$   $C$ ,  $\{10\bar{1}0\}$   $M$ ,  $\{11\bar{2}0\}$   $A$ , and  $\{01\bar{1}2\}$   $R$  planes at room temperature. These authors observed that two main deformation mechanisms are operational in these essentially dislocation-free alumina micropillars namely; (i) pillar cracking governed by the statistical distribution of pre-existing flaws and (ii) apparent plastic deformation along slip planes governed by dislocation nucleation (see Figure 1.17). The average uniaxial compression stress at the onset of gliding was 13.6, 11.1, 23.7, and 13 GPa for  $M$ ,  $A$ ,  $C$ , and  $R$  compression planes, respectively. The authors note, however, that the observed onset of plasticity in the tested pillars is significantly lower than the theoretical shear stress  $\approx G/10$ , most likely due to either (i) dislocation nucleation due to the inhomogeneous stress field in the vicinity of the contact with the

diamond punch or (ii) the FIB induced damaged layer and tapered geometry of pillars, which are often regarded as a main limitation of the micropillar compression test.

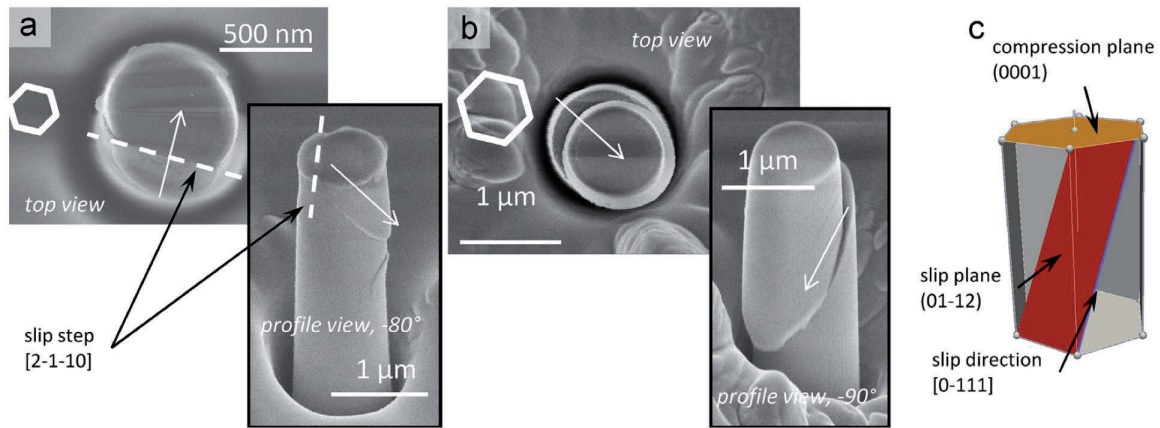


**Figure 1.17 – Single crystal  $\alpha$ -alumina micropillar compression in the  $\langle 0001 \rangle$  direction. The crystal after compression exhibits apparent step formation and gliding along the  $\{01\bar{1}2\}1/3\langle 0\bar{1}11 \rangle$  slip system. Its activation was identified at a critical uniaxial compression stress near 23.7 GPa and critical resolved shear stress equal to 10.7 GPa. The figure is reproduced from Ref. [75] with permission of Elsevier.**

#### 1.6.4 Microtensile testing

With the use of FIB micromilling techniques, ways of testing microscopic portions of material in tension were also explored. Kiener et al. [295] were among the first to demonstrate how FIB micromachining can be used to produce a dog-bone shaped tensile specimen that protrudes from a needle-shaped bulk material sample (see Figure 1.18a). The FIB milled dog-bone was tested in tension by pulling it after insertion into an *in-situ* SEM microindenter fitted with a dovetail shaped tungsten micro-gripper, also prepared by FIB micromachining (see Figure 1.18b). This method enabled to study the deformation mechanisms and flow stress size effects in tension in metals [275,295–297] and can in principle be used to measure the strength of brittle material including (micromachined) microscopic ceramic particles. The method is, however, more difficult to perform than for example bending of a microbeam, discussed in what follows. It also requires *in situ* micromechanical testing machine for precise alignment of the specimen, and fabrication of rather sophisticated micro-gripping tool. Additionally, and perhaps most importantly, it suffers from the surface FIB damage problem, as is the case with micropillar compression.

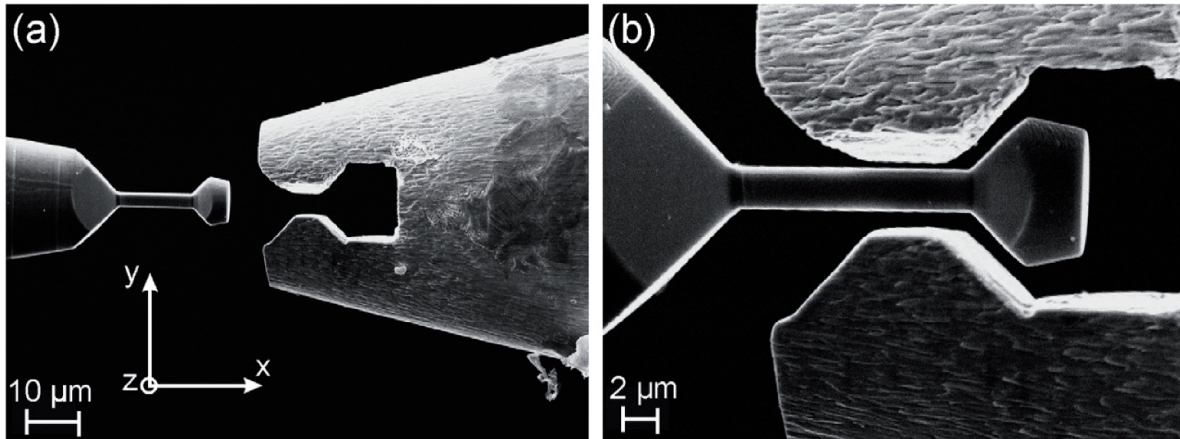


**Figure 1.18 – *In-situ* SEM microtensile test of a FIB milled copper dog-bone specimen protruding from a copper needle. The specimen is pulled using FIB machined tungsten microgripper fitted in a *in-situ* microindenter apparatus. The figure is reproduced from Ref. [295] with permission of Elsevier.**

#### 1.6.5 Microbend testing

The fabrication of microbeams using FIB-milling with subsequent *ex situ* or *in situ* SEM testing in bending has also been explored [298]. One of the main advantages of microbeam testing compared to micropillar compression or microtension of FIB milled specimens is that in principle it allows to keep at least one of the microbeam free surfaces in its pristine FIB unaffected condition; preferably this is the surface subject to tension during the bend test. This is useful in testing the flexural strength of cantilever beams of, for instance, thin films, leaving the film free surface subject to tension unaffected by FIB [299]. The method can also be adapted to test partially embedded particles in a matrix, as will be shown in Chapter 5 of this thesis.

An approach to test the flexural strength of plate-like microparticles was recently developed by Mueller et al. [300]. The method starts by FIB machining a straight beam with a trapezoidal cross-section out of a flat parallel facet particle. The machined beam-shaped particle is subsequently transferred over a rectangular hole dug into the steel substrate by FIB milling, and loaded in three-point bending configuration by a nanoindenter fitted with a wedge-shaped diamond punch (see Figure 1.19). The beam surface subject to tension is left unaffected by FIB and the beam trapezoidal cross-section with its wider side in tension additionally alters the stress-state in such a way that the peak tensile stress is reached in the central region of the tensile surface just below the load application point while the tensile stress progressively decreases as one approaches the edge of the beam (see Figure 1.19e). The difference between the peak tensile stress and the highest tensile stress attained at one of the edges depends on the exact geometry and can vary on the order of 10% to 20%. The fracture of such trapezoidal beam in three-point bending thus most likely initiates away from the FIB machined edges and thus provides the flexural strength of the particle material free of FIB induced damage. Mueller et al. also put this approach to practice, testing silicon plate-like particles leached out of an Al-Si alloy showing that these particles can be exceptionally strong with strength values on the order of 9 GPa provided that they are free of microstructural defects in the form of pin-holes and trench-like interfaces, both of which significantly diminish the particle strength.

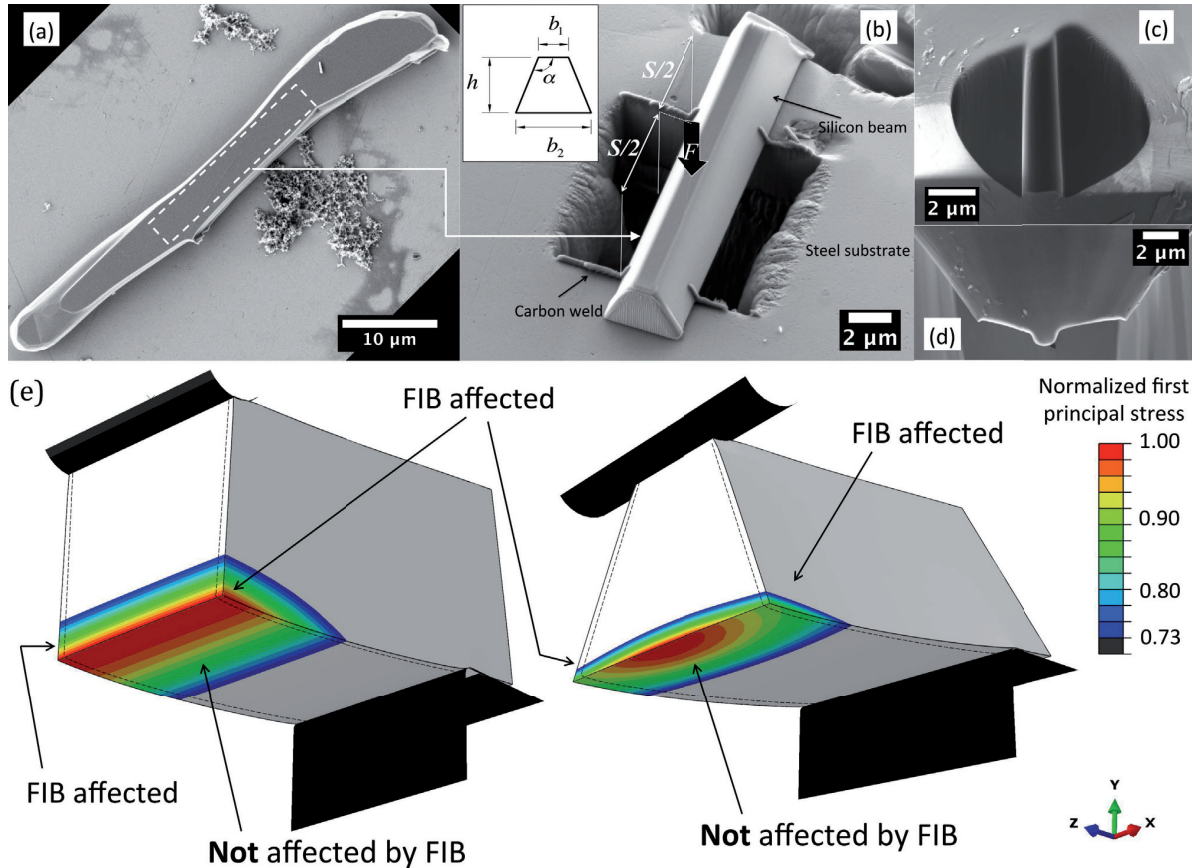


**Figure 1.19** – Microscopic three-point bending test of (a) a plate-like Si particle leached out of an Al-Si alloy. (b) The FIB milled bend beam features a trapezoidal cross-section and (c and d) is loaded with a wedge-shaped diamond probe. (e) The trapezoidal geometry of the beam results in a stress distribution such that the peak stress along the FIB unaffected surface subject to tension is 10% to 20% higher than the stress along one of the FIB milled beam edges. Images in the figure are reproduced from Ref. [300] available under the terms of the Creative Commons Attribution License (CC BY).

This approach, although without the trapezoidal beam cross-section and hence with the possibility for an influence of FIB-induced artefacts, was used by Feilden et al. [301] to measure the flexural strength of individual alumina platelets with thickness 400-900 nm, often used as the reinforcement phase in bioinspired brick-and-mortar “nacre-like” composites [1–3,302,303]. A micrograph of these particles was presented earlier, in Figure 1.4d in Section 1.2.3. The statistical strength of platelets obtained from 10 tests and described with two-parameter Weibull distributions exhibited characteristic strength of 5.8 GPa and Weibull modulus  $m \approx 4$ . Growth step edges with steps 10-30 nm in height were identified as critical defects. On the other hand, platelet edges that appeared to contain more imperfections and were curved in a notch-like geometry (see Figure 1.4d) were not probed for strength.

In this three-point bending method the pieces of tested particles are typically ejected upon failure due to the sudden release of the stored strain energy, rendering fractography impossible, in turn limiting the study of the strength-flaw size relationship only for gross surface imperfections observable before



testing [300]. In this regard, the cantilever beam test method in which one part of the fracture surface is held fixed in place might be more useful.

#### 1.6.6 FIB damage

Focused ion beam micromachining is a powerful technique, which makes it possible to fabricate various materials with a precision on the order of tens of nanometers; however, as was indicated earlier, it introduces extensive damage along the surface of the milled material; as does in fact any machining process that induces material removal [304–306]. It is well documented that bombardment by  $\text{Ga}^+$  ions may in crystalline materials result in formation of a few tens of nanometers thick amorphous layer. The thickness of this layer depends primarily on the kinetic energy of the ions (controlled by the accelerating voltage) and the milled material. Ensuing surface amorphization is well-documented in silicon and other semiconductors [307–311] and is expected to take place also in metals such as copper [304]. Implantation of gallium atoms into the surface of the milled material is another artefact that is induced during FIB milling; the ion implantation depth depends on the ion energy, incident angle and the material itself [311]. Other irradiation-type damage can be induced, such as the formation of point defects and dislocation loops as well as local heating of the sample [260,304,311]. Redeposition may also be of concern. When atoms are ejected from the parent material due to the bombardment by primary ions, these ejected (sputtered) atoms will generally deposit back onto the milled sample surface or neighbouring surface regions [312]. Yet another aspect that needs to be considered when probing the material strength along a FIB milled surface is surface topology and roughness introduced by the FIB. Surface irregularities called “curtains” in the FIB community may appear on the milled surface by the process of self-exaggerating selective sputtering due to the variation in the sputter yield with incidence angle [313,314]. Even very carefully prepared flat FIB milled surface may still exhibit roughness on the order of 10 nm [304].

In the case of alumina, which this thesis is mainly focused on from the material perspective, seemingly only one study by Norton et al. [315] has been devoted to understanding the effects of FIB milling in detail. These authors studied single crystal  $\alpha$ -alumina surface irradiated by 30 kV  $\text{Ga}^+$  in the HRTEM (see Figure 1.20). Two main findings were reported: (i) gallium implants a surface layer as thick as 20 nm which was confirmed with EDX showing Ga content approximately 3 at% in the implanted layer (Figure 1.20a) and (ii) irradiation by 30kV  $\text{Ga}^+$  does not cause surface amorphization in alumina, which was confirmed by nanobeam diffraction (Figure 1.20b-c). The roughly 2nm thick amorphous layer observed along the surface of the TEM studied specimen was reported by authors as redeposition.

As a consequence of the implantation by  $\text{Ga}^+$ , significant compressive residual stress developed in the implanted layer. The magnitude of this residual stress was deduced from measuring TEM lamella curvature assuming no other sources of internal stress. A compressive residual stress with magnitude  $16\pm 6$  GPa was estimated. Additional nanoindentation experiments on the irradiated layer showed an increase in nanoindentation hardness for indentation depths below 20 nm. Annealing of the specimen at 1200°C did not change the Ga content in the implanted layer. Based on the microcantilever fracture toughness results, however, authors presumed that annealing removed most of the residual stresses.

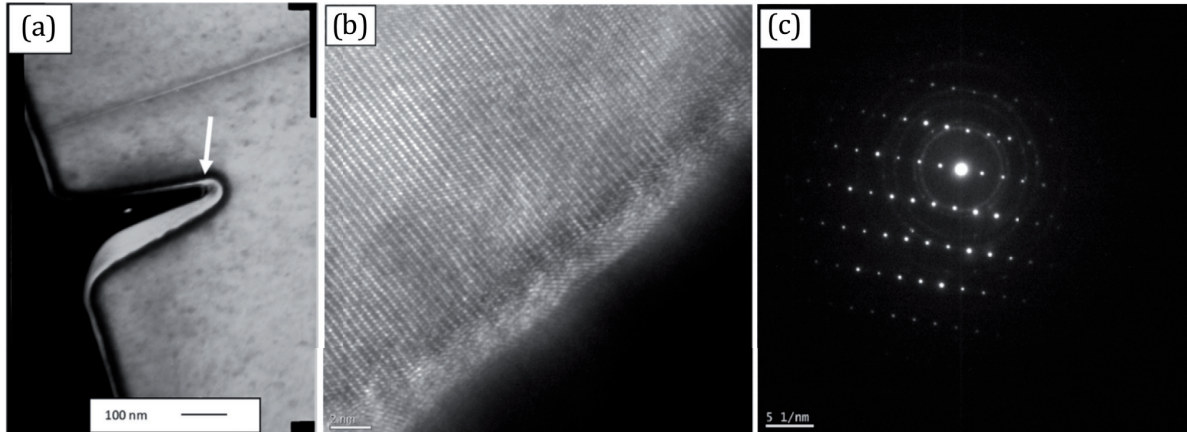


**Figure 1.20** – TEM micrographs of  $\alpha$ -alumina surface irradiated by 30 kV  $\text{Ga}^+$ . (a) A microcantilever specimen with FIB milled notch exhibits  $\approx 20$  nm thick Ga implanted layer, which appears as a dark film on the surface of the specimen and is indicated by the arrow. (b) High resolution TEM showing that FIB milling did not cause surface amorphization. The minute  $\approx 2$  nm thick amorphous layer was reported as a result of redeposition. (c) Nanobeam diffraction pattern from the implanted layer, confirming crystallinity. Images in the figure are reproduced from Ref. [315] with permission of Elsevier.

## 1.7 Concluding remarks

It is clear that the particle strength leads to a remarkable difference in the mechanical properties of particulate MMCs. With weak particles, the composite is in general both weaker and more brittle. Alumina can, however, be very strong, especially when microscopic: this is for example demonstrated on alumina whiskers or engineering fibres nowadays used in composites. There is a priori no reason why alumina particles could not achieve similar strengths as their whisker and fibre counterparts. A blind spot exists in our knowledge and understanding of the strength of ceramic of the size scale used in particulate composite reinforcements. This is mostly because it is difficult to measure the strength of such microscopic and often irregularly shaped particles.

In what follows, we build on the state-of-the-art in micromechanical testing methods with special emphasis on testing strength in convex, low-aspect-ratio, microscopic particulate samples of material, aiming to avoid problems typically associated with FIB machining. We in turn present two newly developed methods to test the strength of alumina and alumina-based ceramic microparticles that have the potential to be used as reinforcements in metal matrix composites.



## Chapter 2 Compression testing spherical particles for strength: Theory of the meridian crack test and implementation for microscopic fused quartz

### 2.1 Disclaimer

This chapter was published as an article in a scientific journal with the open-access (CC BY 4.0) licence; its bibliographic reference is given below. The postprint version of the published article is presented here with its Introduction section abbreviated to avoid repetition of what was already mentioned in Chapter 1 of this thesis (extracts, including a few literal reproductions of full paragraphs of this article's Introduction, are included in Chapter 1 of this thesis). The candidate, herewith V.P., designed and implemented the testing method under the supervision of Andreas Mortensen (A.M.) and Goran Žagar (G.Ž.). V.P. carried out all experiments and measurements, analysed the data, and interpreted the results. Raphael Charvet (R.Ch.) and Cyril Dénéréaz (C.D.) designed and built the instrumented crushing test device. V.P. and A.M. wrote the manuscript and all authors provided feedback.

Pejchal, V., Žagar, G., Charvet, R., Dénéréaz, C., Mortensen, A.; *Compression testing spherical particles for strength: Theory of the meridian crack test and implementation for microscopic fused quartz*. Journal of the Mechanics and Physics of Solids 99, 2017, 70–92. doi:10.1016/j.jmps.2016.11.009

### 2.2 Introduction

In the work presented here we extend the approach of Shipway and Hutchings [9,10] (see Section 1.5.1) to present a testing approach in which a collection of elasto-plastic platens of tailored hardness are used to generate series of data from which the statistically distributed strength of small glass spheres  $\sim 40 \mu\text{m}$  in diameter can be measured and interpreted using the methodology of survival analysis. We deliberately tailor the hardness of the platens to produce fracture events past a relative contact radius ( $a/R$ ) value of 0.65, this being a region of relative contact radii that was not explored by Shipway and Hutchings. We use a custom-built instrumented crushing apparatus designed to work in displacement-controlled mode, which features a stiff load-train so as to ease fractography. Using analytical solutions for the stress distribution within the particle, we show how this modification of

the crushing test can produce unambiguous measurements of the intrinsic tensile strength distribution within strong brittle microscopic particles.

### 2.3 Theory

Consider the compression of a brittle elastic spherical particle of radius  $R$  between a pair of soft (relatively to the particle) elasto-plastic platens under an applied force  $F$  (Figure 2.1a). As the platens compress the particle, they deform plastically, producing an indent of contact radius  $a$ . As particle compression continues,  $a$  gradually increases with increasing applied compressive force  $F$ . We neglect the effect of friction between the platens and the compressed particle and assume that the compressive force is uniformly distributed over the spherical cap as pressure  $q = F/A$ . Any material pile-up arising from the indentation of the platen is accounted for via the contact radius  $a$ . The cap has an area  $A = 2\pi R h$  where  $h$  is the contact depth (Figure 2.1a). This is the boundary value problem analysed by Hiramatsu and Oka, or Shipway and Hutchings (HO-SH).

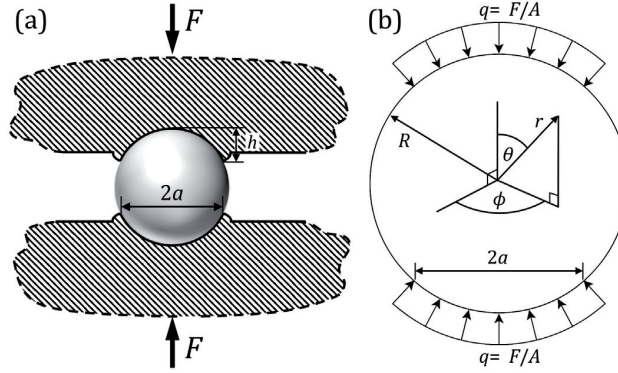


**Figure 2.1 - (a) Sketch of a spherical particle of radius  $R$  compressed between two elasto-plastic platens under load  $F$ . (b) Simplified boundary value problem associated with the sketch in (a). Pressure distribution in the region of contact, i.e. over the area of the spherical cap defined by the contact radius  $a$  and contact depth  $h$ , is assumed to be uniform: shear contact forces arising from friction and variations in normal stress are neglected. Possible pile-up of the platen material due to indentation is assumed comprised via the contact radius definition.**

The HO-SH analysis is conveniently carried out in the spherical coordinate system having its origin placed in the center of the sphere and variables being the radial distance  $r$ , the polar angle  $\theta$ , and the azimuthal angle  $\phi$ . Due to spherical symmetry, for given  $F$ ,  $R$  and  $A$  (related to the contact radius  $a$ , see Figure 2.1b), the stress field in the sphere has four independent components:

$$\sigma_r = \frac{F}{\pi R^2} \cdot \tilde{\sigma}_r \left( \frac{a}{R}, \frac{r}{R}, \theta, \nu \right) \quad (2.1a)$$

$$\sigma_\theta = \frac{F}{\pi R^2} \cdot \tilde{\sigma}_\theta \left( \frac{a}{R}, \frac{r}{R}, \theta, \nu \right) \quad (2.1b)$$

$$\sigma_\phi = \frac{F}{\pi R^2} \cdot \tilde{\sigma}_\phi \left( \frac{a}{R}, \frac{r}{R}, \theta, \nu \right) \quad (2.1c)$$

$$\tau_{r\theta} = \frac{F}{\pi R^2} \cdot \tilde{\tau}_{r\theta} \left( \frac{a}{R}, \frac{r}{R}, \theta, \nu \right) \quad (2.1d)$$

In Eqs. (2.1a-d),  $\tilde{\sigma}_r$ ,  $\tilde{\sigma}_\theta$ ,  $\tilde{\sigma}_\phi$  and  $\tilde{\tau}_{r\theta}$  are the normalized components of the local stress tensor; these are given in Appendix 2.A. Note that, besides the geometrical parameters, the stress field given by Eqs. (2.1a-d) explicitly depends also on the Poisson's ratio,  $\nu$ , of the sphere material.

The quantity of interest in brittle fracture is the first principal stress field,  $\tilde{\sigma}_1 \left( \frac{a}{R}, \frac{r}{R}, \theta, \nu \right)$ , and this, for a spherical particle, can be computed from Eqs. (2.1a-d) by solving the eigenvalue problem defined by the local stress tensor,

$$\det \left( \begin{bmatrix} \tilde{\sigma}_r - \lambda_i & \tilde{\tau}_{r\theta} & 0 \\ \tilde{\tau}_{r\theta} & \tilde{\sigma}_\theta - \lambda_i & 0 \\ 0 & 0 & \tilde{\sigma}_\phi - \lambda_i \end{bmatrix} \right) = 0 \quad (2.2)$$

such that  $\tilde{\sigma}_1 \left( \frac{a}{R}, \frac{r}{R}, \theta, \nu \right) = \max \{ \lambda_i \left( \frac{a}{R}, \frac{r}{R}, \theta, \nu \right) \}$  for all points within the sphere. By symmetry, the first principal stress everywhere along the compression axis is  $\tilde{\sigma}_\theta = \tilde{\sigma}_\phi$ . On the surface along the equatorial line and at sufficiently large distance away from the contact perimeter the first principal stress corresponds to  $\tilde{\sigma}_\phi$ .

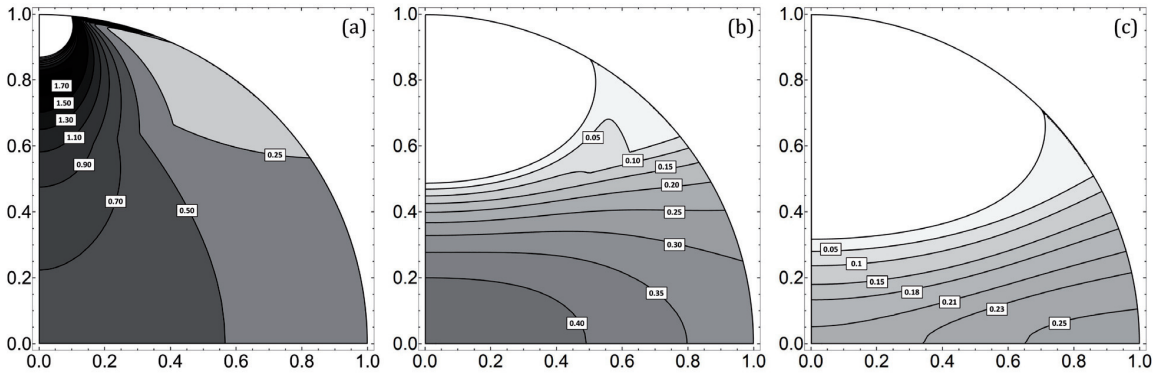


**Figure 2.2** – Distribution of the positive (tensile) normalized first principal stress,  $\tilde{\sigma}_1 = \sigma_1 \pi R^2 / F$ , calculated by solving Eq. (2.2), for relative contact radius values  $(a/R) = 0.1$  (a),  $0.5$  (b) and  $0.7$  (c). Regions of the sphere where  $\tilde{\sigma}_1$  is negative (*i.e.*, compressive) are shown in white. Poisson's ratio of the sphere is taken as  $\nu = 0.17$ , typical of glass. Given spherical symmetry only one quarter of the  $\{r, \theta\}$ -plane is considered. The axes represent normalized radial distance  $r/R$ .

The first principal stress fields,  $\tilde{\sigma}_1 = \sigma_1 \pi R^2 / F$ , calculated via Eq. (2.2) for relative contact radius values  $(a/R) = 0.1, 0.5$  and  $0.7$  and a Poisson's ratio  $\nu = 0.17$  (typical of quartz and glass) are shown in Figure 2.2. In Figure 2.2 we plot only the positive, *i.e.* tensile values of the  $\tilde{\sigma}_1$ -field (indicated by

the grey scale) since only those regions are potentially interesting for the Mode I failure of a brittle material. In Figure 2.3 we directly plot the values of the first principal stress in the sphere center,  $\tilde{\sigma}_{1c} = \tilde{\sigma}_1(r = 0, \theta = 0)$  and along the equatorial line,  $\tilde{\sigma}_{1s} = \tilde{\sigma}_1(r = R, \theta = \frac{\pi}{2})$ , versus  $a/R$ , along with the value for the global maximum of the  $\tilde{\sigma}_1$ -field. From Figure 2.2 and Figure 2.3 it is evident that the  $\tilde{\sigma}_1$ -field distribution is very sensitive to  $a/R$ . For low  $a/R$ , up to 0.3,  $\tilde{\sigma}_1$  is highly concentrated just outside the contact perimeter over which the load is applied and/or along the loading axis; in those locations it is oriented along the  $\theta$  direction,  $\tilde{\sigma}_1 = \tilde{\sigma}_\theta$  (Figure 2.2a). At intermediate contact radii,  $0.3 < (a/R) < 0.65$ , the highest values of  $\tilde{\sigma}_1$  are found away from the contact, deeper within the sphere with the peak value located near the sphere center (Figure 2.2b). Finally, for  $(a/R) > 0.65$  (Figure 2.2c), the region of highest tensile stress  $\tilde{\sigma}_1$  is shifted towards the sphere surface: the peak tensile stress within the particle is now situated along the sphere equator and is a hoop stress,  $\tilde{\sigma}_1 = \tilde{\sigma}_\phi$ .

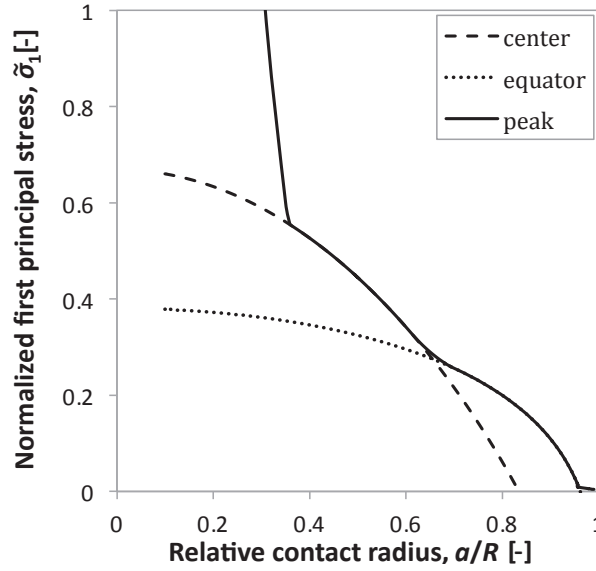


Figure 2.3 – Normalized first principal stress  $\tilde{\sigma}_1 = \sigma_1 \pi R^2 / F$  vs. the relative contact radius  $a/R$ , obtained by solving Eq. (2.2), in the centre of the sphere  $\tilde{\sigma}_{1c} = \tilde{\sigma}_1(r = 0, \theta = 0)$  (dashed line) and on the surface equator  $\tilde{\sigma}_{1s} = \tilde{\sigma}_1(r = R, \theta = \frac{\pi}{2})$  (dotted line). The value of the global maximum,  $\max(\tilde{\sigma}_1)$ , is shown with the solid line. Poisson's ratio of the sphere is taken as  $\nu = 0.17$ , typical of glass.

Consider a particle that is gradually compressed between a pair of defined metallic platens. As the load increases, the particle gradually indents the platens. If we assume that, when pressed against the deforming metal platens, the hard particle behaves as if it were rigid, then the relation linking  $F/\pi R^2$  with  $a/R$  is entirely dictated by the platen material deformation law. This behaviour is known to be described, for fully plastic deformation of the platen material, by the empirical Meyer law classically used in the interpretation of hardness tests [316]:

$$\frac{F}{\pi R^2} = k \left( \frac{a}{R} \right)^n \quad (2.3)$$

where  $k$  and  $n$  are characteristic of the indented material. The exponent  $n$  varies typically from 2 (typical of fully strain-hardened metals) to 2.5 (typical of fully annealed metals) and coefficient  $k$  is associated with the material hardness [316,317].

Inserting Meyer's law, Eq. (2.3), into the HO-SH solution given by Eqs. (2.1a), one obtains the following expressions for the dimensionless stress field components within a sphere compressed by a pair of symmetric elasto-plastic platens,

$$\frac{\sigma_r}{k} = \left(\frac{a}{R}\right)^n \cdot \tilde{\sigma}_r\left(\frac{a}{R}, \frac{r}{R}, \theta, \nu\right) \quad (2.4a)$$

$$\frac{\sigma_\theta}{k} = \left(\frac{a}{R}\right)^n \cdot \tilde{\sigma}_\theta\left(\frac{a}{R}, \frac{r}{R}, \theta, \nu\right) \quad (2.4b)$$

$$\frac{\sigma_\phi}{k} = \left(\frac{a}{R}\right)^n \cdot \tilde{\sigma}_\phi\left(\frac{a}{R}, \frac{r}{R}, \theta, \nu\right) \quad (2.4c)$$

$$\frac{\tau_{r\theta}}{k} = \left(\frac{a}{R}\right)^n \cdot \tilde{\tau}_{r\theta}\left(\frac{a}{R}, \frac{r}{R}, \theta, \nu\right) \quad (2.4d)$$

in which the only independent parameter is now the relative contact radius  $a/R$ . Similarly the first principal stress field can be expressed as a function of  $a/R$  knowing the platen material:

$$\frac{\sigma_1}{k} = \left(\frac{a}{R}\right)^n \cdot \tilde{\sigma}_1\left(\frac{a}{R}, \frac{r}{R}, \theta, \nu\right) \quad (2.5)$$

Using Eq. (2.5), in Figure 2.4 we plot the evolution of the  $k$ -normalized first principal stress,  $\sigma_1/k$ , versus the relative contact radius  $a/R$  for the sphere center (dashed line) and the surface equator (dotted line) together with the global maximum of the  $\sigma_1$ -field (solid line) for the two limiting values of  $n$ .

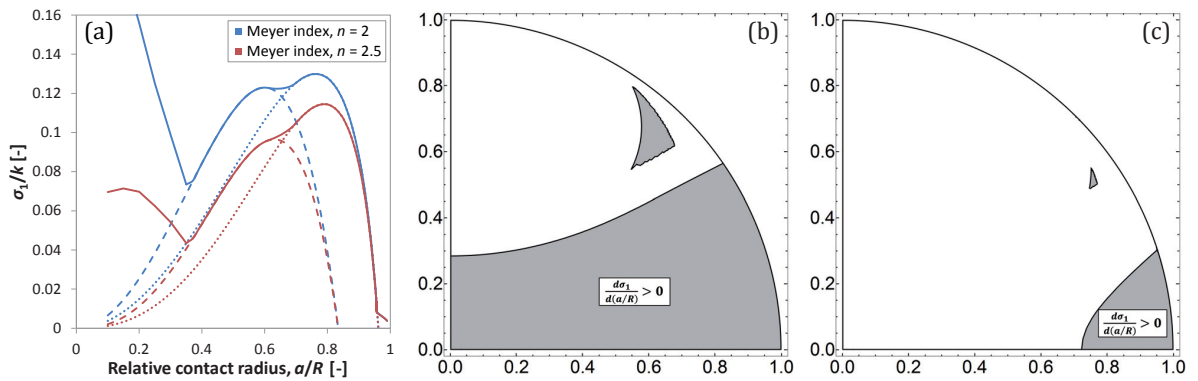


**Figure 2.4 – (a) Evolution of the normalized first principal stress  $\sigma_1/k$  in the sphere center (dashed line) and along the surface equator (dotted line) versus the relative contact radius  $a/R$ , as obtained from Eq. (2.5). The global maximum of the field is shown with the solid line. The exponent of Meyer's law,  $n$ , used in calculations is 2 (blue) and 2.5 (red). In (b) and (c) grey areas show regions within the particle where the maximum tensile principal stress is increasing; (b):  $(a/R) = 0.5$ ; (c):  $(a/R) = 0.7$ ; for both, the platen Meyer index,  $n$  equals 2. Poisson's ratio of the sphere is  $\nu = 0.17$ .**

Over the course of a compression test,  $a/R$  increases steadily; thus, based on Figure 2.2 and Figure 2.4 and the discussion that precedes, the test can be divided into four successive stages or domains:

- Domain I: At the very beginning of a test,  $(a/R) < 0.3$  and the highest tensile stress value within the particle is found near the sphere surface, either around the contact perimeter or along the compression axis just below the contact. Whether cracks will nucleate in those regions depends on the platen hardness relative to the particle strength.
- Domain II: Once  $a/R$  reaches  $\approx 0.3$ , the location of the first principal stress global maximum shifts to the sphere center. Thereafter, magnitudes of the first principal stress in the center, and also along the equatorial belt, increase steadily as  $a/R$  increases. The former remains higher than the latter, the difference being as high as 40%. Therefore, if particle failure occurs in this portion of the test, cracking can have initiated in either of the center of the sphere, or from its surface (Figure 2.4b).
- Domain III: Then, at  $(a/R) \approx 0.65$ , the stress at the center of the sphere starts decreasing while the peak stress location moves from the sphere center to its equator. From that moment on, stress levels in the central region of the particle have culminated while the tensile stress in the equatorial belt region keeps increasing. Therefore, if a particle has survived up to  $(a/R) = 0.65$  and then fails, its failure was caused by a flaw located near its equator, where tensile stress is still increasing (see Figure 2.4c).
- Domain IV: Beyond  $(a/R) \approx 0.78$ , regardless of the platen material, the stress starts decreasing everywhere within the particle: if it has not been broken yet it will (in principle) not do so in the test. So if loading is continued past this point, it will (in principle) only cause further embedding of the sphere into the platens - until the platens meet with the particle completely embedded and  $(a/R) = 1$ .

This division of the test into four domains has several implications.

- The first is to show advantages inherent in the use of a platen material that is initially sufficiently soft and work hardens significantly: if  $n$  is near 2.5 then the peak stress value reached near the point of contact in early stages of the test (Domain I) remains lower than what can be attained later elsewhere within the sphere.
- The second is to show that if a sample fails within Domain III, then one *knows* that it failed at a flaw situated along its surface, near the equator. Here too, a platen with a high rate of work hardening is beneficial if surface defects are to be probed because the higher  $n$  is, the greater is the difference between the peak stress attained within the particle compared with the peak value attained later, near its surface, Figure 2.4a.
- Finally, note that the optimal platen material must also be selected with an appropriate value of constant  $k$  in the Meyer law, Eq. (2.3), or in other words with an appropriate hardness, if it is to sample particle fracture stresses in their appropriate range. Since the Meyer hardness (in MPa) is roughly equal to  $k$  [317], the platen material should be selected to have a hardness roughly equal to 8 times the expected particle fracture stress. Figure 2.5 represents the relation between the required platen Meyer hardness for the expected particle strength assuming a platen material with  $n = 2$  and using



Eq. (2.5) for three different particle Poisson ratio values. Note that with strong particles (failure stress on the order of few GPa), it may be difficult to find an appropriate platen material because hard materials tend to be brittle, which may lead to premature cracking of platens before reaching the required relative contact radius  $\approx 0.7$ .

Values given above for the transitions between Domains I to IV were calculated for  $\nu = 0.17$ ; for other values of  $\nu$ , the test retains its qualitative features including the four domains but transitions occur at slightly different  $a/R$  values. In general, as  $\nu$  increases, Domain III starts earlier and ends later in terms of  $a/R$ .

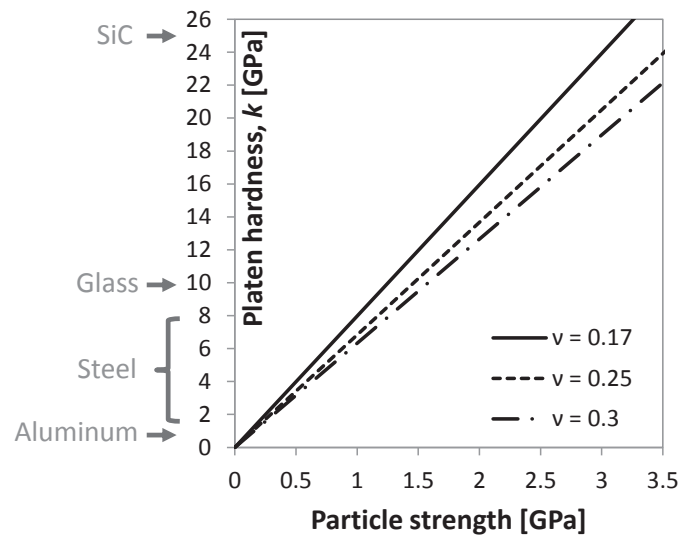


**Figure 2.5 – Required platen Meyer hardness to test particles of given strength, assuming platen material with  $n = 2$  and relative contact radius at the moment of failure ( $a/R$ ) = 0.7. The three lines represent the relationship for three values of the particle Poisson ratio  $\nu$ . Hardness values of the four materials indicated on the left are conversions to SI units of Brinell or Vickers hardness values from the literature (close although not exactly equal to Meyer hardness values).**

## 2.4 Materials and methods

Microscopic fused quartz particles were tested using the custom-built instrumented compression apparatus depicted in Figure 2.6. The apparatus was designed to have a stiff load-train in order to minimize displacement of the load application platen upon failure of a tested particle, so as to minimize damage to the particle fracture surfaces. The device was therefore equipped with a high-stiffness miniature load cell XFTC300 (Measurement Specialties, Hampton, VA, United States) featuring a 10 N range and having a compliance near  $0.1 \mu\text{m}/\text{N}$  (Figure 2.6d). The relative force measurement error is typically below 1% in the range above 1 N. Upper platen movement during a compression test is controlled by a piezo actuator (Figure 2.6c, article number P-843.60 by Physik Instrumente GmbH & Co., Karlsruhe, Germany), with a  $90 \mu\text{m}$  displacement range. The compliance of the piezo actuator is also on the order of  $0.1 \mu\text{m}/\text{N}$  and its theoretical displacement precision is  $\approx 10 \text{ nm}$ . For general positioning, the apparatus features a system of three high-precision linear stages for  $x$ -,  $y$ - and  $z$ -axis motion (Figure 2.6a). The measured overall load-train compliance of the apparatus is on the

order of  $1 \mu\text{m}/\text{N}$ . The testing apparatus is additionally equipped with an imaging system composed of a long working distance 20x objective (Figure 2.6e) fitted to a 1.3 megapixel monochromatic camera (Figure 2.6b). The whole set-up is mounted on an active vibration isolation table (Figure 2.6h) in order to keep the noise amplitude in the load signal below 10 mN.

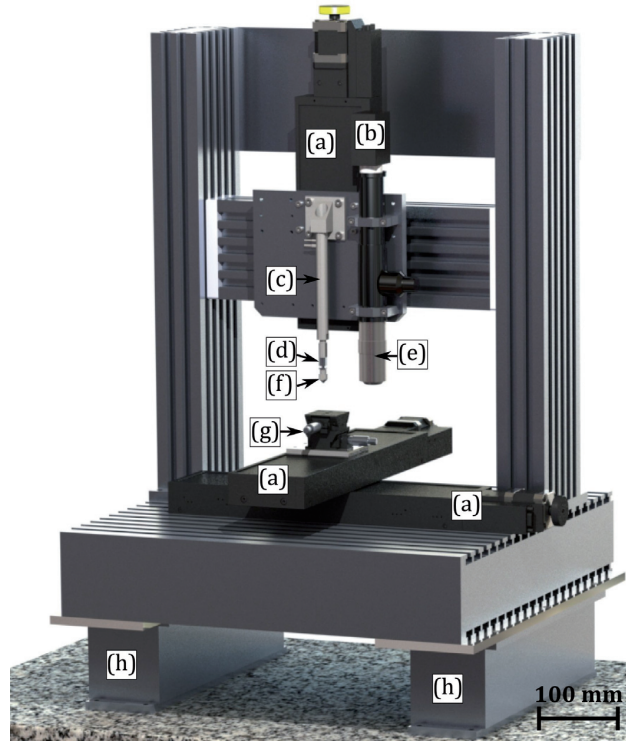


**Figure 2.6 – Custom-built instrumented compression apparatus. (a)  $x$ -,  $y$ - and  $z$ -axis linear motion stages, (b) monochromatic camera, (c) piezo actuator, (d) high-stiffness load cell, (e) objective, (f) flat-end conical tip, (g) two-axis goniometric tilt stage, (h) active vibration-isolation system.**

The load is applied at the top of individual particles, using interchangeable conical tips with a flat-end made of various materials that can be machined by conventional means (Figure 2.6f), while a substrate in the form of a disk ca. 10 mm in diameter and 2 mm thick is used as the lower platen. This substrate is attached to a two-axis goniometric tilt stage (Newport Corp., Irvine, CA, United States) fixed onto the positioning stage (Figure 2.6g), which was used in order to correct for any misalignments between the upper and lower platens. The two platens were thus kept plane-parallel within  $\sim 0.5^\circ$ .

The conical tips and substrates were made of two different steels, namely AISI W1 and AISI 630. Steel AISI W1 was used in three different heat-treatment conditions resulting in four sets of platen materials covering the range of hardness between 450 and 950 HV; platen material details are presented in Table 2.1. The flat-end of the conical tip and the substrate were ground and polished using a diamond suspension prior to testing. Tip grinding and polishing was conducted using a fixture that kept the polished platen surface perpendicular to the axis of the tip, while protecting the edges with a small amount of epoxy resin that was subsequently removed by dissolution in acetone. The resulting diameter of the polished tip flat-end ready for testing particles was typically in the range of 200-

300 $\mu\text{m}$ . The Vickers Hardness of the tips and substrates was measured with a FM-300 (Future-tech Corp., Kawasaki, Japan) microhardness tester using a 0.5 or 0.3 kgf load on representative samples of the material. For all four platen materials, the spatial distribution of the hardness and elastic modulus values was analysed using a series of 144 indents with contact area upon unloading on the order of 1  $\mu\text{m}^2$  using the TI 950 TriboIndenter<sup>®</sup> (Hysitron<sup>®</sup> Corporation, Minneapolis, MN, United States) nanoindentation apparatus equipped with a diamond Berkovich probe. In all cases the hardness and elastic modulus exhibited a unimodal distribution indicating homogeneous material behaviour at contacts above 1  $\mu\text{m}^2$  in area, despite the known presence of fine carbides and precipitates in the AISI W1 and AISI 630 steels.

The compression tests were performed on amorphous spherical  $\text{SiO}_2$  particles Denka FB-40S (Denka, Tokyo, Japan) of diameter typically between 20 and 60  $\mu\text{m}$ . To observe the fractured particles after the test and prevent particle flyoff during fracture, a layer of isopropanol-based colloidal graphite paint (Pelco<sup>®</sup>, Redding, CA, United States) a few micrometres thick was applied using a brush along the substrate surface. The colloidal graphite layer keeps particles in place during the test and additionally works as a soft coating into which the particle sinks in the earliest phases of the test. The resulting soft belt of coating surrounds the particle along its equator, preventing particle fragments from flying off upon failure (as they otherwise will typically do). Particles of high sphericity were selected for testing, based on SEM images from which their diameter was measured to an estimated precision on the order of 2%. Prior to testing, individual particles were placed upon the graphite-coated substrate, and if necessary separated using a miBot<sup>™</sup> (Imina Technologies SA, Lausanne, Switzerland) micromanipulator equipped with a tungsten needle.

The compression tests were performed using a constant upper platen displacement rate of 1  $\mu\text{m/s}$ , lowered in a few instances to 0.5  $\mu\text{m/s}$ . During a test, while the load gradually increases the steel platens deform plastically where they contact the particles. These gradually indent the upper and lower steel platen surfaces, increasing in turn the area of contact over which the load is applied to the particle. If the steel is hard enough to prevent the particle from completely sinking into the platens, then the tensile stress that develops within the particle and/or along its surface can cause failure from pre-existing flaws in regions of the particle that are not in direct contact with the platens, as shown above (Section 2.3).

The device was programmed to stop moving once an abrupt drop in load is detected. After each test, each individual indent left in the upper platen by the particles was observed using an optical microscope (Zeiss<sup>™</sup> Axioplan 2, Oberkochen, Germany). Since the projected area of the indent does not change significantly upon unloading [316], in data interpretation the measured indent radius is taken equal to the contact radius at the moment of failure,  $a$ . Relative error in  $a$  is estimated to be on the order of 5%. Each conical tip was used for up to five particle compression tests before it was changed, to ensure that all compression tests are performed using flat and polished regions of the tip several micrometres away from indents left by previous tests. Between two consecutive tests, the tip was cleaned of broken particle debris by pressing it against the graphite-coated substrate with a force of

~5 N; this traps debris left along the flat steel tip surface within the graphite. All tests were carried out at room temperature in air (relative humidity between ~20 and ~50%).

The micron-sized graphite particles present in the colloidal graphite paint, tiny debris particles that might be present on the surface of the tested fused quartz particles, fine carbide particles or other precipitates present in the steel platens or even a possible dislocation pile up near the platen-particle contact interface may locally concentrate stress along the platen/particle interface during the test, potentially causing a second, alternative failure site. If one takes a worst-case scenario and assumes that all such local contact perturbations (graphite particles, debris, precipitates, etc.) act as minute elastic spherical particles that indent the surface of the compressed sphere, by performing a simple analysis using Hertzian elastic contact theory (Supplementary material, Section 2.12.2), one finds that the only place where such a local inhomogeneity may cause, locally, significant tensile stress in the surface of the compressed particle is when the inhomogeneity is along the platen-particle contact perimeter. Having the inhomogeneity situated precisely there is of course unlikely. Moreover, the fact that the volume of the tested particle exposed to the local tensile stress concentration created by such an extraneous stress-concentrator is significantly smaller than the volume of the particle that is exposed to elevated tensile stress around the equatorial belt reduces further the probability of failure from such stress concentration sites along the contact perimeter. In our analysis we thus do not consider the possibility that failure of the compressed particle is initiated by local stress concentrators such as those enumerated above.

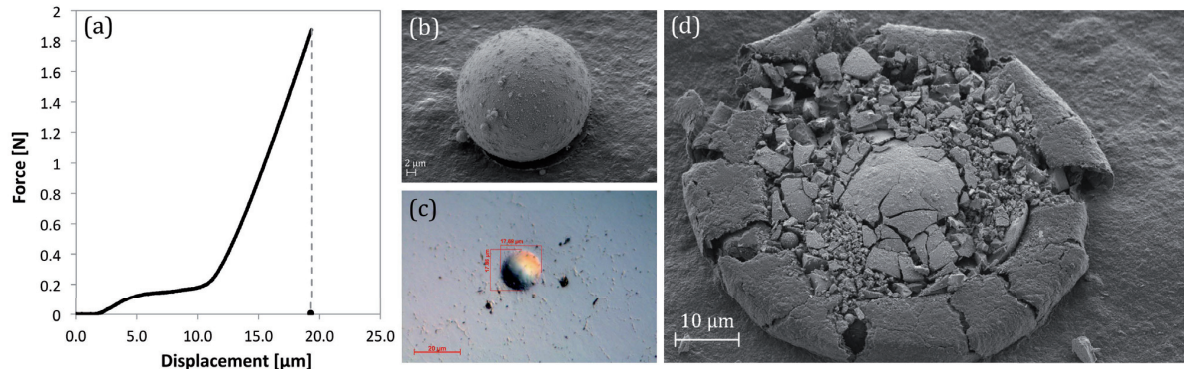
Table 2.1 – The four platen materials.

Platen designation	Steel grade and condition	Nominal chemical composition (%)	Average measured Vickers Hardness
HV950	AISI W1, Q		930
HV750	AISI W1, QT	1.05 C, 0.2 Si, 0.2 Mn, remainder Fe	740
HV600	AISI W1, QT		600
HV450	AISI 630, AH	0.04 C, 0.25 Si, 0.4 Mn, 15.3 Cr, 4.5 Ni, 3.25 Cu, 0.3Nb, remainder Fe	450

Note: letters after the steel grade designate the heat treatment condition: Q-quenched, QT-quenched and tempered, AH-age hardened.

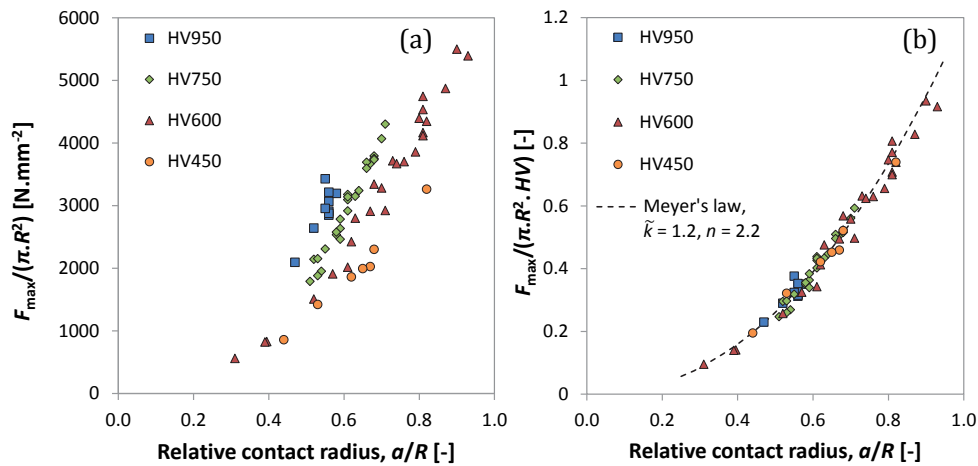
## 2.5 Results

Eighty-five (85) spherical fused quartz particles were tested in compression; of these, twenty-five (25) particles were tested for each platen having hardness HV450, HV600 and HV750, while 10 particles were tested using the platen of hardness HV950. Figure 2.7 shows a typical force-displacement curve recorded during a compression test, along with pictures of the particle before and after the test, and also of the indent left in the steel platen after the test (giving the contact radius at the moment of failure).



**Figure 2.7** – Typical uniaxial compression test of a fused quartz particle: (a) force-displacement curve. Initial non-linear part of the response represents the embedding of the particle in the soft colloidal graphite layer. Contact between the particle and the steel platen is marked by a significant increase of the response slope; (b) and (d) scanning electron microscopy images of the particle before and after the test; (c) optical image of the upper platen surface showing the indent left by the particle after the test.

At the start of each test, the upper platen travels at constant displacement rate until it touches the particle. The particle then starts to sink into the soft  $\approx 10 \mu\text{m}$  thick colloidal graphite layer; this phase is exhibited by the first shallow non-linear force displacement response. Once the particle touches the underlying steel platen the force-displacement curve steepens significantly. The force then increases up to the moment of failure, reaching its critical (particle fracture) value typically indicated by a sharp drop in load; at this moment the test is automatically terminated. The full set of experimental data is given in Appendix 2.B of Section 2.9, Table 2.3.



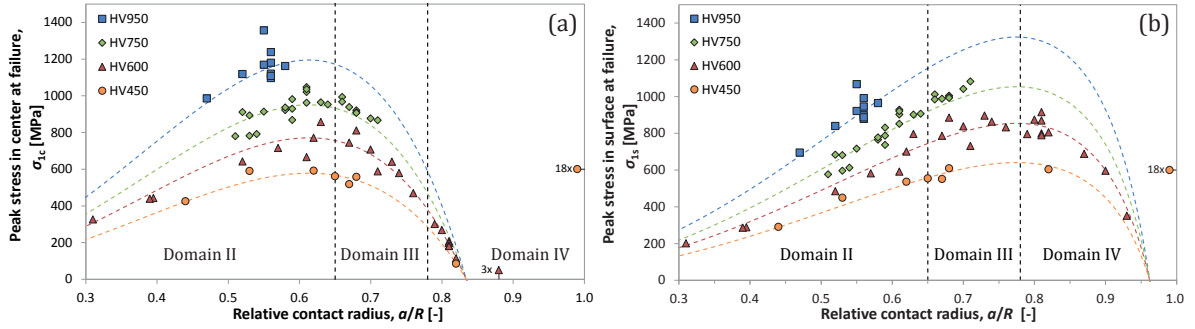
**Figure 2.8** – (a) Experimentally measured values of the critical force divided by the particle cross-sectional area,  $F_{\text{max}}/\pi R^2$ , versus the relative contact radius  $a/R$ . (b) The data align on a master curve when normalized by the Vicker's hardness  $HV$  in SI units. The dashed line represents the least squares fit of Meyer's law giving  $\tilde{k} = k/HV = 1.2$  and  $n = 2.2$ .

Figure 2.8 gives the measured values of the critical force divided by the particle cross-sectional area,  $F_{\text{max}}/\pi R^2$  versus the relative contact radius  $a/R$  at particle failure for the four different platen materials. As seen, after normalization of  $F_{\text{max}}/\pi R^2$  with the Vicker's hardness  $HV$  (in SI units) of the relevant platen, all the data collapse onto a single curve, as predicted by Meyer's law, Eq. (2.3).



Fitting the master curve with a power law, we find  $n = 2.2$  and  $\tilde{k} = k/HV = 1.2$ . Note that exponent  $n$  is related to the strain-hardening coefficient of the platen material; since each of the platens is of hardened steel, that all four platens have a similar strain-hardening exponent is reasonable.

Figure 2.9 gives values of the first principal stress within each particle at the moment of failure, as calculated using the HO-SH analysis using measured values of  $(F_{\max}, a/R)$ . Figure 2.9a gives the calculated first principal stress in the centre of the sphere,  $\sigma_{1c}$ , while Figure 2.9b plots the first principal stress along the equatorial line,  $\sigma_{1s}$  at that moment. The dashed lines in Figure 2.9 trace the predictions for the evolution of the first principal stresses,  $\sigma_{1c}$  and  $\sigma_{1s}$ , versus  $a/R$ , calculated using the HO-SH solution coupled with the particular platen Meyer law obtained in Figure 2.8 according to Eq. (2.5). As can be seen, the curves fit the data, showing that the two calculations are mutually consistent.



**Figure 2.9 – First principal stress versus the relative contact radius  $a/R$ : (a) in the centre of the compressed particle,  $\sigma_{1c}$  and (b) along the surface equator,  $\sigma_{1s}$ . Symbols represent calculated stress values using the HO-SH analysis, Eq. (2.2), based on measurements of the critical load at failure  $F_{\max}$  and corresponding relative contact radius  $a/R$ . Dashed lines give predictions for  $\sigma_{1c}$  and  $\sigma_{1s}$  based on the HO-SH solution and Meyer’s law (Figure 2.8 and Eq. (2.5)). Symbol shape and colour indicate the platens used: HV450 (circle, orange), HV600 (triangle, red), HV750 (diamond, green) and HV950 (square, blue). Vertical lines separate different failure domains, as discussed in the Theory section.**

Dashed vertical lines in Figure 2.9 indicate the four failure domains of internal particle stress distribution that were discussed in the Theory section. Domain I, where  $(a/R) \leq 0.3$ , is absent as no data lie within this region: particle failure hence did not initiate from the near-contact regions in the present tests. Of the 85 tests, we find that 23 failure events occurred with  $(a/R) \pm \Delta(a/R)$  situated within the range from 0.65 to 0.78, *i.e.*, in Domain III within experimental error. According to the analysis presented above, we know that failure of those 23 particles was initiated from the particle surface, along the equatorial belt.

Let us ignore for now other particles, and consider only those 23 particles. In Domain III, each platen probes particle strength values situated within a specific range determined by the following bounds:

- the surface stress  $\sigma_{1s}$  value at the moment when the central stress  $\sigma_{1c}$  starts to decrease, *i.e.* when  $(a/R) \approx 0.65$  for fused quartz ( $\nu = 0.17$ );
- the highest value of stress  $\sigma_{1s}$  attainable by each platen, which is reached for fused quartz ( $\nu = 0.17$ ) when  $(a/R) \approx 0.78$ . In Domain III particle strength values must therefore fall in the range  $550 \leq \sigma_{1s} \leq$



650 MPa for platens with HV450,  $700 \leq \sigma_{1s} \leq 900$  MPa for platens with HV600,  $900 \leq \sigma_{1s} \leq 1100$  MPa for platens with HV750 and  $1100 \leq \sigma_{1s} \leq 1300$  for the hardest platen, of HV950.

Of the 85 tested particles, 27 other particles entered Domain IV, where  $(a/R) > 0.78$ . Of these, 18 particles that were tested using the softest HV450 platen did not crack at all: those were fully embedded and the platens contacted; in graphs in Figure 2.9 these are shown with the symbol to the far right. More surprisingly, 9 other particles that entered Domain IV actually failed, even though according to theory  $\sigma_1$  was decreasing everywhere within the particle. A likely cause of these nine failure events is delayed fracture, known to operate when fused quartz material is tested in (humid) ambient air (see Section 2.6.3). To test this hypothesis, one particle was compressed using HV600 platens up to  $(a/R) \approx 0.87$ , whereupon platen movement was paused, thereby leaving the particle under static compressive loading with the tensile stress peaking along the surface equatorial belt at a value around 600 MPa. This test is summarized in Appendix 2.C, Section 2.10; after several tens of seconds, the particle failed with an abrupt drop in load, thus giving indirect proof that slow crack growth is operative in the tested particle material.

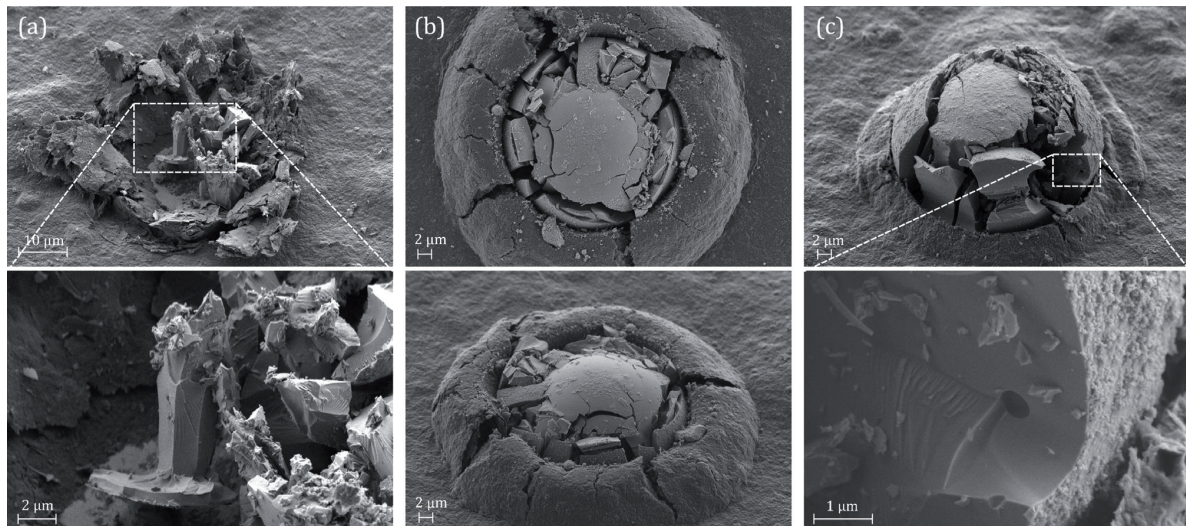


**Figure 2.10** – SEM images of particles after uniaxial compression testing. (a) Particle that failed at  $(a/R) < 0.65$  (in Domain II), shattered into many pieces but leaving a central column roughly extending from the lower surface to the particle centre, along which river markings suggest crack growth from the particle centre to a point of load application. (b) and (c) show two particles that failed at relatively mild surface peak stress values, namely 610 and 450 MPa, respectively. The particle in (b) failed at  $(a/R) > 0.65$  (Domain III): several meridian cracks are visible, consistent with the predicted stress distribution at that moment. The particle in (c) failed at  $(a/R) < 0.65$  (Domain II); a subsurface pore can be observed along the path of one meridian crack, with river markings suggesting crack growth away from the pore.

The colloidal graphite paste proved effective in retaining the broken particles pieces after fracture, see Figure 2.7d and Figure 2.10. Most failed particles show extensive shattering (Figure 2.7d and Figure 2.10a); with such fragmented particles it was generally impossible to determine the cause of failure by means of fractography. In some cases the colloidal graphite paste could not contain all

particle pieces after shattering, suggesting the presence, within the particles, of regions under substantial compressive stress [318]. Particles that broke at lower tensile stress values showed a much smaller number of fragments.

In some cases, when shattered particle fragments were big enough, we could observe a few fractographic details related to the cracking process. An example from a particle that broke in Domain II after testing with the HV950 platen is shown in Figure 2.10a. This fragment represents one-half of a central column extending roughly from the particle centre to the bottom platen surface. By detailed observation of the fragment, river markings can be identified, which indicate the local direction of crack growth [60]. For this example, the river pattern indicates that the prevailing crack growth direction along the column surface was from the particle centre towards the area of contact with the platen.

Two other examples of particles that failed at relatively low stress levels are presented in Figure 2.10b and Figure 2.10c. Both particles were tested with the HV450 platens and their fragmentation was limited. In Figure 2.10b, the particle failed in Domain III, which is consistent with the observed failure pattern consisting of several meridian cracks, with the region of contact with the metallic platens essentially intact, unlike what is seen when hard platens are used [242,319].

The particle in Figure 2.10c failed with  $(a/R) = 0.53$ , i.e., well within Domain II, however, a subsurface pore can be found along the fracture surface of one meridian crack near the particle equator. The fractographic pattern with river markings present near the pore is consistent with it being the origin of failure (although this evidence is not conclusive since not all fragments could be examined).

## 2.6 Discussion

### 2.6.1 Survival analysis for data points known to be measure of the surface strength

To interpret the present strength data, we adopt a point of view similar to that of Shipway and Hutchings [10], namely that compressed particles will generally break either near their centre, or near their equator, meaning from defects situated either in the midst or along the surface of the particles. For simplicity, we ignore the influence of particle size. To simplify writing, in what follows Domain III will be used to designate those particles for which  $\left[\frac{a}{R} + \Delta\left(\frac{a}{R}\right)\right] > 0.65$  and  $\left[\frac{a}{R} - \Delta\left(\frac{a}{R}\right)\right] < 0.78$ , where  $\Delta\left(\frac{a}{R}\right)$  is the estimated absolute uncertainty in relative contact radius measurement. The rest belongs either to Domain II ( $\left[\frac{a}{R} + \Delta\left(\frac{a}{R}\right)\right] < 0.65$  at fracture) or Domain IV ( $\left[\frac{a}{R} - \Delta\left(\frac{a}{R}\right)\right] > 0.78$  during the test). Terms *surface stress* and *centre stress* will be used for the instantaneous local peak value of the tensile first principal stress along the equatorial line,  $\sigma_{1s}$ , and particle centre,  $\sigma_{1c}$ , respectively.

The strength of the tested particles is statistically distributed: we thus do not aim to assess an average particle strength, but rather aim to measure the particle statistical strength distribution. To this end, we rely on the extensive statistical analysis work that has been developed over the past few decades to analyse banks of data of similar nature, commonly found in medical studies and pertaining to survival probabilities; Ref. [320] gives a clear, user-friendly, overview.

If we replace time, commonly used in Survival analysis, with stress, and acknowledge that we have here two competing causes for failure (centre failure and surface failure), we have here a survival analysis problem with two somewhat peculiar characteristics, namely:

(i) whereas time in classical lifetime analysis is a common parameter used to track all causes of mortality, here failure at the centre or at the surface of the particles is caused by one of two (local) stress values that differ at each instant; and

(ii) because those two local stresses do not always increase together (Section 2.3), the present data have the peculiar feature that there is a window of surface stress values within which one knows the cause for failure: all strength data that occurred in Domain III are *known* to relate to meridian cracking initiated at, or very near, the equator surface.

Furthermore, by varying the hardness of the platens, one varies the range of surface stresses imposed on a particle. Therein lies one of the most attractive features of what we call here the meridian test.

With these specificities noted, statistical methods of survival analysis can be transposed to the present situation. We assume that flaw distributions within the centre and along the surface of the particles are independent; *a priori* this should be reasonable given their different nature (pores versus surface cracks). Since surface flaws are known to be at the origin of failure in several of the present particles (all those that broke in Domain III; see also Figure 2.10c), we focus on this cause for failure first, to then later turn our attention to the possibility of failure starting in the centre: as will be seen its importance for particles tested here is comparatively minor, as could be anticipated for glass spheres. Two approaches can be used, namely non-parametric analysis (which assumes nothing of the flaw size distribution) or a parametric approach, which assumes that the particle surface strength is Weibull distributed. We present both in turn; Appendix 2.D (Section 2.11) shows a comparative illustration of the two approaches on a hypothetical set of Weibull distributed data with features similar to those in the present experiments.

*Non-parametric survival analysis* - Here, we assume nothing of the flaw or strength distributions along the centre or surfaces of the particles. To estimate the failure probability at a given stress level we use the Kaplan-Meier product limit estimator [320,321] adapted for left-truncation and right-censoring of the data.

Particle failure within Domain III is known to have originated from the particle surface; hence in an analysis of the surface strength distribution of particles, such events provide hard, unambiguous data. Additionally, particles from Domain IV survived the maximum attainable stress that can be imposed by the given platen material (regardless of whether a few failed later on). In other words we know a lower bound of their surface strength; in survival analysis, events of Domain IV are named right-censored data of Type I [320]. Those events include 8 particles tested using HV600 platen (which failed in Domain IV, most probably due to slow crack growth as explained above) - and 19 particles tested using the HV450 platen, one of which also failed in Domain IV, again likely due to slow crack

growth, while the remaining 18 sank into the platens without breaking. The censoring level of surface stress values are 900 MPa for HV600 and 650 MPa for HV450 platens, respectively.

Those data from Domains III and IV trace only a portion of the strength distribution, since strength is bound from below by the surface stress value at which Domain III starts for a given platen material. In the language of survival analysis, all events, being either failure or right-censored, from Domains III and IV, are left-truncated for values of (surface) strength below the onset of Domain III: the left-truncation surface stress values were approximately 900 MPa for HV750, 700 MPa for HV600 and 550 MPa for HV450 platens, respectively.

Consider now the ensemble of data from Domains III and IV: there are  $D$  distinct known surface failure stresses  $\sigma_{1s}^1 < \sigma_{1s}^2 < \dots < \sigma_{1s}^D$  for events in Domain III, and  $C$  right-censored events of Domain IV. Note that if two particles fail at the same surface stress,  $\sigma_{1s}$ , this translates here into one value of  $\sigma_{1s}^i$ ; therefore  $D$  is a number lower or equal to the number of particles that failed within Domain III.

One can thus analyse the data using the non-parametric product-limit estimator defined as follows:

$$P_i(\sigma_{1s}) = \begin{cases} 1 & \text{if } \sigma_{1s} < \sigma_{1s}^1 \\ \prod_{j=1}^i \left(1 - \frac{d_j}{Y_j}\right) & \text{if } \sigma_{1s} \geq \sigma_{1s}^1 \end{cases} \quad (2.6)$$

where index  $i \in \{1, \dots, D\}$ ,  $P_i$  is the probability of survival at stress  $\sigma_{1s}^i$ ,  $d_j$  is the number of particles that failed at the stress equal to the  $\sigma_{1s}^j$  and  $Y_j$  is the number of particles that have survived at least stress  $\sigma_{1s}^j$  and at the same time have a left-truncation stress  $T$  lower or equal to the failure stress  $\sigma_{1s}^j$ , including censored particles; this quantity represents the number of particles *at risk*. Data used for non-parametric survival analysis of the surface strength are given in Table 2.2.

Table 2.2 – Results used for surface strength survival analysis.

Platen	Measured failure/censoring peak surface stress [MPa]	Censoring indicator <sup>1</sup>	Left-truncated at [MPa]	Platen	Measured failure/censoring peak surface stress [MPa]	Censoring indicator <sup>1</sup>	Left-truncated at [MPa]	
HV750	990	0	900		650	1	550	
	1000	0	900		650	1	550	
	1080	0	900		550	0	550	
	1040	0	900		650	1	550	
	1000	0	900		650	1	550	
	990	0	900		650	1	550	
	910	0	900		650	1	550	
	900	0	900		650	1	550	
	1010	0	900		650	1	550	
	980	0	900		650	1	550	
HV600	900	1	700	HV450	650	1	550	
	900	1	700		650	1	550	
	900	0	700		650	1	550	
	890	0	700		610	0	550	
	870	0	700		650	1	550	
	860	0	700		650	1	550	
	800	0	700		650	1	550	
	840	0	700		650	1	550	
	790	0	700		650	1	550	
	900	1	700		650	1	550	
	900	1	700		550	0	550	
	900	1	700		650	1	550	
	830	0	700					
	900	1	700					
	900	1	700					
800	0	700						
730	0	700						

<sup>1</sup> when 0, the surface stress represents the surface strength measurement, otherwise value 1 indicates right-censoring and the value in the surface stress column represents lower-bound of the surface strength.

*Parametric survival analysis* – Alternatively, we can assume that the surface strength of the fused quartz particles follows a given distribution and estimate parameters of that distribution. Here, we use the two-parameter Weibull distribution with shape parameter  $m$  and scale parameter  $\sigma_0$ . Using similar left-truncation and right-censoring of the data, we estimate those parameters by maximizing the log-likelihood function given by [322]

$$\log L = \sum_{j=1}^N \{-(1-\delta_j) \cdot \log(1/m) + \delta_j \cdot m(\log \sigma_{1s}^j - \log \sigma_0) - \exp[m(\log \sigma_{1s}^j - \log \sigma_0)]\} + \sum_{j=1}^N \nu_j \exp[m(\log T_j - \log \sigma_0)] \quad (2.7)$$

where,  $\sigma_{1s}^j$  is an observed event (a failure or a censored surface stress value),  $\delta_j$  is the censoring indicator equal either to  $\delta_j = 1$  if the  $j$ -th observation is censored or 0 if the data point corresponds to an observed failure event,  $T_j$  is the corresponding left-truncation peak surface stress value,  $\nu_j$  is the



truncation indicator (in our case always with value 1) and  $N$  is the total number of particles in Domains III and IV.

Statistical analysis of the data was conducted using the computational program *Mathematica* v. 10.1 (Wolfram Research Inc., Champaign, Illinois) with built-in functions *SurvivalModelFit* for the Product-limit estimator and *EstimatedDistribution* for the Maximum likelihood estimation using data from Table 2.2.

The result is shown in Figure 2.11; as seen the two estimations come close to one another. The parametric estimation gives  $m = 6.3$  and  $\sigma_0 = 890$  MPa.

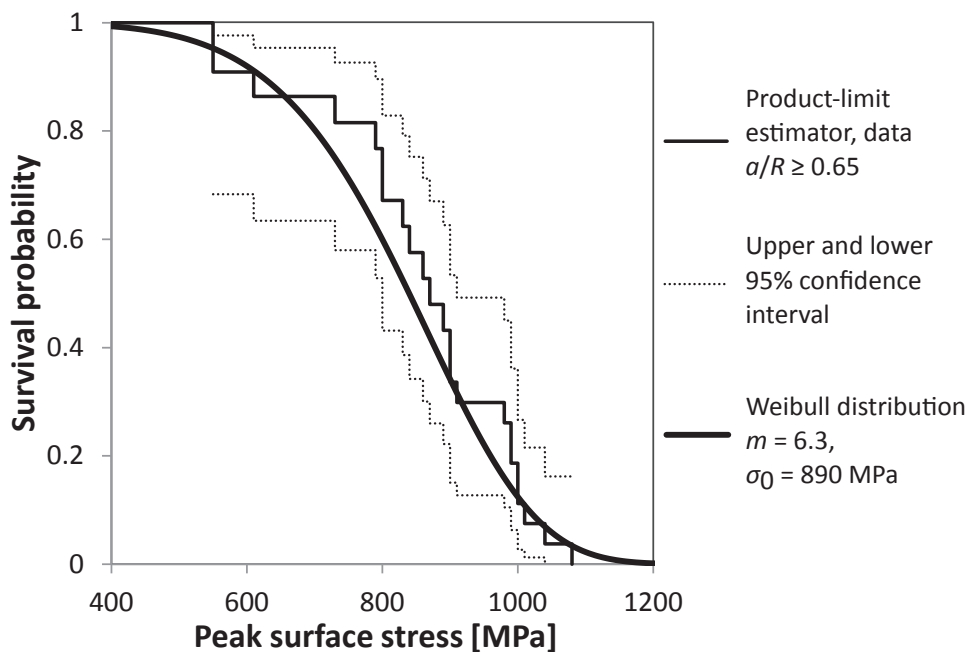


**Figure 2.11 – Estimated particle surface strength distribution computed using only data for which  $(a/R) \geq 0.65$  (Domains III and IV), using left-truncation and right-censoring according to the non-parametric Product-limit estimator, plotted together with 95% point-wise confidence intervals, or alternatively assuming Weibull statistics coupled with a maximum likelihood estimation of parameters.**

### 2.6.2 Interpreting data for competing centre and surface failure

Four particles failed at low stress values, namely  $\sigma_1 \sim 300\text{-}400$  MPa in the centre, and displayed along their fracture surface large and clearly apparent internal pores. Exempting those four particles (which represent roughly 5% of all tested particles) from further consideration, given how different their fracture stress and failure mode are from what was found with all other particles, we now examine particles that failed in Domain II. With those particles, we do not know whether fracture was initiated from a flaw along their surface near its equator (the only scenario in Domain III) or from a volumetric flaw situated near their centre. Knowing the above estimation of the surface strength derived from consideration of data in Domains III and IV, however, we can test whether data in Domain II indicate the presence of another cause for failure (necessarily flaws in the particle centre) or whether, on the



contrary, those data are consistent with surface flaws being the dominant determinant of strength for the particles at hand.

To this end, we repeat the non-parametric product-limit analysis as well as the maximum likelihood estimation of Weibull strength distribution parameters using the surface peak stress values,  $\sigma_{1s}$  at the moment of failure, looking now only at data points in Domain II. Here, each platen measures the surface stress only up to a certain value that is again given by the platen material, which equals the values used for the left-truncation in the precedent analysis. In survival analysis terms, we now right-truncate the data of Domain II by the value of  $\sigma_{1s}$  at the onset of Domain III. In practice, due to scatter in the data along the theoretical surface stress vs.  $(a/R)$  relation (Figure 2.9b), the highest observed value of  $\sigma_{1s}$  for  $(a/R) < 0.65$  for each platen dataset was taken as the right-truncation value. Left-truncation is now irrelevant (we observe failure events starting at  $\sigma_{1s} = 0$  MPa). Additionally, we exclude from the analysis the four low-stress particle failure events for which a big internal pore was observed (see Appendix 2.C, Figure 2.16). The construction of the product-limit estimator is somewhat different than in the case of left-truncated/right-censored data [320]; here we again use *SurvivalModelFit* function of the computational program *Mathematica* v. 10.1.

The survival analysis of data from Domain II in terms of the surface stress is presented in Figure 2.12 along with the analysis derived from the data set in Domains III and IV discussed in Section 2.6.1. As seen, the two essentially coincide. There is thus, in the present data, insufficient evidence to reject the hypothesis that all except four particles tested here failed by cracking from a flaw situated along their surface.

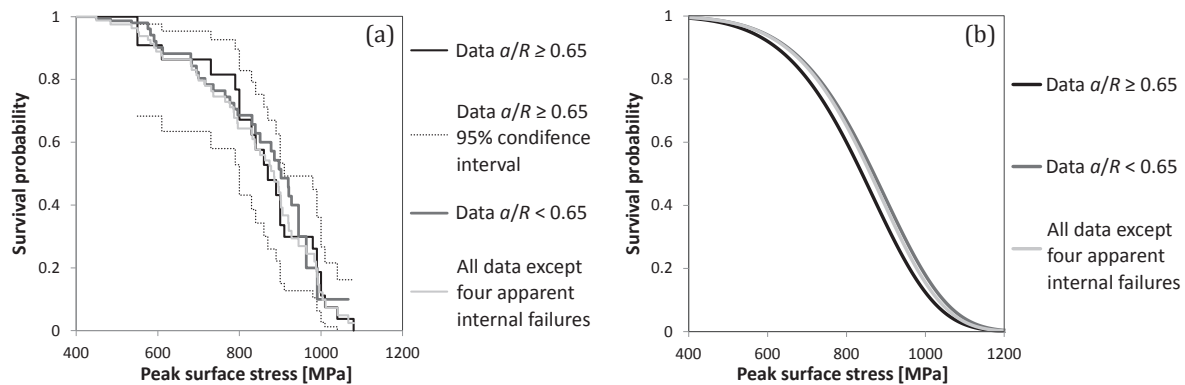


**Figure 2.12 – (a) Product-limit estimation of particle surface strength for particle populations from (black) Domains III and IV (left-truncated/right-censored data), together with (black dotted) corresponding 95% point-wise confidence intervals, (dark-grey) data from Domain II (right-truncated data), and (light-grey) ensemble of all data points (right-censored) except for four particles containing evident large pores, which failed at low stress. (b) The same three data sets with their maximum likelihood estimation of two-parameter Weibull distribution parameters: (black)  $m = 6.3$  and  $\sigma_0 = 890$  MPa, (dark-grey)  $m = 6.5$  and  $\sigma_0 = 920$  MPa, (light-grey)  $m = 6.6$  and  $\sigma_0 = 910$  MPa.**

If we now lump together all data (from Domains II, III and IV) excepting still the four particles with big internal pores, we have 54 surface failure events and 27 right-censored data in the form of particles that entered Domain IV. Using the built-in function *EstimatedDistribution* in the *Mathematica* com-

putation software, the maximum likelihood estimation of the two-parameter Weibull distribution particle strength distribution become  $m = 6.6$  and  $\sigma_0 = 910$  MPa; the change in these values is by only 6 and 2 percent compared with the initial estimate based on the subset of data from Domains III and IV alone. Since data are consistent with surface failure being the dominant failure mode in the present particles, this can be viewed as a reliable estimator of their surface strength distribution.

The characteristic strength value  $\sigma_0 = 910$  MPa translates to a critical half penny-shape surface crack situated along the equator,  $c = 370$  nm if we use the linear-elastic fracture mechanics expression,  $c = \left(\frac{K_{IC}}{Y \cdot \sigma_0}\right)^2$  where the fracture toughness,  $K_{IC}$  of fused quartz is  $0.65 \text{ MPa}\cdot\text{m}^{1/2}$  [323,324] and the geometric factor,  $Y$  for a half penny-shape crack of negligible size with respect to the size of a particle is  $0.66 \cdot \sqrt{\pi}$ . For comparison, the pore observed near the surface on one of the tested particles in Figure 2.10c has a diameter of roughly 500 nm, which is thus consistent with the calculated Weibull strength parameter value.

Surface flaws as well as humidity are well known to govern the strength of fused quartz [325,326]. Unless a protective coating is applied, surface flaws will generally be caused by surface abrasion during storage and handling of the powder. Comparing particles tested here with other data for fused quartz one finds that the present particles are, with their strength on the order of 1000 MPa, strong compared to macroscopic fused quartz or silica glass particles, which typically fail at 200 MPa or lower [10,327]. Yet the particles are far less strong than what can in principle be achieved: fibres of fused quartz tested in vacuo at  $-196^\circ\text{C}$  approach the theoretical strength value of 15 GPa, while the strength in air at room temperature of these almost defect-free fibres was in the range of 4 – 7 GPa with evident dependence on the stress rate [326]. The industrial-scale manufacturing of spherical fused quartz particles much stronger than those tested here should, thus, be possible.

### 2.6.3 Effect of slow-crack-growth

Particle strength data measured above were obtained in ambient air, in which it is well known that fused quartz is susceptible to delayed cracking caused by slow-crack-growth (SCG) [325,328–331]. As indicated above, the observation that a few particles failed within Domain IV, coupled with the steady load test reported in Appendix 2.C (Section 2.10), are strong indicators that SCG was active in the present particles. We therefore estimate the influence of the phenomenon on the strength of the present particles, in an attempt to derive what their strength distribution might be in the absence of the phenomenon, *e.g.*, in an inert environment, or when they are embedded within a composite material having a matrix impervious to water.

The kinetics of SCG are often modelled assuming the power-law characteristic of the first stage of SCG (*i.e.*, by assuming that crack tip velocity saturation has not been reached) given by

$$\frac{dc}{dt} = AK_I^r \quad (2.8)$$

where  $c$  represents the instantaneous size of a sharp crack,  $t$  is time,  $K_I$  is the Mode I stress intensity factor and  $A$  and  $r$  are constants that depend on the material and environment. Assuming for simplicity

that loading is conducted with a constant stress rate,  $\dot{\sigma}$ , then the stress at failure in the presence of SCG of a solid containing an initial flaw of size  $c_i$ , as derived by [53], is

$$\sigma_{\text{SCG}} = \left( \frac{2(r+1)\dot{\sigma}}{(r-2)AY^r c_i^{\frac{r-2}{2}}} \right)^{\frac{1}{r+1}} \quad (2.9)$$

where  $Y$  is the geometric factor giving the stress intensity factor as  $K_I = Y\sigma\sqrt{c}$ . In the absence of SCG, the same solid containing the same initial flaw of length  $c_i$  would fail at stress

$$\sigma_t = \frac{K_{IC}}{Y\sqrt{c_i}} \quad (2.10)$$

where  $K_{IC}$  is the fracture toughness. SCG parameters for fused quartz at room temperature and  $\sim 70\%$  relative humidity are given in the literature as  $r = 34$  and  $A = 8 \times 10^6$  [329]. With  $Y = 0.66 \cdot \sqrt{\pi}$  for a half-penny crack of size negligible compared to that of the tested body, a fracture toughness  $0.65 \text{ MPa}\cdot\text{m}^{1/2}$  [323,332] and  $c_i$  in the range of  $0.1 - 1 \text{ }\mu\text{m}$ , with  $\dot{\sigma} = 1 \text{ GPa/s}$ , SCG will reduce the strength to between  $61\%$  and  $68\%$  of the inert strength  $\sigma_t$ . In order to measure at least  $95\%$  of the inert strength,  $\dot{\sigma}$  would have to be far above what can be achieved by conventional means. The effects of SCG must therefore be considered in interpreting the present data.

The majority of tests in the present study used an upper platen displacement rate that was  $dh/dt = 1 \text{ }\mu\text{m/s}$ ; in a few cases the rate was  $dh/dt = 0.5 \text{ }\mu\text{m/s}$ . Considering perfectly spherical particles, the relative contact radius as a function of time is given by

$$\frac{a}{R} = \sqrt{\frac{\frac{dh}{dt} \cdot t}{R} - \frac{\left(\frac{dh}{dt} \cdot t\right)^2}{4R^2}} \quad (2.11)$$

Combining Eqs. (2.11) and (2.5) and taking a typical value for  $R = 15 \text{ }\mu\text{m}$ , with a Meyer's law index  $n = 2.2$  as observed for the platens of this work and  $dh/dt = 1 \text{ }\mu\text{m/s}$ , one obtains the evolution of the adimensional stress  $\frac{\sigma_1}{k}$  as a function of time  $t$  presented in Figure 2.13. As can be seen from the figure, in a typical test of this work it takes  $\sim 7$  seconds from the beginning of the test to reach Domain III. Thereafter, the surface stress in Domain III still increases for about  $\sim 3.5$  s, and once in Domain IV it remains at a relatively high level for another  $\sim 3.5$  s. Thus, the total time, on the order of couple of seconds, that a tested particle spends at high surface stress in Domains III and IV, might be sufficient for a surface flaw to grow due to SCG to reach a critical size, and thereby cause a particle to fail when it would not in an inert environment. This explains the occurrence of several failure events past the point of maximum surface stress.

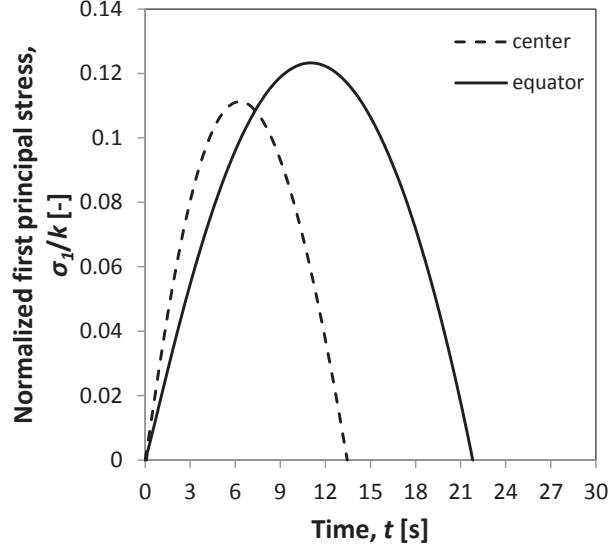


**Figure 2.13 – Evolution of the normalized first principal stress for a fused quartz particle with 15  $\mu\text{m}$  radius loaded with upper platen displacement rate 1  $\mu\text{m/s}$  and Mayer’s law index of the platen  $n = 2.2$ .**

With SCG active, the measured strength depends on the stress rate. Inserting Eq. (2.10) into Eq. (2.9), one obtains the relation linking the inert strength  $\sigma_t$  and the measured strength,  $\sigma_{SCG}$ , as reduced by SCG

$$\sigma_t = \left( \sigma_{SCG} / \left[ \frac{2(r+1)}{(r-2)} \frac{\dot{\sigma}}{A \cdot Y^2 K_{IC}^{r-2}} \right]^{\frac{1}{r+1}} \right)^{\frac{r+1}{r-2}} \quad (2.12)$$

where  $\sigma_{SCG}$  now represents the measured surface strength  $\sigma_{1s}$  in this work in Domain III and a lower bound of the strength for particles from Domain IV. We assume surface half-penny shape flaws of size well below  $R$ , SCG kinetics according to Eq. (2.8), and (although this is not true here) loading under a constant stress rate. Specifically, we take  $\dot{\sigma}$  equal to the secant stress rate, that is, we divide  $\sigma_{1s}$  at the moment of failure by the time under load up to failure. Typical values of the secant stress rate were on the order of 100  $\text{MPa}\cdot\text{s}^{-1}$ , with the range of values between 20 and 130  $\text{MPa}\cdot\text{s}^{-1}$ . The estimated intrinsic surface strength,  $\sigma_t$  from Eq. (2.12) then represents the surface strength that the particle would display in the absence of SCG, as given by Eq. (2.10). For particles that entered Domain IV (for these we only know a lower bound of their surface strength), we take  $\sigma_{SCG}$  equal to the maximum attainable peak surface stress during the test for the relevant platen. Equation (2.12) then gives a lower bound for  $\sigma_t$ : in other words, these again form right-censored data.

Correcting the strength values of the data from Domains III and IV for the effects of SCG gives again a left-truncated and right-censored dataset on which we can use the Survival analysis methods as exposed earlier. For simplicity the left truncation level was taken as the lowest observed SCG corrected surface strength,  $\sigma_t$  for each platen dataset (HV750, HV600, HV450). Figure 2.14 gives the resulting estimated particle strength distribution: as seen, SCG causes the high-strength part of the distribution to shift to significantly higher strength values: it is thus likely these particles would be

far stronger in an inert humidity-free environment, notably when used as a reinforcement in a composite with a matrix impervious to moisture. This said, even after correction for the effects of SCG, the measured strength distribution remains far below what is achieved in glass fibres: particles such as these should be sized and handled with greater care if they are to be used as a composite reinforcement.

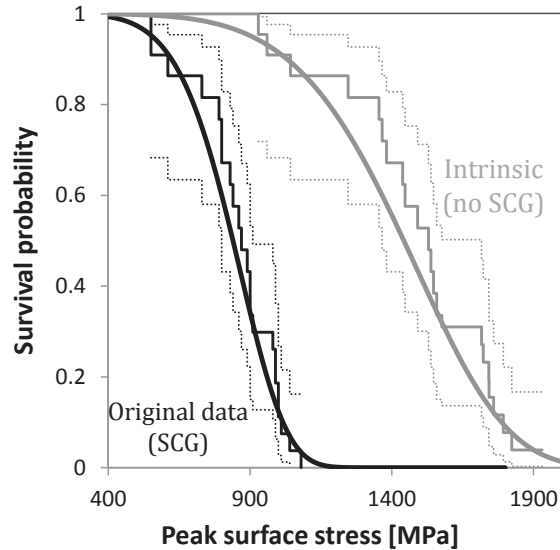


**Figure 2.14 – Comparison of the peak surface strength distribution of the (black) original data (influenced by SCG) and (grey) same after correction for the effect of SCG. Smooth solid curves represent the estimated Weibull distributions using a maximum likelihood method; corresponding parameters are  $m = 6.3$ ,  $\sigma_0 = 890$  MPa and  $m = 5.6$ ,  $\sigma_0 = 1540$  MPa for the original and SCG corrected data, respectively. The solid stepped curves represent the Product-limit estimator, together with corresponding dotted curves representing 95% point-wise confidence intervals of the Product-limit estimator.**

## 2.7 Conclusion

Building on the approach of Shipway and Hutchings, we show how uniaxial particle compression testing can be improved if one uses a pair of elasto-plastic platens of tailored hardness, selected to be sufficiently soft relative to the particle such that measured strength values do not reflect the influence of Hertzian contact stress concentration, while being sufficiently hard to crack the particles in the appropriate range of indent to particle radius ratio values. The different trajectories of peak tensile stress near the center, and along the surface of the particles, are such that the distribution of central and surface strengths can be separately assessed from test data conducted using appropriately chosen platen materials and the methods of survival probability analysis.

The approach is demonstrated using commercially available spherical microscopic fused quartz particles 30  $\mu\text{m}$  in average diameter (Denka FB-40S produced by Denka, Tokyo, Japan). Tested in air with a loading rate on the order of  $100 \text{ MPa}\cdot\text{s}^{-1}$  the particles show strengths between 500 MPa and 1100 MPa with a characteristic strength value near 900 MPa. Roughly 5% of the particles fail at far lower strength values, in the range  $\sim 300\text{-}400$  MPa, that are caused by the presence of large internal pores. The remaining 95% of the particles have surface-flaw limited strength distributions that can be

described using two-parameter Weibull distributions of parameter values  $m = 6.6$ ,  $\sigma_0 = 910$  MPa for the particles tested in air, corresponding to estimated values of  $m = 5.6$ ,  $\sigma_0 = 1540$  MPa if the particles are protected from humidity.

## 2.8 Appendix 2.A

Hiramatsu and Oka published a solution for the stress tensor components within particles compressed as in Figure 2.1b [212]. The original paper contained some typos and errors, which were corrected in later publications: corrected expressions for  $\tilde{\sigma}_\theta$ ,  $\tilde{\sigma}_\phi$ ,  $\tilde{\tau}_{r\theta}$  were published in [333] and the expression for  $\tilde{\sigma}_r$  can be found in [214]). Corrected expressions used here are (typos in the original equations from [333] are highlighted in red):

$$\begin{aligned} \tilde{\sigma}_\theta = & -\frac{1}{2} \left[ 1 + \sum_{i=1}^{\infty} \left( \frac{-(4i+1)(i-1)+(4i+1)^2\nu}{2i(4i^2+2i+1)+2i(4i+1)\nu} \left( \frac{r}{R} \right)^{2i} + \right. \right. \\ & \left. \frac{(4i+1)(4i^2+4n-1)+2(4i+1)\nu}{2(4i^2-1)(4i^2+2i+1)+2(4i+1)(4i^2-1)\nu} \left( \frac{r}{R} \right)^{2i-2} \right) \cdot (1 + \cos \alpha) \cdot P'_{2i}(\cos \alpha) \cdot P_{2i}(\cos \theta) + \\ & \left. \sum_{i=1}^{\infty} \left( \frac{-(4i+1)(2i+5)+4(4i+1)\nu}{4i(2i+1)(4i^2+2i+1)+4i(2i+1)(4i+1)\nu} \left( \frac{r}{R} \right)^{2i} + \frac{(4i+1)(4i^2+4n-1)+2(4i+1)\nu}{4i(4i^2-1)(4i^2+2i+1)+4i(4i+1)(4i^2-1)\nu} \left( \frac{r}{R} \right)^{2i-2} \right) \right. \\ & \left. (1 + \cos \alpha) \cdot P'_{2i}(\cos \alpha) \cdot \frac{\partial^2 P_{2i}(\cos \theta)}{\partial \theta^2} \right] \end{aligned} \quad (2.13)$$

$$\begin{aligned} \tilde{\sigma}_\phi = & -\frac{1}{2} \left[ 1 + \sum_{i=1}^{\infty} \left( \frac{-(4i+1)(i-1)+(4i+1)^2\nu}{2i(4i^2+2i+1)+2i(4i+1)\nu} \left( \frac{r}{R} \right)^{2i} + \right. \right. \\ & \left. \frac{(4i+1)(4i^2+4n-1)+2(4i+1)\nu}{2(4i^2-1)(4i^2+2i+1)+2(4i+1)(4i^2-1)\nu} \left( \frac{r}{R} \right)^{2i-2} \right) \cdot (1 + \cos \alpha) \cdot P'_{2i}(\cos \alpha) \cdot P_{2i}(\cos \theta) + \\ & \left. \sum_{i=1}^{\infty} \left( \frac{-(4i+1)(2i+5)+4(4i+1)\nu}{4i(2i+1)(4i^2+2i+1)+4i(2i+1)(4i+1)\nu} \left( \frac{r}{R} \right)^{2i} + \frac{(4i+1)(4i^2+4n-1)+2(4i+1)\nu}{4i(4i^2-1)(4i^2+2i+1)+4i(4i+1)(4i^2-1)\nu} \left( \frac{r}{R} \right)^{2i-2} \right) \right. \\ & \left. (1 + \cos \alpha) \cdot P'_{2i}(\cos \alpha) \cdot \cot \theta \cdot \frac{\partial P_{2i}(\cos \theta)}{\partial \theta} \right] \end{aligned} \quad (2.14)$$

$$\begin{aligned} \tilde{\sigma}_r = & -\frac{1}{2} \left[ 1 + \frac{1}{1-\cos \alpha} \sum_{i=1}^{\infty} \frac{2(1+\nu)(1-2\nu)(4i+1)(\cos \alpha \cdot P_{2i}(\cos \alpha) - P_{2i-1}(\cos \alpha))}{(8i^2+8i+3)2\nu+(8i^2+4i+2)(1-2\nu)} \cdot \right. \\ & \left. \left( \frac{(4i^2-2i-3)\nu}{(1+\nu)(1-2\nu)} \left( \frac{r}{R} \right)^{2i} + \frac{(2i+1)(2i-2)}{2(1+\nu)} \left( \frac{r}{R} \right)^{2i} - \frac{4i^2(2i+2)\nu}{(2i+1)(1+\nu)(1-2\nu)} \left( \frac{r}{R} \right)^{2i-2} - \frac{2i(4i^2+4i-1)}{2(2i+1)(1+\nu)} \left( \frac{r}{R} \right)^{2i-2} \right) \cdot \right. \\ & \left. P_{2i}(\cos \theta) \right] \end{aligned} \quad (2.15)$$

$$\begin{aligned} \tilde{\tau}_{r\theta} = & -\frac{1}{2} \sum_{i=1}^{\infty} \frac{-(4i+1)(4i^2+4i-1)-2(4i+1)\nu}{4i(2i+1)(4i^2+2i+1)+4i(2i+1)(4i+1)\nu} \cdot \left( \left( \frac{r}{R} \right)^{2i} - \left( \frac{r}{R} \right)^{2i-2} \right) \cdot (1 + \\ & \cos \alpha) \cdot P'_{2i}(\cos \alpha) \cdot \frac{\partial P_{2i}(\cos \theta)}{\partial \theta} \end{aligned} \quad (2.16)$$

with

$$\alpha = \frac{\arccos(1 - 2(a/R)^2)}{2} \quad (2.17)$$



where  $\nu$  denotes the Poisson ratio of the (linear elastic) sphere material and  $P_{2i}(\cos \theta)$  denotes the Legendre polynomial of degree  $2i$ . The derivative  $P'_{2i}(\cos \alpha)$  is defined as

$$P'_{2i}(\cos \alpha) = \frac{\partial P_{2i}(\cos \alpha)}{\partial \cos \alpha} = \frac{P_{2i}(\cos \alpha)}{(-1)(\sin^2 \alpha)^{1/2}} \quad (2.18)$$

The first and second partial derivatives of the Legendre polynomials  $P_{2i}(\cos \theta)$  with respect to  $\theta$  can be simplified as follows:

$$\frac{\partial P_{2i}(\cos \theta)}{\partial \theta} = \frac{[(-1 - 2i) \cos \theta P_{2i}(\cos \theta) + (1 + 2i)P_{2i+1}(\cos \theta)] \cdot \sin \theta}{\sin^2 \theta} \quad (2.19)$$

$$\frac{\partial^2 P_{2i}(\cos \theta)}{\partial \theta^2} = -\cos \theta \left( \frac{P_{2i}(\cos \theta)}{(-1)(\sin^2 \theta)^{1/2}} \right) + \sin^2 \theta \left( \frac{P_{2i}^2(\cos \theta)}{(-1)^2(\sin^2 \theta)} \right) \quad (2.20)$$

where  $P_{2i}^2$  is associated Legendre polynomial of degree  $2i$  and of order 2.

The stress tensor coefficients, Eqs. (2.13)-(2.16) are given in the form of an infinite series, which has to be truncated. *Mathematica* v. 10.1 (Wolfram Research Inc., Champaign, Illinois) was used to perform summations to  $p$  terms and to calculate the stress quantities of interest. Along the sphere vertical axis, where  $\cos \theta = 1$ , the expressions in Eqs. (2.13)-(2.16) yield an indeterminate solution; hence for simplicity the axis was represented in calculations by using numerical value of  $\theta = 0.001$  as  $|\sigma_1|_{\theta=0} = \lim_{\theta \rightarrow 0} \sigma_1$ . Likewise, the center of the sphere is defined here as  $(\theta, r/R) = (0.001, 0.001)$ . With very low relative contact radii  $a/R$  and especially for the stress components along the surface ( $r/R = 1$ ), convergence is achieved for relatively high numbers of summation terms  $p$ . For example, in the center of the sphere for  $(a/R) = 0.1$  the convergence or in other words the result with relative error smaller than 1% is obtained for as few as 10 summations, whereas along the surface near the equator for the same relative contact a relative error below 1% is obtained only for 1000 or more summation terms. In order to compute the stresses along the surface close to the contact perimeter along the  $\theta$  direction, where the stress peaks for very small contacts below  $(a/R) = 0.3$ , as many as 100,000 summations had to be used due to the highly oscillatory nature of the expression. This produced near-perimeter stress values with an estimated relative error below 5%.

## 2.9 Appendix 2.B

Table 2.3 – Experimental and numerical data of tested particles.

Substrate	Particle #	R [μm]	a/R [μm]	F <sub>max</sub> [N]	σ <sub>1c</sub> [MPa]	σ <sub>1s</sub> [MPa]	Substrate	Particle #	R [μm]	a/R [μm]	F <sub>max</sub> [N]	σ <sub>1c</sub> [MPa]	σ <sub>1s</sub> [MPa]
HV950-#1	1	14.6	0.58 ± 0.02	2.14	1160	960	HV600-#4	1	15.4	0.80 ± 0.02	3.28	270	870
	2	13.1	0.56 ± 0.02	1.53	1100	880		3	12.7	0.74 ± 0.02	1.85	580	860
	4	17.2	0.56 ± 0.01	2.69	1120	900		4	15.6	0.63 ± 0.02	2.13	860	800
	5	30.7	0.47 ± 0.01	6.19	990	700		5	15.7	0.70 ± 0.02	2.55	710	840
	6	12.8	0.56 ± 0.02	1.47	1110	890		6	16.9	0.67 ± 0.02	2.62	740	790
									7	14.3	0.90 ± 0.02	3.51	-740
HV950-#2	1	11.9	0.52 ± 0.02	1.17	1120	840	9	15.6	0.87 ± 0.02	3.70	-340	690	
	2	12.6	0.56 ± 0.02	1.52	1180	950	10	13.8	0.81 ± 0.02	2.72	200	870	
	3	11.9	0.55 ± 0.02	1.53	1360	1070							
	4	19.2	0.55 ± 0.01	3.43	1170	920	2	14.6	0.76 ± 0.02	2.48	470	830	
	5	11.1	0.56 ± 0.02	1.24	1240	990	3	13.9	0.81 ± 0.02	2.51	180	800	
HV750-#1	1	11.4	0.67 ± 0.02	1.49	940	990	4	16.1	0.81 ± 0.02	3.33	180	790	
	2	13.6	0.68 ± 0.02	2.19	920	1000	5	14.1	0.93 ± 0.02	3.38	-1110	350	
	3	10.9	0.71 ± 0.02	1.61	870	1080	6	17.2	0.61 ± 0.01	1.87	670	590	
	8	17.1	0.61 ± 0.02	2.85	1020	900	7	16.9	0.79 ± 0.02	3.45	300	800	
HV750-#2	1	14.2	0.70 ± 0.02	2.59	880	1040	8	20.2	0.52 ± 0.01	1.93	640	480	
	2	16.6	0.59 ± 0.02	2.29	930	790	9	14.7	0.71 ± 0.02	1.98	590	730	
	3	15.4	0.58 ± 0.02	1.88	920	770							
	4	19.5	0.52 ± 0.01	2.56	910	680	1*	20.9	1	-	-	-	
	5	12.9	0.53 ± 0.02	1.12	890	680	2*	24.0	1	-	-	-	
	6	12.8	0.61 ± 0.02	1.49	960	850	3	11.2	0.67 ± 0.02	0.8	520	550	
	7	21.8	0.59 ± 0.01	4.16	980	830	5*	14.3	1	-	-	-	
	8	15.5	0.58 ± 0.02	1.95	940	780	6	16.3	0.62 ± 0.02	1.56	590	540	
	9	13.8	0.59 ± 0.02	1.48	870	740	7*	11.8	1	-	-	-	
	10	17.7	0.51 ± 0.01	1.77	780	580	8*	17.5	1	-	-	-	
	11	13.3	0.54 ± 0.02	1.09	790	610							
	13	27.7	0.53 ± 0.01	4.52	780	600	1*	11.3	1	-	-	-	
	HV750-#3	1	18.5	0.55 ± 0.01	2.49	910	720	2*	16.2	1	-	-	-
3		16.2	0.68 ± 0.02	3.08	910	1000	5*	16.5	1	-	-	-	
4		13.4	0.68 ± 0.02	2.12	910	990	6*	14.3	1	-	-	-	
5		17.5	0.64 ± 0.01	3.13	950	910	8*	17.5	1	-	-	-	
6		16.8	0.61 ± 0.02	2.81	1050	930							
7		12.8	0.63 ± 0.02	1.61	960	900	1	13.2	0.53 ± 0.02	0.78	590	450	
8		13.9	0.66 ± 0.02	2.25	990	1010	3*	17.7	1	-	-	-	
9		16.3	0.66 ± 0.02	3.00	970	980	4	14.4	0.82 ± 0.02	2.12	85	600	
10		14.9	0.61 ± 0.02	2.2	1040	920	5	12.1	0.68 ± 0.02	1.05	560	610	
							6*	16.8	1	-	-	-	
HV600-#1	1	12.2	0.82 ± 0.02	2.03	110	810	7*	13.3	1	-	-	-	
	2	16.4	0.39 ± 0.02	0.7	440	290							
	3	21.9	0.57 ± 0.01	2.88	720	580	1*	13.2	1	-	-	-	
	4	12.5	0.39 ± 0.02	0.4	440	290	2*	18.5	1	-	-	-	
	5	11.6	0.81 ± 0.02	2.02	210	920	3*	13.9	1	-	-	-	
	6	14.4	0.73 ± 0.02	2.43	640	900	4*	13.9	1	-	-	-	
	7	14.7	0.31 ± 0.02	0.38	330	200	5	22.6	0.44 ± 0.01	1.37	430	290	
	9	16	0.68 ± 0.02	2.69	810	890	6	22.2	0.65 ± 0.01	3.1	560	550	
	11	15.5	0.62 ± 0.02	1.82	770	700	7*	13.2	1	-	-	-	

\* - Particle embedded completely with no failure detected.

## 2.10 Appendix 2.C

Figure 2.15 summarizes a static fatigue test in which a particle was loaded and held for several seconds under constant load until failure was detected. This demonstrates that slow crack growth is operative in the particles under conditions of the present tests. In Figure 2.16 we show optical and SEM images of four particles, which contained apparent internal defects.

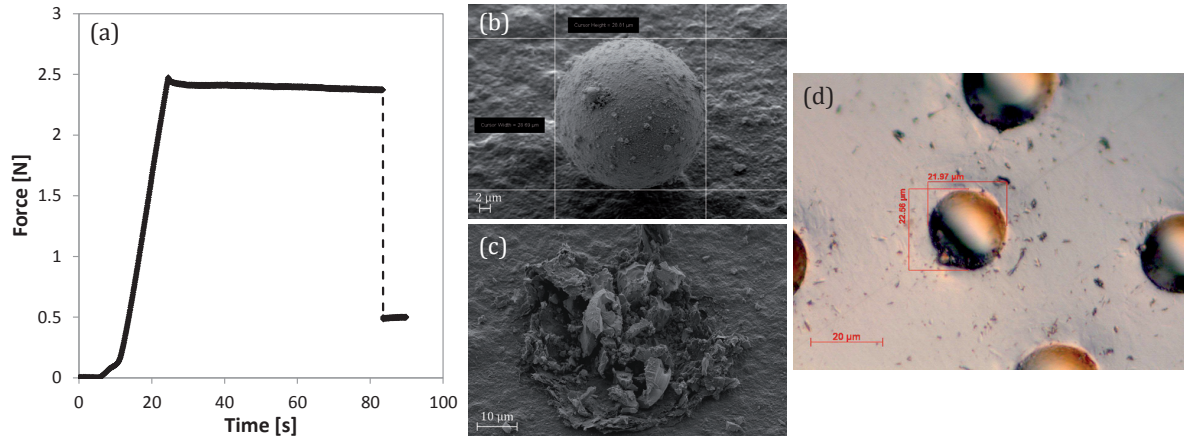


**Figure 2.15** – The uniaxial compression test done in the same conditions as the other test in this work except that loading was deliberately interrupted before failure and particle was left under the static load of roughly 2.5 N with the relative contact radius of  $\sim 0.87$  resulting in roughly 600 MPa peak surface stress for approximately 60 s after which the particle failure occurred accompanied by a sharp drop in load. The particle failed in shattering mode into many pieces as was typical for the majority of particles tested in the study. This experiment shows that particle may fail even after the maximum attainable peak tensile surface stress was applied when SCG operates.

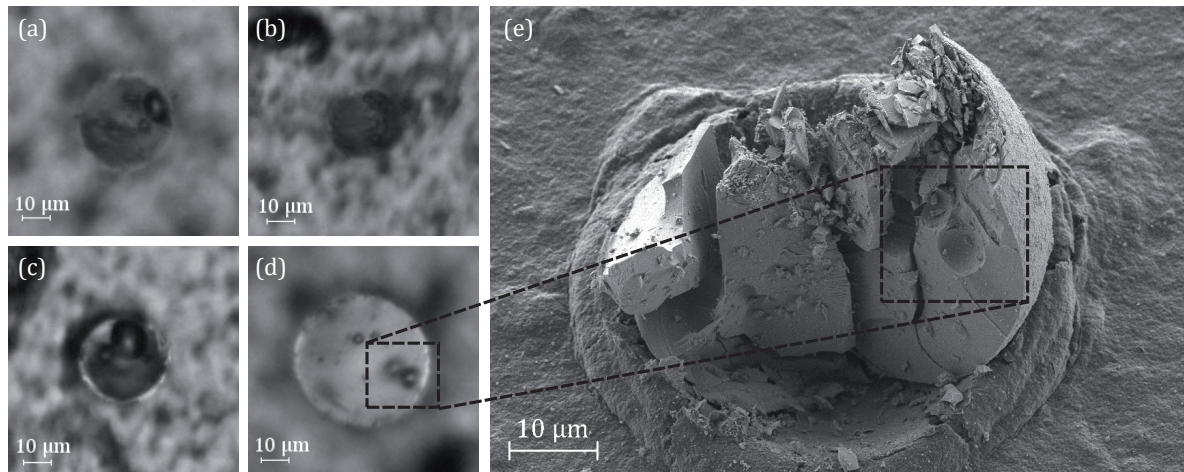


**Figure 2.16** – Particles with apparent internal pores that were not considered in the surface failure statistics. (a), (b), (c), (d) optical images before the test of particles HV600-#1-2, HV600-#1-4, HV600-#1-7 and HV450-#5-5, respectively. (e) SEM image made at  $33^\circ$  tilt after the test of the particle A564-AH-450-#5-5 with two big pores present on the fracture surface that match the two distinct dark spots on the optical image.

## 2.11 Appendix 2.D

Using the computational software *Mathematica* 10.1 we show here on a hypothetical sample that when both the surface and the centre strength are Weibull-distributed and the two are independent, then if one applies the left-truncation, right-censoring survival analysis scheme and the testing method exposed in the main body text, then the obtained distribution converges to the pre-defined surface strength distribution.

Assume that the surface strength and strength in the particle centre are Weibull distributed. Let us first generate 3 random samples from the predefined Weibull distribution of the surface strength and 3 random samples from the Weibull distribution of the centre strength, keeping the two at equal length. Let the Weibull distribution of the surface strength have shape parameter  $m = 7$  and scale parameter  $s = 900$ , then three random sample examples are:

{845, 1048, 872, 1059, 797, 719, 521, 879, 829, 1165, 1072, 943, 639, 970, 1081, 670, 944, 794, 900, 903, 905, 971, 679, 939, 861, 848, 801, 733, 1001, 560}

{768, 860, 894, 846, 952, 830, 464, 725, 843, 582, 960, 693, 774, 912, 853, 459, 1017, 530, 735, 847, 784, 963, 708, 920, 995, 636, 957, 779, 925, 1038}

{743, 834, 989, 965, 789, 713, 1018, 1010, 913, 804, 961, 766, 743, 752, 844, 600, 836, 1001, 842, 804, 854, 863, 1034, 874, 706, 775, 919, 898, 1038, 1037}

Take the Weibull distribution of the centre strength to have shape parameter  $m = 3$  and scale parameter  $s = 1300$ , then three random samples of equal length as for the surface strength are

{1099, 2026, 895, 1132, 1630, 869, 1322, 1353, 1907, 1812, 605, 1388, 1600, 1121, 1066, 1046, 1487, 1718, 1439, 1656, 940, 1199, 1124, 1859, 1479, 1471, 835, 983, 1594, 826}

{590, 1102, 2077, 2194, 1666, 1258, 1820, 846, 1659, 1210, 1012, 1139, 1291, 534, 1667, 1365, 1574, 1441, 609, 607, 583, 1534, 971, 790, 1009, 1502, 1478, 1284, 1487, 773}

{984, 1408, 1089, 1534, 862, 1177, 1257, 1884, 407, 1305, 1100, 1687, 948, 1097, 811, 936, 1192, 1355, 1102, 1893, 628, 1476, 1632, 1215, 2084, 2186, 619, 282, 1683, 1977}

We can now join three random samples of surface strength with those of central strength and form three sets of duplets. In each duplet the first number represent the surface strength and the second the centre strength. Thus each duplet can be seen as a particle (colours are explained in the next paragraph):

{{845, 1099}, {1048, 2026}, {872, 895}, {1059, 1132}, {797, 1630}, {719, 869}, {521, 1322}, {879, 1353}, {829, 1907}, {1165, 1812}, {1072, 605}, {943, 1388}, {639, 1600}, {970, 1121}, {1081, 1066}, {670, 1046}, {944, 1487}, {794, 1718}, {900, 1439}, {903, 1656}, {905, 940}, {971, 1199}, {679, 1124}, {939, 1859}, {861, 1479}, {848, 1471}, {801, 835}, {733, 983}, {1001, 1594}, {560, 826}}

{768, 590}, {860, 1102}, {894, 2077}, {846, 2194}, {952, 1666}, {830, 1258}, {464, 1820}, {725, 846}, {843, 1659}, {582, 1210}, {960, 1012}, {693, 1139}, {774, 1291}, {912, 534}, {853, 1667}, {459, 1365}, {1017, 1574}, {530, 1441}, {735, 609}, {847, 607}, {784, 583}, {963, 1534}, {708, 971}, {920, 790}, {995, 1009}, {636, 1502}, {957, 1478}, {779, 1284}, {925, 1487}, {1038, 773}

{743, 984}, {834, 1408}, {989, 1089}, {965, 1534}, {789, 862}, {713, 1177}, {1018, 1257}, {1010, 1884}, {913, 407}, {804, 1305}, {961, 1100}, {766, 1687}, {743, 948}, {752, 1097}, {844, 811}, {600, 936}, {836, 1192}, {1001, 1355}, {842, 1102}, {804, 1893}, {854, 628}, {863, 1476}, {1034, 1632}, {874, 1215}, {706, 2084}, {775, 2186}, {919, 619}, {898, 282}, {1038, 1683}, {1037, 1977}

Let us now consider that a first set of the particles (or duplets) is tested with platen material 1 (Platen 1), a second set with platen material 2 (Platen 2) and the third (remaining) set with platen material 3 (Platen 3). Platen 1 is such that, during the test, a particle will be stressed in the centre up to maximum of 600 (say, MPa; however, units are arbitrary). Platen 2 will stress the centre of a particle up to 800 and Platen 3 will stress a particle up to 1000 before the stress in centre starts to decrease (transition from Domain II to Domain III).

Under those circumstances, all particles that are tested with Platen 1 and have a strength in their centre (second number in duplets) lower than 600 will break before the relative contact radius reaches Domain III, in which one knows that failure is caused by a surface flaw. Let us remove for now those particles from consideration and let us also do so for corresponding values of the other two platens. We thus eliminate for now from consideration all duplets that (i) for Platen 1 (Set 1) have central strength lower than 600 (ii) for Platen 2 (Set 2) have central strength lower than 800 and (iii) for Platen 3 (Set 3) have central strength lower than 1000. Such cases are written in red in the list above.

Next, the test is designed such that only particles that enter Domain III are those that “we know” broke by meridian cracking due to a flaw located along their surface. Let the surface stress applied to the particle at the beginning of Domain III be (i) 550 for Platen 1 (ii) 700 for Platen 2 and (iii) 900 for Platen 3. We label therefore those particles (duplets) that will break due to surface failure before reaching Domain III in orange. All particles that are now labelled red or orange will fail, whether due to centre or surface flaws, before reaching Domain III. The surface stress levels at the beginning of Domain III for each platen also represent the left-truncation in the following survival analysis.

Some particles will not break and will rather embed completely, producing right-censored data. Let the maximum applied surface stress during a test be (i) 650 for Platen 1 (ii) 900 for Platen 2 and (iii) 1100 for Platen 3. We label particles that have a surface strength higher than the maximum attainable surface strength for a given platen with the colour green.

Remaining (black ink) particles are ones that will break in Domain III; there are  $2+10+9 = 21$  such valid surface strength measurements, and  $27+7+0 = 34$  right-censored data that entered Domain IV. Now, if we consider all these Domain III and IV data to be left-truncated at (i) 550 for Platen 1 (ii)



700 for Platen 2 and (iii) 900 for Platen 3 we obtain from the test the following data for the particle surface strength:

Table 2.4 – Data from a hypothetical test.

Platen	Failure/censoring peak surface stress [MPa]	Censoring indicator <sup>1</sup>	Left-truncated at [MPa]	Platen	Failure/censoring peak surface stress [MPa]	Censoring indicator <sup>1</sup>	Left-truncated at [MPa]
	650	1	550		860	0	700
	650	1	550		894	0	700
	650	1	550		846	0	700
	650	1	550		900	1	700
	650	1	550		830	0	700
	650	1	550		725	0	700
	650	1	550		843	0	700
	650	1	550		900	1	700
	650	1	550	Platen 2	774	0	700
	650	1	550		853	0	700
	650	1	550		900	1	700
	639	0	550		900	1	700
	650	1	550		708	0	700
Platen 1	650	1	550		900	1	700
	650	1	550		900	1	700
	650	1	550		779	0	700
	650	1	550		900	1	700
	650	1	550		989	0	900
	650	1	550		965	0	900
	650	1	550		1018	0	900
	650	1	550		1010	0	900
	650	1	550	Platen 3	961	0	900
	650	1	550		1001	0	900
	650	1	550		1034	0	900
	650	1	550		1038	0	900
	650	1	550		1037	0	900
	650	1	550				
	650	1	550				
	560	0	550				

<sup>1</sup> when 0, the peak surface stress represents the surface strength measurement, otherwise value 1 indicates right-censoring and the peak surface stress represents lower-bound of the surface strength.

If we now apply the product-limit estimator using the *Mathematica* built-in function *SurvivalModelFit* on the data from Table 2.4 we get the result plotted in Figure 2.17a. The estimated Weibull distribution using the maximum likelihood method via the *Mathematica* built-in function *EstimatedDistribution* is  $m = 7.2$  and  $s = 910$  (the original values were  $m = 7$  and  $s = 900$ ). The same procedure can be applied also for much larger sample sizes, for example with 10 000 random variate duplets for each platen. The result is shown in Figure 2.17b. As can be seen the Maximum likelihood estimation converges to the original distribution (estimated parameters  $m = 7.01$  and  $s = 902$ ), while the Product-limit estimator is somewhat inaccurate for low surface strength values (this is caused by the fact that the data are truncated at 550 therefore cannot be precise around that value). On the other hand the Product-limit estimator does not require any assumption on the nature of the surface strength distribution.



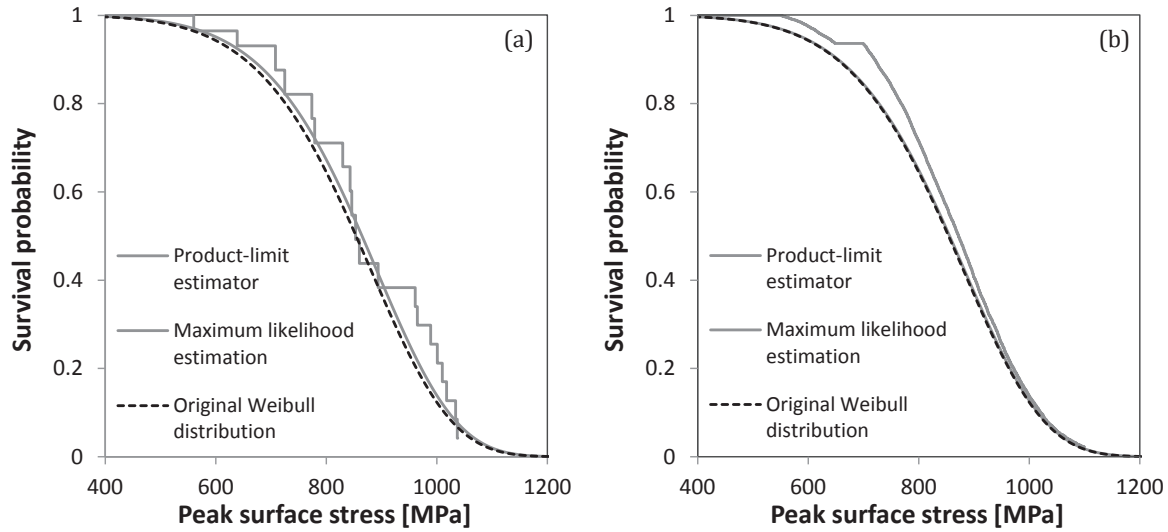


**Figure 2.17 – (a) Product-limit estimator of the left-truncated and right-censored data from the Table 2.4 obtained from hypothetical three sets of 30 duplets representing particles tested in the Meridian crack test along with the Maximum likelihood estimation of two parameter Weibull distribution ( $m = 7.2, s = 910$ ). (b) Product-limit estimator of the left-truncated and right-censored obtained from hypothetical three sets of 10,000 duplets representing particles tested in the Meridian crack test along with the Maximum likelihood estimation of two-parameter Weibull distribution ( $m = 7.01, s = 902$ ). In both cases the original Weibull distribution of surface strength was with parameters  $m = 7, s = 900$ .**

## 2.12 Appendix 2.E: Supplementary information

### 2.12.1 Finite element analysis of a spherical particle crushing test

The stress field obtained from Hiramatsu and Oka equations, Eqs. (2.1a-d), for compressed spherical particle, is here briefly compared with results obtained via a basic finite element model of the problem at hand, which was implemented in the Abaqus FEA v 6.11 (Dassault Systèmes Simulia Corp., Providence, RI, USA) software.

We model the particle as an isotropic, linear-elastic solid of elastic modulus of Young’s modulus 72 GPa and Poisson ratio 0.17 (these values are characteristic of fused quartz). The platen material is considered to be an isotropic, elastic-perfectly-plastic steel of Young’s modulus 200 GPa, Poisson’s ratio 0.3 and yield strength 1.3 GPa (these properties are characteristic of one of the platen materials used here, namely HV450, Table 2.1 of the main text, and were measured by tensile testing in our laboratory).

The finite element mesh used for this problem, is shown in Figure 2.18a; due to symmetry we only account one-half of the axisymmetric model in the problem. Elements used to discretize the particle and the platen parts are quadratic (cax8) quadrilaterals. Contact between particle and platen in the model is explicitly included; this includes hard contact formulation in the normal direction of the contact surface and Coulomb friction characterized by a constant friction coefficient  $\mu$  in the tangential direction. Loading is by prescribing vertical displacement  $u_y$  of the top surface of the platen. Preliminary runs were performed to optimize the mesh size and the size of the platen domain in order

not to affect the predicted first principal stresses in the center and at the equator of the particle. During simulations we monitor the contact pressure distribution over the entire particle surface; from this we calculate the contact radius  $a$  as the  $x$ -coordinate of the point on the particle surface at which the contact pressure drops to zero.

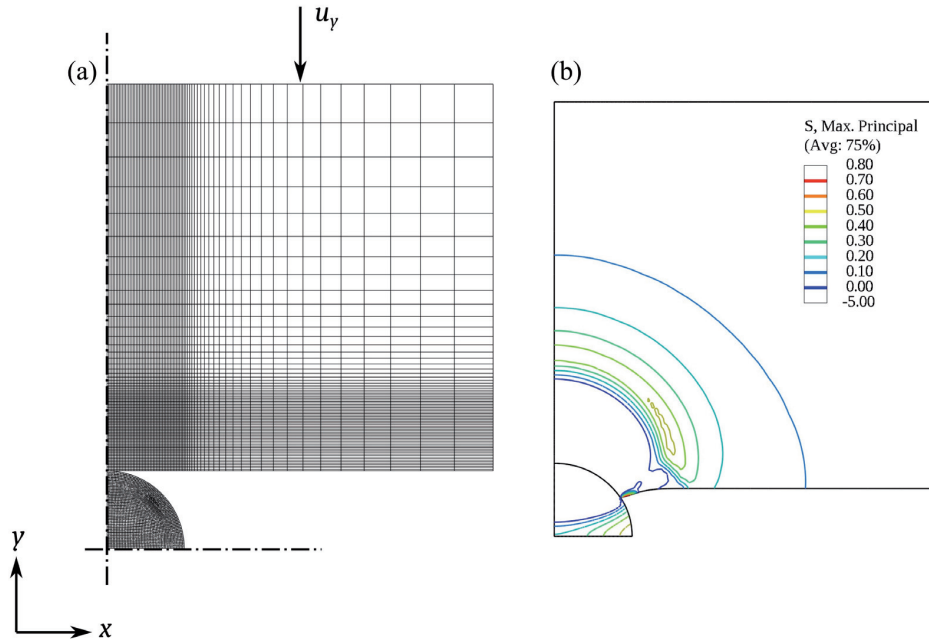


**Figure 2.18 – (a) Sketch of an axisymmetric finite element mesh used for modelling the crushing test of spherical particles by elastic-perfectly-plastic platen. Prescribed vertical boundary displacement  $u_y$  along the top platen surface was used to load the system. (b) Stress field contour map for particle compressed up to contact radius  $a/R \approx 0.85$  for case of frictionless contact between the sphere and the platen.**

In Figure 2.19a we compare the evolution of the normalized first principal stress,  $\sigma_1 \pi R^2 / F$ , in the center and along the equator of a spherical particle as calculated via the Hiramatsu and Oka solution for a particle Poisson's ratio equal to 0.17 (black) and via FEM (coloured lines). Due to the unknown experimental contact friction coefficient, in Figure 2.19a we explore FEM calculations over a range of  $\mu$  values. Although the Hiramatsu and Oka solution generally follows the same trend as the FEM results, the Hiramatsu and Oka solution seems to increasingly underestimate the first principal stress as the relative contact radius increases; up to  $a/R \sim 0.8$ , the first principal stress at the particle equator is underestimated by a factor of  $\sim 1.3$ . The main reason for this discrepancy could originate from the assumption that the contact pressure distribution in the Hiramatsu and Oka treatment is considered to be uniform, while the FEM calculations (Figure 2.19b), although somewhat noisy, indicate that this assumption is approximately valid only for  $a/R < 0.3$ . Still, as can be seen, given the complexity of the problem and the presence of unknown boundary conditions (of friction notably), one can see that the Hiramatsu and Oka solution is a relatively faithful descriptor of the stress state in hard elastic spheres as they are compressed between two elastoplastic platens.

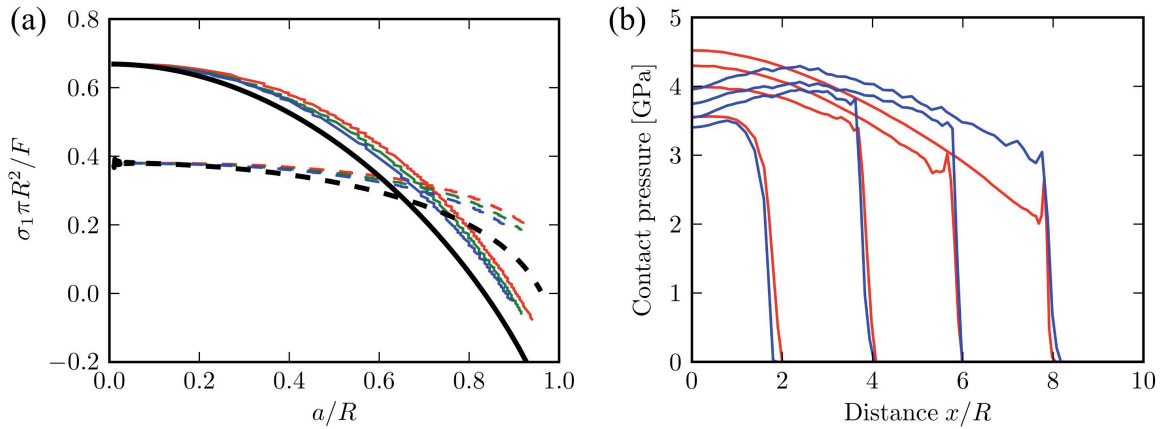


**Figure 2.19 – (a) Normalized first principal stress  $\sigma_1 \pi R^2 / F$  as a function of the relative contact radius  $a/R$  in the center of the sphere (dashed lines) and on the surface equator (solid lines). Solution by Hiramatsu and Oka (Eqs. (2.1a-d), main text) is shown with black lines and results of FEM calculations with coloured lines. FEM calculations are carried out for three values of the contact friction coefficient: 0 (red), 0.1 (green) and 0.3 (blue). (b) Distribution of the contact pressure at contact radii  $a/R = 0.2, 0.4, 0.6$  and  $0.8$  and for the case of contact friction  $\mu = 0$  (red) and  $0.3$  (blue).**

### 2.12.2 Elastic contact with a particle representing an inhomogeneity along the platen-particle contact area

Let us imagine a situation where, during the compression test (as described in the main text of the present paper), a debris particle gets trapped between the fused quartz particle (here considered to have radius  $R=20\mu\text{m}$ ) and the steel platen (see Figure 2.20a). The debris particle is located at some point  $A$  on that portion of the surface of a fused quartz particle that is in direct contact with the platen. Let the perimeter of the contact between the compressed fused quartz particle and the platen be designated as the ensemble of Points  $B$ . The debris particle may be a graphite particle from the colloidal paint used in this study or from other sources, e.g. visible debris that is covering the tested particles (Figure 2.7b, main text). The presence of a debris particle has the potential to locally redistribute the stress; we examine here the question in detail.

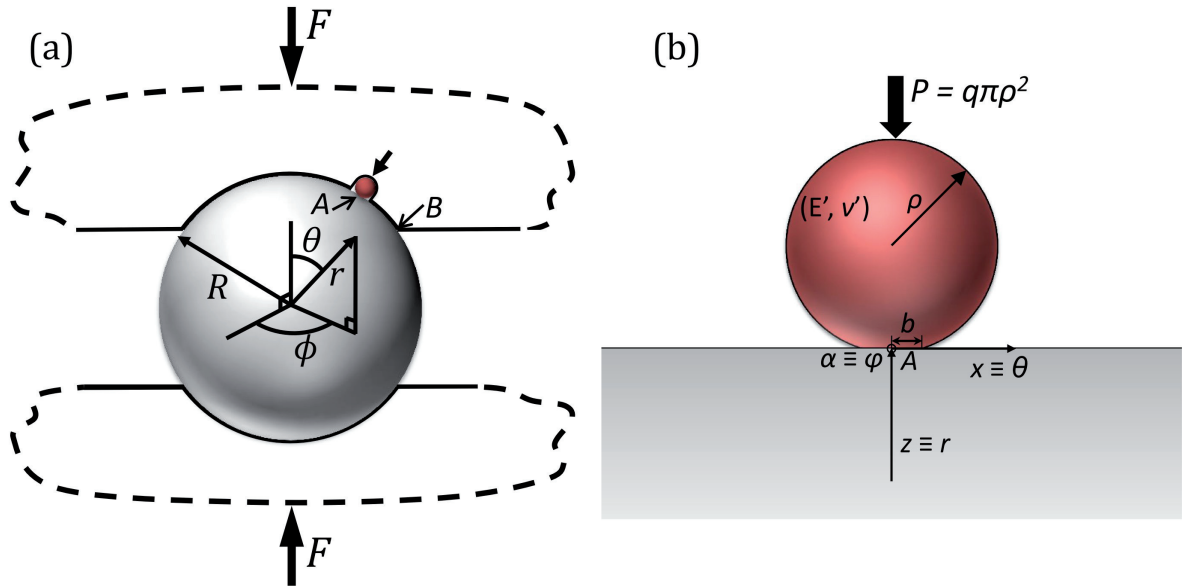


Figure 2.20 – (a) Sketch of a spherical particle of radius  $R$  compressed between two elasto-plastic platens under load  $F$  with a far smaller debris particle present in-between the compressed particle and platen at Spot  $A$ . The contact perimeter between the compressed particle and steel platen is indicated by the letter  $B$ . (b) The debris particle of Young's modulus  $E'$ , Poisson's ratio  $\nu'$  and radius  $\rho$  (red) indents the larger tested particle (grey) under uniaxial compression with a force  $P$ , creating a local elastic contact of radius  $b$ . The local cylindrical coordinate system  $x, z, \alpha$  is at the debris particle plane of symmetry taken to be homothetic with the compressed sphere coordinate system  $\theta, r, \phi$ .

For simplicity, let us consider that both the compressed fused quartz particle and the debris particle are elastic solids of Young's modulus and Poisson's ratio  $E, \nu$  and  $E', \nu'$ , respectively. Also, let us assume that the debris particle is spherical with radius  $\rho$  considerably smaller than that of a fused quartz particle ( $\rho \ll R$ ). In the limit of elastic contact between the two particles, the local situation under loading can be approximated as the indentation of a debris sphere into the fused quartz half-space, as described by Hertz's theory (see sketch in Figure 2.20b).

The stress field equations for the Hertzian indentation can be found for example in [334]; in the cylindrical coordinate system  $(x, z, \alpha)$  it has four non-zero components;  $\sigma_x, \sigma_z, \sigma_\alpha, \sigma_{zx}$ . The highest tensile stress attained due to indentation of a debris particle will be located on the fused quartz particle surface where the shear component  $\sigma_{zx}$  vanishes; the remaining three normal stress components on the surface then automatically become the principal stresses, of which only  $\sigma_x$  is positive with its peak value located at the perimeter of the contact characterized by the radius  $b$  (see Figure 2.20b). Because the debris particle is located in the contact zone between the steel platen and the fused quartz particle (point  $A$ , Figure 2.20a), and is compressed by pressure  $q$ , the force  $P$  with which the debris is pressed against the fused quartz is approximated here as  $P \approx q\pi\rho^2$  (somewhat higher values may obtain; however, this should give the right order of magnitude). With this, the only relevant (positive) Hertzian stress component  $\sigma_x$  as a function of a coordinate  $x$  can be easily calculated. A few examples of normalized  $\tilde{\sigma}_x(x) = \sigma_x(x) \cdot \pi R^2 / F$  for different debris particle sizes and their elastic parameters at arbitrary point  $A$  are shown in Figure 2.21 with colour lines.

For a fused quartz particle compressed by the platens, this local  $\sigma_x$  will superimpose onto the Hiramatsu and Oka stress field. Because the shear component  $\sigma_{r\theta}$  of the Hiramatsu and Oka solution also vanishes on the surface of a fused quartz particle, from the remaining three principal components,  $\sigma_\theta$ ,  $\sigma_r$  and  $\sigma_\phi$ , only  $\sigma_\theta$  is worth considering, because only  $\sigma_\theta$  can become significantly positive (tensile) after superposition with  $\sigma_x$ . Note that, at Point  $A$  of the contact in the plane of symmetry of the debris particle, the local cylindrical system  $(z, x, \alpha)$  is homothetically related to the global coordinate system  $(r, \theta, \phi)$  (see Figure 2.20a), which means that the stress components  $\sigma_z$  and  $\sigma_r$ ,  $\sigma_x$  and  $\sigma_\theta$  and  $\sigma_\alpha$  and  $\sigma_\phi$ , are directly additive; however, because  $\sigma_r$ ,  $\sigma_\phi$ ,  $\sigma_z$  and  $\sigma_\alpha < 0$ , only the addition of  $\sigma_x$  and  $\sigma_\theta$  can give a positive (tensile) value. Normalized Hiramatsu and Oka stress component  $\tilde{\sigma}_\theta = \sigma_\theta \cdot \pi R^2 / F$  particle with radius  $R=20\mu\text{m}$  compressed with relative contact radius  $(a/R) = 0.7$  and for Meyer's law describing HV600 platen is traced in Figure 2.21 as the black line.

From Figure 2.21 it is evident that, if the debris particle at point  $A$  is located far away from the perimeter point  $B$  (the distance between points  $A$  and  $B$  is  $|\overline{AB}| > \rho$ ), then the compressive stress  $\tilde{\sigma}_\theta$  is so high that even indentation by a very stiff debris particle (with properties similar to alumina) can not locally raise the total stress,  $\tilde{\sigma}_\theta + \tilde{\sigma}_x$ , along the fused quartz surface to make it positive (tensile). High tensile stress on the fused quartz particle surface is only possible when the debris particle is located very near the contact perimeter at  $B$ , i.e.  $|\overline{AB}| \approx \rho$ , where  $\tilde{\sigma}_\theta$  is steeply rising to a value that is close to zero (Figure 2.21, black line); only at this relative position will the local stress  $\tilde{\sigma}_x$  induce the total stress on the fused quartz surface to be tensile. If this happens, we find that for any debris particle size or debris elastic properties, the total stress at point  $B$  is  $\tilde{\sigma}_\theta + \tilde{\sigma}_x \approx 0.3$ , which is comparable to the peak stress at the equatorial plane for the investigated relative contact radius  $(a/R) = 0.7$  (see Figure 2.2, main text). The volume of the stressed material around the Hertzian indentation is also much smaller than the volume of material exposed to tension around the equator. Hence, failure from tensile stresses along the equator will be a far more probable outcome than failure induced by a small debris particle.

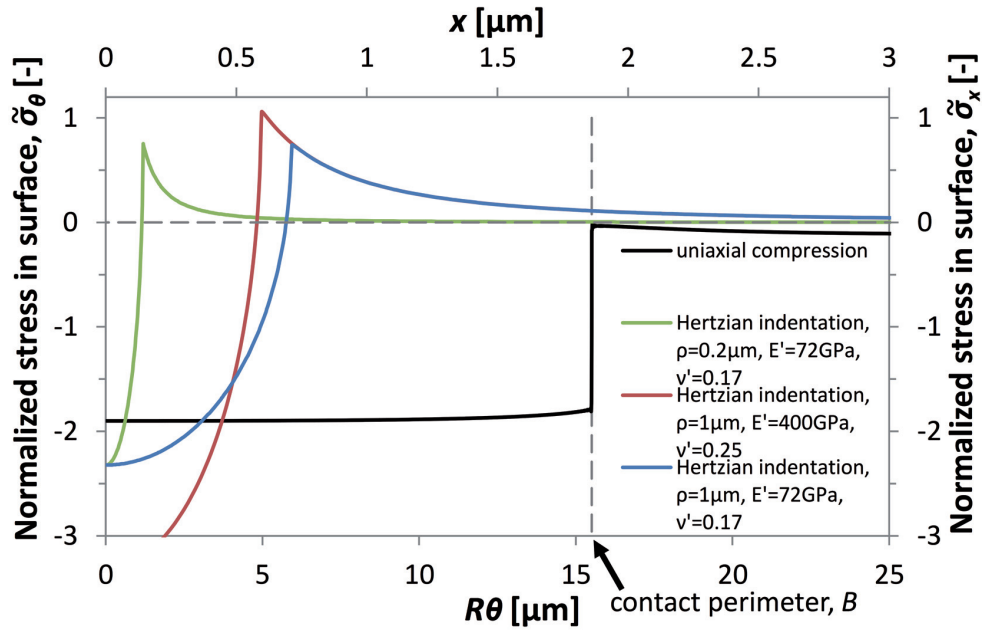


Figure 2.21 – Distribution of the normalized stress  $\sigma_\theta$  along the surface of a compressed fused quartz particle due to (black) uniaxial compression with relative contact radius  $(a/R)=0.7$  and platen with Meyer's constants representing HV600 steel platen, (green) a Hertzian indentation stress along the surface of fused quartz particle by a debris particle with relative radius  $\rho = 0.2\mu m$ , elastic modulus of 72 GPa and Poisson's ratio 0.17, (red) a Hertzian indentation stress along the surface of fused quartz particle by a debris particle with relative radius  $\rho = 1\mu m$ , elastic modulus of 400 GPa and Poisson's ratio 0.25 and (blue) a Hertzian indentation stress along the surface of fused quartz particle by a debris particle with relative radius  $\rho = 1\mu m$ , elastic modulus of 72 GPa and Poisson's ratio 0.17. The dashed vertical line represents the contact perimeter defined by the compressed particle-platen contact radius  $a$ .



# Chapter 3 Meridian crack test strength of plasma-sprayed amorphous and nanocrystalline ceramic microparticles

## 3.1 Disclaimer

This chapter was submitted as an article in a scientific journal with the open-access (CC BY 4.0) licence and its provisional bibliographic reference is given below. The preprint version of the article is presented here with its Introduction section abbreviated to avoid repetition of what was already mentioned in Chapter 1 of this thesis (extracts, including a few literal reproductions of full paragraphs of this article's Introduction, are included in Chapter 1 of this thesis). The candidate, here-with V.P., designed the experiment under supervision of Andreas Mortensen (A.M.). Most of the uniaxial compression tests were carried out by two undergraduate students Grégory Riesen (G.R.) and Romain G. Martin (R.G.M.) under supervision of V.P. in the framework of their respective semester projects at EPFL. V.P. carried out additional experiments to improve statistical significance of the data. V.P. carried out most of other experimental work, specifically fractography, and the microcantilever machining and testing. V.P. analysed the final set of data and interpreted results. The writing of the manuscript was mainly by V.P.

Pejchal, V., Fornabaio, M., Žagar, G., Riesen, G., Martin, R. G., Medřický, J., Chráska, T., Mortensen, A.: *Meridian crack test strength of plasma-sprayed amorphous and nanocrystalline ceramic microparticles*. Submitted, 2017.

## 3.2 Introduction

It has been widely demonstrated that nanostructured ceramics in both bulk and fiber form can exhibit exceptional mechanical properties [28,99,335–340]. It should, therefore, be possible to produce nanostructured microparticles with strengths approaching those of today's engineering fibers. One way to produce such particles is to use thermal spraying techniques in which the feedstock material is introduced into a high temperature jet where it is melted and propelled in the form of droplets towards a fluid quenching medium. The resulting high cooling rates on the order of  $10^6$  K/s can be advantageously used to prepare amorphous and nanostructured microscopic particles of ceramics that are not strong glass formers [111,112]. In the present work we test such particles for strength, using the meridian crack testing method, to show how the intrinsic flaw-controlled strength of plasma-

sprayed ceramic micro-particles based on the  $\text{Al}_2\text{O}_3\text{-ZrO}_2\text{-SiO}_2$  ternary system can be probed, and improved.

### 3.3 Materials and methods

#### 3.3.1 Amorphous Eucor powder

The powder feedstock material from the ternary system  $\text{Al}_2\text{O}_3\text{-ZrO}_2\text{-SiO}_2$  is based on the bulk cast ceramic material called Eucor<sup>TM</sup>. The Eucor material has a near-eutectic composition, which was confirmed by semi-quantitative X-ray fluorescence; the powder feedstock contained 46.5 wt.% of  $\text{Al}_2\text{O}_3$ , 34.5 wt.% of  $\text{ZrO}_2$ , 14.5 wt.% of  $\text{SiO}_2$ , and 4.5 wt.% of other oxides (of alkali and alkaline earth metals). It was previously reported that the near-eutectic composition of the material facilitates formation of amorphous phases when the molten material is rapidly solidified [341,342].

Fully crystalline, crushed and sieved, powder feedstock was plasma sprayed in air at atmospheric pressure using the hybrid water-stabilised plasma torch WSP-H 500 (IPP CAS, Prague) operating at 160 kW power. The powder was injected into the plasma jet, where individual particles were melted and thus turned into spheres. To retain the spherical shape of the particles while ensuring rapid solidification, sprayed molten particles were collected in a vessel filled with a liquid quenching medium which was positioned 300 mm downstream from the plasma torch exit nozzle. Saturated water solution of boric acid, cooled down to 0 °C and mixed with ice, was used as the quenching medium for its high heat extraction ability. After spraying, the collected powder was rinsed with clean water to remove the residue of boric acid and then dried in an oven at 150 °C. This process resulted in fully amorphous powder of nearly spherical particles.

#### 3.3.2 Nanostructured Eucor powder

To produce nanocrystalline particles, the as-sprayed powder was annealed in air at 1300°C for 1h, with heating and cooling rates of 5 °C/min. Crystalline phases were analyzed by X-Ray Diffraction (XRD) measurements carried out using PANalytical X'Pert Pro MPD diffractometer with a  $\text{Cu K}_\alpha$  radiation. Scanning was performed in the 10-90° 2 $\theta$  range using a step size of 0.0170° and time per step 29.210 s. Crystalline phase quantification was performed by Rietveld refinement using the X'Pert High Score Plus software with rutile as an external standard [343]. Scanning Electron Microscopy (Zeiss Merlin, Oberkochen, Germany) was used to investigate the microstructure of as-received and annealed Eucor particles. To this end, particles were dispersed in an epoxy resin made by mixing Bisphenol A diglycid ether (DGEBA, Sigma Aldrich) with Diethylenetriamin 99% (DETA Sigma Aldrich, 99%) which was then hardened to create a composite. This composite was then polished down to 1  $\mu\text{m}$  polishing medium particle size and observed along its polished surface. Local chemical analyses were conducted by means of Energy Dispersive X-Ray spectrometry (EDX) with an electron acceleration voltage of 10 kV. About 20 random particles were analyzed in order to investigate possible variation in composition from particle to particle.

### 3.3.3 The meridian crack test

To measure the tensile strength of the plasma sprayed Eucor particles we have employed the Meridian Crack Test method; its principle and theoretical background are published elsewhere [344]. To perform the uniaxial compression tests we used age hardened AISI 630 steel, and AISI W1 steel in two different heat treatment conditions. This produced three different sets of platens namely (i) quenched AISI W1 steel tempered at 250 °C for 90 minutes (ii) quenched AISI W1 steel tempered at 320 °C for 90 minutes and (iii) AISI 630 steel age hardened at 480 °C for 60 minutes. The resulting average Vickers hardness of the three platen materials measured with a FM-300 (Future-tech Corp., Kawasaki, Japan) using a 0.5 kgf load were HV 710, 620 and 440 for materials (i), (ii) and (iii) respectively. The three platen materials are hereafter designated as HV700, HV600 and HV450, respectively.

Uniaxial compression tests were performed on individual particles 25-35  $\mu\text{m}$  in diameter using a custom-built instrumented compression apparatus equipped with 10 N load cell and interchangeable conical tips made of the three platen materials. The cone tips were polished, to have an approximately 300  $\mu\text{m}$  flat-end tip diameter serving as the upper platen. As the bottom platen, disc-shaped substrates  $\sim 10$  mm in diameter and  $\sim 2$  mm thick were used. Both tips and substrates were ground and polished using diamond suspensions down to 1  $\mu\text{m}$  diamond particle size. Along the substrate surface a layer a few micrometres thick of soft colloidal graphite paint (Pelco®, Redding, CA, United States) was applied; its role was to retain the broken particle pieces in place after testing. Additionally, an adhesive tape (scotch-tape type) was applied and removed from the carbon-coated substrate. This left a very thin (several times thinner than the graphite paint layer) and scattered film of the tape adhesive, which helped to hold particles in place during manipulation of the particle-covered substrates prior to testing.

Individual particles were deposited using a miBot<sup>TM</sup> (Imina Technologies SA, Lausanne, Switzerland) remote controlled microarm equipped with sharp tungsten needle, using the following procedure: (i) by approaching with tungsten needle over the selected particle the particle adhered to the needle due to electrostatic forces, (ii) the particle attached to the tip of the needle was then transferred over the carbon-coated substrate at locations featuring an adhesive film layer, which then held the particle in place. To measure its diameter  $2R$ , each particle was imaged top-down under an optical microscope (Olympus Vanox model AHMT, Olympus Corporation, Tokyo, Japan) equipped with a digital camera system. Additional diameter measurements on a subset of the particles was also conducted using a scanning electron microscope (SEM) (Zeiss Merlin, Oberkochen, Germany). The optical microscopy diameter measurements were found to be within 5% of electron microscopy measurements.

Particles were compressed by displacing the flat-end conical tip using a constant displacement-rate of 1  $\mu\text{m/s}$ . The test was interrupted either when a drop in load was recorded or, in case of particularly strong particles that embedded completely into the platens, when the two platens contacted. Relative error on load readings was below 1%. Each flat-end conical tip was used to test approximately 5 particles before it was exchanged, so that each particle be compressed by a new, flat and polished, portion of the tip surface. Indents left by tested particles in the flat surface of the conical tip were

subsequently imaged using an optical microscope (Zeiss<sup>TM</sup> Axioplan 2, Oberkochen, Germany) equipped with a digital camera to measure the contact radius at the moment of failure,  $a$ , with an estimated relative error of 5 %. Tested fractured particles were then imaged in the SEM in order to identify the strength-limiting defects.

## 3.4 Results

### 3.4.1 Eucor particles microstructure

The plasma spraying technique that was used to produce the particulate Eucor material resulted in particles of high sphericity and with a broad size range, particles having diameter ranging from a few micrometers to several tens of micrometers. To check that the particle shape was close to that of a sphere, 2230 polished random as-sprayed particle cross-sections were imaged via SEM and fitted to an ellipse. It was found that the average ellipse aspect ratio, defined as the ratio of its minor to the major axes, was 0.92. A small fraction (<5%) of those particles exhibited aspect ratio values below 0.7; these particles furthermore contained crystalline regions, which were observable in the SEM along the polished cross-sections. It is thus likely that those 5% of the particles were not completely melted during the plasma-spraying process.

Scanning electron microscopy (SEM) micrograph of as-sprayed Eucor after sieving through a 45  $\mu\text{m}$  pore size sieve is shown in Figure 3.1a. XRD analysis (Figure 3.1b) of as-sprayed Eucor particles shows that they are almost completely amorphous with a relative amorphous phase content of 85wt% according to Rietveld refinement. The SEM micrograph in Figure 3.2a displays the cross-section of a typical spherical as-sprayed particle with no apparent chemical contrast, indicating a high-homogeneity of the composition within the particle. Compositional homogeneity within this particle was confirmed with EDX analysis performed at different spots of the particle cross-section. EDX performed on 20 randomly selected particles revealed some variation in composition from particle to particle, with average values and standard deviations across the particles of the chemical elements equal to  $(20.0 \pm 1.3)$ ,  $(6.9 \pm 0.5)$  and  $(3.2 \pm 1.2)$  at% for Al, Zr and Si, respectively, and oxygen atoms representing the remainder.

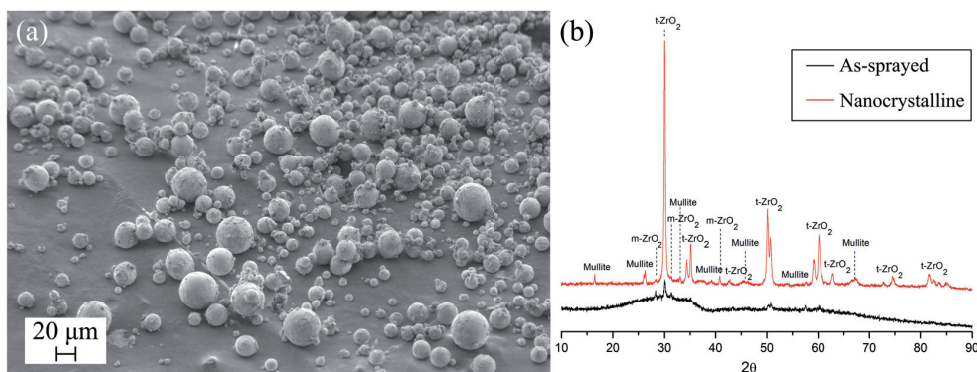


**Figure 3.1 – (a) Overview of as-sprayed Eucor particles after sieving through 45  $\mu\text{m}$  sieve. (b) XRD pattern of (black) as-sprayed and (red) annealed powder. t = tetragonal, m = monoclinic.**



After annealing particles at 1300 °C for 60 minutes the powder becomes fully crystalline, as shown by XRD analysis (Figure 3.1b) revealing mullite, tetragonal and monoclinic zirconia as primary phases. These results are in good agreement with XRD analysis of plasma-sprayed coatings prepared from similar precursor material [345]. Phase quantification by Rietveld refinement established contents of 60wt% tetragonal zirconia, 28wt% mullite, 4wt% monoclinic zirconia and a remaining amorphous phase representing 8wt%. The microstructural observations in SEM (Figure 3.2b-c) revealed grains of two phases with an apparent chemical contrast; (dark-gray) mullite and (light-gray) grains of tetragonal and/or monoclinic zirconia. Two main microstructural morphologies were observed: (i) particles of very fine microstructure with equiaxed grains a few nanometers to a few tens of nanometers in size (Figure 3.2b) and (ii) particles of coarser microstructure featuring a mixture of equiaxed and needle-like grains from a few tens of nanometers to a few hundred nanometers in size (Figure 3.2c). In all cases mullite grains appeared as the matrix forming phase. EDX analyses performed on 20 polished nanocrystalline particles showed similar variations in chemical composition among particles as were found within the as-sprayed powder: averaged values and corresponding standard deviations for Al, Zr and Si chemical elements were  $(19.4 \pm 1.1)$ ,  $(7.4 \pm 1.4)$  and  $(3.4 \pm 1.7)$  at%, respectively. Annealing of the powder did not lead to a formation of evident flaws (such as microcracks that might be caused by anisotropic or differential thermal expansion of the several phases present). Micropores were on the other hand readily observed in numerous particle cross-sections of both amorphous (Figure 3.2a) and nanocrystalline particles.

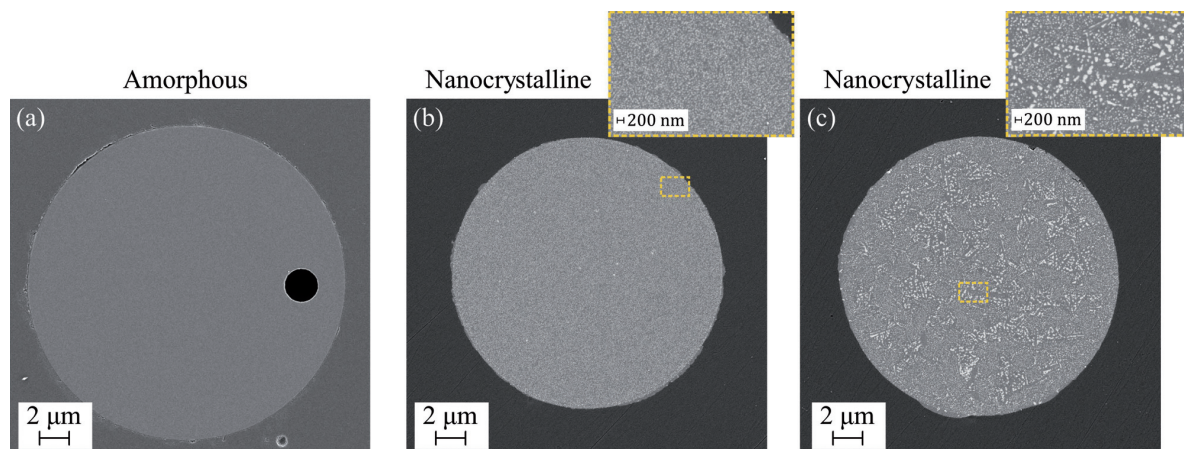


**Figure 3.2** – (a) SEM micrograph of polished cross-section of as-sprayed amorphous Eucor particles. Panel (a) shows an amorphous particle. Panels (b) and (c) are micrographs of nanocrystalline Eucor particles obtained after 1h annealing at 1300°C revealing nanostructured grains of (gray) mullite and (light) tetragonal and monoclinic zirconia. A micropore is evident in the cross-section of the amorphous particle (a).

### 3.4.2 Uniaxial compression

In total, fifty-four (54) amorphous Eucor particles were tested using HV600 (33 particles) and HV450 (21 particles) platens. Of the nanocrystalline Eucor, sixty-two (62) particles were tested using HV700 (40 particles) and HV450 (22 particles) platens. The average diameter of particles selected for testing

was 29.7  $\mu\text{m}$  and 29.9  $\mu\text{m}$  and ranged between 23.1-34.7  $\mu\text{m}$  and 24.5-35.5  $\mu\text{m}$  for amorphous and nanocrystalline particles, respectively.

The results are summarized in Figure 3.3 where the force at failure,  $F_{\text{max}}$ , normalized by the particle cross-sectional area  $\pi R^2$  is plotted against the relative particle-platen contact radius  $a/R$ , where  $a$  is the contact area radius and  $R$  that of the particle. Particles that did not fail during the test and hence survived until platens contacted ( $a/R \approx 1$ ) are indicated with a symbol at the far right of the figure. For these particles, the value of  $F_{\text{max}}/(\pi R^2)$  is not representative, since the measured force when  $a/R \approx 1$  is affected by platens being in contact; therefore, a figurative value was selected to visualize these events in the figure to its far right.

The plot was used to determine the elasto-plastic behavior of each platen material (HV700, HV600, and HV450) as described by the empirical Meyer's law:  $F_{\text{max}}/(\pi R^2) = k(a/R)^n$  where  $k$ ,  $n$  are the Meyer's law parameters. Fitting the data, the estimated Meyer's law parameters were  $k = 8150$ ,  $n = 2$  for HV700 platens,  $k = 5900$  and  $n = 1.8$  for HV600 platens, and  $k = 3990$ ,  $n = 1.7$  for HV450 platens. Note that data for particles that did not break during the uniaxial compression until platens contacted were not considered for platen Meyer's law determination (due to lack of precision in the force when  $a/R \approx 1$ , as already mentioned above).

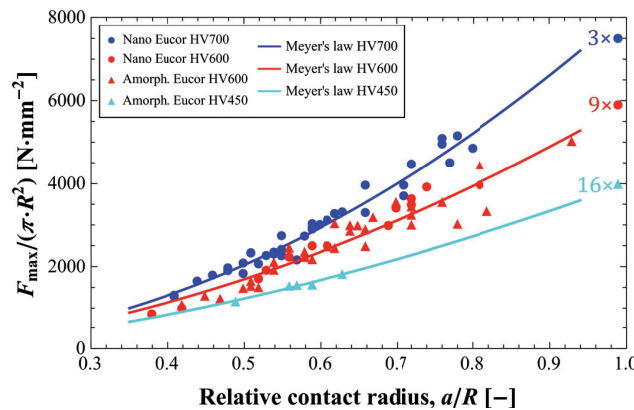


**Figure 3.3** – Experimentally measured values of the critical force at failure normalized by the cross-sectional area of the tested particle,  $F_{\text{max}}/(\pi R^2)$  for (triangles) amorphous and (circles) nanocrystalline Eucor particles tested with (blue) HV700, (red) HV600, and (cyan) HV450 platens, respectively. Solid lines represent best fit with the power-law function  $f(a/R) = k(a/R)^n$  representing the platen material Meyer's law. Values of the fitted parameters were (blue)  $k = 8150$ ,  $n = 2$  for HV700 platens, (red)  $k = 5900$  and  $n = 1.8$  for HV600 platens, and (cyan)  $k = 3990$ ,  $n = 1.7$  for HV450 platens.

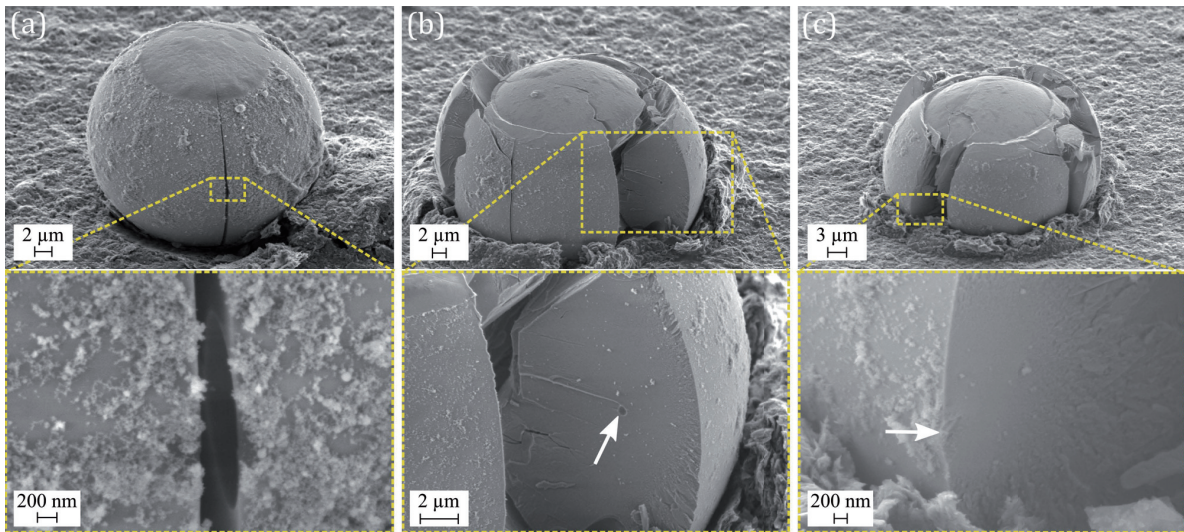
### 3.4.3 Fractography

Figure 3.4 and Figure 3.5 show representative specimens of tested amorphous and nanocrystalline Eucor particles, respectively. As seen, the soft colloidal graphite layer was effective in retaining pieces of broken particles after the failure and for which flaws present on one of the meridian cracks were observed. Particles were typically broken into several pieces indicating initiation and growth of secondary cracks, likely due to the sudden release of stored elastic energy after initial crack formation. The number of fragments typically scaled with the maximum load at which the particle broke. Only



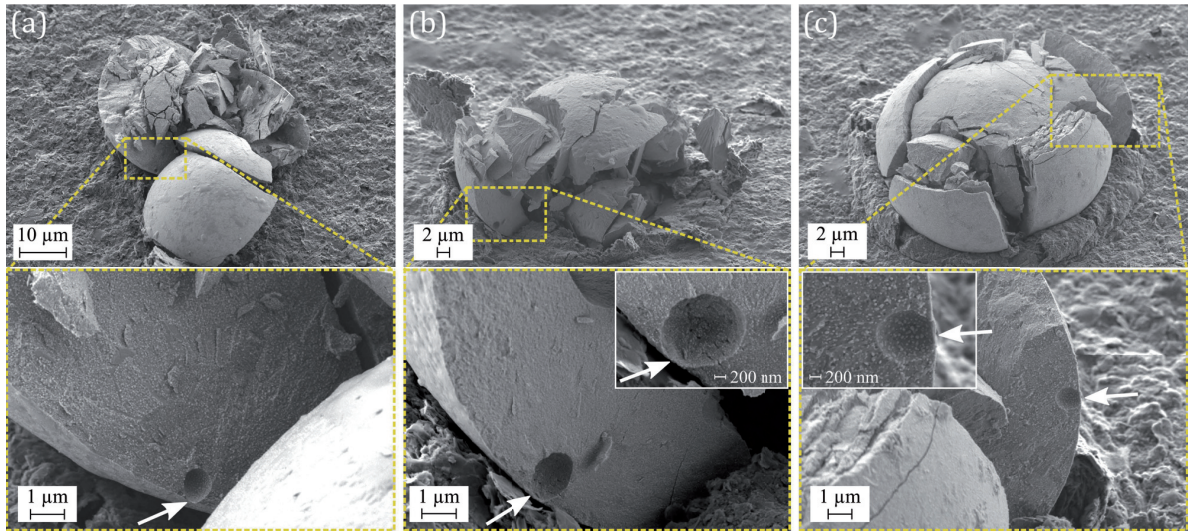
in the case when particles broke for low loads were one or few meridional cracks observed with the rest of the particle intact.

Figure 3.4a shows a particle for which only one meridional crack was observed after failure, with an evident surface pore present. Given that the first principal stress along the surface is the hoop stress,  $\sigma_{\phi\phi}$ , where  $\phi$  is the azimuthal angle and peaks at the equatorial plane, the observed pore on the meridional crack fracture surface close to the equatorial plane is the likely cause of failure at low load of this particle (although it broke at  $a/R$  of Domain II, see Discussion).



**Figure 3.4** – SEM images of amorphous Eucor particles after uniaxial compression, illustrating particles for which distinct flaws were observed at one of the meridional cracks. (a) One meridional crack was observed for this particle, which broke at relatively low load. A pore of diameter  $\approx 1 \mu\text{m}$  was observed just below the surface on the meridional crack surface. (b) The mirror-mist and hackle fractographical features point to a subsurface pore as the origin of failure. (c) shows the only particle fracture surface along which a flaw other than a pore was identified as the origin of the failure, this being a surface inclusion. The fracture surface of amorphous Eucor particles is typically very smooth and featureless in the “mirror” region close to the origin of failure.

Other examples of pores that one can trace as likely origins of failure for amorphous and nanocrystalline Eucor particles are shown in Figure 3.4b and Figure 3.5a-c, respectively. Distinct mirror-mist and hackle features surrounding pores are located on one of the meridional cracks close to the peak of the surface stress, making these pores the likely cause of failure of those particles. A surface or subsurface pore was determined as the failure origin in all investigated particles when a clear mirror-mist-hackle pattern could be observed on one of the meridional cracks, with one exception shown in Figure 3.4c. For this particle, fractographical features suggest that a surface inclusion was the failure origin.



**Figure 3.5** – SEM images of nanocrystalline Eucor particles after uniaxial compression. Panels (a), (b), and (c) illustrate three different particles for which mirror-mist-hackle patterns surrounding a pore present at one of the meridional crack fracture surfaces can be observed. In each case a surface pore was identified as the origin of failure. The fracture surface exhibits greater roughness compared to amorphous particles (Fig. 3.4). The grain structure is revealed on fracture surfaces, showing transgranular fracture of mullite grains (gray) and intergranular decohesion of zirconia grains (bright) close to the fracture initiation point (panel (c)).

The fracture surface of amorphous (Figure 3.4a-c) Eucor particles was very smooth and featureless in the mirror region of the fracture surface. As expected, fracture surfaces of nanocrystalline Eucor particles exhibited higher roughness compared to amorphous particles. From higher magnification micrographs (Figure 3.5c) one can observe the grain structure of nanocrystalline particles. A closer look at the pore surface in Figure 3.5b reveals the presence of microcracks along the pore free surface. Close to the failure origin a mixed trans- and inter-granular crack path can be observed (Figure 3.5c). Grain cleavage is dominant for mullite grains (dark-gray) while intergranular decohesion, leaving protruding grains and pore-like features along the fracture surface, is evident for zirconia grains. This indicates the presence of effective crack deflection by zirconia grains.

## 3.5 Discussion

### 3.5.1 The meridian crack test evaluation

A solution for the stress distribution within a linear elastic sphere diametrically compressed between a pair of platens was first given by Hiramatsu and Oka [212], and was recently refined using finite element calculations in Ref. [346]. During the compression test, the relative contact radius  $a/R$  gradually increases and the peak of the tensile first principal stress, considered here as the fracture stress, is located for large enough relative contact radius ( $a/R > 0.3$ ) either in the center of the sphere,  $\sigma_{1c}$  or in the particle surface equatorial belt,  $\sigma_{1s}$  [344]. The tensile first principal stress in the sphere center and equatorial belt can be expressed as

$$\sigma_{1c} = \frac{F}{\pi R^2} \cdot \tilde{\sigma}_{1c} \left( \frac{a}{R}, \nu, \mu \right) \quad (3.1)$$

$$\sigma_{1s} = \frac{F}{\pi R^2} \cdot \tilde{\sigma}_{1s} \left( \frac{a}{R}, \nu, \mu \right) \quad (3.2)$$

respectively, where  $F$  is the compressive force applied to the particle,  $R$  is the particle radius and  $\tilde{\sigma}_{1c}, \tilde{\sigma}_{1s}$  are adimensional functions of the relative contact radius  $a/R$ , where  $a$  is the radius of the projected particle-platen contact area,  $\nu$  is particle's Poisson's ratio, and  $\mu$  is the friction coefficient in the particle-platen contact. The adimensional functions  $\tilde{\sigma}_{1c}, \tilde{\sigma}_{1s}$  for different values of the three variables can be found in [346]. Details of the friction and Poisson's ratio estimation are given in the Supplementary Information (Section 3.7.1). The (kinematic) friction coefficient was found to be approximately  $\mu = 0.28$ . The particle Poisson's ratio was estimated to be approximately equal  $\nu = 0.28$  for both amorphous and nanocrystalline Eucor particles (that  $\nu$  and  $\mu$  are equal is a coincidence). For values  $\nu = 0.28$  and  $\mu = 0.28$  functions  $\tilde{\sigma}_{1c}, \tilde{\sigma}_{1s}$  from [346] read

$$\tilde{\sigma}_{1c} = 0.623 + 0.062 \left( \frac{a}{R} \right) - 0.837 \left( \frac{a}{R} \right)^2 - 0.202 \left( \frac{a}{R} \right)^3 + 0.508 \left( \frac{a}{R} \right)^4 - 0.409 \left( \frac{a}{R} \right)^5 \quad (3.3)$$

$$\tilde{\sigma}_{1s} = 0.429 - 0.036 \left( \frac{a}{R} \right) + 0.189 \left( \frac{a}{R} \right)^2 - 1.092 \left( \frac{a}{R} \right)^3 + 1.563 \left( \frac{a}{R} \right)^4 - 0.903 \left( \frac{a}{R} \right)^5 \quad (3.4)$$

Knowing the platen empirical elasto-plastic indentation behaviour as described by Meyer's law (Figure 3.3) and combining this with Eqs. (3.1)-(3.2) one can calculate and plot *average* stress trajectories in particles compressed between platens of a given steel as a function of the relative contact radius:

$$\sigma_{1c} = k \cdot \left( \frac{a}{R} \right)^n \cdot \tilde{\sigma}_{1c} \quad (3.5)$$

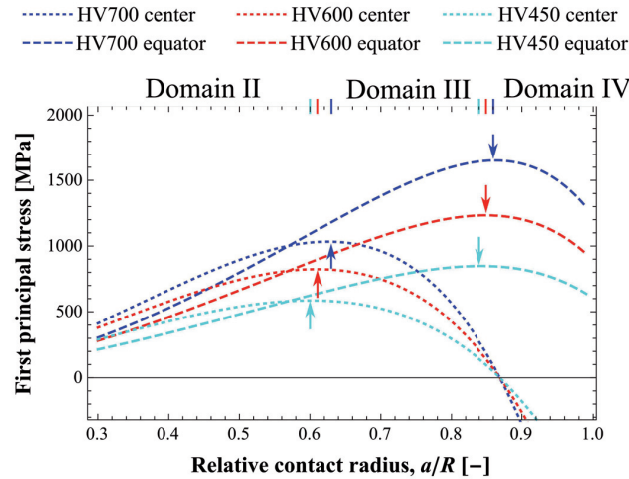
$$\sigma_{1s} = k \cdot \left( \frac{a}{R} \right)^n \cdot \tilde{\sigma}_{1s} \quad (3.6)$$

Figure 3.6 presents the evolution of the first principal stress at the center, and along the surface equatorial belt of a particle versus the relative contact radius, with  $\nu = 0.28$  and  $\mu = 0.28$  during uniaxial compression with HV700, HV600 and HV450 steel platens. As described in Ref. [344] four different domains can be defined:

- (i) the contact stress dominated Domain I starts from the beginning of the test ( $a/R = 0$ ) and extends until  $a/R$  is approximately equal to 0.3 (not plotted here as no particle failed in this domain),
- (ii) Domain II starts at  $a/R \approx 0.3$  and is a region where tensile stress peaks in the central portion of the particle. As compression continues,  $a/R$  increases and central and surface stresses increase simultaneously;
- (iii) the stress in the particle centre then peaks, leading to a transition into Domain III where it is only within the surface equatorial belt that the tensile stress continues to increase as compression progresses; elsewhere stress values have started to decrease;



(iv) finally, Domain IV is characterized by tensile stresses decreasing everywhere in the compressed sphere, including along the surface equatorial belt.



**Figure 3.6 – Average (tensile) stress trajectories during uniaxial compression of spherical particles with Poisson’s ratio 0.28, particle-platen friction coefficient 0.28 and tested with (blue) HV700, (red) HV600, and (cyan) HV450 platens calculated using Eqs. (3.5)-(3.6). The stress trajectories are plotted for (dotted) the center of the particle and (dashed) the particle surface equator versus the relative contact radius. Arrows indicate maxima for each stress trajectory and as such represent boundaries (in terms of  $a/R$ ) between different Domains.**

The boundary between Domains II and III was here defined as the moment (in terms of  $a/R$ ) when the first principal stress in center reaches its maximum value, i.e.  $\frac{d\sigma_{1c}}{d(a/R)} = 0$ . In our previous work with fused quartz particles [344], the boundary between Domain II and III was defined as the crossover between the center and surface equator stress trajectories. With particles of higher Poisson ratio compared to that of fused quartz, such as the nanocrystalline Eucor tested here, the crossover between the central and equator stress is located slightly before the central stress reaches its maximum value (see Figure 3.6).

While tensile stresses increase simultaneously both in central and surface portion (Domain II) particle failure may occur either in the particle center or along its surface, with the central and surface stress values differing by up to roughly 40%. If a particle breaks within Domain III, i.e., after the central stress reaches its peak, then the only region where the tensile stress is still increasing is around its equatorial belt and the surface equatorial stress;  $\sigma_{1s}$ , can therefore be considered as the particle failure stress.

One can observe failure events in Domain III only for particles that are sufficiently strong to enter it. Failure events in Domain III are therefore, in the language of survival analysis, left-truncated (only values for the strength of particles stronger than a certain value can be observed). The left-truncation value  $\sigma_T$  depends on the platen material and can be estimated from the curves of the average stress trajectories (Figure 3.6) as the stress value at which Domain III begins. There is, however, scatter in data points used to derive Meyer’s law (Figure 3.3). For this reason, some of the measured surface strength values (computed knowing  $a/R$  from the measured load) of data points situated, according

to the value of  $a/R$ , in Domain III may be slightly lower than the  $\sigma_T$  value determined from the average stress trajectory curves (Figure 3.6). Therefore, the lower of the two values determined as (i) the surface equatorial stress  $\sigma_{1s}$  for the  $a/R$  value at which  $\frac{d\sigma_{1c}}{d(a/R)} = 0$  from the average stress trajectory curves and (ii) the lowest actual measured strength value ascertained to be, by its value of  $a/R$ , in Domain III (lowered by a negligible value namely 1 MPa as the observed value cannot be equal to the left-truncation value) was taken as  $\sigma_T$ . To observe failure events of weaker particles in Domain III (i.e. to decrease the left-truncation value) one has to decrease the hardness of the platens used.

If a particle is strong enough to (in the language of survival analysis) *survive* the maximum attainable stress in the equatorial belt of Domain III, it enters Domain IV. The boundary between Domains III and IV is defined as value of  $a/R$  at which the tensile stress in the surface equatorial belt reaches its maximum, i.e.  $\frac{d\sigma_{1s}}{d(a/R)} = 0$ . Particles that have entered Domain IV cannot in principle break anymore since, according to mechanical analysis, the tensile stress decreases thereafter everywhere in the sphere. One therefore only knows a lower-bound of the strength of such particles; in Survival analysis terminology – the stress at this transition is a *right-censoring* stress value,  $\sigma_C$ . This value is found as the maximum on the average equatorial stress trajectory curve, for a given platen material (Figure 3.6).

The  $a/R$  values representing boundaries between Domains are indicated in Figure 3.6 with arrows and are listed in Table 3.1. The left-truncation and right-censoring values for each platen-particle material combination used in this work obtained from Figure 3.6 and from experimental data points (Figure 3.7) are also listed in Table 3.1.

Table 3.1 – Values of the relative contact radius  $a/R$  at the beginning and end of Domain III for tested amorphous and nanocrystalline Eucor particles ( $\nu = 0.28$ ,  $\mu = 0.28$ ) and the tensile stress values identified as the left-truncation,  $\sigma_T$ , and right-censoring,  $\sigma_C$  values.

Platen material	Domain III start		Domain III end	
	$a/R$	$\sigma_T$ (MPa)	$a/R$	$\sigma_C$ (MPa)
<b>HV700</b>	0.63	1030	0.86	1650
<b>HV600</b>	0.61	820	0.85	1230
<b>HV450</b>	0.60	590	0.84	850

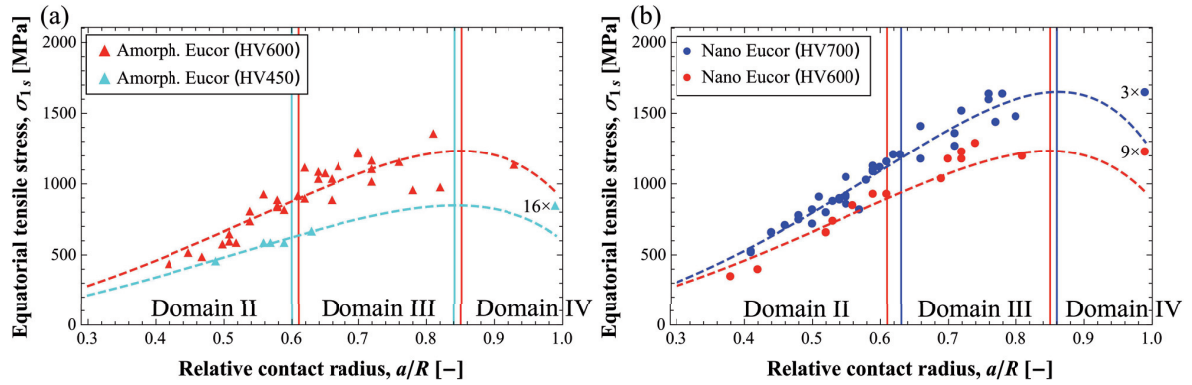


Figure 3.7 – Surface equatorial stress at the moment of failure for tested particles versus the relative contact radius  $a/R$  for (a) amorphous and (b) nanocrystalline Eucor particles. Dashed lines represent the average stress trajectories and solid vertical lines represent predicted boundaries between Domains III and IV for given platens. Symbols at the far right represent particles that survived until platens contacted.

Measured experimental values of the stress in the equatorial belt of each tested particle according to Eq. (3.2) together with the average stress trajectory Eq. (3.6) are shown in Figure 3.7. With amorphous Eucor particles, 18 particles tested with HV600 platens and 1 particle tested with HV450 platens failed in Domain III. One particle tested with HV600 platen entered Domain IV although it failed later on. When tested with HV450 platens 16 particles survived until platens contacted (Domain IV).

For nanocrystalline Eucor particles, 11 particles failed in Domain III when tested with HV700 platen and 7 particles tested with HV600 platens. Three particles tested with HV700 and 9 particles tested with HV600 platens survived until platens contacted (Domain IV).

The reason why one particle failed in Domain IV might be explained by slow-crack-growth, as was proposed for particles in Ref. [344]; alternatively it can represent an outlier for which the transition between Domains III and IV was far off the predicted value. In collating particle strength data, this particle was considered to have survived the right-censoring value,  $\sigma_c$  of the platen that it was tested with (HV600). The ensemble of the surface failure events (Domain III) and events for which we only know the right-censored value and all data that were left-truncated for the value of Domain III beginning for the corresponding platen are presented in Table 3.2.



Table 3.2 – Ensemble of the Domain III and IV results used to calculate the surface stress survival probability.

Amorphous Eucor				Nanocrystalline Eucor			
Platen	Measured failure/censoring peak surface stress [MPa]	Censoring indicator <sup>1</sup>	Left-truncated at $\sigma_T =$ [MPa]	Platen	Measured failure/censoring peak surface stress [MPa]	Censoring indicator <sup>1</sup>	Left-truncated at $\sigma_T =$ [MPa]
HV600	1110	0	820	HV700	1180	0	1030
	1130	0	820		1410	0	1030
	900	0	820		1440	0	1030
	890	0	820		1480	0	1030
	1170	0	820		1520	0	1030
	920	0	820		1270	0	1030
	1040	0	820		1210	0	1030
	1230	0	820		1600	0	1030
	1360	0	820		1360	0	1030
	1160	0	820		1640	0	1030
	1080	0	820		1640	0	1030
	960	0	820		1650	1	1030
	1220	0	820		1650	1	1030
	980	0	820		1650	1	1030
	1020	0	820		1230	0	820
1090	0	820	930	0	820		
1120	0	820	1180	0	820		
1040	0	820	1290	0	820		
1230	1	820	1180	0	820		
HV450	670	0	590	HV600	1200	0	820
	850	1	590		1040	0	820
	850	1	590		1230	1	820
	850	1	590		1230	1	820
	850	1	590		1230	1	820
	850	1	590		1230	1	820
	850	1	590		1230	1	820
	850	1	590		1230	1	820
	850	1	590		1230	1	820
	850	1	590		1230	1	820
	850	1	590		1230	1	820
	850	1	590		1230	1	820
	850	1	590		1230	1	820
	850	1	590		1230	1	820
	850	1	590		1230	1	820

<sup>1</sup> when 0, the surface stress represents the surface strength measurement, otherwise value 1 indicates right-censoring and the value in the surface stress column represents a lower-bound of the surface strength.

### 3.5.2 Surface strength distribution

Figure 3.8 shows estimated survival distribution using (i) the non-parametric Kaplan-Meier product-limit estimator and (ii) the two-parameter Weibull distribution using the data from Table 3.2. The two survival distributions were estimated with the Wolfram Mathematica 10.1 (Wolfram Research, Inc., USA) computation program using incorporated functions *SurvivalModelFit* and *EstimatedDistribution* for product-limit estimator and Weibull distribution parameter estimation, respectively. Plotting the non-parametric and parametric estimations over one another shows that they are mutually consistent. The estimated Weibull modulus  $m$  and the characteristic strength (scale parameter)  $\sigma_0$  are  $m = 7.8 \pm 1.5$  and  $\sigma_0 = (1130 \pm 30)$  MPa for amorphous Eucor particles, and  $m = 6.0 \pm 1.3$ ,  $\sigma_0 = (1490 \pm 70)$  MPa for the nanocrystalline Eucor particles. The standard error in the parameter estimation was assessed using a bootstrapping technique; specifics are presented in the Supplementary Information (Section 3.7.4).

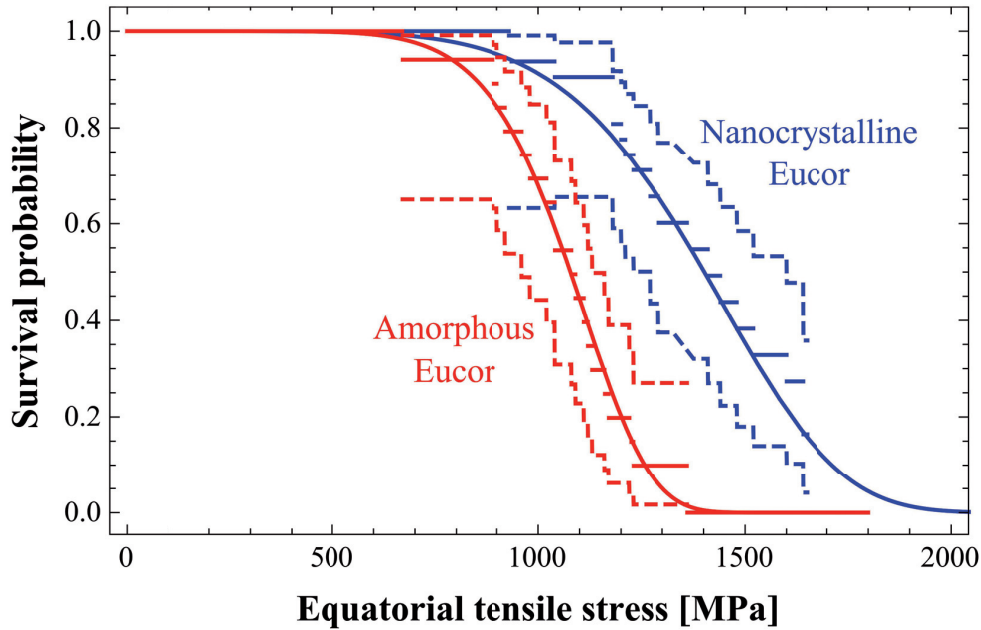


**Figure 3.8 – Survival probability of (red) amorphous and (blue) nanocrystalline Eucor particles with respect to the surface equatorial stress evaluated from Domain III and IV events. (continuous solid lines) two parameter Weibull distribution, (stepped lines) Kaplan-Meier product-limit estimator, (dashed stepped lines) 95% confidence intervals for the Kaplan-Meier estimation.**

In order to assess the effect of uncertainty in the Poisson's ratio estimation on results we have reevaluated the data with two extreme values of the expected particle's Poisson's ratio, namely 0.25 and 0.3. Changing the particle Poisson's ratio  $\nu$  had little effect on the Weibull modulus results; this is owing to the fact that the Domain's boundaries in  $a/R$  terms are not sensitive to the exact value of  $\nu$ . The value of the Poisson's ratio has, on the other hand, some effect on the scale parameter of the resulting Weibull distribution: the characteristic strength  $\sigma_0$  changes within 5% relative to the value determined with  $\nu = 0.28$ . This difference is, however, lower than the error of the stress calculation using Eq. (3.2), which is approximately 5-10% [346]. The sensitivity of the Weibull parameters to the value of the friction coefficient  $\mu$  is small: when  $\mu$  is changed to 0.25 or 0.3 their variation is well below 5% (see Supplementary Information, Section 3.7.2 for details).

From Figure 3.8 it is evident that after annealing the particle strength increases noticeably, by roughly 30% on average. The Weibull modulus decreases only slightly, which means that there is slightly more scatter in observed results, which may be attributed to the presence of slightly greater microstructural differences between individual nanocrystalline particles (Figure 3.2). This difference in the scatter is, however, only marginal given the accuracy of the measured Weibull modulus.

The fact that after crystallization annealing the strength of particles increases while the Weibull modulus remains relatively unaffected suggests that observed changes in particle strength distribution are mostly the result of an increase in the fracture toughness of the material while the particles' flaw distribution remains mostly unchanged. For both types of particles, micropores produced during the powder processing by trapping air when in molten state were linked to the fracture origin: that these would not be altered by the annealing treatment is reasonable. We thus conclude that the difference

in observed strengths between amorphous and nanocrystalline particles is explained by an increase in the fracture toughness of the particle material after annealing. Nanocrystallisation apparently made the particles tougher by a value that is high enough to increase their strength on the order of 30% or more since, as we discuss later, pores in nanocrystalline particles have likely a more detrimental effect on strength than in amorphous particles.

### 3.5.3 Strength limiting defects

In glasses and glass ceramics it is known that the mirror region size surrounding the fracture origin can be directly linked to the fracture stress. In amorphous particles the size of mirrors,  $r_m$ , present on meridional cracks surrounding critical flaws can thus be linked with the measured surface equatorial fracture stress if one assumes that the particle fracture toughness is in the range 0.4-1.0 MPa.m<sup>1/2</sup> depending on the mirror-constant-to-fracture-toughness ratio used (this varies in the literature between 2.3-3 [347–349]. This deduced fracture toughness range is in good agreement with what one would expect for the present amorphous Eucor particles material, since it is comparable to that of silica and aluminate-glasses [323,332,350] (see Supplementary Information, Section 3.7.3 for details).

In nanocrystalline Eucor the mirror size surrounding fracture origins is less well defined. We have therefore tested whether the measured surface equatorial fracture stress can be linked with the observed surface and subsurface pores if these are assimilated to sharp penny-shape flaws. The rationale behind such an assimilation of pores for nanocrystalline particles to sharp flaws is based on observations of Rice [351] as well as our own observation of microcracks along the pore internal surface in one of the nanocrystalline particles. The measured fracture stress could be linked with observed pores acting as sharp flaws for material fracture toughness values in the range of 1.0 – 2.2 MPa.m<sup>1/2</sup> (see Supplementary Information, Section 3.7.3 for details). This is again in good agreement with the expected fracture toughness of the present nanocrystalline particle material: its lower bound should be near the toughness of the amorphous powder while the upper bound is expected to be close to that of (coarse grained) mullite ( $\approx 2$  MPa.m<sup>1/2</sup>) [352–354] or mullite reinforced with zirconia grains, of toughness value in the range of 2.5-6 MPa.m<sup>1/2</sup> depending on the preparation method and grains size and shape [355–357].

### 3.5.4 Data for competing centre and surface failure – Domain II

A few particles failed for  $a/R$  values that situate their fracture within Domain II; these particles showed surface or subsurface pores that could be identified as the origin of failure and were such that the pore or associated mirror size correlated well with the measured surface equatorial belt stress value for the particle in question (see Figure 3.11 and Figure 3.12 in Supplementary Information). We hence reanalysed all data to probe whether *all* particle failures could have originated at a surface flaw.

We therefore assumed that all Domain II particles failed due to a flaw along their surface and included Domain II failure events, with the predicted surface equatorial stress as the failure stress, into the

Survival-analysis data set of Domain III failure events (Section 3.5.1). Adding data points from Domain II with identified (surface) failure stress values, effectively removes any left-truncation in such event data (as Domain II starts for very low  $\sigma_{1s}$ ). Figure 3.9 compares the thus-obtained surface strength distribution with the distribution obtained by only considering data points that were within Domains III and IV (i.e., with left-truncation). The evident discrepancy between the two strength distributions shows that at least for some of the particles that failed in Domain II, there was a failure origin other than a surface defect. Most probably there was, for some of these particles, a flaw in its central region. This is supported by observations of large (a few micrometers in diameter) pores close to the central region in several particles that failed in Domain II. Two such particles with evident pores of this type revealed before testing by means of light microscopy, are shown in Figure 3.9: these two particles were among the weakest tested for amorphous and nanocrystalline Eucor, respectively (the central stress at the moment of failure for the two particles was  $\sigma_{1c} = 580$  MPa and  $\sigma_{1c} = 660$  MPa for the amorphous (Panel a) and nanocrystalline (Panel b) particle, respectively).

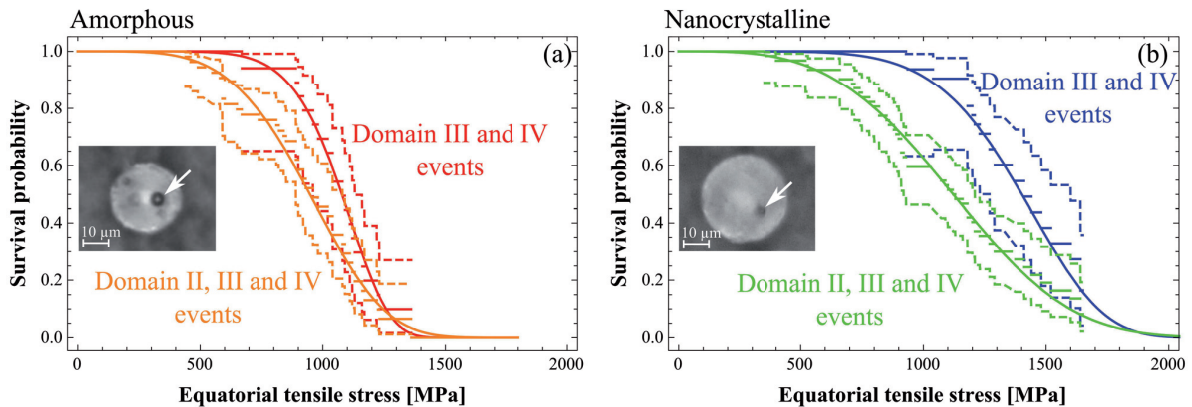


**Figure 3.9 – Comparison of the surface equatorial stress survival distribution of (a) amorphous and (b) nanocrystalline Eucor particles obtained using events from Domains III and IV and Domains II, III and IV where failure events from Domain II are considered all to be due to the surface stress. Two optical microscopy pictures represent amorphous and nanocrystalline particles observed before testing and which failed at relatively low loads in Domain II: one notices the presence of micrometric pores near the particle center. These (a) amorphous and (b) nanocrystalline particles failed for central stress values  $\sigma_{1c} = 580$  MPa and  $\sigma_{1c} = 660$  MPa, respectively.**

### 3.5.5 Comparison with other microscopic ceramic fibre/particle strength data

The measured surface strengths of particles from the present study are comparable to values reported for  $\text{Al}_2\text{O}_3\text{-La}_2\text{O}_3\text{-Gd}_2\text{O}_3\text{-ZrO}_2$  (ALZG) microscopic particles, of composition 58/15/5/22 by molar ratio, tested in compression between a pair of hard (sapphire) platens [236]. Amorphous ALZG particles exhibited average strength on the order of 1100 MPa while after annealing their strength gradually increased, reaching peak average strength of 1800 MPa after a 1300 °C anneal, decreasing down to approximately 1200 MPa for 1400 °C annealing. Note that, although these strengths are comparable to values measured here, the method used (hard platens) provides strength results only for the central portion of particles; additionally, the method may potentially affect results by the nucleation of extraneous flaws along the immediate periphery of the platen/particle contact regions.

The observed microstructure and composition of present nanocrystalline Eucor particles, composed mainly of mullite reinforced with zirconia grains, are somewhat similar to those of nanocrystalline high-strength Nextel™ 720 fibres. The microstructure of these fibres is composed of mullite reinforced with nanometric alumina grains [358]. The reported Weibull strength distribution of these fibers is  $m \approx 7-8$  and  $\sigma_0 \approx 2000-2100$  MPa [335]. The surface strength of particles from this study thus approaches (reaching  $\approx 70\%$ ) that of chemically and microstructurally comparable engineering fibres used as reinforcements in composites; however, the present Eucor particles cannot rival the strongest ceramic fibres available (see Figure 3.13 in Supplementary Information), the reason being the deleterious influence of micropores present within the plasma-remelted powder. Removing those defects would therefore result in significantly stronger ceramic particles, with the implication that there is ample scope for the production of Eucor particles of significantly higher strength.

### 3.6 Conclusion

We use the Meridian Crack Test method to measure the local strength of individual amorphous and nanocrystalline ceramic particles based on  $\text{Al}_2\text{O}_3\text{-ZrO}_2\text{-SiO}_2$  eutectic ternary system prepared using a plasma-spraying technique from Eucor™ as the feedstock powder. Results show that nanocrystalline particles obtained by annealing the amorphous powder at  $1300^\circ\text{C}$  for 1h are on average 30% stronger than amorphous particles. The Weibull modulus for nanocrystalline particles was found to be approximately 6 with a characteristic strength of 1490 MPa. Spherical pores of size ranging from few hundred nanometers to few micrometers were identified as the principal strength limiting-defects for both amorphous and nanocrystalline particles. Similar Weibull modulus values and fractographic observation suggest that the 30% increase in particle strength obtained after annealing results from an increase in the fracture toughness of nanocrystalline particles of at least 30% over that of the same particles in the amorphous state.

### 3.7 Supplementary information

#### 3.7.1 Particle Poisson's ratio and platen-particle friction

To calculate the strength of particles from the data of uniaxial compression tests (Figure 3.3) one needs to determine the Poisson's ratio of the particles. In the literature, the typical value of Poisson's ratio of aluminate and silico-aluminate glasses falls in the range of 0.25-0.3 [359,360]. In binary  $\text{Al}_2\text{O}_3\text{-SiO}_2$  glass, an increase in  $\text{Al}_2\text{O}_3$  concentration enhances the atomic packing density and hence the Poisson ratio (see below) due to its high dissociation energy; for 0.6 molar fraction of  $\text{Al}_2\text{O}_3$  (the composition of mullite) a Poisson's ratio value of 0.274 was reported [361]. To get an estimate for the ternary alumina-zirconia-silica glass system, one microscopic cantilever beam was machined in a particle partially embedded within a polymer matrix using focused ion beam (FIB) machining (see Figure 3.10), and was then loaded in bending using a nanoindenter apparatus. Using finite element (FEM) analysis of the bent beam the Young's modulus, treated as an unknown parameter, was found to be  $(145 \pm 5)$  GPa. Using the Makishima and Mackenzie [362,363] formula for Young's modulus (in GPa)  $E = 8.36 V_t \sum_i G_i X_i$  where  $G_i$  stands for dissociation energy of  $i$ th oxide in our case 32  $\text{kcal.cm}^{-3}$ , 23.2  $\text{kcal.cm}^{-3}$ , 15.4  $\text{kcal.cm}^{-3}$  for  $\text{Al}_2\text{O}_3$ ,  $\text{ZrO}_2$  and  $\text{SiO}_2$ , respectively where  $X_i$  is the mole



fraction of the component  $i$ , we can get the atomic packing density  $V_i$  of a multicomponent oxide glass. The Poisson's ratio  $\nu$  can be then calculated as  $\nu = 0.5 - (7.2 V_i)^{-1}$ . Using this approach we obtained a value for the Poisson's ratio of the amorphous Eucor of  $\nu = 0.29 \pm 0.01$ . Given that the Makishima and Mackenzie formula for Young's modulus often underestimates the real value especially for high-modulus glasses [359,364], the calculated atomic packing density  $V_i$  using the formula with measured Young's modulus may be overestimated using this value. In summary, we deem that the best estimate for amorphous Eucor particles Poisson's ratio is 0.28.

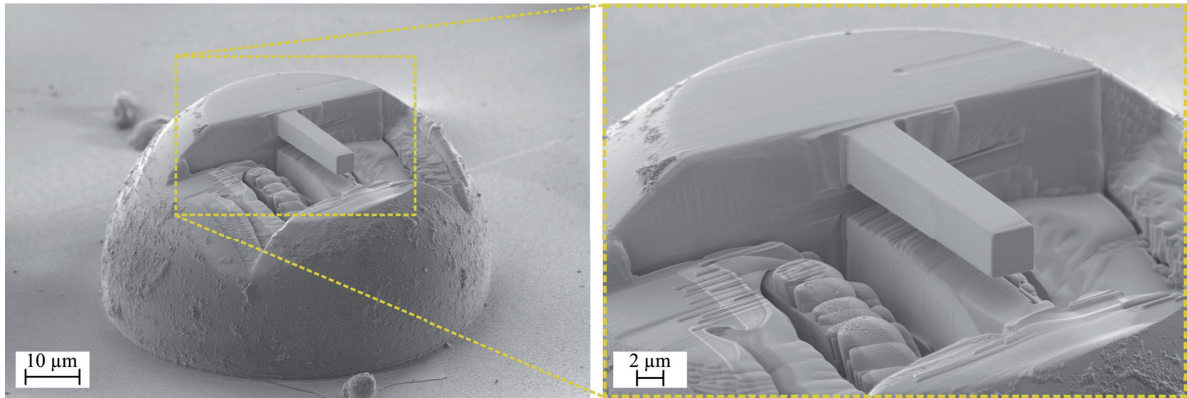


**Figure 3.10 – FIB machined cantilever beam at the top of an amorphous Eucor particle partially embedded in a polymer matrix.**

As for the nanostructured Eucor particles, based on a Rietveld refinement of the XRD spectra, and in light of microstructural observations, the material can be considered as mullite reinforced with tetragonal (and some monoclinic) zirconia particles. The reported Poisson's ratio of the polycrystalline mullite lies in the range 0.266-0.281 [365,366] and the theoretical value for orientation averaged Poisson's ratio for tetragonal zirconia (using the Voigt approximation) is 0.29. Hence, an estimated Poisson's ratio near 0.28 is also obtained for the nanostructured Eucor particles of the present study.

The particle-platen (kinematic) friction coefficient was inferred by measuring the angle of an inclined plane at which a layer of as-sprayed particles partially embedded in a several micrometers thick layer of nail polish (used as an adhesive) along the surface of an aluminium SEM stub slid freely along the polished piece of steel used as a platen following a minute impulse to overcome static friction. The (kinematic) friction was found using the usual force-balance method to be approximately  $\mu = 0.28$ .

### 3.7.2 Effect of the particle Poisson's ratio and platen-particle friction coefficient on results

Given that the stress magnitude in a compressed particle depends on the particle's Poisson's ratio  $\nu$  and also on the platen-particle friction coefficient, we have performed an evaluation of the effect on estimated particle strength distributions of two extreme values of the estimated Poisson's ratio and estimated friction coefficient, i.e. we have reevaluated the strength distribution using  $\nu = 0.25$ ,  $\nu = 0.30$  and  $\mu = 0.25$ ,  $\mu = 0.3$  for data collected on both amorphous and nanocrystalline Eucor and using solution in Ref. [346].



For simplicity we report only the two-parameter Weibull distribution results in Table 3.3 and Table 3.4. As can be seen, changing the value of the particle's Poisson's ratio from 0.25 to 0.3 has very little effect on the Weibull modulus relative to the precision of its estimation that was deduced to be near  $\pm 1.5$  (see below). The value of the Poisson's ratio has some effect on the scale parameter of the resulting Weibull distribution: the characteristic strength  $\sigma_0$  changes within 5% relative to the value determined with  $\nu = 0.28$ . This difference is, however, lower than the error in the stress calculated using the Eq. (3.2), this being approximately 5-10% [346]. Changing the platen-particle friction coefficient to 0.25 and 0.3 has even less effect on the estimated Weibull parameters (see Table 3.4). We therefore consider the precise value of these parameters as being without significant consequence on the present strength measurements.

Table 3.3 – The effect of different Poisson's ratio on results of surface Weibull strength distribution of Eucor particles. Particle-platen friction fixed at 0.28.

Poisson's ratio, $\nu_p$	Amorphous Eucor		Nanocrystalline Eucor	
	Weibull modulus, $m$	Characteristic strength, $\sigma_0$ [MPa]	Weibull modulus, $m$	Characteristic strength, $\sigma_0$ [MPa]
0.25	7.4	1070	5.7	1400
0.28	7.8	1130	6.0	1490
0.30	8.0	1170	5.9	1540

Table 3.4 – The effect of different platen-particle friction coefficient on results of surface Weibull strength distribution of Eucor particles. Particle Poisson's ratio fixed at 0.28.

Friction, $\mu$	Amorphous Eucor		Nanocrystalline Eucor	
	Weibull modulus, $m$	Characteristic strength, $\sigma_0$ [MPa]	Weibull modulus, $m$	Characteristic strength, $\sigma_0$ [MPa]
0.25	7.8	1140	5.9	1510
0.28	7.8	1130	6.0	1490
0.30	7.9	1130	5.9	1480

### 3.7.3 Fracture stress vs. defect size and estimation of the particle fracture toughness

Fractography of tested particles revealed that pores were the origin of failure in the vast majority of cases, in which a clear mirror-mist and hackle feature could be observed on one of the meridian cracks. It was shown by Rice [351] that, to cite the author, "pores in glasses are less severe sources of failure than sharp flaws of the same dimensions". The mirror region surrounding the pore in fractured amorphous particles is very well defined and can be relatively precisely measured from the fractographs. The mirror size can be linked with the measured surface equatorial fracture stress through the well-established empirical formula  $\sigma_{1s} = A_m / \sqrt{r_m}$ , where  $A_m$  is the mirror constant and is related to the (Mode I) fracture toughness of the material,  $K_{IC}$  as  $A_m = k_m \cdot K_{IC}$ , where  $k_m$  is reported to lie between 2.3-3 [347–349]. The measured equatorial fracture stress  $\sigma_{1s}$  should therefore increase linearly with  $r_m^{-1/2}$  with  $k_m \cdot K_{IC}$  equal to the slope of the correlation, as shown in Figure 3.11. A linear fit through the data and the origin yields  $k_m \cdot K_{IC} = 1.6 \text{ MPa} \cdot \text{m}^{1/2}$ , with plausible minimum and maximum observed values of  $k_m \cdot K_{IC}$  equal to  $1.3 \text{ MPa} \cdot \text{m}^{1/2}$  and  $2.4 \text{ MPa} \cdot \text{m}^{1/2}$ . Given that  $k_m$  lies between

2.3-3, this translates to  $K_{IC}$  in the range 0.4-1.0  $\text{MPa}\cdot\text{m}^{1/2}$  based on the observed mirrors sizes. This is in good agreement with what one would expect for the material: the expected fracture toughness should lie between that of fused quartz ( $\approx 0.65$  [323,332]) and that obtained for example for Zerodur<sup>TM</sup> a lithium-aluminosilicate glass-ceramic ( $\approx 1.26$   $\text{MPa}\cdot\text{m}^{1/2}$  [350]). In other words the measured surface strengths are in good agreement with what can be deduced from observed fractographical features using expected fracture toughness values.

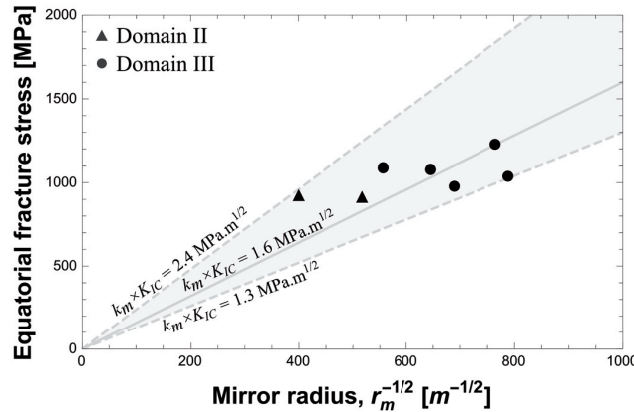


**Figure 3.11 – The measured equatorial fracture stress versus the observed mirror diameter surrounding pores identified as failure origin for (circles) 5 particles that failed in Domain III and (triangle) 2 particle that failed in Domain II. Straight lines represent different slopes of different values of  $k_m \cdot K_{IC}$ .**

In nanocrystalline particles, the mirror region surrounding pores identified as the failure origin is much less well-defined. As observed by Rice [351], pores in polycrystalline solids behave much more like sharp flaws having roughly the same diameter as the pore. We have therefore assimilated the measured pores sizes with penny shaped cracks of the same dimension. Assuming that they are small compared to the dimensions of the particle and subjected to uniaxial tension with a stress magnitude equal to the measured equatorial stress at the moment of failure, one can write  $\sigma_{1s} = K_{IC} / (Y \sqrt{r_p})$  where  $Y = 1.13$  [367] and  $r_p$  is the pore radius. Figure 3.12 displays the  $\sigma_{1s}$  vs.  $r_p^{-1/2}$  correlation for three particles that failed in Domain III and five particles that failed in Domain II but for which the fractography reveals that they most probably also failed due to a surface or subsurface pore. The data give an average deduced fracture toughness value 1.4  $\text{MPa}\cdot\text{m}^{1/2}$  and a value range from 1.0 to 2.2  $\text{MPa}\cdot\text{m}^{1/2}$ .

One can observe from Figure 3.12a that two particles (from Domain III) failed with a comparable equatorial fracture stress but with surface pores of very different size both located close to the particle equator. In one case the observed fracture stress-flaw size can be justified with  $K_{IC} = 2.2$   $\text{MPa}\cdot\text{m}^{1/2}$  in the other case with  $K_{IC} = 1.1$   $\text{MPa}\cdot\text{m}^{1/2}$ . As can be seen from Figure 3.12b and Figure 3.12c the microstructure of the two particles is different. The particle with the higher deduced fracture toughness has a relatively rough microstructure (similar to that in Figure 3.2c of the main text) while the other particle exhibits a very fine microstructure with equiaxed grains of few ten nanometers in size (Figure 3.2b in the main text). The significant difference in the deduced fracture toughness is therefore likely due to the observed microstructural difference.

On average, the fracture toughness that is deduced by linking the observed fracture stress with flaw sizes is, as was the case with amorphous particles, consistent with what one would expect for the present nanocrystalline material. Its lower bound is expected to be equal or slightly higher than the toughness of the amorphous powder while the upper bound is close to that of (coarse grained) mullite ( $\approx 2 \text{ MPa}\cdot\text{m}^{1/2}$ ) [352–354]. By reinforcing mullite with zirconia one can achieve higher fracture toughness in the range of  $2.5\text{--}6 \text{ MPa}\cdot\text{m}^{1/2}$  depending on the preparation method, grains size and shape [355–357].

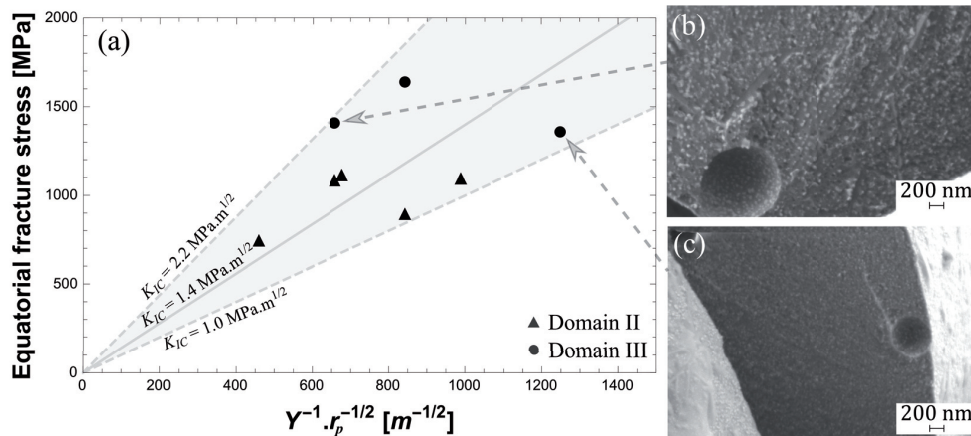


**Figure 3.12** – (a) The measured equatorial fracture stress versus the observed radius  $r_p$  of surface or subsurface pores identified as the failure origin and assimilated to sharp penny-shape cracks with a geometry factor  $Y = 1.13$ , for (circles) 3 particles that failed in Domain III and (triangles) 5 particles that failed in Domain II. Straight lines represent different slopes for different values of the (Mode I) fracture toughness  $K_{IC}$ . (b) SEM micro-fractograph of a nanocrystalline particle with a surface pore that was visibly the origin of failure, exhibiting a relatively rough fracture surface giving a relatively high deduced fracture toughness  $\approx 2.2 \text{ MPa}\cdot\text{m}^{1/2}$ . (c) SEM micro-fractograph of a particle that exhibits a very fine microstructure with equiaxed grains a few tens of nanometer in diameter and a small (relative to the previous case) pore as the failure origin. This particle exhibits a relatively low deduced fracture toughness  $\approx 1.1 \text{ MPa}\cdot\text{m}^{1/2}$ .

### 3.7.4 The precision of Weibull parameter estimation

Estimation of the precision of the Weibull parameters was performed using a bootstrapping method. First, data are resampled 1000 times using the estimated surface strength Weibull parameters to obtain 1000 random variates of different lengths simulating datasets obtained with different platens. For instance, in the case of amorphous particles, platens HV600 and HV450 were used each to test in total 33 and 21 particles, respectively. Therefore 1000 variates with length 33 and 1000 variates with length 21 are simulated using the estimated Weibull parameters. One thousand pairs of variates with 33 and 21 elements form a simulated dataset of the surface strength measurements with two platens. Each of the datasets is stripped of those simulated strength values that are found to be outside of the Domain III defined by the left-truncation and right-censoring values for each platen. Values that are higher than the right-censoring value for the given platen are replaced by the right-censoring value.

For the one thousand left-truncated and right-censored two-platen datasets, Weibull parameters are estimated and the standard deviation in the estimated parameters is calculated assuming a normal

distribution. Note that this simple bootstrapping procedure does not take into account the fact that some particles fail due to internal flaws (something that was shown to be a possibility in the present powder); however, if we assume that the surface and internal strength distributions are independent we deem that the simple bootstrapping method gives a reasonable estimate of the Weibull parameter precision. This method gave estimates reported above for the Weibull modulus  $m$  and the characteristic strength (scale parameter)  $\sigma_0$ , namely  $m = 7.8 \pm 1.5$  and  $\sigma_0 = (1130 \pm 30)$  MPa for amorphous Eucor particles, and  $m = 6.0 \pm 1.3$ ,  $\sigma_0 = (1490 \pm 70)$  MPa for nanocrystalline Eucor particles.

### 3.7.5 Comparison of the particle strength with Nextel fibres

Figure 3.13 compares the surface strength of nanocrystalline Eucor particles with that of selected high-strength engineering fibres. The present nanocrystalline Eucor particles approach to within 70% the strength of chemically and microstructurally comparable Nextel™ 720 fibres; note, however, that those fibre strength values were measured along much larger volumes (25 mm gauge length with 10  $\mu\text{m}$  in diameter) [335]. There are also stronger fibres: for example, nanocrystalline alumina Nextel™ 610 fibres attain characteristic strengths on the order of 3.5 GPa along 25 mm of tested gauge length with 10  $\mu\text{m}$  diameter [335]. Locally, Nextel™ 610 fibres are even stronger: when tested along roughly 10  $\mu\text{m}^3$  of volume, the estimated local characteristic strength is near 5 GPa [324]. Clearly, there is thus high potential for improvements in the production of nanocrystalline microparticles, notably by the removal of internal porosity.

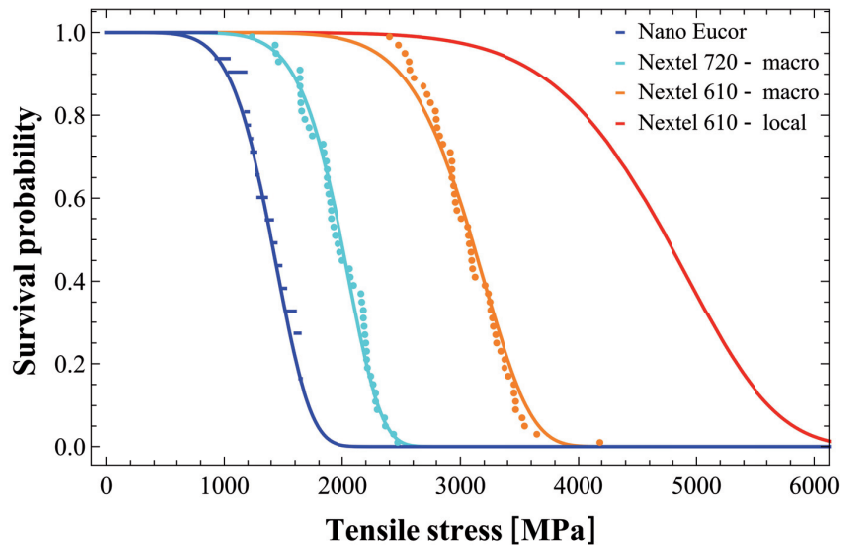


Figure 3.13 – Comparison of the strength distribution of nanocrystalline Eucor from this study with (cyan) chemically and microstructurally similar 3M Nextel™ 720 fibres and (orange) 3M Nextel™ 610 nanocrystalline alumina fibres both tested along 25 mm gauge length in tension in [335]. In red is the estimated local strength distribution of the Nextel™ 610 fibres for the effective volume 10  $\mu\text{m}^3$  tested using the micromechanical C-shaped sample test in [324].

## Chapter 4 The local strength of microscopic alumina reinforcements

### 4.1 Disclaimer

This chapter was published as an article in a scientific journal with the open-access (CC BY 4.0) licence and its bibliographic reference is given below. The postprint version of the published article is presented here with its Introduction section significantly abbreviated to avoid repetition of what was already mentioned in Chapter 1 of this thesis (extracts, including few literal reproductions of full paragraphs of the article Introduction are included in Chapter 1). The candidate, herewith V.P., was involved in conception and implementation of the testing method. V.P. performed roughly half of all experimental work equally shared with Martin G. Mueller (M.G.M). Data analysis was carried out mainly by Goran Žagar (G.Ž). V.P. was involved in interpretation of results and contributed in writing Methods section and provided feedback on the manuscript, the writing of which was mainly in charge of G.Ž.

Žagar, G., Pejchal, V., Mueller, M.G., Rossoll, A., Cantoni, M., Mortensen, A.: *The local strength of microscopic alumina reinforcements*. Acta Materialia 100, 2015, 215–223. doi:10.1016/j.actamat.2015.08.026

### 4.2 Introduction

Here we present a micromechanical testing approach by which one can measure, free of micromilling artifacts and directly, the local strength of individual small second phase elements in a multiphase metallic material. The novelty of the approach presented here lies in that (i) it can be adapted to variously shaped convex second phases (thus, it is not restricted, for example, to thin films) and (ii) it probes the strength of material, the surface of which is unaffected by micromachining or polishing.

The method was inspired by a recently proposed solution to the problem posed by the mechanical characterization of macroscopic ceramic spheres or cylinders used in bearings: such smooth spheroids are strong, brittle, and are as difficult to grip for loading in tension or bending as are convex second phases in metallic materials [247,249,250] (see Section 1.5.2). The idea behind the test is to machine a wide notch, so that compressive loading can put the remaining ligament outer surface into a state of localized tensile stress. Besides the fact that fracture in this specimen configuration takes place in material the surface of which is unaffected by FIB micromilling, the method has the advantage that

applied loads are small enough not to cause the brittle microphase to shatter upon fracture. This in turn enables fractographic analysis and the identification of fracture-inducing flaws.

The method is in principle suited for any convex inclusion of brittle material that can be carved by FIB milling. To develop the method and explore what it teaches on a material of engineering significance, we have chosen to use  $\sim 12\ \mu\text{m}$  diameter nanocrystalline alumina fibers embedded in an aluminum matrix as a testbench material. Reasons for this choice are (i) that these fibers are an engineering material with a regular convex shape and an isotropic microstructure (which in turn eases data interpretation), and (ii) that continuous fibers such as these can also be tested for strength using conventional tensile testing of macroscopic samples. Hence, strength data obtained here by means of the present microscopic testing method can be confronted to strength data reported in the literature from another testing method conducted on the same fibers [99,100,335].

As will be seen in what follows, the two testing methods yield different strength distributions for the same material: the reason is obviously that the tested volumes of material are so different from one test to the other (tested areas are centimeters long in tensile tests, ten or so micrometers long in the present method). This difference, in turn, points to the fact that size-scaling of strength data, such as given by Weibull statistics, cannot be used to extrapolate strength distributions in brittle second phases across dimensional scales. Phenomena that are driven by highly localized stresses, such as the propagation of damage from one brittle inclusion to the next or crack tip processes, are governed by different defects and hence different strength distributions than are phenomena such as damage initiation across large volumes of material subjected to a homogeneous state of tensile stress. We show here how strength distributions pertinent to the former, microscale, can be measured directly, by coupling microtesting of carved C-shaped brittle phase regions with bespoke finite element simulations, taking due account of friction effects since these take particular importance at the microscale of the present strength measurement method.

## 4.3 Methods

### 4.3.1 Notched sample preparation

We probe here high-strength nanocrystalline Nextel<sup>TM</sup> 610 alumina fibres produced by 3M<sup>TM</sup> (St. Paul, MN, USA). These fibres are in particular used to reinforce a pure aluminium matrix composite wire of  $\sim 2\ \text{mm}$  in diameter, also produced by 3M<sup>TM</sup>. The Nextel<sup>TM</sup> 610 fibre is 99.5%  $\alpha\text{-Al}_2\text{O}_3$ . The fibres are  $\sim 12\ \mu\text{m}$  in diameter and their typical microstructure is characterized by equiaxed grains with a mean diameter of  $\sim 65\ \text{nm}$  [99]. The orientation of the fibres in a composite wire is such that the fibre axis is roughly collinear with the wire axis.

Prior to FIB micromachining of the test samples, the composite wire was prepared so as to enable cutting a rectangular notch perpendicular to the axis of individual fibres. First, a  $\sim 1\ \text{cm}$  long segment of the composite wire was cut using a diamond cutting wheel (Accutom-50, Struers, Denmark) and mounted in epoxy resin. The mounted wire was then ground and polished along two planes, one cross-sectional and the other longitudinal, the latter placed roughly midway across the wire. This produced a sharp  $\sim 90^\circ$  edge passing roughly through the centre of the wire. Next, the fibres were exposed by



deep etching the aluminium matrix with 20 wt. pct. NaOH for approximately 1 hour at room temperature, followed by rinsing in distilled water. Fibres that remained loosely attached near the  $\sim 90^\circ$  edge after deep etching were manually removed, using sharp tweezers under an optical microscope. The result of this procedure is a sample showing several tens of micrometre of exposed fibres, which lower down are embedded in the aluminium matrix, and whose top was gently polished during final metallographic preparation while side surfaces are in pristine condition (Figure 4.1a-b).

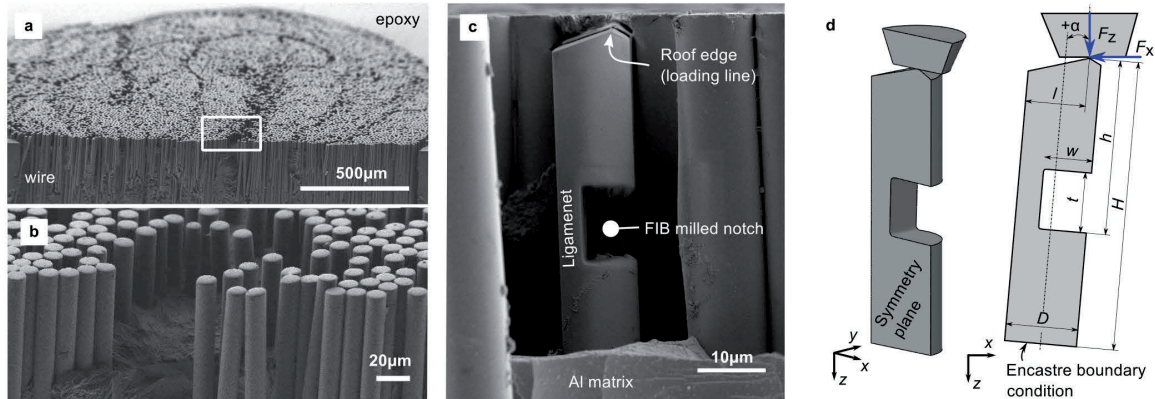


**Figure 4.1 – Notched micro-strength test specimen prepared in an alumina fibre embedded within an aluminium matrix composite. (a) Composite wire polished in two planes with a  $\sim 90^\circ$  edge passing roughly through the wire diameter. (b) Alumina fibres exposed by deep etching the Al matrix. (c) Typical notched sample prepared by FIB milling. (d) Sketch of the one half of a notched specimen (left) with dimensions defined within the specimen plane of symmetry (right).**

Fibres to be probed were selected based on their geometrical separation from neighbouring fibres; indeed, some space around the fibre is required for access of the ion beam during milling, and also for the fibre to be free to bend during the mechanical test. The notch and the rooftop were then FIB-milled into each of the selected fibres with the beam direction oriented parallel to the polished surface of the wire.

The first feature to be machined is a several  $\mu\text{m}$ -wide rectangular notch oriented in a way such that the notch faces are parallel or perpendicular, respectively, to the fibre axis. Then a two-sided roof is machined along the top of the fibre, with its edge situated eccentrically relative to the ligament neutral axis (Figure 4.1c). Note that these two features can be milled also in a fibre that is located (when looking along the ion beam path) behind another fibre (see Figure 4.2); such was the case for  $\sim 3/4$  of the specimens tested in this work.

The FIB machining process was performed either with a Zeiss NVision<sup>TM</sup> 40 (Oberkochen, Germany), or (more seldomly) with a FEI Nova 600 NanoLab, both being dual beam (SEM/FIB) instruments. Both FIBs featured a 30 kV Ga<sup>+</sup> gun and were used with currents of 6.5 nA for the initial coarse milling steps, subsequently reduced to 1.5 or 0.7 nA for the final steps. Prior to the FIB machining process, a  $\sim 5$ -10 nm carbon layer was deposited using a Cressington<sup>TM</sup> 208 Carbon Coater (Watford, England, UK) to avoid charging of the alumina fibres while irradiating with electron or ion beams. Before testing, each FIB milled fibre sample was extensively imaged with SEM in order to

retrieve the characteristic dimensions (Figure 4.1c and Table 4.1 in Supplementary information, Section 4.7.2) that are needed for the finite element modelling and data analysis.

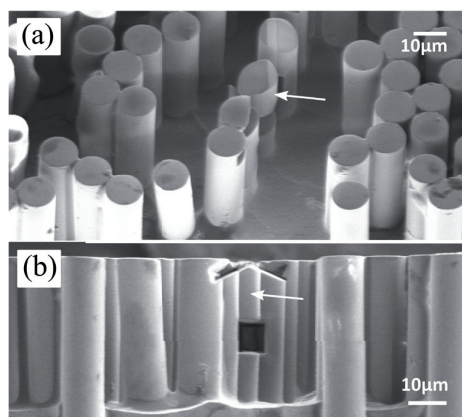


**Figure 4.2 - Notched specimen with ligament outer surface that is shielded by other fibres from being directly exposed to the FIB. (a) Perspective and (b) view along the FIB machining direction of the same notched fibre sample (indicated by an arrow).**

#### 4.3.2 Mechanical testing

Mechanical testing of the fibres was carried out with a TI 950 TriboIndenter<sup>TM</sup> (Hysitron Corp., Minneapolis, MN, USA) nanoindentation apparatus, additionally equipped with a two-axis goniometric tilt stage (Newport Corp., Irvine, CA, USA). The nanoindenter has two transducer heads operating in parallel: (i) a low-load transducer that allows to perform Scanning Probe Microscopy (SPM), which was exploited for alignment using a sphero-conical diamond tip ( $\sim 220$  nm tip radius), and (ii) a high-load MultiRange NanoProbe<sup>TM</sup> (MRNP) transducer capable of measuring the (applied) force and displacement along the vertical direction (only). All fiber fracture tests were conducted using the MRNP transducer equipped with a  $\sim 10$   $\mu\text{m}$  flat diamond tip (Hysitron TI-0145). Alternatively, to study in more detail the general system response and the fiber-indenter contact properties the MRNP was replaced by the high-load 3D OmniProbe<sup>TM</sup> transducer, which is capable of simultaneously measuring vertical and lateral forces. All tests were carried out at room temperature in air (relative humidity between  $\sim 20$  and  $\sim 50\%$ ).

Prior to testing, individual samples were carefully aligned as follows. A wire sample containing several FIB milled fibres was mounted on the tilt stage in the nanoindenter device. A first coarse alignment was carried out using the optical microscope of the indenter and the tilt stage, to bring the polished wire surface roughly perpendicular to the indentation axis. Then, the top edge of the FIB machined fibre roof was aligned parallel to the flat surface of the indenter tip with a precision of  $< 1^\circ$  such that the load can be applied evenly along the line of a roof edge. This was achieved by iteratively scanning the roof of the fibre with the SPM, and adjusting the tilt of the stage accordingly. The misalignment of the fibre axis with respect to the top polished surface of the wire was determined from SEM images. The tilt angle with respect to the normal of the flat indenter surface, i.e. the angle  $\alpha$  around the bending axis coaxial with direction  $y$  (Figure 4.1c), was then adjusted with the tilt stage, to a precision better than  $\sim 2^\circ$  for most of the samples (see Table 4.1 in Supplementary information).

Since a small positive misalignment actually helps in promoting ligament bending such that the highest tensile stress is developed on the ligament outer (non-FIB milled) surface as opposed to the inner surface (location of the machined notch), for a few specimens a somewhat higher positive misalignment was allowed. The misalignment angle  $\alpha$  was taken into account during modelling. The misalignment of the fibre rooftop edge (and hence of the FIB milled notch faces) with respect to the axis of the fibre was, however, not explicitly measured nor taken into account in the analysis, mainly because measurements better than a few degrees are difficult to produce (SEM images should be taken along a direction perpendicular to the polished surface, and the misalignment would then need to be estimated from the projection of the fibre length). Fibres that were severely tilted around the  $x$ -axis and thus not perpendicular to the polished top of the wire were not tested.

To produce a clean and reproducible force-displacement signal with a relatively stable friction coefficient, it was found that a key precondition is to maintain the surface of the indenter tip in sufficiently clean condition. To this end, before testing, indenter tips were cleaned using separate fibres that had been machined as if they were to be tested for strength, but were instead subjected to multiple ( $\sim 100$ ) load-unload cycles that “scrubbed” the flat indenter surface, pushing contamination residue aside using the relative sliding of the fibre roof.

Most tests (76%) were run in the nanoindenter’s displacement control mode, at displacement rates between 15 and 2000 nm/s. Remaining tests were carried out in load control at loading rates between 4.5 and 11 mN/s. With loading rates used here, the bending ligament was effectively loaded with stress rates in the range of  $\sim 0.1$  to  $\sim 1$  GPa/s. Between 1 and 7 partial unloadings were performed during each test, to extract information necessary for data interpretation (see below), before final fracture occurred at peak load.

After the test, the sample was removed from the nanoindenter for SEM examination. This was done to measure the cross-sectional dimensions of the ligament, the position at which the specimen failed, and to conduct fractographic analysis of the sample, aiming in particular to identify the location of failure initiation as well as the size and nature of the critical flaw. A total of 26 fibres were prepared and tested, coming from different regions of the same wire spool.

## 4.4 Results

### 4.4.1 General response of a notched micro-specimen

The specimens tested here were prepared by FIB milling small segments of alumina ceramic fibers that were previously exposed by selectively dissolving the aluminum matrix on a composite wire (Figure 4.1). Each test specimen of length  $H$ , embedded at the bottom in the metal, is micromachined to feature: (i) a notch of width  $w$  and height  $t$  with the notch base situated at a distance  $h$  from the top of the fiber, and (ii) a rooftop above the notch with its apex line aligned with the notch and placed eccentrically at a distance  $l$  away from the ligament outer surface. The notched specimen is loaded using a nanoindentation apparatus (Hysitron, Minneapolis, MN, USA) equipped with a flat diamond probe. Prior to loading, the sample is aligned in relation to the indentation device such that the rooftop

apex line lies parallel to the flat probe surface. The presence of the rooftop thus defines exactly where the load is applied, this being required for calculation of the ligament bending moments.

A representative, experimentally measured notched specimen response for the vertical ( $z$ -axis) and lateral ( $x$ -axis) directions in a sample vertically loaded were measured using the three-dimensional force and displacement-sensing transducer of the nanoindentation instrument (Figure 4.3). The test comprised three consecutive load–unload cycles, all three conducted up to vertical load of  $\sim 10$  mN. Each cycle measured both the vertical (Figure 4.3a) and the lateral force (Figure 4.3b) as a function of vertical displacement. As seen, each cycle contains three distinctive nearly linear portions. The first part of the cycle is recorded during loading, where the vertical and lateral force components both increase with the vertical displacement. This is marked as Region I in Figure 4.3. The unloading part of each cycle contains a kink that separates the load–displacement curves into two parts. At first, unloading of the vertical force occurs at a higher rate while the lateral force changes sign (Region II). After the kink, the vertical load in Region III decreases at a much smaller rate than in Region II, while the lateral force vanishes slowly with full sample unloading. The fact that during Region II the lateral (frictional) force changes sign simply means that unloading causes the specimen to deflect back to its original position. Figure 4.3c shows how the apparent friction coefficient  $\mu$ , computed as the ratio of the lateral and vertical load, changes during the three regions of the load–unload cycle. It can be seen that, in each of Regions I and III,  $\mu$  varies weakly with the vertical load; its value in Region I and III is  $\approx 0.15$  and  $\approx 0.08$ , respectively.

Vertical loading of the notched specimen tested in Figure 4.3, deformed up to comparable vertical displacements, was modelled with a quasi-static three-dimensional Finite Element (FE) method. The model domain contains a linear-elastic indenter part, the nonlinear-elastic notched specimen and features explicit contact behaviour between the indenter part and the notched specimen (isotropic Coulomb friction in the tangential direction and “hard” contact in the normal direction). The geometry of each notched specimen was reconstructed on the basis of dimensions extracted from Scanning Electron Microscopy (SEM) images of the test specimen (for FE model details see Supplementary Section 4.7.1). The vertical and lateral responses of the FE model calculated for a load–unload cycle and several values of the (constant) friction coefficient  $\mu$ , are shown first with symbols in Figure 4.3. In these computations, unloading was not carried out down to zero vertical load, as was the case in the experiment described above. As a result, the simulated load–unload cycle exhibits a fourth region (Region IV) in addition to the three regions previously seen in experimental data. This new region has the same slope as Region II and is situated along the initial loading part of a reloading cycle. During loading in Region IV, the lateral force on the indenter again changes sign while the vertical force increases rapidly up to another kink, after which the load–displacement curve retraces the previously traced curve in Region I. In addition to two cyclic loading cases corresponding to two finite friction coefficients (magenta down-triangles for  $\mu=0.08$  and green circles for  $\mu=0.15$ ), in Figure 4.3 we also show the response predicted for two limiting fibre-indenter contact laws. The first limit is frictionless contact, i.e.  $\mu=0$  (blue triangles): here, the lateral force in the contact is mandated to vanish, thereby leaving lateral deflection of the rooftop edge completely unconstrained. The second

limit is that of perfectly sticking contact, i.e.  $\mu \rightarrow \infty$  (red squares); here, lateral motion of the rooftop edge relative to the indenter is blocked.

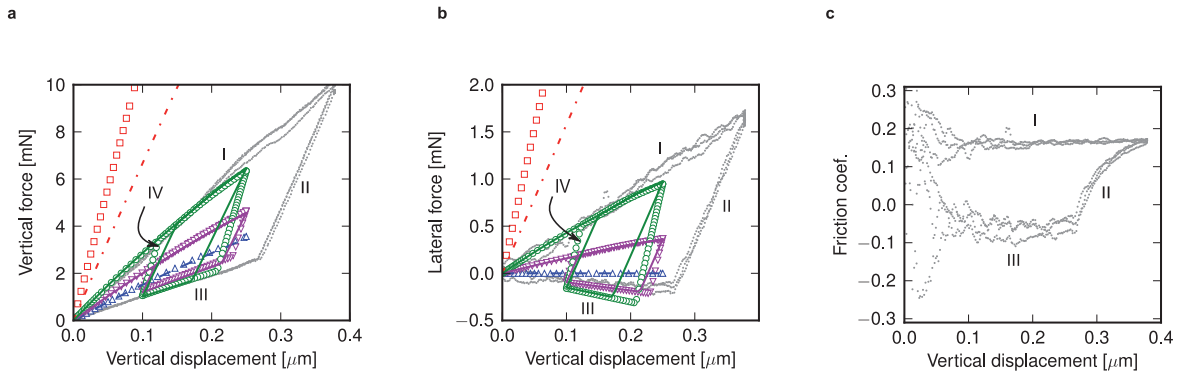


**Figure 4.3 – Notched specimen response to load-unload cycle. (a) Vertical force, (b) lateral force, and (c) apparent friction coefficient as a function of vertical displacement. The experimentally measured response is shown in light grey. The response obtained by finite element calculations from non-optimized models and for a friction coefficient  $\mu = 0.08$  is shown with (magenta) inverted triangles and for  $\mu = 0.15$  with (green) circles. The corresponding responses after optimization of models are indicated with solid line.**

#### 4.4.2 Role of friction

It is clear from Figure 4.3 that  $\mu$  significantly affects the system response. This is seen in the load–unload cycles, and notably in the stiffness of the system as represented by the slope. The system stiffness during loading in Region I, and thereby the vertical and lateral force reached at the prescribed maximal vertical displacement, increase substantially with increasing  $\mu$ . The slope of unloading Region III by contrast varies only slightly with  $\mu$ . During unloading in Region II or reloading in Region IV the system stiffness also does not seem to depend on  $\mu$  at all. Moreover, the slope of both Regions II and IV is the same as the slope of the response corresponding to perfect sticking contact between the rooftop and the indenter (infinite  $\mu$ , red squares). This leads to conclude that no relative sliding motion occurs between the rooftop and the indenter in Regions II and IV. The implication is that, in experimental curves, the slope that is displayed in this portion of the signal is characteristic of the intrinsic elastic deformation of the notched specimen under the simpler condition of a fully constrained rooftop. This being easily measured and informative, unload/reload cycles were systematically performed in all tests of this work.

By comparing in Figure 4.3 the slopes of Regions II calculated with the FE model (green circles, magenta down-triangles or red squares) with those of the experimentally measured Region II (shown in grey), it is clear that the model, based on the dimensions measured from SEM images of a notched specimen alone, does not capture correctly this intrinsic stiffness of the system measured in experiment, despite the very good agreement for responses in Regions I for  $\mu = 0.15$  and Region III for  $\mu = 0.08$ : the modelled system in Region II is substantially stiffer than the experimentally measured system. This discrepancy cannot be explained by imprecision in model geometrical parameters without seriously violating consistency with the dimensions observed on SEM images.



The greater observed specimen compliance is most realistically ascribed to the encastre conditions that were assumed, in the calculations, to hold along the plane where fibre enters the matrix: apparently, there is a non-negligible contribution from fibre deformation within the matrix and from deformation of the matrix itself in the apparent notched specimen compliance. To correct for this effect, we assume that the embedded fibre and the surrounding matrix both deform elastically, and simply assimilate these to an extra length of exposed fibre. Thus, using iteration to match the Region II slopes in experiment and the model, we prolong in the model the fibre portion situated below the ligament by the added length  $H_m$  that brings measured and simulated slopes to become identical. With the sample shown in Figure 4.3 for example, the extent of added fibre length after this optimization is  $H_m \approx 0.35H$ .

The system response recalculated using the effective fibre length,  $H+H_m$ , is drawn in Figure 4.3 using solid lines. As seen, elongating in this way the sample affects parts in the cyclic response curve where relative motion between fibre and indenter is absent (Regions II and IV), while the stages during which the fibre deflects laterally (Regions I and III) remain almost unchanged. The response in Regions I and III is thus defined predominantly by the lateral deflection and localized bending of the fibre ligament, while in Regions II and IV, where the rooftop is essentially held fixed, the whole fibre (ligament, upper part and the lower part of the sample) contributes to the response as if the entire sample was simply compressed. The effect of constraint at its bottom therefore becomes more significant for higher friction coefficients, i.e., when lateral constraint of the rooftop is stronger.

The value of  $\mu$  also affects the stress distribution on the outer surface and within the ligament (Figure 4.4). For very low  $\mu$ , a large tensile first principal stress,  $\sigma_1$ , appears on and near the ligament outer surface close to the plane of axial symmetry (Figure 4.4a and Figure 4.4b). The highest tensile  $\sigma_1$  value is found on the ligament surface in the plane of axial symmetry, where it is relatively constant over a wide portion of the ligament length for low friction coefficients (blue/triangles and magenta/down-triangles data sets, Figure 4.4b). With increasing  $\mu$ , the distribution of  $\sigma_1$  on the surface along Line PQ, becomes increasingly distorted, with a pronounced maximum value that shifts upwards (green circle/lines in Figure 4.4b). Ultimately, for  $\mu \rightarrow \infty$ ,  $\sigma_1$  develops a pronounced peak on the surface opposite the upper notch corner (red squares and lines in Figure 4.4c). Moreover, excessive lateral confinement caused by high  $\mu$  values (short sample in Figure 4.4c), tends to distort the entire  $\sigma_1$  field within the ligament, to the point that, due to a large shear stress, additional regions of high  $\sigma_1$  stress develop at the lower corner of the notch and at the bottom where the sample is constrained, as indicated with arrows in Figure 4.4c. Note also that this undesirable stress field distortion can further be enhanced, and can also directly be produced, by a negative angular misalignment,  $\alpha < 0$ . As was observed above for the slopes of Regions I and III, the length of fibre below the ligament has little effect on the stress distribution  $\sigma_1$  within the ligament for low  $\mu$  (blue, magenta and green, symbols vs. lines in Figure 4.4b). With strong lateral roof confinement, on the other hand, additional high stressed regions within the specimen can get much attenuated by accounting the effect of deformation within the matrix (Figure 4.4b).



To summarize, contact between the notched specimen and the indenter can strongly affect the stress state within the ligament. To produce a predominantly bending-dominated tensile stress distribution along the ligament outer surface without large shearing components, it is desirable to reduce  $\mu$  to the lowest value possible. At such microscopic scales as are being explored here, where the applied loads are generally small, the sliding friction coefficient between two relatively smooth surfaces (such as the FIB milled fibre roof and the flat indenter tip): (i) is strongly influenced by the adhesion forces between the materials, (ii) can be load-dependent, and (iii) is difficult to reduce or suppress by means of conventional lubrication [368]. In our experiments, we have found that contamination of two surfaces in contact (specimen rooftop and the indenter tip) dramatically affects the friction coefficient and the measured force-displacement signal. To obtain a reproducible response signal under stable friction, a simple cleaning procedure of the indenter tip was therefore developed and used (for details see Section 4.3.2).

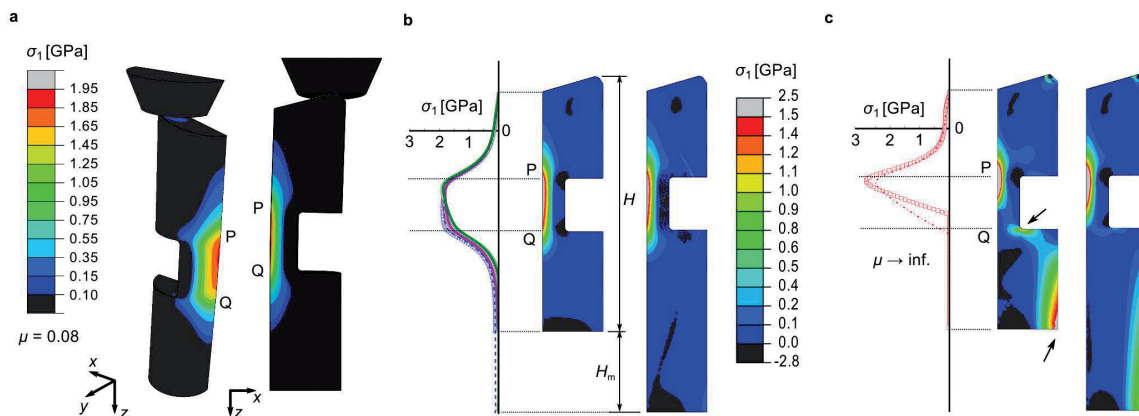


**Figure 4.4** – Effect of friction on the first principal stress distribution,  $\sigma_1$ , at vertical displacement  $0.25 \mu\text{m}$ . (a)  $\sigma_1$  distribution map on the surface of the specimen for  $\mu = 0.08$ . (b)  $\sigma_1$  distributions along the Line PQ for non-optimized ( $H$ ) and optimized ( $H+H_m$ ) notched specimen length as a function of  $\mu$ . Line colouring in graph is the same as in Figure 4.3.  $\sigma_1$  maps in plane of axial symmetry for the case  $\mu=0.15$  are shown to the right. (c)  $\sigma_1$  distribution along the Line PQ and in the plane of axial symmetry for the case  $\mu \rightarrow \infty$ . Data for the non-optimized and optimized specimen length are indicated with symbols and dash-dotted line, respectively. The colour scheme for  $\sigma_1$  maps in panels (c) is the same as that indicated in panel (b). Arrows denote additional regions of elevated stress in non-optimized models that may develop under certain circumstances; see the main text for discussion.

#### 4.4.3 Strengths measurements and fractography

We tested twenty-six notched specimens up to fracture. For simplicity, fracture tests of notched specimens were carried out using the uniaxial transducer of the indentation instrument, which only measures forces and displacements along the vertical  $z$ -axis. Therefore, data on the lateral forces and friction coefficients were not directly gathered in the tests. Despite the importance of friction in the test, this is in fact not necessary because the testing procedure and specimen FE modelling can be used to deduce, based on insights provided by results exposed above, the relevant value of  $\mu$  from vertical load and vertical displacement data. Knowing  $\mu$ , one can then calculate consistent tensile first principal stress distributions in the ligaments at the moment of fracture (see Supplementary Sections 4.7.2 and 4.7.3).

SEM examination of fracture surfaces performed after the tests shows that catastrophic failure of all tested specimens starts at the outer surface of the ligament, roughly halfway along the ligament height (Figure 4.5a-b). The fracture surface of the ligaments for all specimens furthermore shows consistent features similar to what is found in macroscopic tests of polycrystalline alumina with much larger grains or in glass [60,246]; namely, a relatively small mirror region, which encompasses the region of the fracture initiating flaw, surrounded by somewhat less distinctive mist and hackle regions (Figure 4.5c). While the mirror region in our samples features predominantly transgranular fracture, the fracture surface within the mist and hackle region is mainly intergranular. The critical flaws are in all samples associated with a small, often irregularly shaped, region of a few debonded grains, commonly located close to the ligament outer surface at, or near, the symmetry plane of the ligament (Figure 4.5c-h). This location is also where the first principal stress  $\sigma_1$  is predicted by FE computations to reach its maximum value. As a measure for the effective size of the critical flaw (outlined in Figure 4.5e-h), we use the radius of the semi-circle,  $c$ , that covers the same area as the observed debonded grains. In this way a defined effective critical flaw size  $c$ , thus observed on ligament fracture surfaces, was found to be in the range from  $\sim 120$  to  $\sim 380$  nm (see Table 4.1 in Supplementary information, Section 4.7.2).

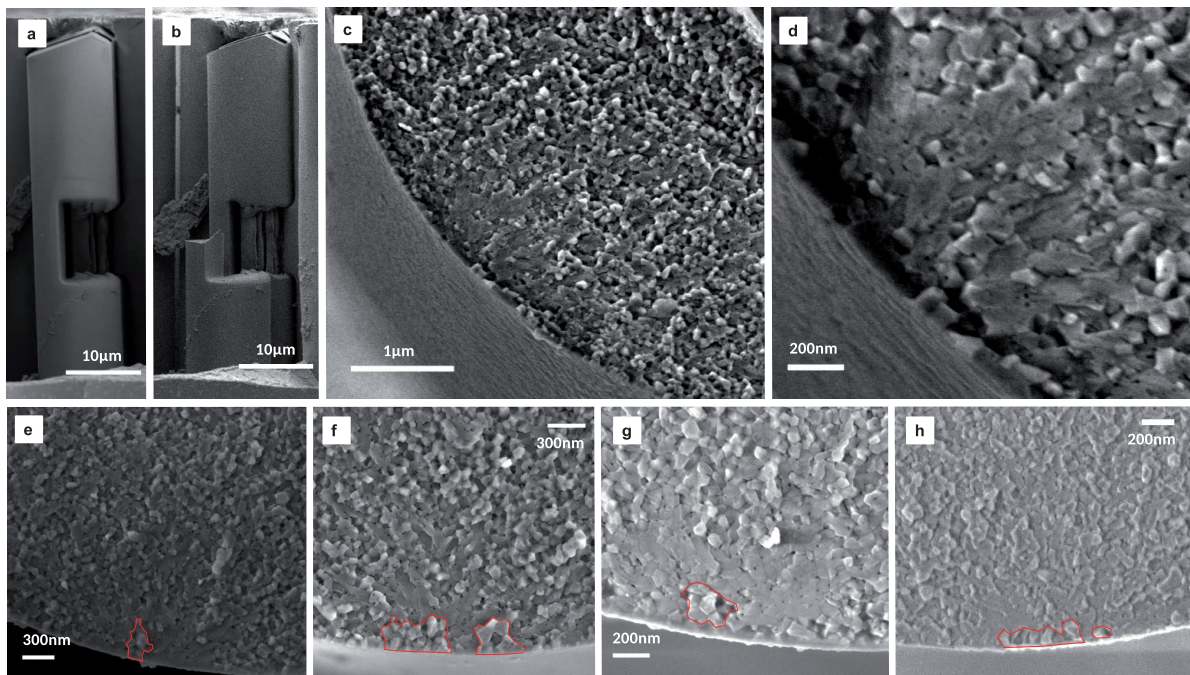


**Figure 4.5 – Fracture of a notched specimen. Specimen before (a) and after (b) fracture. (c) Fractured surface of the ligament sample shown in panel (b) investigated by high resolution SEM. (d) High magnification image of the critical flaw region from panel (c). (e)–(h) Representative examples of the mirror region encompassing the zone of debonded grains indicating the critical defect (outlined in red) as observed on the fracture surfaces of other broken ligaments.**

## 4.5 Discussion

### 4.5.1 Critical flaws

The strength of alumina fibres, from which we produced our notched samples, has been previously measured in (macroscopic) uniaxial tension experiments with fibre gage lengths in the range from 25 to 254 mm [99,100,335]. With a mean fibre diameter of  $\sim 12 \mu\text{m}$ , these gage lengths correspond roughly to fibre volumes in a range from  $\sim 2.8 \times 10^6$  to  $\sim 28 \times 10^6 \mu\text{m}^3$ . Critical defects that govern the strength of the fibres in macroscopic tests have been classified as internal or surface defects [99]. Internal defects were identified as single spherical or non-spherical pores, while surface defects included weld-lines, blisters, surface cracks and nodules. In about  $\sim 38\%$  of all macroscopic tests, however, the defects could not be simply identified.

The notched sample test probes much smaller volume of the fibre material than does macroscopic tensile testing; typical ligament volumes are in the range from  $V_L \sim 100 \mu\text{m}^3$  to  $\sim 500 \mu\text{m}^3$  (see Table 4.1 in Supplementary information, Section 4.7.2) and only a fraction of this volume is under tensile stress. Still, the region of debonded grains identified here as the critical flaw corresponds in its size and its irregular shape to “unidentified” surface defects previously reported after macroscopic tensile fibre tests [99]. Interestingly, the strength of this defect type measured here (peak stress  $\sigma_{1c}^P$  in the range from  $\sim 3.8$  to  $\sim 6.5$  GPa, Table 4.1 in Supplementary information, Section 4.7.2) exceeds by up to a factor near two the strength values measured in macroscopic tensile tests (the characteristic fibre strength for a gauge length of 25 mm corresponding to material volume of  $\sim 2.8 \times 10^{-3} \text{ mm}^3$  is  $\sim 3.3$  GPa) [99,335].

The dependence of strength on the defect size was analyzed (for macroscopic fiber test data) by Cantonwine and by Wilson & Visser in terms of Griffith’s criterion for brittle fracture

$$\sigma_f = \frac{K_{Ic}}{Y} \frac{1}{\sqrt{c}} \quad (4.1)$$

where  $\sigma_f$  is the strength,  $K_{Ic}$  is the fracture toughness, and  $Y$  and  $c$  are the crack geometrical factor and size, respectively [99,100]. By assuming that the semi-circular surface cracks are small relative to the fibre diameter ( $Y = 2/\sqrt{\pi} \approx 1.12$ ) and estimating the fracture toughness of the fibre to be that of alumina with equivalent nano-sized grains (e.g.  $K_{Ic} \approx 2.75 \text{ MPa}\sqrt{\text{m}}$ ), both Cantonwine and Wilson & Visser concluded that Griffith’s equation in most cases (for most of the defect types) significantly overestimates the critical crack size when compared to the defects identified on the micrographs. This in turn led Cantonwine to consider the possibility of sub-critical crack-growth before final failure. Indeed, environmentally assisted sub-critical crack growth is a phenomenon that alumina, in general, is well known to be susceptible to [52,56,246]. Since for the range of stress rates used in the present work the correlation between peak ligament stress  $\sigma_{1c}^P$  and applied stress rate was found to be very weak, we estimate that the effect of test environment can be neglected in our experiments. Thus, the sizes of the small intergranular decohesion regions surrounded by a region of transgranular fracture (the mirror) on fractured surfaces of the ligaments (outlined in Figure 4.5) most likely reflect the true

sizes of the critical defects that caused ligament failure. Note, also, that the irregular shapes of these decohesion zones makes it unlikely that these were caused by the etchant that was used to dissolve the matrix (defects would line the fibre surface were this the case).

Figure 4.6 compares strength data for fibres versus the defect size obtained from macroscopic tensile tests (triangles) with data obtained from the notched specimens (circles). From macroscopic tests, only samples the failure of which was due to surface defects are considered, since the tensile stress that results from ligament bending probes mainly flaws in the region near the outer ligament surface. In addition, we assume that the onset of catastrophic failure is by intergranular fracture. This assumption is motivated by a recent study where a fracture toughness of  $\sim 2.34 \text{ MPa}\sqrt{\text{m}}$ , most likely corresponding to the intrinsic grain boundary toughness of the material making the fibre, was measured with a microscopic chevron-notched cantilever method [332]. This value of fracture toughness is somewhat smaller than the value assumed by Cantonwine and by Wilson & Visser; however, not by much. Knowing the intrinsic grain boundary fracture toughness, strength-limiting flaws may be slightly smaller than the whole region of debonded grains outlined in Figure 4.5 if final failure is preceded by a small amount of stable crack growth, the magnitude of which is undetectable given the irregular shape of the intergranular zones. As seen in Figure 4.6, the data points obtained from notched specimen tests, despite the unavoidable uncertainty in decohesion zone size and shape, are consistent with the trend set by macroscopic specimens that did not contain internal defects.

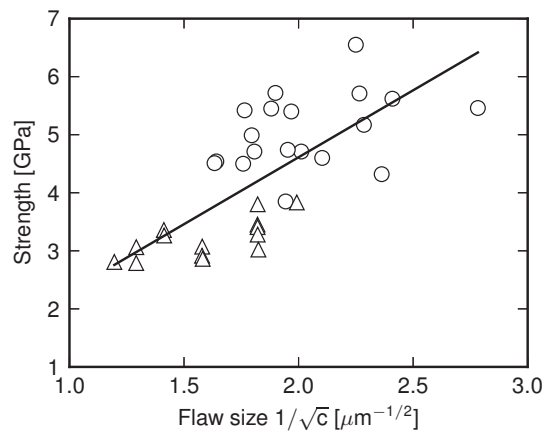


**Figure 4.6 – Strength as a function of surface defect size for alumina fibre. Triangles represent strength data obtained by macroscopic tensile tests in samples for which the critical defect was identified as a surface flaw. Circles represent data obtained from the present work (peak stress  $\sigma_{1c}^p$  and critical flaw size  $c$  reported in Table 4.1 in Supplementary information, Section 4.7.2). The solid line is a linear fit of Eq. (4.1) to the data points with  $K_{Ic} = 2.34 \text{ MPa}\sqrt{\text{m}}$  and a geometrical factor  $Y=1.04$  (treated as a fitting parameter).**

#### 4.5.2 Statistical strength analysis

The strength of brittle materials is commonly a distributed (statistical) quantity, which reflects the size distribution of the critical flaw population(s) present in the material [369]. The size of the critical flaw that initiates the catastrophic failure thus varies from specimen to specimen and varies with specimen volume. The strength of brittle materials is represented by a cumulative failure probability



distribution function,  $P_f(\sigma, V)$ , which is generally a function of some convenient measure of the stress amplitude,  $\sigma$ , and depends on the specimen volume  $V$  [89]. The distribution function  $P_f$  can be described by several statistical models [370,371]; we adopt here the two-parameter Weibull distribution [372,373], mainly because the strength of macroscopic tensile fibre specimens was previously analysed in this way [99,100,335].

In Weibull “weakest-link” theory, where the material is imagined as a chain of independent volume elements and the global failure of a complete chain is associated with the failure of the weakest individual element, the strength is described by a distribution function that contains two parameters: the Weibull modulus  $m$  and the scaling constant, *e.g.*  $S_0 = V_0\sigma_0^m$ , where  $V_0$  is a reference material volume and  $\sigma_0$  the characteristic strength associated to the reference volume  $V_0$ .

For constant modulus  $m$  (*i.e.*, assuming that  $m$  is a material parameter), an intrinsic property of the theory is the size effect,  $V_0\sigma_0^m = V\sigma^m$ , by which the characteristic strength  $\sigma$  at arbitrary material volume  $V$  can be extrapolated knowing the characteristic strength  $\sigma_0$  at volume  $V_0$ . Applying Weibull statistical analysis to tested notched specimens (see Supplementary Section 4.7.4 for details), we find that the Weibull modulus of the fibre  $m = 7.2$  with a characteristic strength of  $\sim 5.3$  GPa for an effective material volume of  $\sim 7 \mu\text{m}^3$  (mean effective volume of the ligaments). By comparison, the Weibull modulus of the fibre determined *via* macroscopic uniaxial tension tests is documented to be in the range from  $\sim 9$  to  $\sim 11$ , and can drop to  $\sim 7$  if the fiber is heat-treated. In addition, it was shown that the fibre strength follows Weibull scaling over gauge lengths in the range of 25 to 254 mm with a consistent value of  $m \sim 9.7$  [100].

The present data for the strength of the nano-crystalline alumina fibre measured by the notched specimen method are thus consistent with fractographic evidence, microtoughness data, and also with data obtained for fibres that failed due to surface flaws in macroscopic tensile tests reported in the literature (Figure 4.6). The strength data for the fibre also show consistency across macroscopic and small-scale tests as concerns the Weibull modulus; however, the local strength measured with the present notched specimen test ( $\sim 5.3$  GPa) is very different from that found after macroscopic tensile testing ( $\sim 3.3$  GPa). Figure 4.7 shows individual measurements of the strength of the fibre versus the probed effective material volume, obtained from macroscopic uniaxial tests (triangle, square and diamond) or from microscopic notched sample tests (circles). This leads to conclude that Weibull scaling cannot be used to predict the strength of the fibre at small effective volumes from macroscopic test data, or vice-versa: Weibull statistical analysis fails across large variations in volumetric scale with this material.

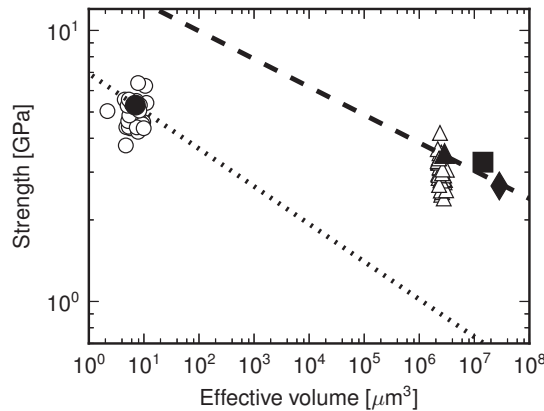


**Figure 4.7 – Alumina fibre size effect.** Weibull scaling from literature data measured by macroscopic tensile tests on alumina fibres of gauge length  $L = 25$  mm (triangles), 125 mm (squares) and 254 mm (diamonds) [99,100,335]. The slope of the dashed line is  $-1/m$  with  $m = 9.7$ . The strength data obtained from present notched microspecimen tests are indicated by circles. Weibull scaling based on microscopic strength statistics is indicated by the dotted line with slope of  $-1/7.2$ . Open symbols represent results obtained for individual tests indicating the range of effective volumes. Solid symbols represent the characteristic strength values corresponding to representative effective volumes of the tests.

This measured difference in fibre strength statistics could reflect changes in the fibre properties introduced by the composite wire-making process: the notched fibre specimens used in the present study are prepared from fibre segments that were extracted from the composite wire. This scenario, however, is unlikely because wire processing temperatures (somewhat above the melting point of aluminium, *i.e.*, around 700 °C) are well below the range where fibre properties have been documented to be affected by heat treatment; the fibre exposed to  $\sim 1100$  °C still retains its strength of  $\sim 3.3$  GPa, while the Weibull modulus decreases to  $\sim 7$  [99]. In addition, measurements of damage accumulation during tensile deformation of the composite wire from which these fibres were extracted are consistent with statistics derived from macroscopic fibre tensile tests [374–376].

More likely, the inapplicability of Weibull scaling across a large range in specimen volume highlights the difference between microscopic and macroscopic measures of the strength of brittle second phases such as the fibres explored in this work. This breakdown of Weibull size effect can have several causes [377,378]: (i) for  $m > 6$  and decreasing effective volume, Weibull scaling eventually can lead to sizes of the critical flaws that are too large to fit the specimen effective volume, and (ii) at small specimen volumes the density of critical flaws might rise to an extent where flaws begin to interact, which directly violates the assumption that flaws are independent of each other. Since the critical flaws in notched tests are observed to be regions of a few debonded grains, these flaws could indeed be reasoned as being clusters of smaller interacting defects, each one grain wide. If this is the case, *i.e.* if the smallest flaw of this kind found here represents only a small number of grain areas, then the local strength values measured here most likely represent the limit for the attainable ultimate strength of the alumina fibre material tested here.

The implication of the observed fibre strength size-effect is that there are two scales of critical flaw population, and hence of damage accumulation statistics, that govern the behaviour of a composite



made of these fibres. It is known that the macroscopic fibre strength distribution, measured by tensile testing individual fibres, governs damage accumulation in the composite when it is deformed in uniform tension. This same macroscopic population governs its tensile strength under global load sharing condition when it is tested in tension and also under local load sharing when the final damage avalanche that breaks the composite in half during a tensile test comprises only a few fibres in a low-strength matrix [374–376]. On the other hand, when damage and fracture of the composite are governed by local processes, as are found at the tip of a crack, or with a strong matrix in fibres neighbouring a broken fibre for example, then it is the microscopic strength distribution that will govern the process and hence the composite behaviour. To analyse or model such processes, data from the present testing method are therefore more appropriate than would be, for example, strength data from tensile tests conducted on fibres samples several centimetres long.

#### 4.6 Conclusion

The local strength of nanocrystalline alumina fibres  $\sim 12\ \mu\text{m}$  in diameter extracted from a composite wire by deep etching the aluminium matrix can be measured free of ion-milling artefacts using an adaptation of a method devised to test ceramic ball bearings. FIB micro-machining is used to shape exposed fibres to produce (i) a wide and deep notch in the central part of the fibre and (ii) a roof parallel to the notch situated at the top of the fibre and eccentrically placed on the notched fibre side. Upon loading to fracture the notched fibre specimen vertically along the roofline with a flat diamond tip of a nanoindenter, the circular segment cross-section ligament is bent to develop a state of tensile stress, which peaks on the curved outer ligament surface opposite the notch, in a region of material free of damage from ion milling. It is consistently observed that brittle catastrophic failure takes place in the ligament, roughly halfway along its height.

Each test is analysed with a bespoke finite element model based on specimen dimensions measured from SEM images, to obtain the stress distribution in each fibre ligament at the moment of fracture. It is shown that friction developed along the line of contact between the indenter tip and the fibre affects strongly the measured force–displacement signal. With a sufficiently clean indenter tip the contact behaviour is observed to be stable, with a relatively constant friction coefficient and a smooth, reproducible loading response signal. The friction coefficient, despite being more or less constant during each particular experiment, is found to change significantly from experiment to experiment: a procedure is described that estimates, using partial-unload/reload cycles, its value to produce realistic simulations of each test. The resulting ligament stress fields are shown to be relatively insensitive to uncertainty in most geometrical parameters of the model; two parameters, namely the notch depth and the fibre diameter, have the greatest influence and must thus be measured with precision.

Twenty-six tests are conducted and reported. Analysis of fractured surfaces of the notched fibre ligaments shows that fracture is initiated from regions close to the outer ligament surface, where the tensile stress is predicted to be highest. Initial flaws are consistently observed to be regions of a few debonded grains. Compared to the fibre strength measured by macroscopic tensile tests of individual fibres, strength values obtained by the present notched fibre technique are higher, as one would expect since the method probes much smaller fibre volumes. The measured values are consistent with the

observed size of flaws knowing the fracture toughness of the material. Strength data can be fitted to a Weibull distribution: the Weibull modulus  $m = 7.2$  and the characteristic strength of  $\sim 5.3$  GPa is associated to an effective material volume of  $\sim 7 \mu\text{m}^3$ . These values are realistic in view of the measured flaw size and fracture toughness values; yet they differ significantly from values found after testing macroscopic fibre lengths, indicating that the microscopic and macroscopic strength distributions of this material are governed by different flaw populations.

## 4.7 Supplementary information

### 4.7.1 Notched specimen FE model with explicit contact friction

To interpret measurements conducted in mechanical tests, the deformation of each notched specimens is simulated using the Finite Element method implemented in Abaqus FEA v. 6.11 software (Dassault Systèmes Simulia Corp., Providence, RI, USA). By symmetry, we consider only half of the notched fibre and the indenter in the model. The contact behaviour in the tangential direction between the two elastic materials is modelled assuming classical, isotropic Coulomb friction,  $\tau = \mu \times p$ , to relate the shear contact stress  $\tau$  with the contact pressure  $p$ , assuming a constant friction coefficient  $\mu$ . The normal contact direction is modelled as being hard; thus volume overlap between indenter and notched specimen is not allowed.

The flat diamond indenter is taken as a truncated  $60^\circ$  cone with a flat tip of radius  $10 \mu\text{m}$ . It is discretized using linear hybrid hexahedral (C3D8H) finite elements. The indenter material is assumed isotropic and linear elastic with a Young's modulus of 1141 GPa and a Poisson's ratio of 0.07, these values being characteristic of diamond.

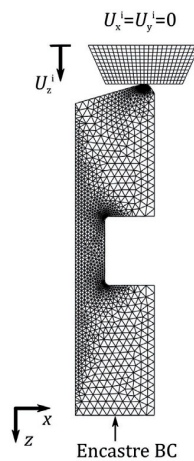


**Figure 4.8 – Example of 3D FE mesh used in modelling notched specimen.**

The geometry of each notched fibre is reconstructed based on dimensions previously measured from SEM images of the notched fibre in question. The fibre material is then discretized using tetrahedral finite elements. Mesh regions around the notch corners, along the outer ligament surface, and in the area of the fibre roof where the indenter contacts the fibre (Figure 4.8) are all refined in order to obtain

both a converged overall system response and also a converged local maximum principal stress distribution within the ligament and along its outer surface. The default type of finite element used for fibre discretization is quadratic tetrahedral (C3D10). For the contact region we use quadratic tetrahedral elements with an improved surface stress formulation (C3D10I).

The material forming the nano-crystalline Nextel™ 610 fibre is considered to be isotropic, nonlinear (third-order) elastic [379]. The linear (second order) elastic material parameters of Nextel™ 610 were taken from the literature with values for the Young's modulus of 373 GPa and Poisson's ratio of 0.235 [100,380]. The third order fibre constants are estimated on the basis of the measured elastic constants for polycrystalline alumina [381], which are additionally corrected for porosity as inferred from the ratio between the Young's modulus of Nextel™ 610 and that of dense alumina (403.4 GPa according to [382]).

The bottom surface of the notched fibre part is fixed by an encastre boundary condition (all displacements and rotations are zero), while loading is applied by prescribing a vertical displacement of the indenter top surface. The two lateral displacements of the indenter top surface are fully constrained. The vertical and lateral response of the model system is represented by the dependence of each of the vertical and lateral forces on the prescribed vertical displacement. Vertical and lateral forces are calculated by summing the nodal reaction forces in the  $z$  and  $x$  direction, respectively, over the indenter top surface.

#### 4.7.2 First principal stress distribution at the moment of ligament fracture

The loading function for the nano-indentation instrument was programmed in such a way as to conduct at least one or more load/partial-unload cycles before increasing the load or displacement to values at which the notched specimens typically fracture. Figure 4.9 shows typical vertical responses (black line) up to the point of catastrophic failure (square symbol at point C). From tests in which load-unload cycles were performed periodically at steadily increasing vertical force (Figure 4.9a), it was observed that slopes of Regions II and IV do not change significantly as the load is increased up to the critical value, indicating that deformation of the notched specimen remains elastic and reversible. An abrupt unloading after the critical point is a typical signature of brittle fracture. The experimental data for critical vertical loads,  $F_z^c$ , and displacements,  $U_z^c$ , collected for all notched specimens are given in Table 4.1.

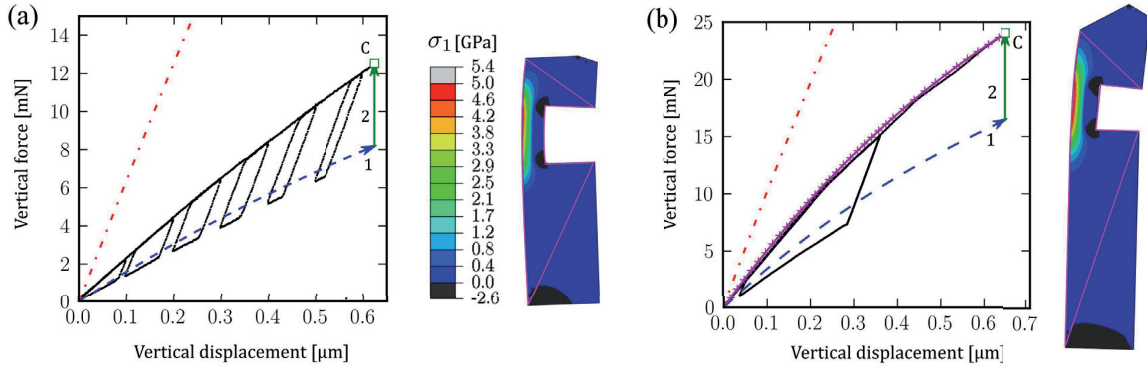


**Figure 4.9** – Vertical response of two notched specimens up to the moment of fracture and corresponding tensile first principal stress distribution,  $\sigma_{1c}$ , at the critical point C indicated with the square symbol. The experimentally measured response is plotted in black. Corresponding response obtained from FE calculations is indicated in colour. The predicted response assuming fully constrained lateral motion of the rooftop is shown in red. The two-step calculations used to obtain the stress distribution at the critical point are: (1) frictionless sliding up to the critical vertical displacement  $U_z^c$  (blue) and (2) lateral pullback deflection at constant vertical displacement  $U_z^c$  up to the critical load  $F_z^c$  (green). The response of the model in panel (b) assuming constant, back-calculated friction coefficient (see text for details) is shown with magenta crosses. The scale bar for the stress map in panel (b) is the same as in panel (a). The tensile first principal stress field contained within the volume outlined in pink is used for the statistical strength analysis.

SEM images collected before and after the test of each notched specimen are used for quantification of the specimen geometry (Table 4.1). Since each FIB milled specimen has a somewhat different geometry, each specimen is analysed with its own FE model. Bespoke FE models resembled the FE model used in the main text to illustrate the general response of the notched specimen; however, since friction coefficients in fracture tests are not directly measured, we simplify the FE models by omitting both the indenter and explicit modelling of the frictional contact behaviour at the rooftop edge. This simplification significantly improves the speed of the individual test analysis while causing no significant loss of accuracy in computing the stress within the ligament or the global response, since the specimen is elastic and the stress distribution at the line of loading at the roof is sufficiently far from the bending ligament (Saint-Venant’s principle).

Table 4.1 – Experimental and numerical data of tested notched fiber specimens.

fiber #	$D$ [ $\mu\text{m}$ ]	$H$ [ $\mu\text{m}$ ]	$H_m$ [ $\mu\text{m}$ ]	$w$ [ $\mu\text{m}$ ]	$t$ [ $\mu\text{m}$ ]	$h$ [ $\mu\text{m}$ ]	$l$ [ $\mu\text{m}$ ]	$\alpha$ [ $^\circ$ ]	$V_L$ [ $\mu\text{m}^3$ ]	$F_z^c$ [mN]	$U_z^c$ [ $\mu\text{m}$ ]	$c$ [nm]	$U_x^c$ [ $\mu\text{m}$ ]	$F_x^c/F_z^c$ [-]	$\sigma_{1c}^p$ [GPa]
1	11.5	25.3	19.84	7.1	6.9	15.3	9.1	-0.6	252	21.63	0.47	375	0.517	0.20	4.51
2	11.1	34.3	15.04	7.1	6.5	19.6	8.9	0.9	204	14.04	0.52	324	0.973	0.17	4.50
3	11.2	30.4	19.08	6.3	6.7	24.5	9.7	1.2	278	34.84	0.54	371	0.956	0.21	4.54
4	12.1	27.7	14.38	8.5	9.9	18.4	8.8	-1.9	284	12.53	0.62	262	1.053	0.18	4.74
5	12.1	37	17.39	7.5	9.1	20.1	10.2	-0.8	365	18.10	0.58	179	0.909	0.16	4.32
6	11.2	41.5	3.75	7.3	6.8	13.9	9.5	4.4	208	12.67	0.77	283	0.792	0.23	5.45
7	13.1	45.3	37.41	11.4	8.1	17.1	6.1	3.1	83	1.61	0.88	-	1.863	0.09	5.14
8	12.5	44.1	25.83	7.8	11.4	24.4	9.3	0.4	481	26.45	0.94	-	2.009	0.11	6.37
9	11.3	40.6	19.97	7.5	10.4	22.9	7.2	1.9	308	18.33	0.92	198	2.216	0.13	6.55
10	11	45	0.99	7.8	9.7	17.2	7.8	1.8	223	10.38	0.84	195	1.232	0.22	5.71
11	12.7	44.2	22.49	8.9	10.8	30.1	9.4	0.4	344	9.31	0.84	247	2.423	0.06	4.71
12	10.9	42.7	16.33	6.8	9.6	30.9	9.3	-0.5	308	12.33	0.71	306	2.327	0.08	4.71
13	11.4	39.7	15.55	6.4	9.1	30.2	9.9	2.5	392	19.72	0.91	-	2.477	0.08	5.52
14	11.9	42.9	18.72	7.8	10.8	29.8	9.3	0	367	11.25	0.74	226	2.233	0.06	4.60
15	11.4	46	21.07	7.8	9.7	32.9	8.9	0.4	268	9.50	0.91	-	2.923	0.10	5.22
16	11.4	45.9	9.02	7.4	10.7	31.6	9.7	1.76	342	12.65	0.84	-	2.184	0.18	4.51
17	12	48.1	7.72	9.2	11.1	31.6	9.6	2.75	223	4.50	0.96	265	2.295	0.21	3.85
18	12	54.3	5.91	8.2	9.2	30.3	7.6	-0.2	283	24.53	0.58	310	1.970	0.14	4.99
19	11.7	34.5	15.88	8.4	8.8	21.8	7.1	1.3	219	12.42	0.72	-	1.778	0.14	5.56
20	11.2	37.1	22.66	7.2	8.4	19.5	7.9	0	265	18.29	0.64	172	1.441	0.08	5.62
21	12.2	38.4	23.38	7.7	8.5	23.2	8.1	1.5	333	24.03	0.65	321	1.589	0.11	5.42
22	11.4	38	63.46	6.7	7.7	19.8	7.9	1.8	306	25.90	0.57	191	1.123	0.08	5.17
23	11.1	53.5	22.66	8	8.5	24.1	6.6	0.7	188	8.22	0.68	277	2.172	0.06	5.40
24	11	37.8	13.28	7	7.1	21.5	7.7	-0.4	222	16.83	0.56	129	1.577	0.07	5.46
25	11.2	37.2	14.91	7.4	7.4	22.1	7.4	1.2	218	20.84	0.61	277	1.507	0.15	5.72
26	11.7	35.8	15.26	7	8.9	23.1	9.5	0.5	359	18.00	0.59	-	1.397	0.09	4.48

To reliably deduce the ligament stress state at the moment of fracture, the FE calculations were decomposed into several steps. At first, the effective length of the notched specimen,  $H+H_m$ , in each model is optimized with respect to the experimentally measured slope of corresponding response in Region II of partial-unload/reload cycles. These calculations are conducted for fully constrained lateral roof deflection and are indicated by the (red) dash-dotted line in Figure 4.9. Then, after optimization, each notched FE model is loaded up to the experimentally measured critical point,  $(U_z^c, F_z^c)$ , in order to obtain the stress distribution within the ligament at the moment of fracture (Point C in Figure 4.9). Since the sample deformation is elastic, the notched specimen represents a conservative system whose stress state depends only on the coordinates of the critical point in a force–displacement diagram, regardless of the path along which the critical point was reached. Thus, a convenient way to obtain the stress field at the critical point is to prescribe the loading in two consecutive steps.

In the first step (dashed blue line, Figure 4.9), the model is loaded by prescribing a vertical displacement of the rooftop up to the critical vertical displacement  $U_z^c$ , while the lateral force during this step is kept at zero. In this way, the specimen is first deflected as it would be with no friction ( $\mu=0$ ). At the end of this first step the rooftop edge reaches a lateral displacement which is the maximum attainable lateral displacement that can be expected for a given critical vertical displacement  $U_z^c$ . In the following, second, loading step (solid green line in Figure 4.9), the vertical displacement is kept constant at its critical value  $U_z^c$ , while the lateral displacement is decreased until the vertical force reaches the measured critical value  $F_z^c$ . In this way, the effect of friction is taken into account, as the lateral displacement at the critical point is smaller than what it would be in a frictionless test. The tensile first principal stress fields of the models calculated at the end of the second deformation step around the ligament (region outlined in pink in Figure 4.9) are then used for strength analysis. The peak

values of the computed first principal stress at the critical point,  $\sigma_{1c}^p$ , in the ligament of each specimen are given in Table 4.1, along with computed test friction coefficient,  $\mu = F_x^c/F_z^c$ , where  $F_x^c$  is the lateral force at the critical point extracted from FE model and  $U_x^c$  is the corresponding lateral displacement.

The distribution of  $\sigma_{1c}$  fields along the ligament surface in the plane of axial symmetry (along Line PQ) obtained from the FE calculations at the critical point for all tested notched specimens is shown in Figure 4.10.

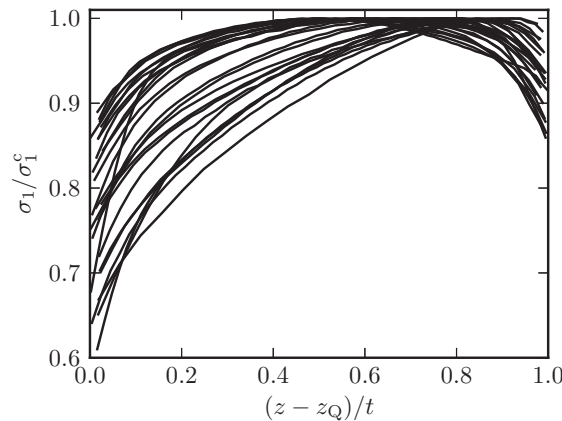


**Figure 4.10 – Distribution of normalized first principal stress  $\sigma_{1c}$  at the moment of ligament fracture on the surface of a ligament in the plane of axial symmetry along the relative ligament height (Line PQ) for all 26 tested specimens. The first principal stress  $\sigma_{1c}$  is normalized by the corresponding peak stress  $\sigma_{1c}^p$  in the ligament. The ligament length is  $t$ , while the beginning of the ligament is measured by  $z$ -coordinate of point Q, e.g.  $z_Q$  (see also main text, Figure 4.4).**

As can be seen, for most specimens the distribution is fairly uniform over the central part of the ligament, while for a few tests the  $\sigma_{1c}$  distribution shows a peak that is somewhat shifted towards the upper portion of the ligament. Severely distorted stress fields characterized by two or more high stressed regions, as discussed in the main text, were never predicted in simulations of tested samples. Thus, for all tested notched specimens, the  $\sigma_{1c}$  stress field can be described using only one peak value,  $\sigma_{1c}^p$ , which was always located at, or near, the centre of the outer region of the ligament.

Because the friction coefficient for each fracture test is not known *a priori*, the computed model responses cannot be verified for consistency with the experiments in a direct way, as was done for the sample tested in main text, Figure 4.3. Still, confidence in the validity between models and experiments can be established in the following way. Back-calculation of the friction coefficients at the critical point for each model, i.e.  $\mu = F_x^c/F_z^c$ , shows that, over the tests conducted,  $\mu$  takes various values in the range between  $\sim 0.06$  to  $\sim 0.23$  (Table 4.1). Thus, all friction coefficients are within reasonable limits. Moreover, each calculated response during the first loading step (frictionless sliding, blue dashed line, Figure 4.9) was always found to pass in-between measured Regions I and III in such a way that it is situated closer to Region III. This is consistent with the observation that Region III of the response is characterized by a smaller  $\mu$  value than Region I. In addition, when the simulation is repeated by maintaining the back-calculated friction coefficient constant (the simplified notched



specimen model is deformed laterally in a way such that the ratio  $F_x^c/F_z^c$  is maintained constant), the response of the model shows excellent agreement with the experimentally measured response, as is demonstrated in Figure 4.9b (magenta crosses). Thus, although friction conditions for each test were not gleaned by direct measurement of the lateral force, the observed consistency between model and experiment confirms that contact behaviour is properly accounted for in simulations and that possible errors in the stress fields computed at the critical point due to uncertainty of the contact behaviour are small.

#### 4.7.3 Sensitivity and error analysis

We attribute the main source of uncertainty in the computed stress fields and general responses to imprecision in measuring the geometrical parameters from the SEM images. To investigate the sensitivity of the computed stress fields on geometrical parameters of the notched specimens, we performed a set of calculations in which the notched specimen geometry is perturbed by a small finite amounts, one parameter at a time, starting with the reference configuration reported in Table 4.1. Specifically, for this sensitivity study we used the geometry of Specimen No. 4, the geometry and response of which are shown in Figure 4.9a and given in Table 4.1. Of the various parameters describing the geometry of a notched specimen (see main text, Figure 4.1), the sensitivity of model predictions on the length  $H$  and on the position of the notch along the fiber  $h$  was not considered, since the effect of these two parameters is shadowed by the optimization procedure during which the effective length  $H+H_m$  of the fiber is determined.

In investigating the sensitivity to remaining geometrical parameters, each perturbed model of a notched fiber was first reoptimized for the effective length  $\hat{H} = H + \hat{H}_m$  in the same way as was done for all tested specimens; the effective length of the perturbed model was thus determined for the case where the rooftop is fully fixed, by requiring that the initial stiffness of the perturbed model be the same as the experimentally measured stiffness of the tested sample in Region II. The stress distribution in the ligament of perturbed and optimized models and its peak value,  $\hat{\sigma}_1^c$ , were then obtained by driving the model to the critical point ( $U_z^c, F_z^c$ ) via the two-step deformation that was exposed above.

Table 4.2 – Sensitivity of the ligament peak stress on notched sample geometry perturbations.

Perturbed dimension	$\hat{H}$ [ $\mu\text{m}$ ]	$\hat{\sigma}_1^c$ [GPa]	$\frac{\hat{H}}{H + H_m}$	$\frac{\hat{\sigma}_1^c}{\sigma_1^c}$
$\hat{\alpha} = \alpha - 1^\circ$	42.5055	4.81	1.01	1.01
$\hat{\alpha} = \alpha + 1^\circ$	41.6425	4.68	0.99	0.99
$\hat{l} = 0.95l$	44.9299	4.87	1.07	1.03
$\hat{l} = 1.05l$	38.8066	4.65	0.92	0.98
$\hat{w} = 0.95w$	49.3609	4.89	1.17	1.03
$\hat{w} = 1.05w$	33.5468	5.06	0.80	1.07
$\hat{t} = 0.95t$	43.0709	4.83	1.02	1.02
$\hat{t} = 1.05t$	40.7272	4.66	0.97	0.98
$\hat{D} = 0.95D$	25.9709	5.39	0.62	1.14
$\hat{D} = 1.05D$	55.1477	-	1.31	-

The outcome of this sensitivity analysis is summarized in Table 4.2. Results show that the peak value of the first principal stress in the ligament is only weakly dependent on the angular misalignment  $\alpha$ ,

the offset distance of the fibre roof loading edge  $l$  or the notch length  $t$ ; for all these parameters, a variation of the dimension by  $\pm 5\%$  leads to a relative variation in the ligament peak stress that is below  $\pm 3\%$ . The stress field in the ligament depends more strongly on precision in the value of the notch depth  $w$  and even more so on that of the fibre diameter  $D$ . It is interesting to note that, whether the notched depth  $w$  is decreased or increased by 5% from the reference value, the peak stress of the ligament increases in both cases. For lowered  $w$  the variation of the peak ligament stress is small and comparable to what happens when varying  $\alpha$ ,  $t$  or  $l$ . For increased notch depth  $w$ , however, one finds a somewhat surprising increase of the peak stress: this is explained by the fact that the fibre that was used for the sensitivity analysis has a negative misalignment  $\alpha$ , such that making the ligament more slender leads to a significant shift of the peak ligament stress upwards along the ligament surface. This causes pronounced stress redistribution within the ligament when compared to the more uniform reference stress field distribution along the surface of the ligament (this effect and the ensuing development of a pronounced peak near the top part of the ligament are discussed in the main text, Figure 4.4).

The overall outcome of the sensitivity analysis is that the value of the fiber diameter has the greatest impact on the magnitude of the stress field in the ligament: a 5% decrease in  $D$  with other parameters fixed at reference values can distort the ligament stresses thereby increasing the peak value by up to  $\sim 15\%$ . For increased  $D$ , however, the response of the notched fibre model, already for frictionless deformation (unconstrained roof lateral deflection), is found to be stiffer than the experimentally measured response. This is inconsistent with the experimental data, giving a warning that the geometrical parameters used in the model were erroneous and need to be re-evaluated.

In conclusion, with the exception of the fibre diameter  $D$  and the notch depth  $w$ , uncertainty in geometrical parameters causes no significant error for the stress distribution within the ligament and its peak value. Since it is possible for the fibre diameter to vary somewhat along the fibre length itself (this change can reflect either a change in diameter or a deviation of the fibre cross-section from a circular shape), for reliable and relevant stress field computation, diameter measurements were obtained from high resolution SEM images taken after the test with the sample strictly aligned along the fibre axis. In addition, special care was exercised in measuring the notch depth  $w$ , and agreement between the responses of the model and the corresponding sample were checked for each sample once it was modelled, so as to ensure consistency.

Note also that some uncertainty in calculated stress field is additionally possible due to the misalignment of the fibre with respect to the loading line at the roof, i.e. misalignment represented by the angle between the fibre axis and the normal to the polished surface of the sample projected on the  $y$ - $z$  plane. Uncertainty associated with this misalignment was not investigated, since it is difficult to measure its value from SEM images reliably when it is small (fibre specimens with obvious misalignment of this kind were not used in this study). We expect the effect of such misalignment to be of similar magnitude as the effect associated with angle  $\alpha$ . The resulting stress field distortion would most likely cause a slight shift of the peak stress location along the circumference of the ligament outer surface, or in other words would cause the peak stress location not to be exactly situated in the plane of axial specimen symmetry.

#### 4.7.4 Statistical strength analysis

According to Weibull theory, a specimen made of a brittle material is seen as a linear chain of independent volume elements each of which comprises a single flaw. Failure of a specimen, i.e. failure of the whole chain, is triggered by failure of the “weakest” individual element in the chain. In uniaxial tension, where the stress field is uniform across the specimen of volume  $V$ , a convenient loading measure is given by the (uniform) tensile stress at failure, e.g.  $\sigma_f$ . The two-parameter Weibull failure probability function [89,372,373] then reads as

$$P_f(\sigma_f, V) = 1 - \exp\left(-\frac{V\sigma_f^m}{V_0\sigma_0^m}\right) \quad (4.2)$$

where the independent parameters of the distribution are the Weibull modulus  $m$  (which cannot generally be considered a material parameter [383]) and the scaling constant  $V_0\sigma_0^m$ , with  $V_0$  being the reference volume and  $\sigma_0$  the characteristic strength associated to the reference volume  $V_0$ . The material strength according to Eq. (4.2) is commonly evaluated for a set of specimens with identical nominal volume  $V$ , in which case further simplification to Eq. (4.2) can be introduced by taking  $V_0 = V$  [383]. Common examples of strength analysis that make use of Eq. (4.2) are ceramic fibres and filaments subjected to uniaxial tension [384].

For a set of identical tensile specimens, the parameters of the Weibull distribution in Eq. (4.2) are conveniently determined by fitting a straight line to data plotted in a so-called Weibull plot defined by coordinate axes  $\ln(\sigma_f)$  vs.  $\ln(-\ln(1 - P_f))$ . For a set of  $N$  experiments, the strength data are ordered in ascending order and ranked (indexed) according to an increasing value, while the failure probability for each strength is evaluated with an estimator, such as e.g.  $P_{fi} = (i - 0.5)/N$ , where  $i \in [1, \dots, N]$  is the ranked experiment index. The slope of the data in a Weibull plot is then related to the Weibull modulus  $m$  while the intercept is related to the quantity  $m \ln \sigma_0$  from which  $\sigma_0$  can be obtained knowing  $m$ . By treating the Weibull modulus  $m$  as a material constant, the strength at different specimen volumes can, in principle, be extrapolated via the size effect that follows from Eq. (4.2), namely,  $V_0\sigma_0^m = V\sigma^m$ , where  $\sigma$  is the extrapolated characteristic strength associated with an arbitrary specimen of volume  $V$ .

When the stress field is not uniform, as is the case for specimens loaded in bending, the failure probability function  $P_f$  is generalized to [89],

$$P_f(\sigma(x, y, z)) = 1 - \exp\left[-\left(\frac{S}{S_0}\right)^m\right] \quad (4.3)$$

where  $S = \left\{\int_v [\sigma(x, y, z)]^m dv\right\}^{1/m}$  is the so-called Weibull stress [385], and  $S_0 = (V_0\sigma_0^m)^{1/m}$  is the scaling constant. Commonly, in Eq. (4.3) the nominator within the exponential is decomposed into two terms: (i) some representative scalar of the stress field, like the maximum (peak) stress,  $\sigma_p = \max\{\sigma(x, y, z)\}$ , and (ii) the effective volume,  $V_e = \int_v [\sigma(x, y, z)/\sigma_p]^m dv$ , such that  $S^m = V_e\sigma_p^m$ . Integration of the stress field  $\sigma(x, y, z)$  as required for calculation of  $S$  or  $V_e$  in Eq. (4.3) needs to be

carried out over a relevant volume  $v$  of the specimen that encloses the peak stress  $\sigma_p$  and where failure is highly likely to originate. Since the strength of brittle materials depends on the size distribution of defects, for a sufficiently large defect, (Mode I) fracture of the specimen can *a priori* originate at any point where the first principal stress is tensile. Thus, the region of integration  $v$  should generally be the volume of the specimen where  $\sigma_1(x, y, z) \geq 0$ . Often, however, smaller integration volumes are taken by excluding locations that only see small tensile stress values.

For some simple cases of non-uniform stress fields (e.g. plane bending), when the integration of the effective volume  $V_e$  can be carried out analytically, one can determine the parameters of the Weibull distribution via the Weibull plot using the ranked ascending values of variable  $S_i$ .

A more general and statistically more correct way to estimate parameters of  $P_f$  (or any other distribution) is by maximizing the likelihood function (or its logarithm) of  $N$  fracture experiments,  $\mathcal{L} = \prod_{i=1}^N p(S_i)$ , where  $S_i$  is the Weibull stress of the  $i$ -th experiment and  $p_f(\sigma) = dP_f(\sigma)/d\sigma$  is the general Weibull probability density function (see [370] and references therein). By using the maximum log-likelihood method, the Weibull modulus  $m$  is first found from:

$$\frac{\sum_{i=1}^N S_i^m \ln S_i}{\sum_{i=1}^N S_i^m} = \frac{1}{m} + \frac{1}{N} \sum_{i=1}^N \ln S_i \quad (4.4)$$

followed by a determination of the scaling constant from:

$$S_0^m = \frac{1}{N} \sum_{i=1}^N S_i^m \quad (4.5)$$

We use here the latter approach to analyse local nano-crystalline alumina strength statistics shown by the notched sample tests, mainly because the integration of the Weibull stress  $S$  or effective volume  $V_e$  allows one to estimate the Weibull modulus  $m$  via Eq. (4.4) and the scaling constant  $S_0$  via Eq. (4.5) from a set of specimens whose geometry need not to be constant, as is the case for FIB machined notched specimens in this work (Table 4.1). Note, however, that by using a set of specimens with different effective volumes, we implicitly assume that the Weibull modulus  $m$  of a given material over the range of these volumes is constant – given the relatively small range of volumes (to within the same order of magnitude), this assumption seems reasonable. Because all of our notched specimens fracture exclusively in the region of the ligament, the stress field relevant for the strength analysis is the (tensile) first principal stress,  $\sigma_1(x, y, z) > 0$ , in the region surrounding the ligament (outlined in pink in Figure 4.9). By numerically evaluating for each of the  $N = 26$  specimens,  $S_i^m = \int_{v_i} [\sigma_{1i}(x, y, z)]^m dv_i$  using the stress field  $\sigma_{1i}(x, y, z)$  obtained from FE computations as described above, the Weibull modulus  $m$  is first obtained from Eq. (4.4). With known  $m$ , the corresponding scaling constant  $S_0$  is then calculated from Eq. (4.5). The resulting failure probability distribution function  $P_f$  obtained from 26 notched specimens is shown in Figure 4.11.

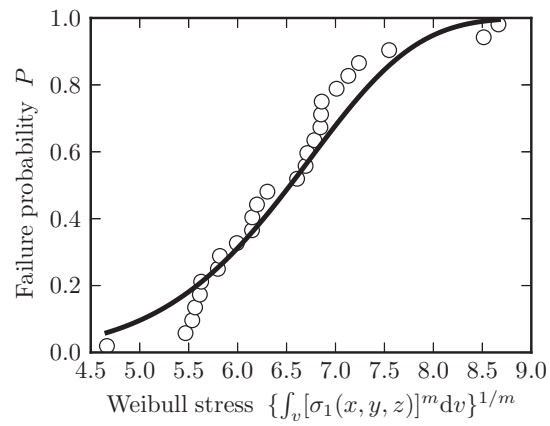


**Figure 4.11** – The Weibull failure probability distribution for nano-crystalline alumina fiber obtained from the 26 notched specimens is characterized by the Weibull modulus  $m = 7.2$  and the scaling constant  $S_0 = 6.88 \text{ GPa}\cdot\mu\text{m}^{3/7.2}$ .





# Chapter 5 The local strength of individual alumina particles

## 5.1 Disclaimer

This chapter was published as an article in a scientific journal with the open-access (CC BY 4.0) licence and its bibliographic reference is given below. The postprint version of the article is presented here with its Introduction section significantly abbreviated to avoid repetition of what was already mentioned in Chapter 1 of this thesis (extracts, including a few literal reproductions of full paragraphs of the article Introduction, are given in Chapter 1). The candidate, herewith V.P., designed the experiment under the supervision of Andreas Mortensen (A.M.). V.P. performed most of the experimental work. Particularly, the candidate FIB machined and tested all C-shape and cantilever beam specimens, analysed all tests via FEM, performed fractography, and interpreted results. V.P. and A.M. wrote the manuscript and all other authors provided feedback.

Pejchal, V., Fornabaio, M., Žagar, G., Mortensen, A.: *The local strength of individual alumina particles*. Journal of the Mechanics and Physics of Solids 109, 2017, 34-49, doi.org/10.1016/j.jmps.2017.08.005.

## 5.2 Introduction

In the present chapter, we extend the approach from Chapter 4 towards testing microscopic particulate composite reinforcements of irregular shape and low aspect ratio. Specifically, we report here observations of directly determined strength measurements conducted on Sumicorundum® (Sumitomo Chemical Co. Ltd., Tokyo, Japan) alumina particles of diameter in the range 15-30  $\mu\text{m}$ , which have been shown to provide superior reinforcement in infiltrated aluminum- or copper-based metal matrix composites [19,116,154,156,386]. As will be seen, the measured strength of the alumina particles can be higher than what is measured for high-strength nanocrystalline alumina fibres, or in alumina platelets a few hundred nanometers thick that have been used in bio-inspired composites. Their strength approaches that of high-perfection alumina whiskers and microcrystals where specific defects are absent. We identify those specific defects as: (i) grain boundaries and grain boundary grooves, (ii) micropores and (iii) other shape irregularities. We show that random grain boundaries are particularly deleterious to the strength of alumina particles, leading to an overall conclusion that alumina has great potential as a particulate reinforcement in composite materials provided it is (i) smooth in shape and (ii) single- or nano-crystalline.

## 5.3 Materials and Methods

### 5.3.1 Material

Particles investigated in this work were high-purity  $\alpha$ -alumina particles (AA-18, Sumicorundum<sup>®</sup> grade) produced by Sumitomo Chemical Co. Ltd. (Tokyo, Japan) by in-situ chemical vapour deposition. The typical particle size is between 15 and 30  $\mu\text{m}$  [110]. XRD analysis performed in our laboratory confirmed that the particles are entirely of  $\alpha$ -alumina. Chemical analysis provided by the manufacturer states as main impurities Si (< 50 ppm), Fe (< 20 ppm), Na (< 15 ppm), Mg (< 10 ppm), and Cu (< 10 ppm). The as-received powder particles have polyhedral shapes and consist generally of (i) single crystal particles with a low aspect ratio or (ii) particles consisting of two or more polyhedral crystallites linked along a grain boundary, which forms a groove at the particle surface. By investigating 200 SEM images of random Sumicorundum particles from this study, we estimate that roughly half of all the particles are single-crystalline while the other half is made of two or more crystallites forming grain-boundary grooves.

### 5.3.2 Micromechanical testing

#### *C-shaped particle test method*

To measure the local strength of the particles we extend to particles the approach presented in Žagar et al. [324]. The approach requires having particles partially embedded in a matrix that holds each particle in place during load application. To this end, a Sumicorundum particle – polymer matrix composite with a low fraction of the alumina particles (a few percent) was produced. The polymer matrix was then deep-etched, or alternatively in one specimen it was cracked, so as to cause particles partially embedded in the matrix to protrude by several micrometres out of the matrix. To prevent sample charging in the FIB/SEM and to protect the surface of particles from FIB damage and/or redeposition, the sample with partially embedded particles was coated with  $\approx 40 \mu\text{m}$  of thermally evaporated carbon. Selected particles were FIB milled to form a C-shaped particle specimen, outlined in Figure 5.1 and featuring (i) two parallel and roughly vertical sides, (ii) a wide rectangular notch machined with the beam oriented perpendicular to the previously machined sides, and (iii) a roof situated at the top of the particle cut parallel to the notch. The wide rectangular notch is machined in such a way that one of its sides is aligned parallel with a selected facet of the polyhedral particle (Figure 5.1a). This, together with the two FIB milled sidewalls and the vertical portion of the machined C-notch, forms what we call hereafter the *ligament* of C-shaped particle specimens. This ligament has a rectangular cross-section (Figure 5.1b).

This FIB-machined C-shaped specimen, sketched in Figure 5.1c, is then tested using a TI 950 TriboIndenter<sup>™</sup> (Hysitron Corp., Minneapolis, MN, USA) nanoindentation apparatus equipped with a  $\approx 10 \mu\text{m}$  tip diameter flat-end diamond probe and with a 3D OmniProbe<sup>™</sup> transducer capable of measuring vertical and lateral force simultaneously. Prior to testing, the roof of the C-shaped specimen is aligned parallel to the 3D OmniProbe flat-end diamond probe using a tilt stage fixed on the nanoindenter base stage (Figure 5.1d). As the C-shaped particle specimen is loaded vertically by the flat-end diamond probe, its ligament bends, causing the appearance of high tensile stresses along the

back-surface of the ligament. While the ligament bends, the specimen roof moves laterally and slides along the flat-end diamond probe, causing the appearance of a lateral friction force between the edge of the roof and the diamond. Using a multidirectional nanoindentation probe this lateral force was measured, to derive a friction coefficient, which was taken into account in data analysis (Figure 5.1e); see also Ref. [324]. Further details of the C-shaped particle test are provided in the Appendix, Section 5.7.

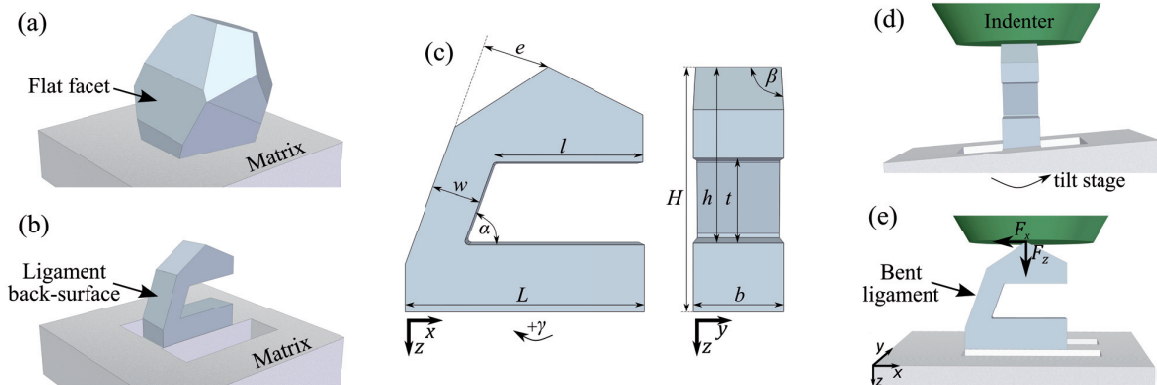


**Figure 5.1** – Schematic representation of a C-shaped particle test. (a) A polyhedral Sumicorundum particle partially embedded in a polymer matrix is (b) FIB machined into a C-shape configuration, and then tested in compression to bend a ligament of rectangular cross-section. The back surface of the ligament is left unaffected by the FIB milling operation, by design of the machining process and by coating the particle surface with a layer of weak carbon  $\approx 40$  nm thick. The roof machined at the top of the particle defines the load application line. (c) Sketch of a notched specimen with dimensions defined. (d) As a result of the machining process, the roof and notch side are oriented at a shallow angle ( $<5^\circ$ ) with respect to the matrix free surface normal (see Appendix, Section 5.7), such that the roof-edge and indenter can be aligned using a tilt stage so as to be parallel in the nanoindentation apparatus prior to testing. (e) Once the notched specimen is loaded by applying a vertical displacement (along the z-axis), the roof slides laterally along the flat indenter surface, introducing a measurable friction force in the lateral direction (along the x-axis).

Besides particles with a flat facet and free of any visible defects, several particles containing flaws of different nature along the ligament back surface to be subjected to tension during the test were prepared. These included particles with twinned jagged surfaces, and particles with grain boundary grooves; the latter were found to exert a particularly deleterious effect on the local particle strength. In a few additional specimens, the back-surface of the ligament was also FIB-machined in order to (i) compare strength results against specimens with an outer ligament surface in pristine (FIB unaffected) condition, (ii) probe the strength governed by pores revealed during sample preparation or (iii) determine the strength of particles containing a grain boundary free of the groove that is generally associated with the emergence along a free surface of such a grain boundary.

#### *Micrometric bend beams*

An alternative approach is to carve microscopic cantilever beams out of individual particles. This approach is suitable if one wishes to probe facets or features along a particle surface that is oriented roughly parallel to the polymer matrix free surface. Two such cantilever beams, both containing a grain boundary groove at the junction of two grain facets, were machined and tested. A sketch of the

cantilever beam configuration used in this work, showing sample dimension definitions, is given in Figure 5.2. In both cantilever specimens the top surface of the cantilever beam, subject to tension during the test, was left unaffected by FIB milling. These beams were then mechanically tested in-situ in the SEM using a FemtoTools FT-NMT03 Nanomechanical Testing System (Buchs-ZH, Switzerland) similarly to the tests exposed for Si particles in aluminium in [387]. Further details of particle cantilever beam specimen preparation and testing are given in the Appendix, Section 5.7.

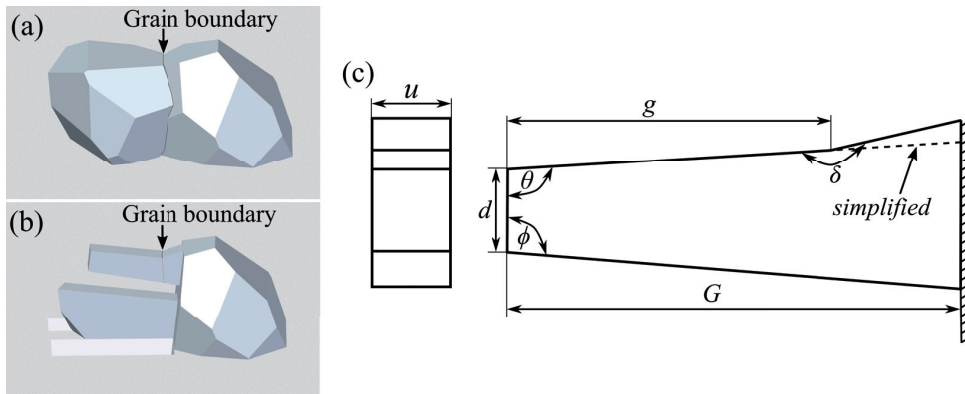


**Figure 5.2 – (a) A partially embedded Sumicorundum particle containing a grain boundary is (b) FIB milled to form a micro-cantilever that contains the grain boundary. The top surface of the micro-cantilever subject to tension during mechanical testing is left in its pristine condition, meaning unaffected by FIB. (c) Sketch of a cantilever beam geometry used in the work with definition of relevant dimensions. The edge defined by angle  $\delta$  is formed where two particle facets meet. The dashed line represents the simplified beam geometry in which the geometry-related stress concentration is eliminated.**

### 5.3.3 Finite Element (FE) simulation

The material forming the Sumicorundum alumina particles is  $\alpha$ -alumina, which is an anisotropic material characterized by six elastic constants. Because the exact crystal orientation of each particle was not determined, we assimilated the particles to an isotropic material having the orientation-averaged Young's modulus,  $E = 400$  GPa, and Poisson's ratio,  $\nu = 0.25$ , of polycrystalline alumina [22,23]. The sensitivity of the computed stress fields on the range of values for the Young's modulus and Poisson's ratio (realistic upper and lower bounds of alumina) is on the order of 5% of the computed value; see the Supplementary Information (Section 5.8.4).

Each individual C-shaped test specimen was simulated by means of a bespoke quasi-static two-dimensional plane-strain Finite element model (FEM), implemented in the Abaqus/Standard<sup>TM</sup> 6.11 software (Dassault Systèmes, Providence, RI, USA); see Figure 5.7a. The bottom surface of the visible part of the particle that is sticking out of the polymer was constrained by an encastre boundary condition (all displacements and rotations are zero). The loading was prescribed at the roof edge with vertical  $F_z$  and lateral  $F_x$  force values measured in the experiment. The FEM analysis included non-linear geometric effects (big displacements). Elements used for discretization of the particles were 2<sup>nd</sup> order quadrilaterals (CPE8).

The 2D model, for one particular C-shaped specimen of representative geometry, was compared against a more realistic three-dimensional (3D) model of the same geometry (see Figure 5.7b). The

3D model consists of the alumina particle embedded within an isotropic, linear elastic polymer-like matrix of Young's modulus  $\sim 1$  GPa (this value was inferred from an independent nanoindentation experiment conducted by ourselves on the polymer used to fix the particles). The Poisson's ratio of our polymer matrix was not determined; however, calculations show that its effect on the stress distribution within the particle ligament is negligible; thus we use a default value of 0.25. The interface between the particle and the matrix was considered as being a fully coupled (tie) contact. The bottom of the matrix was encastred. Elements used in discretizing the particle and the matrix in the 3D model were second order bricks, C3D20 and C3D20R, respectively.

The two cantilever beam tests were analysed by means of 3D cantilever finite element models reconstructed from the geometrical measurements of samples. Both cantilever beam parts that represent in reality different alumina particles (of possible different orientation) were assimilated to the same effectively isotropic alumina material described above. Cantilever beams and supports to which the cantilevers are attached were modelled using C3D20 and C3D20R elements, respectively. A more refined mesh was constructed near the location of particle boundary and near the cantilever's fixed ends. Only the portion of the cantilever from the fixed point up to the point of the load application was considered in the model. Loading was produced by prescribing the vertical point load at the free cantilever end, the force at which (load at failure) is measured by experiments. The bottom of the support was fixed by encastre boundary condition.

Tested cantilever specimens both contained a grain-boundary where two facets meet forming an edge-like feature at the top surface, situated a few hundred nanometres from the beam support and characterized by the angle  $\delta$  (Figure 5.2). The presence of the edge results in a local stress concentration ( $\delta > 180^\circ$ ) or dip in stress ( $\delta < 180^\circ$ ) along the beam top surface. The effect of this edge can be assimilated to that of a notch or protrusion. To evaluate the strength of tested beams with the edge assimilated to a geometrical flaw, we employed a simplified model in which the beam's top surface was taken to be entirely flat by extending the top portion of the beam on the left-hand side of the edge towards the cantilever support ( $\delta = 180^\circ$ ); this is also sketched in Figure 5.2c. The model then gives the nominal stress state along the beam surface treated as a flat surface along which the geometrical stress concentration site is but one of a variety of possible failure-producing flaws.

## 5.4 Results

### 5.4.1 Mechanical testing

The deep-etching sample preparation procedure provided a number of partially embedded particles situated far enough from neighbouring particles to be readily available for FIB machining. Fracturing the polymer composite provided on the other hand only a few partially embedded particles ready for FIB milling. This was mainly due to the partial sedimentation of particles at the bottom of the sample during polymer curing. Therefore, only one tested particle in this work was prepared by the fracturing method. The polymer-particle interface was found to be sufficiently strong to keep particles in place while performing the mechanical tests.

Apart from grain boundary grooves, Sumicorundum particles do not contain readily observable flaws along their surface. Cutting particles by FIB-milling during sample preparation revealed, however, that some particles contain pores of diameter in the range from a few tens to a few hundred nanometres. Pores were observed within individual crystallites as well as along alumina grain boundaries.

In total, seventeen (17) C-shaped particle specimens and two (2) *in-situ* SEM micro-cantilever beams were tested to fracture; specifics of each specimen are provided in the Supplementary Information, Section 5.8.2. Based on the flaws observed before or after testing and the state of the ligament back-surface, the tested specimens were catalogued into the following six categories: we have tested

- (i) five specimens of single crystal particles with the ligament in pristine condition, free of any visible defect (Category I) (Figure 5.3b),
- (ii) two specimens of single crystal particles with the ligament free of any visible defects and FIB machined from all sides including the ligament back-surface (Category II) (Figure 5.5a),
- (iii) three specimens of single crystal particles featuring a pore along the ligament (Category III) (Figure 5.5b),
- (iv) one particle with a twinned jagged ligament back-surface (Category IV) (Figure 5.5c),
- (v) five specimens of polycrystalline particles with all sides machined using the FIB (Figure 5.6a), including the ligament back-surface, and containing a grain boundary oriented roughly normal to the principal tensile stress direction during the test (Category V) and
- (vi) one C-shaped particle specimen and two micro-cantilever specimens containing a grain boundary groove along a ligament surface that was left unaffected by focused ion beam milling (Category VI) (Figure 5.6b).



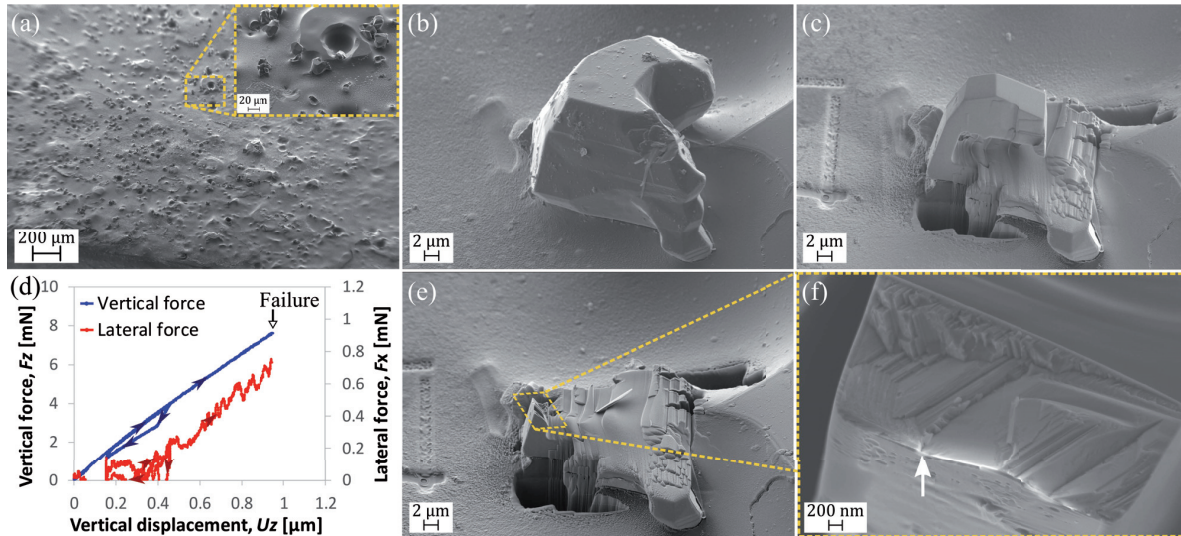


**Figure 5.3 – C-shaped particle test of a typical single-crystalline Sumicorundum AA-18 particle with the ligament back-surface in *pristine* condition, free of FIB damage and apparent defects (Category I, Specimen I-4). (a) SEM image of a polymer-matrix composite sample with particles partially embedded in the matrix after deep-etching. SEM images of the selected particle (b) before and (c) after FIB machining. (d) Vertical and lateral force vs. vertical-displacement response of the notched particle during the test. (e) SEM image of the particle after the test and (f) close-up of the fracture surface with an arrow indicating the apparent failure initiation location suggested by river-markings observed on the fracture surface.**

Figure 5.3 summarizes the course of a typical C-shaped particle test, conducted on a specimen of Category I; namely, a single-crystalline particle with its ligament free tensile surface left in pristine condition without any visible defects. Figure 5.3a represents an overview of the polymer matrix composite after deep etching with the "piranha solution" followed by carbon coating. Partially embedded Sumicorundum alumina particles are readily observable. The selected polyhedral particle for C-shape testing exhibiting a flat facet oriented roughly vertical to the polymer free surface is highlighted in the figure. Figure 5.3b-c represent the selected particle before and after FIB machining, respectively. The vertical force – vertical displacement as well as lateral force – vertical displacement response recorded during the test, shown in Figure 5.3d, exhibit a hysteresis loop produced during one load-unload cycle before the force was ramped up until failure occurred. The hysteresis is due to sliding of the specimen's roof along the flat-end diamond indenter; this is characteristic of the C-shaped sample test method, (see Chapter 4). The value of the friction coefficient, defined as the measured ratio  $F_x/F_z$ , was approximately 0.09. A sudden drop in load and jump in displacement are indicative of specimen failure.

The relatively low loads at which the ligament breaks does not produce extensive shattering of the ligament; hence fractographic examination of the samples could usually be performed (Figure 5.3e-f). The specimen in Figure 5.3f exhibited a heavily faceted fracture surface with no apparent flaw. A pattern of radial ridges observed around the area indicated by the white arrow in the figure suggests that failure initiated near or at the indicated spot. This is an important observation as the failure did not initiate in one of the FIB-machined corners; rather, failure had its origin at or near the surface unaffected by FIB micromaching.

Of the other Category I specimens, one (Specimen I-1) led to a similar conclusion, namely that failure initiated away from the FIB-affected ligament surface. The other three Category I specimens could not be examined for fractography because the fracture surface was situated below the specimen ligament, with the crack trajectory connecting the bottom corner of the specimen rectangular notch with the surface of the particle on the other end (see Figure 5.12a-b in the Supplementary section 5.8.3). This indicates that failure initiated either at (i) a greater flaw remote from the region of peak stress, situated along or just under the specimen surface below the ligament or (ii) along the highly stressed ligament surface followed by subsequent initiation and growth of secondary cracks, possibly emanating from roots of the notch corners where the comparatively small radius of curvature of few hundred nanometres (typically 200 nm - 500 nm) is likely to have concentrated post-fracture stress waves, leading to a loss of the original fracture surface. Two observations suggest that option (ii) is more plausible. First, we have observed no sign of a bigger flaw in the remaining fracture surfaces and secondly, in the specimens that broke within the ligament, we observed the presence of microcracks having their origin in the bottom corner of the specimen notch, which grew for a few hundreds of nanometres towards the other end, along a direction such that they would end below the actual ligament were their growth to continue across the specimen, giving the specimen remainder the shape that was observed in the last three Category I specimens (see Figure 5.12c-d in the Supplementary section 5.8.3).

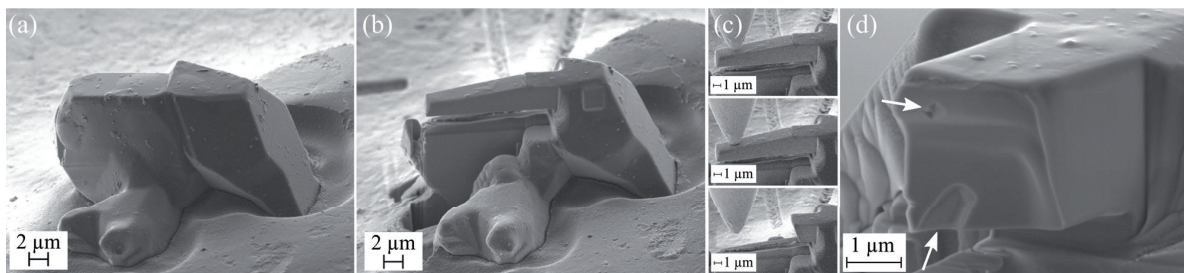


**Figure 5.4 – Summary of cantilever beam testing of a Sumicorundum AA-18 particle containing a grain-boundary groove (Category VI, specimen VI-3). SEM micrographs of (a) selected particle before and (b) after FIB machining. (c) Three frames during the in-situ SEM test using nanomechanical testing instrument equipped with sharp tungsten needle. (d) Close-up of the fracture surface of the beam after the test with arrows indicating two observed pores in the fracture surface.**

Figure 5.4 summarizes the preparation and mechanical testing of one of the micro-cantilever beam specimens. Figure 5.4a and Figure 5.4b display the selected particle before and after FIB machining, respectively. The beam was machined such that the grain boundary is contained within the beam and is oriented roughly perpendicular to the beam longitudinal axis (Category VI). The grain boundary groove was left roughly 2  $\mu\text{m}$  away from the beginning of the support. Figure 5.4c represents three frames from the recorded video of the test; the beginning of the test, the beam loaded just before failure, and the specimen after failure. One part of the fractured beam is missing because it was ejected during the test (due to the sudden release of stored elastic energy). The testing instrument recorded the load at which the beam failed. The load-displacement response was linear until failure, which was manifest as a sudden drop in load.

Figure 5.4d displays the fracture surface after the test. The fracture surface is very different from the other fracture surfaces of tested single-crystalline particles: it is smooth throughout the whole surface, indicating that the crack propagated within the grain boundary. The test also reveals the profile of the grain boundary along the beam cross-section: as seen, it is not perfectly flat. It was impossible to identify the fracture initiation site on this almost featureless fracture surface. Two flaws, one smaller pore  $\approx 300$  nm in diameter and one elongated pore (partially cut by FIB machining) with its size on the order of  $1 \mu\text{m}$ , were observed. The bigger pore was located in the portion of the beam that was in compression. Examples of tested particles from other categories along with fractography are documented in Figure 5.5 and Figure 5.6.

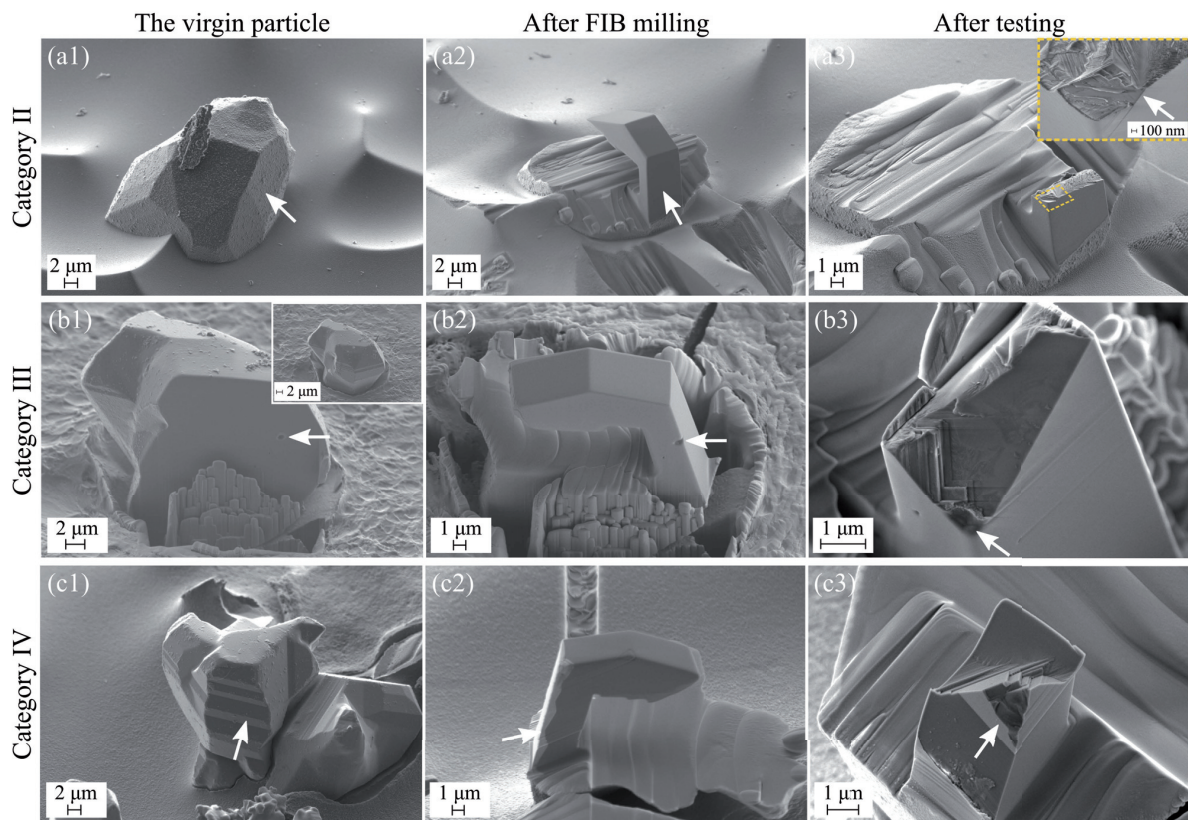


**Figure 5.5 – Overview of tested representative specimens from (a) Category II (II-1), (b) Category III (III-1), and (c) Category IV (IV-1). (a1-2) A few hundred nanometers of pristine ligament back-surface were milled away with the focused ion beam parallel to the original surface. (a3) Radial ridges observed on the fracture surface suggest fracture initiation (arrow). (b1) A pore  $\approx 800$ nm in diameter (arrow) was revealed while machining the sides. (b2) The outer ligament surface was also FIB machined in order to locate the pore close to the ligament surface where the tensile stress peaks during the consequent mechanical test. (b3) Close-up of the fracture surface after the test with fractographical features suggesting that the pore was indeed the origin of the failure. (c1) Twinned surface specimen before and (c2) after FIB machining with visible re-deposition of material on the ligament back-surface. (c3) The same specimen after the test with its fracture surface: re-deposited material has delaminated during the mechanical testing.**



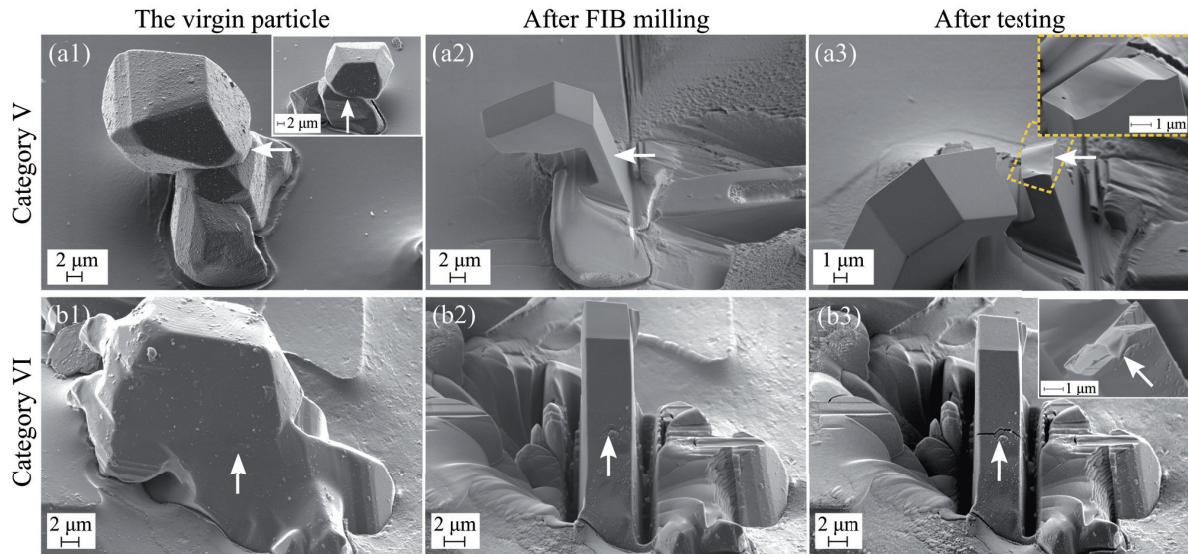
An example of a fully FIB-machined single crystalline specimen (Category II) is shown in Figure 5.5a1-a3. The surface crystallographic orientation was kept the same as the original pristine surface by FIB milling the ligament back-surface with FIB beam oriented parallel to the original surface. The fracture surface was, as for Category I specimens, heavily faceted with radial ridges indicating the site of failure initiation. Additionally, two microcracks could be observed after the test on the ligament back-surface close to the failure initiation oriented roughly at  $45^\circ$  to the horizontal plane of the ligament.

Figure 5.5b1-b3 shows a Category III particle containing a pore approximately 800 nm in diameter along the specimen's ligament surface. The pore was exposed during the FIB machining of one of the side edges of the particle, during the initial stage of the C-shaped specimen preparation (Figure 5.5b1). The back surface of the specimen ligament was then FIB machined in order to locate the pore close to its surface subjected to tension during the test. Fractography revealed that particle failure most likely initiated from the pore, and the fracture surface exhibited steps as in the previous single-crystalline particles of Category I and II. Another example of a tested particle containing a pore is presented in Figure 5.13 in the Supplementary section 5.8.3. In that sample, the pore was only revealed after the test, as it was fully contained within the ligament (note that therefore the material in and near the pore free surface, where the failure initiated, was not exposed to FIB milling).

Figure 5.5c1-c3 presents a tested particle with a twinned, jagged, surface. Redeposition of material after milling on the back-surface of the ligament is evident. After mechanical testing the redeposition layer was absent: it had apparently delaminated, suggesting that the carbon layer played its role in providing a weak interface between the particles and any redeposited material. The fracture surface exhibits again crystallographic steps.

Figure 5.6a1-a3 displays a tested polycrystalline Sumicorundum alumina particle having one grain-boundary with its plane roughly parallel to the polymer free surface. The back-surface of the ligament containing the grain boundary was machined flat by ion-milling, so as to eliminate the grain boundary groove and associated stress concentration. This specimen belongs to Category V. Similar to the Category VI micro-cantilever beam specimen, the fracture surface is very smooth and featureless throughout the whole surface, indicating that the crack propagated within the grain boundary. A minute pore with a diameter of approximately 200 nm was observed and located in the region of the ligament cross-section that was under compression during the test; therefore, it is unlikely that failure initiated there.

Figure 5.6b1-b3 shows the tested C-shape specimen containing a FIB unaffected grain-boundary groove. The grain that formed the grain boundary groove visible along the surface was much smaller than the rest of the particle, and hence essentially represented an inclusion. As a consequence the fracture surface displays a combination of (i) heavily faceted region of the parent single-crystalline particle and (ii) smooth featureless surface typical of a fractured grain boundary. EDX analysis did not reveal any chemical composition difference of the inclusion grain.



**Figure 5.6** – Overview of tested representative specimens from (a) Category V (V-3) and (b) Category VI (VI-1). (a1) A specimen with a grain-boundary oriented roughly horizontal to the free-surface of the polymer matrix and (a2) contained in the ligament with all four sides machined by FIB and therefore a flat ligament back surface (without grain-boundary groove). (b1) The only C-shape specimen from the Category VI with a grain boundary groove. (b2) Specimen contained the grain boundary within its ligament after FIB machining. Compared to the other two specimens from Category VI tested in the cantilever beam configuration, the grain boundary extends only through a portion of the ligament cross-section; see (b3).

#### 5.4.2 FEM analysis

##### *C-shaped particle test analysis*

Figure 5.7a displays a simplified 2D plane-strain model of a representative C-shaped test specimen, together with its dimensions (I-2). Figure 5.7b represents the same particle simulated using a Full 3D FE model that includes the portion of the particle embedded in the polymer matrix. Figure 5.7c shows the vertical force – vertical displacement from the experiment together with the response from the 2D and 3D models of the same C-shape specimen. The curve predicted by a second 3D model is also included: with this model, the (3D) emerging portion of the sample is fully clamped at the bottom where it enters the polymer matrix, such that it has the same boundary condition as the 2D model. As seen, both fully clamped (2D and 3D) models come close to one another (such that simplifying the 3D beam as a 2D plane strain beam has little importance), and exhibit a somewhat stiffer force-displacement response compared to the experimental curve. Modelling the polymer matrix and embedding the 3D model in it, the resulting force-displacement response shifts downwards and follows relatively well the experimental curve. It is now slightly more compliant; however, the agreement also for the 2D model is satisfactory, considering simplifications made, such as the somewhat simplified geometry of the bottom of the particle and the approximation used for the size of the particle portion that is embedded in the matrix. More importantly, the sensitivity of the computed stress field on the exact model used (2D vs. 3D) was found to be negligible: a full 3D representation of the stress field and including the polymeric matrix in the simulation matters more in computing the overall

particle compliance than it does in computing its peak stress distribution. Figure 5.7d compares the distribution of the first principal stress along the mid-plane of the ligament back surface from the two models at the moment of failure. As is evident, the stress distribution is insensitive to the model used, and the simplified 2D plane-strain model provides an equally good stress analysis along the particle ligament free surface as the more realistic but also more complex 3D model. This result also indicates that most of the extra compliance in the force-displacement response between the two models comes from an elastic vertical sink-in of the specimen into the polymer, rather than from rotation of the specimen around the y-axis, as this would affect the bending moment from the applied forces, inducing in turn a visible redistribution of the stress in the ligament.

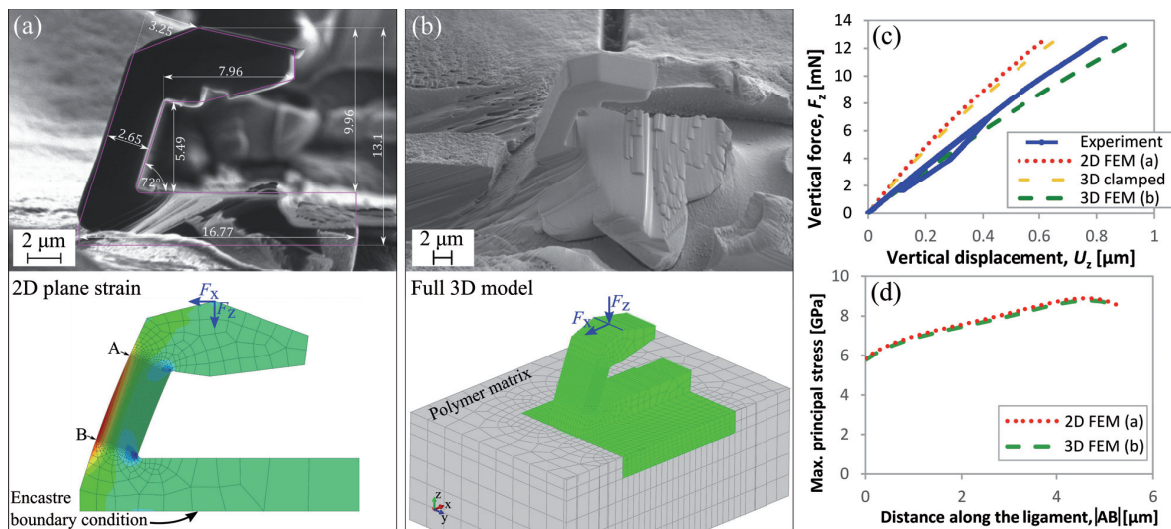


**Figure 5.7 – FEM simulation of a C-shaped specimen test with representative particle dimensions (I-2).** (a) Simplified 2D plane strain FEM model of the particle with dimensions visible by imaging from its side and with encastre boundary condition at its bottom. (b) The full 3D FEM model of the same particle takes into account the portion of the particle embedded in the polymer matrix. (c) The load-displacement curves from (blue) experiment, (dashed-green) the 3D FEM model including the polymer matrix, (dotted-red) the 2D plane-strain FEM model, and (dashed-yellow) 3D model with the same boundary conditions as for the 2D model. A loop in the experimental curve represents one load-unload cycle conducted before the displacement was ramped-up all the way to failure. (d) Comparison of the distribution of the maximum (tensile) principal stress along the ligament outer surface of the full 3D and 2D FEM model loaded with the pair of vertical and lateral force ( $F_x$ ,  $F_z$ ) measured at the moment of failure in the experiment.

*In-situ bend beam analysis*

The two tested specimens contained two facets forming an edge (see Figure 5.4 and Figure 5.8). By considering the edge as a geometric flaw we estimated the nominal strength of the present specimen material. To this end, we used a simplified beam model, as exposed in Section 5.3.3, in which the beam top surface was taken to be entirely flat (Figure 5.8). By doing this, calculated stresses in the beam just past the edge on the right-hand side are not representative; however, on the left-hand side and in the region surrounding the grain boundary and edge (this being where failure took place) the simplified model gives representative nominal stresses within the beam, which were computed as the beam failure stress.



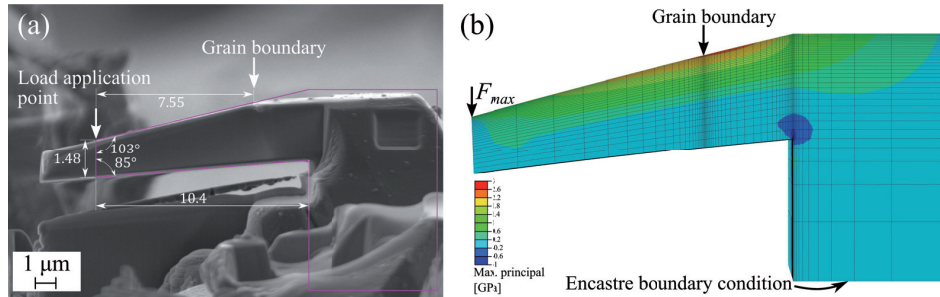


**Figure 5.8 – FEM model of the cantilever beam from Figure 5.4 with visible grain-boundary groove. (a) Dimensions used to produce (b) the 3D FEM model. Note that the simplified beam geometry was used with the beam’s top surface flat as outlined in Section 5.3.2 (Figure 5.2). The strength of the specimen evaluated as the first principal stress at the position of the grain-boundary groove was 2.3 GPa.**

### 5.4.3 Strength measurement results

In the vast majority of the tested specimens we could observe a fracture surface or even the origin of failure (Figure 5.3f). Hence, we often know approximately the position along the bent ligament or cantilever beam of the spot where failure initiated. We have therefore evaluated the specimen strength as the value of the first principal stress obtained from FEM simulations at the moment of failure at that location, that is for maximum measured vertical, and lateral force, in C-shaped specimens, or maximum applied force in cantilever beams, at the position of the observed failure. Note that, as the first principal stress distribution along the C-shape specimen bent ligament changes only marginally (Figure 5.7d), the error introduced due to the imprecision in the determination of failure position is smaller than the error due to imprecisions in the measurement of specimen dimensions (less than 10%).

The strength measurement results are presented in Figure 5.9. The results are sorted along the horizontal axis of the plot according to the specimen category, while the y-axis represents the value of the measured strength for each sample. Based on a sensitivity analysis (see Supplementary section 5.8.4 for more details) the reported strength values are precise within 20%, which defines magnitudes of the error bars.

As mentioned previously, in three C-shape specimens of Category I (pristine surface) the site of the failure could not be determined, visibly due to the initiation and propagation of secondary cracks. Hence, for these three specimens, not knowing the exact failure initiation site, we took simply the peak value of the first principal stress within the ligament at the moment of failure as the failure stress. The results from these three specimens are indicated in the plot using the colour grey. Measured strength values are also given in Table 5.1 and Table 5.2 in the Supplementary section 5.8.2.

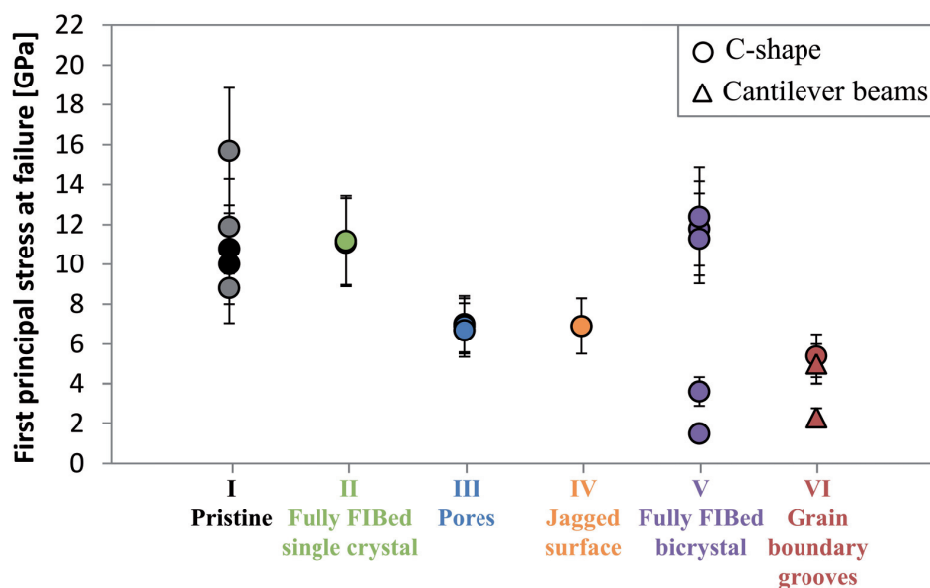


Figure 5.9 – Summary of results obtained by testing C-shape and micro-cantilever beam specimens of Sumicorundum alumina particles. The vertical axis of the plot represents the first principal stress present in the vicinity of the observed fracture initiation at the moment of failure. Specimens are sorted along the horizontal axis by category. Two fully black circles for Category I represent specimens for which the fracture surface could be observed and for which the stress in the vicinity of the observed failure is reported, while the three grey circles represent specimens for which the fracture surface was likely not apparent; for these three specimens, the reported failure stress value is the peak first principal stress in the ligament at the moment of failure.

## 5.5 Discussion

### 5.5.1 Precision of data

Most of the present specimens were prepared by deep etching a polymer composite containing Sumicorundum alumina particles, using the so-called “piranha solution”. This raises the question of a potential effect on alumina properties of the etching procedure; we investigated the matter by means of nanoindentation. The reduced modulus of polished Sumicorundum alumina particles embedded in a matrix of copper were evaluated before and after exposure of the alumina surface to the etchant for durations similar to those used in sample preparation. No significant difference was found in the nanoindentation behaviour between particles with or without exposure. Results are given in Supplementary information, Section 5.8.5. Moreover, the alumina particle obtained by cleaving the epoxy matrix gave a similar result as particles that were subjected to etching. A similar comparison of alumina nanoindentation properties before and after exposure to the etchant was additionally performed using samples of dense alumina (to preclude any effect of the matrix); again results showed no influence of the etching procedure on the properties of the alumina phase along its surface.

We do not expect significant plastic deformation to have taken place in our tests, justifying the use of elasticity in mechanical analysis of the samples' deformation. This is substantiated by (i) the absence of any hysteresis in unload-reload loops that were conducted up to roughly 5 GPa of applied stress in tested C-shape specimens (a representative load-displacement curve is shown in Figure 5.3d),

(ii) the absence within the fractured ligaments of signs of large scale plasticity such as slip bands (iii) the absence in the literature of hard evidence for room-temperature plasticity in alumina at or below stresses (compressive or tensile) around 10 GPa. In more detail, one study [75] reported plasticity in FIB machined alumina micropillars at room temperature to be initiated only at uniaxial compressive stresses above 11 GPa. In another study [65] no significant dislocation activity was observed in nanometric alumina whiskers tested in bending in-situ in the TEM, up to the theoretical strength of sapphire, near 40 GPa.

The sensitivity of the computed stress field on principal test parameters, namely notched specimen geometry, possible misalignments and values of elastic constants used in the model, was analysed by performing a series of calculations in which each parameter was perturbed by a finite amount, one parameter at a time, starting with the reference configuration of measured dimensions of a typical representative specimen. Details are presented in the Supplementary section 5.8.4; the conclusion is that errors in measurements of dimensions, misalignments and other parameters combined can lead strength values reported here to be over- or under- estimated by up to 20% of the reported values. Those are therefore magnitudes of the error bars used in Figure 5.9.

### 5.5.2 Near-theoretical strength in pristine particle regions

Measured strength values for Sumicorundum alumina particles, between 9 and 16 GPa in pristine Category I specimens, are consistent with strength results reported for nearly perfect single crystal  $\alpha$ -alumina whiskers. These values exceed what is reported for (flaw-dominated) nanocrystalline high-strength alumina fibres [324,335] or for a few hundred nanometre thick alumina platelets used in bio-inspired composites [301].

More specifically, reported strengths of high-perfection  $\alpha$ -alumina whiskers in air at room temperature, for whiskers of radius ca. 3  $\mu\text{m}$  prepared using different methods (wet hydrogen process or vapour condensation method), typically lie between 7 and 14 GPa [82,83,85]. Similar values, 7–12 GPa, were reported for  $\alpha$ -alumina needles of comparable size [86]. No prominent dependence of the alumina microcrystal strength on crystal orientation has been reported in the literature, although in one study somewhat higher strength values for A-type ( $\langle\text{hk}0\rangle$ ) whiskers were reported compared to C-type ( $\langle 0001\rangle$ ) whiskers [85]. Alumina strengths higher than those reported in this study or for microscopic whiskers were achieved only for alumina whiskers a few tens of nanometres in diameter [65]. The reported strength of these nanoscale whiskers is on the order of 40 GPa and are consistent with the theoretical strength of alumina [24]. The study of Wang et al. [65] also justifies the use of the purely elastic analysis as these authors did not detect any significant plastic deformation for alumina whiskers approaching theoretical strength in bending.

The measured average local strength of the pristine particle specimens and whiskers of comparable size, on the order of 10 GPa, translate to a critical defect in the shape of a half penny-shape surface crack of radius  $c = 50\text{--}60\text{ nm}$ , if one uses the linear elastic fracture mechanics expression  $c = \left(\frac{K_{\text{IC}}}{Y\sigma_0}\right)^2$  with a fracture toughness,  $K_{\text{IC}}$ , of single-crystal  $\alpha$ -alumina in the range 2.5–3  $\text{MPa}\cdot\text{m}^{1/2}$  [22] and a

geometric factor,  $Y = 0.66 \cdot \sqrt{\pi}$  for a half-penny shape surface flaw of negligible size with respect to the size of the specimen. Such flaws are at the limit of today's capabilities of SEM imaging, and we were indeed not able to directly identify crack initiating flaws in Category I particles. Only indirect fracture surface features (river patterns) that pointed to the (featureless) location of failure initiation could be observed. Bayer et al. in [88], based on the observation that whiskers with chemically polished and unpolished surface behave in qualitatively similar manner when their fracture stress exceeds 8-10 GPa, suggested that such strong crystals may fail by crack nucleation induced by dislocation motion (pile-up or dislocation interaction) regardless of the whisker orientation. This may rationalize the fact that no apparent flaws could be observed on the fracture surfaces of Category I specimens in the present work.

Fully FIB-milled specimens with no apparent defects (Category II) exhibited the same fracture stress as (pristine surface) particles of Category I. This observation suggests that either (i) FIB-machining does not alter the nature of the failure initiation of the present particles or alternatively that (ii) FIB-machining introduces such surface defects that the strength of the particles is in the end the same as that of the pristine (FIB unaffected) surface. The FIB affected layer in alumina irradiated by 30kV Ga<sup>3+</sup> ions has been studied in HRTEM [315], to find that the main FIB artefact is the Ga-implantation of a thin 20 nm layer while the crystalline character of the lattice remains unchanged. The implantation by Ga<sup>3+</sup> leads to high compressive residual stresses within the implanted layer, estimated to be on the order of 12-15 GPa [315]. Hence, failure initiation in the fully FIB machined specimens most probably takes place in the underlying material unaffected by the focused ion beam, which in turn may be under considerable tension up to a certain distance from the FIB affected surface in compression. The estimated critical defect size, on the order of 50 nm, is in any event larger than the depth of the implanted layer. Hence, the observation that similar strength values are found in specimens with pristine surfaces or fully FIB-machined specimens, is consistent with a scenario in which fracture nucleates at a flaw or substructure-induced stress concentration site situated at some distance below the original particle surface.

### 5.5.3 Strength-limiting defects

One of the observed flaws present in the Sumicorundum alumina particles consisted in microscopic pores, a few tens to a few hundred nanometres in diameter. As seen in Figure 5.9, the strength of specimens that contained pores was lower than that of pristine surface specimens by a factor around 2. This is in excellent agreement with the known stress concentration factor of surface or subsurface pores in a fully elastic body [388]. Here again the fact that similar strengths were observed for two samples with pores present along their FIB-machined ligament back-surface and one specimen with a subsurface pore unaffected by FIB (Figure 5.13 in the Supplementary section 5.8.3) suggests that FIB damage did not affect measured strength results in the present material.

Another observed stress concentrator in the present particles is the presence of a jagged surface along some facets, the origin of which is likely a series of parallel twins intersecting the particle free surface. One such tested C-shaped specimen (IV-1) had a strength approximately two times lower than that of Category I specimens. A separate FEM analysis of Specimen IV-1, modelled with a jagged surface

and sharp corners of radius  $0.2\ \mu\text{m}$ , showed that the local stress concentration at the root of the notch formed by twinned surface, can be up to 2.5 compared to a model with a flat ligament surface with an average specimen width  $w$ . Simple stress concentration factors thus again explain the observed failure stress reduction.

The most deleterious strength-limiting defect in Sumicorundum alumina particles is, by far, the grain boundary. All three tested specimens (one in C-shape configuration and two micro-cantilever beams) from Category VI, which contained a grain boundary groove along a surface unaffected by focused ion beam milling, exhibited strength values well below those reported for Category I particles. The weakest specimen also contained a pore along the revealed grain boundary, and exhibited a local strength value of approximately 2.3 GPa; this is roughly 5 times lower than the strength of Categories I and II specimens. Separate estimations of the stress concentration due to the presence of the grain boundary grooves idealized as notches with a measured values for the root radius and depth indicate that the corresponding stress concentration factor is roughly 2–3 [389]: hence, the sole presence of grain boundary grooves does not explain the observed drop in strength. To present this quantitatively, Figure 5.10 shows the stress-concentration-corrected first principal stress at failure for specimens of Categories III (pores), IV (jagged surface), and VI (grain boundary grooves). As seen, all samples then fall in a band of measured strength values between 8 and 16 GPa, exception made for some of the samples that contained a grain boundary, which fall below that band.

We have therefore performed separate tests on specimens containing individual grain boundaries within the C-shape specimen ligament after machining off the grain boundary groove so as to leave the ligament back-surface flat, thus eliminating the geometrical cause for stress concentration and essentially performing microscopic fracture test of randomly oriented flat alumina bicrystals (sample Category V). The strength results exhibit a high variability, showing that the presence of a grain boundary does not weaken the particle *per se*. Rather, in three out of five specimens, the measured strength was essentially the same as for pristine Category I single crystal specimens; however, in two such specimens the strength fell by a factor of more than five. Figure 10 thus underlines the deleterious effect of grain boundaries on the intrinsic particle strength. All single-crystalline particles exhibit comparable strengths when corrected for the stress concentrating effect of the observed flaws, whereas for three out of eight particles containing a grain-boundary the stress-concentration-corrected strength is significantly reduced.

This shows first that grain boundaries are the most potent cause for the reduction in strength of Sumicorundum particles, of greater potency than geometrical features that also exist along the surface of those particles. The results also show that the strength of alumina bicrystals is strongly dependent on the crystal orientations; possible underlying reasons for this include effects of (i) elastic anisotropy [390,391] and/or (ii) residual stresses due to thermal expansion anisotropy [392].

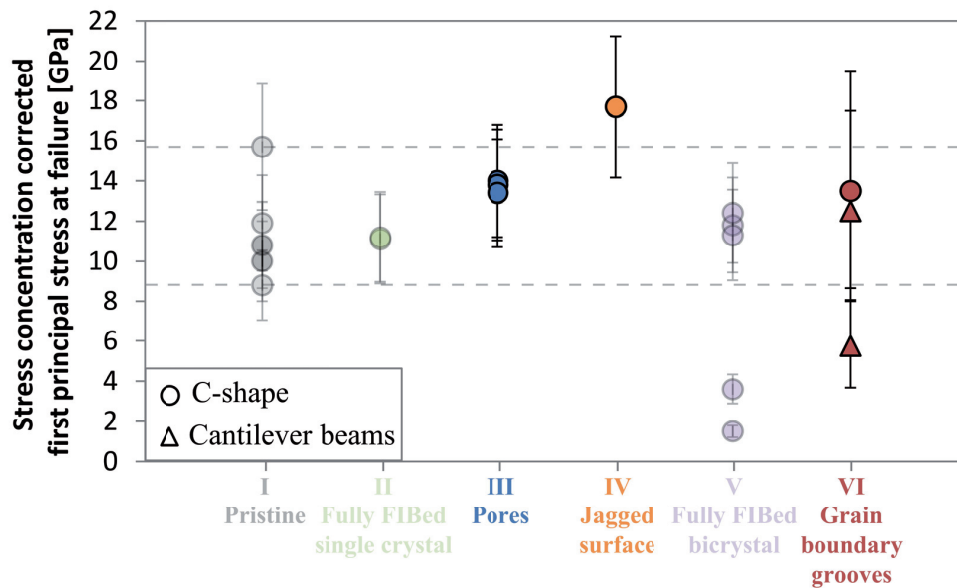


Figure 5.10 – Strength values for Categories III, IV and VI corrected for the corresponding stress concentration factor, namely  $k_t = 2$  for spherical pores,  $k_t \approx 2.5$  for a jagged surface calculated from separate FEM simulation and approximately  $k_t \approx 2-3$  for realistic geometry of the present grain boundary grooves from [389]. Measured values for Categories I, II and V with no visible defects are plotted along as partially transparent symbols. Note that the correction for the jagged surface sample is the value of maximum principal stress in the root of the twinned jagged surface notch; however, the exact location of failure (at the scale of the strong stress gradient around the notch root) is unknown, thus the value presented is an upper bound. In the case of grain boundary grooves, symbols represent correction with the average estimated stress concentration of 2.5 and the uncertainty in this factor (which can be between 2 and 3) translates into bigger error bars.

## 5.6 Conclusion

Microscopic C-shaped specimen and cantilever beam tests are developed to measure the local mechanical strength of hard reinforcing particles of low-aspect ratio. The methods provide strength data free of FIB-induced damage, as the particle surface probed in tension may be left pristine. Combining bespoke finite element analysis and fractography, the method yields measurements of the local stress at the place of the fracture initiation with an estimated relative error of 20 %, mainly due to uncertainties in specimen dimensions and alignment.

The approach is used to measure the local strength of individual Sumicorundum  $\alpha$ -alumina particles that were previously shown to perform well as a reinforcement in metal matrix composites. The results show that alumina particles free of visible defects exhibit very high local strength values, on the order of 10 GPa, similar to values measured on high-perfection alumina whiskers of comparable size.

When such particles contain microstructural flaws, namely micro-pores, surface irregularities, grain boundaries or grain boundary grooves, their strength strongly diminishes. The relative drop in strength caused by pores and surface irregularities is on the order of their associated stress concentration factor, near 2. The most detrimental observed flaws are associated with grain boundaries; these can diminish the local particle strength more than fivefold, down to roughly 2 GPa.



Pooling results, the study shows that the pathway to higher strength  $\alpha$ -alumina particles is the elimination of grain boundaries within the particles or alternatively the production of nanocrystalline particles, in which each grain boundary represents but a small flaw. Should one of these be achieved it is possible that remarkably strong and tough metal matrix composites could be produced.

## 5.7 Appendix: Details of specimen preparation and testing

### 5.7.1 Carbon coating

The sample of polymer with partially embedded particles was prior to FIB milling coated with thermally evaporated carbon using a Cressington<sup>TM</sup> Carbon Coater (Watford, England, UK). This produces a relatively weak (owing to low carbon ion energies associated with thermal evaporation [393–395]) roughly 40 nm thick carbon layer measured by the high resolution thickness monitor system MTM-10 (Cressington<sup>TM</sup>, Watford, England, UK) supplied with the carbon coater. Although the partially embedded particles present a rather complicated topography, their surface is in principle coated uniformly because evaporated carbon films are known to produce highly uniform deposits, even along surfaces that are hidden from lines of sight emanating from the carbon source [396].

### 5.7.2 C-shaped particle FIB machining

FIB machining of partially-embedded and carbon-coated alumina particles was performed in a Zeiss NVision<sup>TM</sup> 40 (Oberkochen, Germany) dual beam (SEM/FIB) instrument using a 30 kV Ga<sup>3+</sup> ion beam. Micromachining was done in such a way that one of the flat facets of the polyhedral particle to be tested was left intact and served as the back surface of the tested C-shape specimen ligament.

The FIB machining process, outlined in Figure 5.11, comprised the following steps:

- First, roughly vertical (relative to the polymer matrix free surface to which the particle is embedded) sides of the to-be-formed ligament are machined. This can be done either with the focused ion beam arriving roughly perpendicular to the polymer matrix free surface (Figure 5.11(i-b)) or from an opposite side of the selected particle facet, at an incident angle of roughly 26° with respect to the polymer matrix free surface (this being the minimum incident angle when a standard flat SEM pin stub sample holder is used), Figure 5.11(ii-b). The advantage of machining at a shallow angle from the opposite side of the to-be-tested ligament back-surface is that when the particle is FIB imaged (as is necessary to perform the milling procedure) one does not expose the carbon-coated ligament surface to ions, thus eliminating any exposure to ions of the probed surface. On the other hand, a redeposited layer, a few tens of nanometers thick, covering the facet surface is formed in this configuration; protecting the particle, and separating its free surface from such redeposited material, was another purpose of the carbon coating that was deposited prior to FIB machining. The formation of a redeposition layer over the selected facet is avoided when machining with a roughly vertical beam incident angle. In this configuration, a small dose of Ga<sup>3+</sup> may reach the surface of the selected facet during imaging with the focused ion beam; here again the carbon coating protects the facet surface.

- Secondly, a wide rectangular notch is FIB-machined with the beam oriented perpendicular to the previously machined sides (see Figure 5.11(i-c) and Figure 5.11(ii-c)). To this end, the particle-containing sample is mounted on a 45° pin stub sample holder to allow the incident FIB beam to be almost parallel (typically within +3° to +4°) to the polymer matrix free surface.

- Finally, a roof situated at the top of the particle and eccentrically placed with respect to the machined ligament is cut, parallel to the notch. The roofline serves as an unambiguous load-line when testing the machined particles using a flat-end diamond tip in an instrumented nanoindenter. FIB currents used ranged from 6.5 nA in initial rough-milling steps down to 1.5 nA in the last milling steps. Prior to testing, each specimen was examined in the SEM in order to measure its characteristic dimensions.

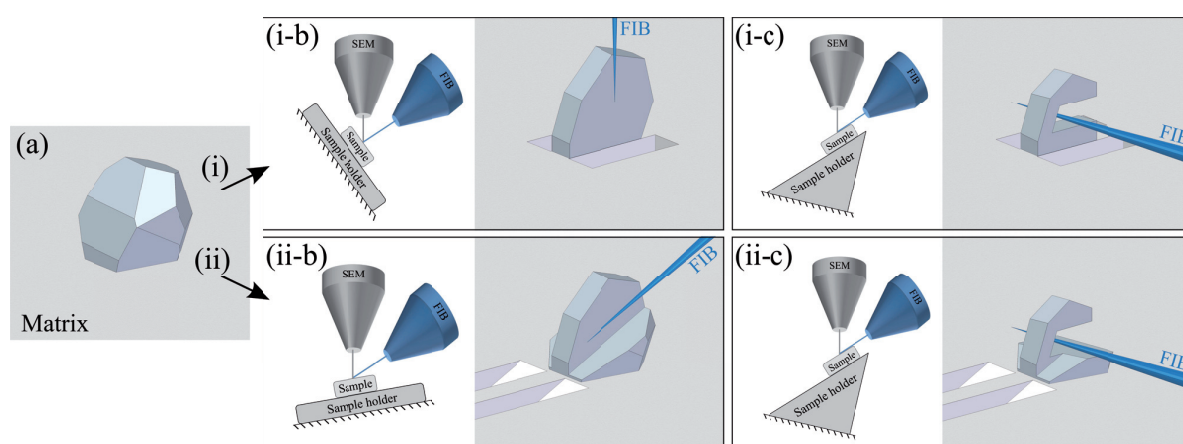


**Figure 5.11** – Two ways to FIB machine a notched specimen from a polyhedral particle (a) partially embedded in a matrix to test in C-shape configuration, by bending a ligament of rectangular cross-section. The particle sides are first machined either (i) with a FIB beam roughly perpendicular to the free surface of the matrix (i-b) or (ii) sideways with the FIB beam at a shallow angle (26°) (ii-b). The last step of a notched specimen preparation involves machining of the wide rectangular notch and single-edge roof, again using the FIB beam, oriented at a very shallow angle (2-5°) roughly perpendicular to the previously machined sides which is identical for both milling strategies (i-c and ii-c).

Mechanical testing of individual FIB machined particles was carried out using a TI 950 TriboIndenter™ (Hysitron Corp., Minneapolis, MN, USA) nanoindentation apparatus equipped with (i) a low-load transducer fitted with a sharp ( $\approx 1 \mu\text{m}$  of tip radius) conospherical diamond probe suitable also for Scanning Probe Microscopy (SPM) and (ii) a 3D OmniProbe™ transducer capable of measuring vertical and lateral force simultaneously with a  $\approx 10 \mu\text{m}$  tip diameter flat-end diamond probe. Prior to testing, the sample containing FIB machined specimens was mounted on top of a single-axis goniometric tilt stage fixed on the nanoindenter base stage, which was used to align the FIB machined specimen roofline parallel to the 3D OmniProbe flat-end diamond probe. To this end, both the specimen roof and flat-end diamond probe indent left in an aluminium sample were scanned using the SPM function of the low-load transducer. The measured misalignment was then corrected using the single-axis goniometric tilt stage within  $\pm 0.5^\circ$  precision such that the load can be applied evenly along the roofline. Once the specimen was aligned the load was applied via the 3D OmniProbe with a flat-end diamond tip using a displacement feedback control with constant displacement rate of 100 nm/s. A few load-unload cycles of amplitude up to 400 nm are first applied before the displacement is

ramped up until fracture; this was done in order to verify the good alignment of the specimen and smoothness of the roof sliding along the diamond probe flat-end, features that are betrayed by a consistent friction coefficient (defined here as the lateral to vertical force ratio). After the test, the sample was removed from the nanoindenter and carefully observed in the SEM (Zeiss Merlin, Oberkochen, Germany), notably in order to conduct fractographic analyses of particle remnants. All C-shape tests were done at room temperature and relative humidity  $\approx 50\%$ .

### 5.7.3 Micrometric bend beams

Sample preparation was, up to FIB machining, identical to that followed to prepare samples for testing in the C-shape test method: the selected particle's sides were first machined with the FIB incident angle roughly perpendicular to the surface of the particle that will form the beam upper surface. Subsequently, the cantilever bottom surface was formed by FIB milling with the beam at a very shallow angle, parallel to the top surface defined by the two facets meeting at the grain boundary (see Figure 5.2a-b). The top surface of the cantilever beam, subject to tension during the test, was left unaffected by FIB milling. The machined cantilever beams are mechanically tested *in-situ* in a Zeiss Merlin<sup>TM</sup> (Oberkochen, Germany) scanning electron microscope (SEM) using a FemtoTools FT-NMT03 Nanomechanical Testing System (Buchs-ZH, Switzerland) equipped with a sharp tungsten needle mounted on the 100 mN range load cell. This nanomechanical testing apparatus is equipped with a rotational and tilting stage, which was used to align the cantilever upper surface such that it is oriented perpendicular to the tungsten needle axis. Cantilevers were loaded with the tip of the needle close to the cantilever far end, using a constant displacement rate of 10 nm/s, up to failure of the beam. During the test, a video using the incorporated option of Zeiss SmartSEM operating software, was recorded, showing the deformation and moment of fracture of the beam.

## 5.8 Appendix: Supplementary information

### 5.8.1 Polymer matrix – alumina particles sample preparation

To test alumina particles using C-shaped particle and micro-cantilever methods one need to obtain particles that are partially embedded in a matrix, which holds particles in place during testing. To this end, a small number of Sumicorundum<sup>®</sup> alumina particles was dispersed in an epoxy resin made by mixing Bisphenol A diglycid ether (DGEBA, Sigma Aldrich) with Diethylenetriamin 99% (DETA Sigma Aldrich, 99%). This produces a polymer matrix composite reinforced with a few percent by volume of the alumina particles. More specifically, DGEBA and DETA were mixed stoichiometrically, assuming that each hydrogen of the amine group reacts with a single epoxy group, in a ratio of 12 wt% on the basis of their epoxide and amine equivalent weight. Al<sub>2</sub>O<sub>3</sub> was then added, such that the volume fraction of particles in the composite was kept below 10%, and then mixed manually. Subsequently, the composite mixture was degassed, poured into a silicon mould coated with a release-agent, and let to cure at 50 °C for 12h. A partial sedimentation of particles at the bottom of the mixture during curing was observed – this was taken into account in defining the right amount of powder to be added.

In order to obtain particles that are partially embedded in the matrix and protrude after etching by several micrometres out of the matrix, two approaches were adopted: (i) deep etching of the matrix or (ii) cracking the composite matrix. In the former case, the epoxy matrix was deeply etched using a mixture of sulphuric acid ( $\text{H}_2\text{SO}_4$  98%, Merck) and hydrogen peroxide ( $\text{H}_2\text{O}_2$ , 30%) in a ratio of 7:1 respectively, informally known as the “piranha solution” and commonly used to clean organic residues [397,398]. The etching was performed typically for roughly 5 minutes. Breaking with a single, clean crack the brittle polymer matrix composite is an alternative way to obtain particles partially embedded in the polymer matrix when the particle strength is superior to that of the particle-matrix interface.

### 5.8.2 Experimental data of tested particles

Table 5.1 presents dimensions and experimental data of all tested C-shaped particle specimens. These are separated into six categories according to the nature of flaws observed along their tested ligaments, namely: (i) pristine ligament of a particle with no visible defects, with its back-surface unaffected by FIB milling, (ii) particle with no visible defects but with its ligament back-surface FIB-machined, (iii) particle ligament containing a micropore, (iv) particle with a twinned jagged ligament back-surface, with its back-surface unaffected by FIB milling, (v) particle containing a grain boundary along the ligament with all four sides FIB machined, and (vi) particle containing a grain boundary and associated grain boundary groove unaffected by FIB machining. In Table 5.2 one finds details of two tested cantilever beam specimens, both of which contained a grain boundary with its associated grain boundary groove (unaffected by FIB) along the tested cantilever beam. Since a particle containing a grain boundary was also tested in the C-shaped configuration (see last line of Table 5.1), the group of grain boundary containing specimens, comprising three specimens, is Category VI.

One can readily see that (i) strength results from Category VI are considerably lower than from other categories (particularly Categories I and II for particles with no visible defect), and (ii) Category V results (boundaries with ligament back-surface FIB machined flat) have rather widely scattered strength values, underlining the likely effect of grain boundary orientation and/or residual stresses on the strength of such bicrystals. For further details see Discussion in the main text.

Table 5.1 – Dimensions and experimental data of tested C-shaped particle specimens.

Sample label	$w$ [ $\mu\text{m}$ ]	$e$ [ $\mu\text{m}$ ]	$l$ [ $\mu\text{m}$ ]	$L$ [ $\mu\text{m}$ ]	$\alpha$ [deg]	$H$ [ $\mu\text{m}$ ]	$h$ [ $\mu\text{m}$ ]	$t$ [ $\mu\text{m}$ ]	$b$ [ $\mu\text{m}$ ]	$\beta$ [deg]	$\gamma$ [deg]	$F_z^{max}$ [ $\mu\text{N}$ ]	$F_x^{max}$ [ $\mu\text{N}$ ]	$\frac{F_x^{max}}{F_z^{max}}$	$\sigma_{1f}$ [GPa]
I-1 <sup>a,d</sup>	1.81	4.80	9.33	12.3	69	10.8	7.97	3.09	5.94	91	4	5100	600	0.12	10.8
I-2 <sup>d</sup>	2.65	3.25	7.96	16.8	72	13.1	9.96	5.49	5.16	93	0	12700	1500	0.12	8.8 <sup>c</sup>
I-3	2.69	2.57	10.1	20.8	86	13.4	8.92	4.43	5.28	93	0	17250	2400	0.14	15.7 <sup>c</sup>
I-4	2.55	5.18	11.8	17.7	73	16.9	12.9	5.55	5.49	90	-3	7500	700	0.09	10.0
I-5 <sup>d</sup>	2.49	7.04	12.9	22.5	93	22.9	14.0	6.30	6.90	91	10 <sup>b</sup>	12000	2000	0.17	11.9 <sup>c</sup>
II-1	2.35	5.89	13.5	17.1	84	14.9	10.2	4.61	6.21	91	4	10400	1200	0.12	11.1
II-2	2.47	2.40	12.5	22.5	59	18.6	12.2	5.52	6.06	91	-3	10950	1200	0.11	11.2
III-1	3.00	6.25	10.6	18.5	79	18.8	11.4	6.24	4.69	91	1	7900	500	0.06	7.0
III-2	2.68	6.34	13.2	17.3	83	16.0	11.4	6.36	5.90	91	-1	11350	1500	0.13	6.9
III-3	2.90	5.04	11.6	16.3	70	21.5	12.2	6.20	5.72	90	0	8250	1100	0.13	6.7
IV-1 <sup>d</sup>	2.74	4.78	9.02	18.3	77	14.6	10.6	6.54	3.53	93	2	5850	700	0.12	6.9
V-1	2.01	4.39	13.6	21.2	73	19.9	14.6	5.63	6.01	90	2	2700	350	0.13	3.6
V-2	2.54	6.48	14.2	19.4	77	20.3	12.9	5.89	8.17	90	-2	13000	1900	0.15	11.8
V-3	2.40	4.29	13.6	13.9	73	19.7	12.2	5.85	6.83	90	-2	2600	450	0.17	1.5
V-4	2.82	5.56	12.1	20.7	73	17.3	11.8	6.45	6.88	90	-1	16300	2400	0.15	11.3
V-5	2.70	5.09	13.9	19.0	73	17.5	12.6	6.02	7.10	90	0	16000	2500	0.16	12.4
VI-1	2.51	2.80	7.54	15.5	55	16.6	12.9	7.57	4.76	93	-1	3500	400	0.11	5.4

Note: the Roman numeral in the specimen label designate the specimen category according to the flaw probed followed by a serial number.  $\sigma_{1f}$  represents the first principal stress determined from FE simulation in the site of observed fracture.

<sup>a</sup> the particle was obtained by polymer composite cleaving.

<sup>b</sup> the sample was deliberately tilted in the nanoindenter instrument.

<sup>c</sup> the peak first principal stress in the ligament was evaluated as failure stress as the site of failure initiation was unknown.

<sup>d</sup> a few tens of nanometers thick redeposition layer was present at the back-surface of the ligament.

Table 5.2 – Dimensions and experimental data of tested micro-cantilever specimens.

Sample label	$G$ [ $\mu\text{m}$ ]	$d$ [ $\mu\text{m}$ ]	$g$ [ $\mu\text{m}$ ]	$\delta$ [deg]	$\theta$ [deg]	$\phi$ [deg]	$u$ [ $\mu\text{m}$ ]	$F_{max}$ [ $\mu\text{N}$ ]	$\sigma_{1f}$ [GPa]
VI-2	7.69	2.10	6.36	192	85	98	2.31	1800	5.0
VI-3	10.4	1.87	7.55	170	103	85	2.79	1170	2.3

Note: the Roman numeral in the specimen label designates the specimen category according to the flaw probed followed by a serial number.  $\sigma_{1f}$  represents the first principal stress determined from FE simulation in the site of observed fracture.

### 5.8.3 Supplementary figures

Figure 5.12a-b shows one of the three C-shaped specimens for which the fracture surface observed after test appeared to be somewhat below the original ligament surface. Two observations indicate that the observed fracture surface is not where failure initiated: (i) no apparent flaw was observed with a size on the order of 200 nm, corresponding to a stress value on the order of 5 GPa calculated for the observed position of the fracture surface and (ii) Figure 5.12c-d of particle from Category II shows that a microcrack originated in the bottom corner of the ligament and grew for a few hundreds of nanometres towards the other end, along a direction such that it would end below the actual ligament had its growth continued across the specimen, something that likely occurred in the three specimens showing a final fracture surface of trajectory similar to that of these secondary microcracks.



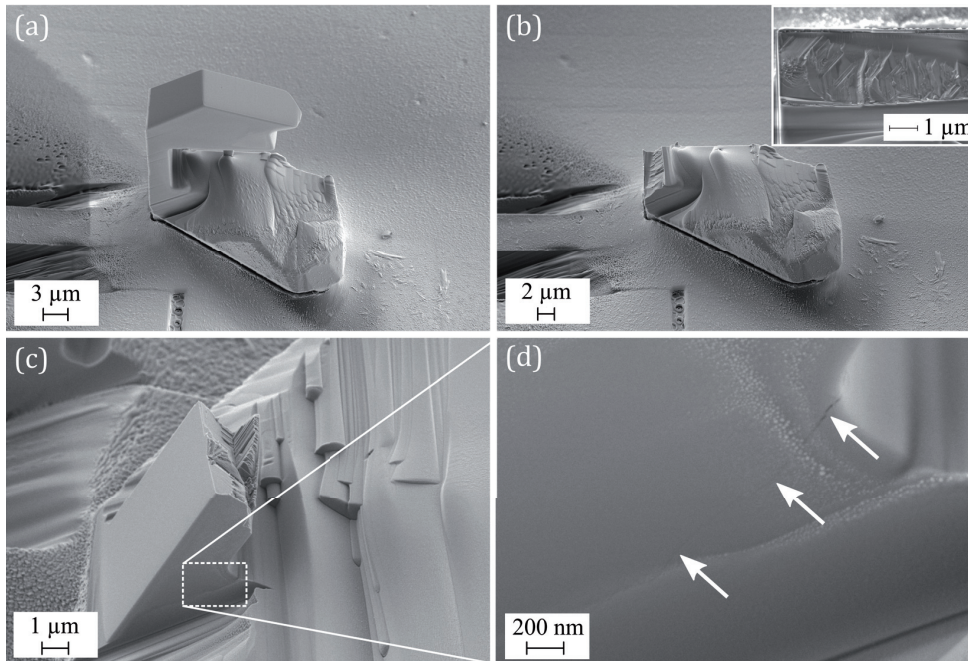


**Figure 5.12** – Panels (a) and (b) represent a particle from Category I (I-5) for which the observed fracture surface appears somewhat below the original ligament in the region that experienced significantly lower tensile stress than along the ligament surface. Panels (c) and (d) show a particle from Category II (II-2) that also broke for relatively high stress along the ligament surface and exhibit secondary microcrack (arrows) propagating from the bottom corner of the ligament towards the opposite end below the ligament.

Figure 5.13 shows a particle of Category III that displayed an elliptical pore fully contained within the ligament. This particle was also FIB machined along the back-surface of the ligament. It was initially indented to be a Category II particle; however, post-testing fractography showed that the ligament contained a pore  $\approx 300$  nm in diameter located below its FIB machined back-surface. Radial ridges emerging from the pore indicate that failure initiated from its surface, which was obviously unaffected by FIB machining. The value of (tensile) first principal stress from FE simulation at the place of the observed failure initiation from the pore surface was therefore considered as this particle's failure stress.

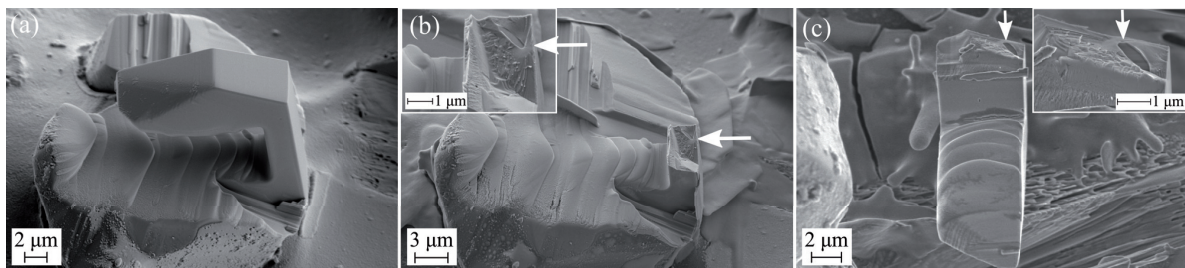


**Figure 5.13** – (a) Specimen of Category III (III-2) with an elliptical pore within the ligament, which was revealed only after the test by observing the (b) lower and (c) upper part of the fracture surface. Although all four sides of the ligament were FIB milled, failure initiated from the pore below the ligament surface, and hence from material unaffected by FIB machining.



#### 5.8.4 Sensitivity analysis

To investigate the sensitivity of the computed stress field on geometrical parameters of the notched specimen, on possible misalignments and on values of elastic constants used in the model, we performed a set of calculations in which each of these parameters was perturbed by a finite amount, one parameter at a time, starting with the reference configuration of measured dimensions of the specimen in Figure 5.7a in the main text. The values by which the model was perturbed represent upper bounds of reasonable experimental imprecision, namely for C-shaped specimens (i) the ligament width  $w$  by  $\pm 5\%$ , (ii) the specimen thickness  $b$  by  $\pm 5\%$ , (iii) the ligament length  $t/\sin(\alpha)$  by  $\pm 5\%$ , (iv) the position of the roof edge and the load application  $e$  by  $\pm 5\%$ , (v) the magnitude of the lateral force by  $\pm 10\%$ , (vi) the distance between the roof edge (load application) and bottom of the notch  $h$  by  $\pm 5\%$ , (vii) the height of the bottom part (support) of the specimen  $H-h$  by  $+100\%$ , (viii) rotation of the specimen around the y-axis by  $\pm 2^\circ$ , (ix) maximum (460 GPa) and minimum (336 GPa) elastic modulus for single crystal alumina and (x) the particle Poisson's ratio was increased to 0.3.

Results show that the greatest difference in the maximum first principal stress results from perturbations (i), (ii) and (viii). For a  $\pm 5\%$  difference in specimen width  $w$  and thickness  $b$  the calculated maximum first principal stress at the moment of failure varies by  $\pm 15\%$  and  $\pm 9\%$ , respectively. For rotation of the specimen around the y-axis (viii) by  $\pm 2^\circ$ , the maximum principal stress changes by 6%. For variations in the elastic modulus (ix), when the minimum value for single crystal alumina is used in the model the maximum principal stress varies by 5%. In all other cases the maximum first principal stress was found to vary by less than 5%.

The sensitivity of results to the geometry parameter  $\beta$  (see Figure 5.1c) was also investigated using a three-dimensional FEM model, because it introduces an out-of-plane bending of the ligament during the test. The analysis showed that in the most extreme case of a departure of the angle  $\beta$  from an ideal right-angle ( $93^\circ$ ), the difference between the maximum principal stress along the surface in the mid-plane of the ligament and one of the sides is at most 5%.

Summarizing the results of the sensitivity analysis, we conclude that errors in measurements of dimensions lead to a maximum  $\pm 15\%$  uncertainty while misalignments can lead to at most  $\pm 6\%$  error in the computed particle strength. Pooling results of these calculations, we estimate that strength values reported here could be over- or under- estimated by up to 20% of the reported values. Those are hence magnitudes of the error bars used in Figure 5.9.

FEM simulation of cantilever beam tests showed a similar sensitivity to imprecision in measured dimensions (maximum first principal stress varies up to 15%) hence we consider the reported strength values for the two tested cantilever beam specimens to be over- or under- estimated by up to 20% as well.

#### 5.8.5 Investigation of the etching effect by means of nanoindentation

All but one of the tested specimens were prepared by deep etching a polymer composite containing Sumicorundum alumina particles, using the so-called "piranha solution". This raises the question of

a potential effect on alumina properties of the etching procedure; we investigated the matter by means of nanoindentation. The reduced modulus of similar Sumicorundum alumina particles, along a polished surface of such particles embedded in a matrix of copper (for ease of polishing and testing) were evaluated before and after exposure of the alumina surface to the etchant for durations similar to those used in sample preparation (5 minutes).

Nano-indentation tests were carried out on several alumina particles by using a Berkovich tip at loads up to 5 mN. At least 15 indentation curves were acquired on different particles before and after chemical exposure. Representative nanoindentation response curves at 5 mN of load are reported in Figure 5.14. Table 5.3 summarizes the average values of reduced modulus of alumina particles before and after the etching procedure.

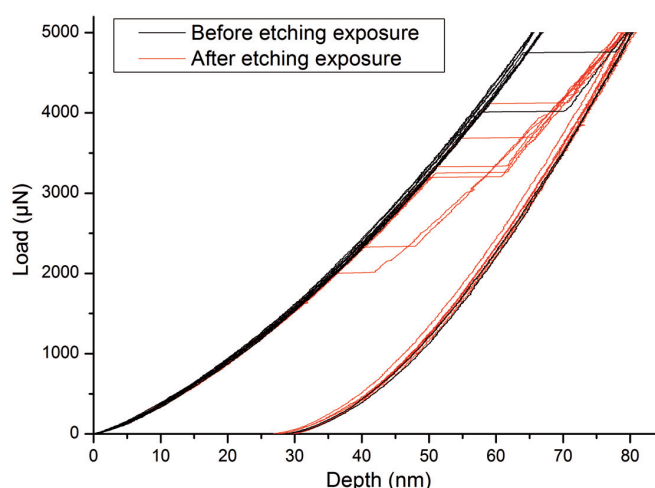


**Figure 5.14 – Representative nanoindentation curves of alumina particles before (black lines) and after (red lines) the etching exposure**

No significant difference was found in the nanoindentation behaviour between particles with or without etching exposure. Leaving aside pop-ins, which occurred for both conditions and spread stochastically the curves into two series, reduced modulus value, at 400 GPa before chemical etching, show no significant difference (within standard deviation) after 5 minutes of exposure to the etchant. Moreover, in a similar (C-shape specimen) mechanical test of an alumina particle seated in epoxy that was produced, not by etching but by cleaving the epoxy matrix, gave a similar result as was obtained with similar particles that had been exposed by etching the matrix with the solution. A similar comparison of alumina nanoindentation properties before and after exposure to the etchant was additionally performed using samples of dense alumina (to preclude any effect of the matrix); again results showed no influence of the etching procedure on the properties of the alumina phase along its surface. Therefore, we exclude an influence of the sample preparation method on strength results.

Table 5.3 – Average and standard deviation values of reduced modulus of Sumicorundum alumina particles before and after etching exposure.

	Before etching exposure	After etching exposure
<b>Reduced modulus (GPa)</b>	400±8	393±6





## Chapter 6 Conclusions

### 6.1 Achieved results

This investigation has placed focus along two principal lines: (i) to develop suitable methods of probing the tensile strength of individual microscopic, low-aspect-ratio, hard and brittle particles directly, avoiding problems related to FIB milling damage that are often encountered when measuring strength at the microscopic scale, and (ii) to implement newly developed methods towards testing the strength of individual alumina-based ceramic microparticles that have the potential to be used as a reinforcement in metal matrix composites. The results achieved in this thesis can be summarized in the following lines:

#### *Development of strength testing methods*

- Building on an earlier contribution by Shipway and Hutchings [9,10] we developed a method by which one can measure unambiguously the strength dictated by the presence of flaws along or just below the surface of spherical (or nearly-spherical) hard and brittle particles by compressing them uniaxially between a pair of elasto-plastic platens of tailored hardness; this is called here the *Meridian Crack Test* (Chapter 2).
- Data obtained from the Meridian Crack Test have the peculiar feature that there is a window of surface stress values within which one knows the cause of failure; this results in a left-truncated and right-censored dataset of range dictated by the platen material. Statistical methods of Survival analysis can be transposed to evaluate such datasets, giving access to measurements of the statistical strength of particles as dictated by their surface or near-surface flaws. By tailoring the hardness of the platens that compress the particle one can probe different particle surface strength values. Steel was found to be a suitable platen material for the tested particles, as its hardness can be varied in a wide range giving access to particle surface strengths from roughly 500 MPa to 2000 MPa.
- To perform the Meridian Crack Test we built in our laboratory a crushing apparatus (dubbed The Nutcracker), which is designed as a stiff machine in order to avoid the particle being crushed into rubble upon failure by the sudden release of elastic energy stored in the load-train. The Meridian Crack Test was successfully benchmarked on microscopic fused quartz particles, showing that the method gives access to the particle surface strength. Fractography can furthermore be performed if the particles can be held in place upon failure and do not shatter into many pieces, giving access to the critical defects causing failure. To hold particle

in place upon failure, the application of a soft layer of colloidal graphite on the surface of the lower platen into which the tested particles partially embed during the test was found suitable.

- By combining Focused Ion Beam (FIB) machining with the use of a nanoindentation apparatus coupled with Finite Element (FE) simulations we developed a method by which one can probe the local strength of hard and brittle second phases in alloys and composites; we call this the *C-shape test* (Chapter 4). The method starts by FIB machining a deep and wide rectangular notch along with a single-edge roof at the top of a particle (or in any convex object for that matter) that is partially embedded in a matrix that can hold it in place. The notched particle is then compressed until it fails, using a nanoindentation apparatus equipped with a flat diamond punch, which is during the test in contact with the C-shaped sample rooftop, thus unambiguously defining the position of the load-line.
- We demonstrated the method on micrometric portions of a nanocrystalline alumina fibre designed to reinforce aluminium. FE analysis of the C-shape test confirms that a region of high tensile stress emerges just opposite the root of the notch; importantly, this region is not affected by FIB milling. We also observed that friction effects at the interface between the roof and the flat punch contact are important in the test but can be accounted for either by FE simulations or simply by measuring the lateral force using a suitable nanoindenter transducer.
- The C-shape test method is shown to be a particularly powerful method to identify the strength-limiting defects as sample fracture takes place at relatively low loads, which prevents extensive sample shattering and renders fractography possible for almost all tested specimens. The technique is also useful if one wishes to probe particle portions of particular interest, such as evident defects along the free surface. When FIB damage can be neglected (as for example gross defects, e.g. micropores, that are several times larger than the FIB damaged layer), even volumetric defects discovered during FIB milling can be probed.
- Building on the microscopic C-shape test method we adopted a cantilever test method to probe the strength of particle portions and/or features that are aligned roughly horizontal in respect with the matrix free surface in which particles are embedded. Here again the surface that is under high tensile stress when the cantilever is bent is left unaffected by the FIB.

#### *The reinforcement strength*

- The strength of plasma sprayed alumina-zirconia-silica (Eucor) particles was found to depend on their microstructure. Nanocrystalline particles produced from amorphous powder by annealing at 1300°C contain nanometric mullite and zirconia grains and are roughly 30% stronger than amorphous Eucor particles. This is attributed to an increase of the particle material fracture toughness when it becomes nanocrystalline (compared to the amorphous state). Nanocrystalline particles were found to exhibit characteristic Weibull strength values near 1.5 GPa and Weibull modulus near 7 and are thus only around 30% less strong than chemically and microstructurally similar alumina-mullite Nextel 720™ fibres produced by 3M.



- The main strength-limiting defects in plasma sprayed Eucor particles are micropores, likely developed during the formation of particles by trapping gas bubbles while the particles are molten in the plasma jet. The presence of pores is more detrimental in the case of nanocrystalline powder than in amorphous powder as a pore in a polycrystalline material acts more closely to a sharp flaw.
- The local strength of Nextel™ 610 fibres produced by 3M evaluated using Weibull distribution can be described with the Weibull modulus  $m = 7.2$  and a characteristic strength of  $\sim 5.3$  GPa associated to an effective material volume of  $\sim 7 \mu\text{m}^3$ . These values are realistic in view of the measured flaw size and fracture toughness values; yet they differ significantly from values found after testing macroscopic fibre lengths, indicating that the microscopic and macroscopic strength distributions of this material are governed by different flaw populations. This implies that, in micromechanical analysis of multiphase materials, highly localized events such as the propagation of internal damage require input data that are measured at the same, local, micro- scale as the event.
- Vapor-grown Sumicorundum® alumina particles that were in the past successfully used as a reinforcement in aluminium and copper alloys are shown to achieve strengths approaching those of high-perfection defect-free alumina whiskers near 10 GPa when the particles are free of identified strength-limiting defects. Identified defects include surface irregularities, micropores, and grain boundaries with associated grain boundary grooves. Grain boundaries are found to be the most detrimental flaws, as these can decrease the particle strength more than five-fold, down to approximately 2 GPa. Surface irregularities and micropores are found to decrease strength in proportion with their associated stress concentration factor, of about two.
- It is found that FIB machining the surface of particles has no effect on the measured strength of the strongest Sumicorundum® particles: such surfaces also achieve strengths near or above 10 GPa. Possible explanations are (i) that in such strong particles dislocation motion (including pile-up formation or dislocation interaction), which can cause crack nucleation, might take place below the FIB damage layer, which is reported in the literature to be  $\approx 20$  nm thick, or (ii) that since critical defects that cause alumina to fail near 10 GPa are near 50 nm in size, they are at least twice the size of the FIB affected surface layer.

In summary, the thesis provides methods by which one can probe the strength of brittle composite reinforcements at microscopic scales; these methods can be transposed also to other microscopic brittle objects. The Meridian Crack Test method can be adopted in many different fields and across different length-scales given the widespread use of the conventional uniaxial compression test on particles over the last decades. This thesis also defines pathways towards the production of strong particles for use as reinforcement in metal matrix composites. Alumina particles must be single-crystalline or alternatively nanocrystalline in order to fully develop their potential as a strong reinforcing phase in composite materials. In this regard thermal spraying coupled with controlled annealing appears to have potential provided that the development of micropores is avoided while the particles are molten. Should strong, defect-free, single- or nano-crystalline alumina particles be achieved it is possible that remarkably strong and tough isotropic metal matrix composites can be produced.

## 6.2 Future developments

Probing the strength of vapor-grown Sumicorundum alumina particles, we have identified grain-boundaries as being the main strength-limiting defect. A possible next step would be to look in more detail into whether there are methods to avoid in particles specifically the presence of weak grain boundaries, given that data show that at least some particles containing grain-boundaries retain high strength comparable to that of defect-free single crystal particles.

The ternary system studied in this thesis, alumina-zirconia-silica was tested only in one crystalline form with a justification that in the fully (nano-) crystalline state the material is expected to have superior fracture toughness. However, we don't know much about micromechanical properties of other intermediate states of this ternary system, which was reported as a composite of nanograins embedded in an amorphous matrix [345]. Additionally, such amorphous matrix nanocomposites may have higher tolerance to micropore defects than the fully-crystalline material.

Thermal spraying techniques have a relatively large and untapped potential in producing strong microscopic particles given that particles prepared with this technique have been seldom tested for strength (there was to the author's knowledge only one study of the strength of plasma-sprayed particles conducted prior to this thesis, by Rosenflanz et al. [236]). Given the relatively large configuration space of possible chemical compositions and microstructures that can be produced by thermal spraying coupled with post-spraying thermal treatment to produce amorphous and/or nanocrystalline particles, a potentially strong reinforcement particles' material structure-property relationship can be first studied in a pressed consolidated state or in a form of thermal sprayed coating as coatings are easier to prepare and handle. For instance, a relatively large compositional and microstructural configuration space can be relatively rapidly sampled by testing individual splats of thermal spray coatings using techniques of nanoindentation to probe their elastic modulus, hardness and possibly also indentation fracture toughness. With the investment of more time and resources, FIB machining, microcantilever bend strength, and chevron-notch fracture toughness testing can be performed.

Further development of the Meridian Crack Test towards testing particles with lower sphericity and eventually particles that are more or less of irregular shape would be an obvious pathway for further work. Analytical and/or numerical simulations may be used to investigate how the shape of the particle affects the stress state along the particle surface. Static compression of ceramic particles, that is, compressing particle until high tensile stress region is developed along its surface followed by holding until particle fractures can be in principle used to assess slow-crack growth parameters of particle material. Due to the non-uniform stress state around the equatorial belt such a test may be, however, difficult to interpret. Being able to compress particles in an inert environment e.g. in oil would be an essential improvement of the test. Another interesting exercise would be to couple the Meridian Crack Test of a transparent brittle material with high-speed camera recording to observe *in situ* initiation and propagation of meridian cracks. Compressing a photoelastic material may be even more interesting.

The C-shape sample or cantilever beam tests can be readily used to probe the strength along relatively flat portions of irregularly shaped particles. One C-shaped sample test was preliminary performed on one of the conventional comminuted white fused alumina particle; it is shown in Figure 6.1. The strength of the tested particle region was found to approach the strength of defect-free vapour-grown Sumicorundum particles, with a measured strength value near 11 GPa. The fracture was found to be associated with minute surface cracks a few tens of nanometre deep running along the C-shape particle ligament and aligned roughly parallel to the tensile stress. This test shows that comminuted particles too can be locally very strong. Should there be a way to heal deep cracks that comminuted particles often contain, these particles might perhaps also be highly performant in reinforcing metals.

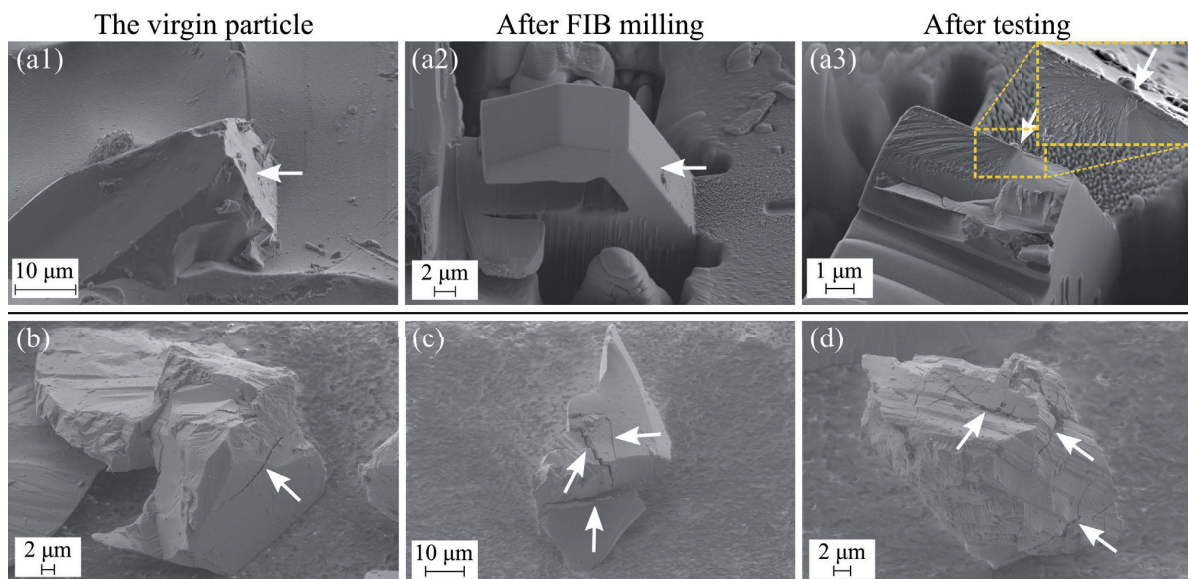


**Figure 6.1 – (a1-a3) A C-shaped sample test conducted on one comminuted “F-series” white fused alumina particle with the ligament machined along a particle flat facet. The strength evaluated using finite element analysis according to Chapter 5 was found to be  $(11 \pm 2)$  GPa. Fracture apparently initiated close to the location of peak maximum principal stress, situated roughly in the centre of the ligament width; the fracture surface presents very clear mirror-mist-hackle features indicating the failure origin, which was associated with one of the shallow surface cracks (white arrow) running along the ligament surface parallel to the tensile stress. Panels (b-d) show deep cracks (white arrows) that are readily observed in other comminuted alumina particles of this type.**

An interesting question that has been answered only in speculative terms is why alumina particles with strengths on the order of 10 GPa appeared not to be affected by FIB machining. Here, a detailed TEM investigation of regions close to the failure initiation may provide more insight on what causes failure of such apparently defect-free strong alumina crystals and whether or not FIB damage plays a role in failure initiation. If the FIB damage is clearly shown to not play an important role in the damage initiation in alumina, it may open doors to more efficient micromechanical probing of the strength of alumina reinforcements.

The advent of three-dimensional X-ray diffraction microscopy (available for instance at ESRF in Grenoble, France) represents a powerful tool to probe the local stress in individual grains and thus also in reinforcing particles at the scale of few micrometers [399,400]. Although this resolution is

lower than that of investigations conducted in this thesis and cannot be simply used to identify the critical defects smaller than few micrometers in size, the technique can be potentially used to relatively rapidly probe failure stress values across a statistically significant number of reinforcing particles *in situ* in the metal matrix composite under macroscopic loading conditions. Therefore, X-ray diffraction techniques and micromechanical testing can be viewed rather as complementary.

Finally, with quantitative knowledge of particle strength distributions one can compare data with back-calculated distributions from tensile testing of macroscopic composite samples containing the reinforcing particles in question. This may provide more insight on the validity of assumptions used in these models and might potentially lead to a significant improvement of the reliability of particle strength distributions obtained with such models.

---

## References

- [1] L.J. Bonderer, A.R. Studart, L.J. Gauckler, Bioinspired Design and Assembly of Platelet Reinforced Polymer Films, *Science*. 319 (2008) 1069–1073. doi:10.1126/science.1148726.
- [2] F. Bouville, E. Maire, S. Meille, B. Van de Moortèle, A.J. Stevenson, S. Deville, Strong, tough and stiff bioinspired ceramics from brittle constituents, *Nat. Mater.* 13 (2014) 508–514. doi:10.1038/nmat3915.
- [3] H. Le Ferrand, F. Bouville, T.P. Niebel, A.R. Studart, Magnetically assisted slip casting of bioinspired heterogeneous composites, *Nat. Mater.* 14 (2015) 1172–1179. doi:10.1038/nmat4419.
- [4] E. Munch, M.E. Launey, D.H. Alsem, E. Saiz, A.P. Tomsia, R.O. Ritchie, Tough, bio-inspired hybrid materials, *Science*. 322 (2008) 1516–1520. doi:10.1126/science.1164865.
- [5] A. Evans, C.S. Marchi, A. Mortensen, *Metal matrix composites in industry: An introduction and a survey*, Springer Science & Business Media, 2013.
- [6] M. Kouzeli, *Tensile Behaviour of aluminium reinforced with ceramic particles*, Ecole Polytechnique Fédérale de Lausanne (EPFL), 2001.
- [7] A. Miserez, *Fracture and toughening of high volume fraction ceramic particle reinforced metals*, École Polytechnique Fédérale de Lausanne, 2002.
- [8] A. Hauert, *Damage propagation and fracture in highly reinforced particulate metal matrix composites*, Ecole Polytechnique Fédérale de Lausanne (EPFL), 2009.
- [9] P.H. Shipway, I.M. Hutchings, Fracture of brittle spheres under compression and impact loading. I. Elastic stress distributions, *Philos. Mag. A*. 67 (1993) 1389–1404. doi:10.1080/01418619308225362.
- [10] P.H. Shipway, I.M. Hutchings, Fracture of brittle spheres under compression and impact loading. II. Results for lead-glass and sapphire spheres, *Philos. Mag. A*. 67 (1993) 1405–1421. doi:10.1080/01418619308225363.
- [11] N. Chawla, K.K. Chawla, *Metal matrix composites*, Springer, New York, 2006.
- [12] T.W. Clyne, Chapter 30 - Metallic composite materials, in: Robert W. Cahn, Peter Haasen (Eds.), *Phys. Metall.* Fourth Ed., North-Holland, Oxford, 1996: pp. 2567–2625. <http://www.sciencedirect.com/science/article/pii/B9780444898753500351> (accessed June 9, 2013).
- [13] I.E. Anderson, J.C. Foley, Determining the role of surfaces and interfaces in the powder metallurgy processing of aluminum alloy powders, *Surf. Interface Anal.* 31 (2001) 599–608. doi:10.1002/sia.1087.
- [14] Y.-W. Kim, W.M. Griffith, F.H. Froes, Surface oxides in P/M aluminum alloys, *JOM*. 37 (1985) 27–33. doi:10.1007/BF03257675.
- [15] M.A. Meyers, K.K. Chawla, *Mechanical Behavior of Materials*, Second Edition, Cambridge University Press, 2008. <http://proquest.safaribooksonline.com/9781107386358> (accessed July 11, 2017).
- [16] A. Hauert, A. Rossoll, A. Mortensen, Ductile-to-brittle transition in tensile failure of particle-reinforced metals, *J. Mech. Phys. Solids*. 57 (2009) 473–499. doi:10.1016/j.jmps.2008.11.006.



- [17] M.F. Ashby, *Materials selection in mechanical design*, 4th ed, Butterworth-Heinemann, Burlington, MA, 2011.
- [18] H.E. Deve, C. McCullough, Continuous-fiber reinforced composites: A new generation, *JOM J. Miner. Met. Mater. Soc.* 47 (1995) 33–37.
- [19] A. Miserez, A. Mortensen, Fracture of aluminium reinforced with densely packed ceramic particles: influence of matrix hardening, *Acta Mater.* 52 (2004) 5331–5345. doi:10.1016/j.actamat.2004.07.038.
- [20] A. Vassel, Continuous fibre reinforced titanium and aluminium composites: a comparison, *Mater. Sci. Eng. A.* 263 (1999) 305–313. doi:10.1016/S0921-5093(98)01161-7.
- [21] M. Wenzelburger, M. Silber, R. Gadow, Manufacturing of light metal matrix composites by combined thermal spray and semisolid forming process – summary of the current state of technology, *Key Eng. Mater.* 425 (2010) 217–244. doi:10.4028/www.scientific.net/KEM.425.217.
- [22] E. Dörre, H. Hübner, *Alumina: processing, properties, and applications*, Berlin a.o. : Springer, 1984.
- [23] J.B. Wachtman, W.E. Tefft, D.G. Lam, R.P. Stinchfield, Elastic constants of synthetic single-crystal corundum at room temperature, *J. Am. Ceram. Soc.* 64A (1960) 213–228.
- [24] S.M. Wiederhorn, Fracture of sapphire, *J. Am. Ceram. Soc.* 52 (1969) 485–491.
- [25] N.H. MacMillan, The theoretical strength of solids, *J. Mater. Sci.* 7 (1972) 239–254. doi:10.1007/BF02403513.
- [26] A.A. Griffith, The phenomena of rupture and flow in solids, *Philos. Trans. R. Soc. Lond.* 221 (1921) 163–198.
- [27] N. Claussen, B. Mussler, M.V. Swain, Grain-size dependence of fracture energy in ceramics, *J. Am. Ceram. Soc.* 65 (1982) C–14–C–16. doi:10.1111/j.1151-2916.1982.tb09933.x.
- [28] Roy W. Rice, *Mechanical properties of ceramics and composites : grain and particle effects*, Marcel Dekker, New York, 2000.
- [29] P. Chantikul, S.J. Bennison, B.R. Lawn, Role of grain size in the strength and r-curve properties of alumina, *J. Am. Ceram. Soc.* 73 (1990) 2419–2427.
- [30] Y.W. Mai, Thermal-stress resistance and fracture toughness of two tool ceramics, *J. Mater. Sci.* 11 (1976) 1430–1438. doi:10.1007/BF00540875.
- [31] L.A. Simpson, Discrepancy arising from measurement of grain–size dependence of fracture energy of Al<sub>2</sub>O<sub>3</sub>, *J. Am. Ceram. Soc.* 56 (1973) 610–611. doi:10.1111/j.1151-2916.1973.tb12435.x.
- [32] J.A. Coppola, R.C. Bradt, Effects of porosity on fracture of Al<sub>2</sub>O<sub>3</sub>, *J. Am. Ceram. Soc.* 56 (1973) 392–392. doi:10.1111/j.1151-2916.1973.tb12697.x.
- [33] L.M. Barker, Short Rod KIC Measurements of Al<sub>2</sub>O<sub>3</sub>, in: R.C. Bradt, D.P.H. Hasselman, F.F. Lange (Eds.), *Flaws Test.*, Springer US, 1978: pp. 483–494. [http://link.springer.com/chapter/10.1007/978-1-4615-7017-2\\_28](http://link.springer.com/chapter/10.1007/978-1-4615-7017-2_28) (accessed July 3, 2013).
- [34] S.W. Freiman, K.R. McKinney, H.L. Smith, Slow crack growth in polycrystalline ceramics, in: R.C. Bradt, D.P.H. Hasselman, F.F. Lange (Eds.), *Fract. Mech. Ceram.*, Springer US, 1974: pp. 659–676. [http://link.springer.com/chapter/10.1007/978-1-4615-7014-1\\_14](http://link.springer.com/chapter/10.1007/978-1-4615-7014-1_14) (accessed July 3, 2013).
- [35] H. Hübner, W. Jillek, Sub-critical crack extension and crack resistance in polycrystalline alumina, *J. Mater. Sci.* 12 (1977) 117–125. doi:10.1007/BF00738476.
- [36] R.W. Davidge, G. Tappin, The effective surface energy of brittle materials, *J. Mater. Sci.* 3 (1968) 165–173. doi:10.1007/BF00585484.
- [37] K.T. Faber, A.G. Evans, Crack deflection processes—I. Theory, *Acta Metall.* 31 (1983) 565–576. doi:10.1016/0001-6160(83)90046-9.
- [38] Y.-W. Mai, B.R. Lawn, Crack-interface grain bridging as a fracture resistance mechanism in ceramics: II, Theoretical fracture mechanics model, *J. Am. Ceram. Soc.* 70 (1987) 289–294. doi:10.1111/j.1151-2916.1987.tb04983.x.



- [39] R.W. Rice, S.W. Freiman, Grain-size dependence of fracture energy in ceramics: II, A model for noncubic materials, *J. Am. Ceram. Soc.* 64 (1981) 350–354. doi:10.1111/j.1151-2916.1981.tb10301.x.
- [40] P.L. Swanson, C.J. Fairbanks, B.R. Lawn, Y.-W. Mai, B.J. Hockey, Crack-Interface Grain Bridging as a Fracture Resistance I, Mechanism in Ceramics: I, Experimental Study on Alumina, *J. Am. Ceram. Soc.* 70 (1987) 279–289.
- [41] P.L. Swanson, Tensile fracture resistance mechanisms in brittle polycrystals: An ultrasonics and in situ microscopy investigation, *J. Geophys. Res. Solid Earth.* 92 (1987) 8015–8036. doi:10.1029/JB092iB08p08015.
- [42] G. Vekinis, M.F. Ashby, P.W.R. Beaumont, R-curve behaviour of Al<sub>2</sub>O<sub>3</sub> ceramics, *Acta Metall. Mater.* 38 (1990) 1151–1162. doi:10.1016/0956-7151(90)90188-M.
- [43] R.H.J. Hannink, P.M. Kelly, B.C. Muddle, Transformation toughening in zirconia-containing ceramics, *J. Am. Ceram. Soc.* 83 (2000) 461–487. doi:10.1111/j.1151-2916.2000.tb01221.x.
- [44] H.P. Kirchner, R.M. Gruver, A fractographic criterion for subcritical crack-growth boundaries in hot-pressed alumina, *J. Mater. Sci.* 14 (1979) 2110–2118. doi:10.1007/BF00688415.
- [45] T. Fett, A fracture-mechanical theory of subcritical crack growth in ceramics, *Int. J. Fract.* 54 (1992) 117–130.
- [46] A.G. Evans, A method for evaluating the time dependent failure characteristics of brittle materials - and its application to polycrystalline alumina, *J. Mater. Sci.* 7 (1972) 1137–1146.
- [47] T. Okada, G. Sines, Crack coalescence and microscopic crack growth in the delayed fracture of alumina, *J. Am. Ceram. Soc.* 66 (1983) 719–725. doi:10.1111/j.1151-2916.1983.tb10537.x.
- [48] J. Mecholsky, S. Freiman, Fractographic analysis of delayed failure in ceramics, in: L. Gilbertson, R. Zipp (Eds.), *Fractography Mater. Sci.*, ASTM International, 100 Barr Harbor Drive, PO Box C700, West Conshohocken, PA 19428-2959, 1981: pp. 246–246–13.
- [49] H.P. Kirchner, R.M. Gruver, Fractographic criteria for subcritical crack growth boundaries in 96% Al<sub>2</sub>O<sub>3</sub>, *J. Am. Ceram. Soc.* 63 (1980) 169–174. doi:10.1111/j.1151-2916.1980.tb10685.x.
- [50] J.J.M. Jr, S.W. Freiman, R.W. Rice, Fracture surface analysis of ceramics, *J. Mater. Sci.* 11 (1976) 1310–1319. doi:10.1007/BF00545152.
- [51] T. Lube, R.G.A. Baierl, Sub-critical crack growth in alumina – a comparison of different measurement and evaluation methods, *BHM Berg- Hüttenmänn. Monatshefte.* 156 (2011) 450–456. doi:10.1007/s00501-011-0035-y.
- [52] A. Krell, E. Pippel, J. Woltersdorf, W. Burger, Subcritical crack growth in Al<sub>2</sub>O<sub>3</sub> with submicron grain size, *J. Eur. Ceram. Soc.* 23 (2003) 81–89. doi:10.1016/S0955-2219(02)00072-9.
- [53] A.G. Evans, H. Johnson, The fracture stress and its dependence on slow crack growth, *J. Mater. Sci.* 10 (1975) 214–222. doi:10.1007/BF00540345.
- [54] A.G. Evans, Slow crack growth in brittle materials under dynamic loading conditions, *Int. J. Fract.* 10 (1974) 251–259. doi:10.1007/BF00113930.
- [55] P. Becher, M. Ferber, Grain-size dependence of the slow-crack growth behavior in noncubic ceramics, *Acta Metall.* 33 (1985) 1217–1221. doi:10.1016/0001-6160(85)90232-9.
- [56] M.E. Ebrahimi, J. Chevalier, G. Fantozzi, Slow crack-growth behavior of alumina ceramics, *J. Mater. Res.* 15 (2000) 142–147. doi:10.1557/JMR.2000.0024.
- [57] H.P. Kirchner, J.M. Ragosta, Crack growth from small flaws in larger grains in alumina, *J. Am. Ceram. Soc.* 63 (1980) 490–495.
- [58] R.W. Rice, Porosity effects on machining direction - Strength anisotropy and failure mechanisms, *J. Am. Ceram. Soc.* 77 (1994) 2232–2236. doi:10.1111/j.1151-2916.1994.tb07129.x.
- [59] R.W. Rice, Comments on “Fracture stress-reflecting spot relations in hot-pressed alumina,” *J. Mater. Sci.* 17 (1982) 1537–1539. doi:10.1007/BF00752272.

- [60] D. Hull, *Fractography: Observing, measuring and interpreting fracture surface topography*, Cambridge University Press, Cambridge, 1999.
- [61] T.A. Michalske, S.W. Freiman, A molecular mechanism for stress corrosion in vitreous silica, *J. Am. Ceram. Soc.* 66 (1983) 284–288. doi:10.1111/j.1151-2916.1983.tb15715.x.
- [62] S.M. Wiederhorn, B.J. Hockey, D.E. Roberts, Effect of temperature on the fracture of sapphire, *Philos. Mag.* 28 (1973) 783–796. doi:10.1080/14786437308220983.
- [63] K.P.D. Lagerlöf, A.H. Heuer, J. Castaing, J.P. Riviere, T.E. Mitchell, Slip and twinning in sapphire ( $\alpha$ -Al<sub>2</sub>O<sub>3</sub>), *J. Am. Ceram. Soc.* 77 (1994) 385–397.
- [64] A. Nakamura, K.P.D. Lagerlöf, K. Matsunaga, J. Tohma, T. Yamamoto, Y. Ikuhara, Control of dislocation configuration in sapphire, *Acta Mater.* 53 (2005) 455–462. doi:10.1016/j.actamat.2004.10.002.
- [65] S. Wang, Y. He, H. Huang, J. Zou, G.J. Auchterlonie, L. Hou, B. Huang, An improved loop test for experimentally approaching the intrinsic strength of alumina nanoscale whiskers, *Nanotechnology.* 24 (2013) 285703. doi:10.1088/0957-4484/24/28/285703.
- [66] H.W. Liu, Stress-corrosion cracking and the interaction between crack-tip stress field and solute atoms, *J. Basic Eng.* 92 (1970) 633–638. doi:10.1115/1.3425090.
- [67] R.N. Stevens, R. Dutton, The propagation of Griffith cracks at high temperatures by mass transport processes, *Mater. Sci. Eng.* 8 (1971) 220–234. doi:10.1016/0025-5416(71)90076-0.
- [68] C. Hsieh, R. Thomson, Lattice theory of fracture and crack creep, *J. Appl. Phys.* 44 (1973) 2051–2063. doi:10.1063/1.1662512.
- [69] D.A. Stuart, O.L. Anderson, Dependence of ultimate strength of glass under constant load on temperature, ambient atmosphere, and time, *J. Am. Ceram. Soc.* 36 (1953) 416–424. doi:10.1111/j.1151-2916.1953.tb12831.x.
- [70] S.N. Zhurkov, Kinetic concept of the strength of solids, *Int. J. Fract.* 26 (1984) 295–307. doi:10.1007/BF00962961.
- [71] J. Lankford, Tensile failure of unflawed polycrystalline Al<sub>2</sub>O<sub>3</sub>, *J. Mater. Sci.* 13 (1978) 351–357. doi:10.1007/BF00647780.
- [72] J. Lankford, Compressive strength and microplasticity in polycrystalline alumina, *J. Mater. Sci.* 12 (1977) 791–796. doi:10.1007/BF00548172.
- [73] J. Staehler, W. Predebon, B. Pletka, G. Subhash, Micromechanisms of deformation in high-purity hot-pressed alumina, *Mater. Sci. Eng. A.* 291 (2000) 37–45. doi:10.1016/S0921-5093(00)00976-X.
- [74] J. Lankford, W.W. Predebon, J.M. Staehler, G. Subhash, B.J. Pletka, C.E. Anderson, The role of plasticity as a limiting factor in the compressive failure of high strength ceramics, *Mech. Mater.* 29 (1998) 205–218. doi:10.1016/S0167-6636(98)00023-4.
- [75] A. Montagne, S. Pathak, X. Maeder, J. Michler, Plasticity and fracture of sapphire at room temperature: Load-controlled microcompression of four different orientations, *Ceram. Int.* 40 (2014) 2083–2090. doi:10.1016/j.ceramint.2013.07.121.
- [76] W.W. Webb, W.D. Forgeng, Growth and Defect Structure of Sapphire Microcrystals, *J. Appl. Phys.* 28 (1957) 1449–1454. doi:10.1063/1.1722675.
- [77] H.E. LaBelle, EFG, the invention and application to sapphire growth, *J. Cryst. Growth.* 50 (1980) 8–17. doi:10.1016/0022-0248(80)90226-2.
- [78] H. Sayir, A. Sayir, K.P.D. Lagerlöf, Temperature dependent brittle fracture of undoped and impurity doped sapphire fibers, in: J.B.W. Jr (Ed.), *Proc. 17th Annu. Conf. Compos. Adv. Ceram. Mater. Ceram. Eng. Sci. Proc.*, John Wiley & Sons, Inc., 1993: pp. 581–589. <http://onlinelibrary.wiley.com/doi/10.1002/9780470314180.ch84/summary> (accessed April 2, 2017).
- [79] N.-W. Chen, D.W. Readey, J.J. Moore, Mechanisms of oxide whisker growth, in: J.B. Watchman (Ed.), *Proc. 18th Annu. Conf. Compos. Adv. Ceram. Mater. Ceram. Eng. Sci. Proc.*, John

- Wiley & Sons, Inc., 1994: pp. 170–180. <http://onlinelibrary.wiley.com/doi/10.1002/9780470314500.ch20/summary> (accessed April 2, 2017).
- [80] V. Valcárcel, A. Souto, F. Guitián, Development of single-crystal  $\alpha$ -Al<sub>2</sub>O<sub>3</sub> fibers by vapor–liquid–solid deposition (VLS) from aluminum and powdered silica, *Adv. Mater.* 10 (1998) 138–140. doi:10.1002/(SICI)1521-4095(199801)10:2<138::AID-ADMA138>3.0.CO;2-A.
- [81] S.S. Brenner, Growth and Properties of “Whiskers,” *Science*. 128 (1958) 569–575. doi:10.1126/science.128.3324.569.
- [82] P.D. Bayer, R.E. Cooper, Size-strength effects in sapphire and silicon nitride whiskers at 20° C, *J. Mater. Sci.* 2 (1967) 233–237. doi:10.1007/BF00555379.
- [83] S.S. Brenner, Mechanical Behavior of Sapphire Whiskers at Elevated Temperatures, *J. Appl. Phys.* 33 (1962) 33. doi:10.1063/1.1728523.
- [84] P. Grenier, A. Kelly, Evolution de la contrainte de rupture des trichites d’alumine en fonction de l’état structural, *Comptes Rendus Académie Sci.* B266 (1968) 859–862.
- [85] R.F. Regester, P.D. Gorsuch, L. Girifalco, Structure and properties of aluminum oxide whiskers, *Nav. Eng. J.* 79 (1967) 957–960. doi:10.1111/j.1559-3584.1967.tb05383.x.
- [86] W.W. Webb, W.D. Forgeng, Mechanical behavior of microcrystals, *Acta Metall.* 6 (1958) 462–469. doi:10.1016/0001-6160(58)90109-3.
- [87] F.P. Mallinder, B.A. Proctor, The strengths of flame-polished sapphire crystals, *Philos. Mag.* 13 (1966) 197–208. doi:10.1080/14786436608211996.
- [88] P.D. Bayer, R.E. Cooper, The effects of chemical polishing on the strength of sapphire whiskers, *J. Mater. Sci.* 2 (1967) 347–353. doi:10.1007/BF00572418.
- [89] A. Kelly, N.H. Macmillan, *Strong solids*, 3rd ed, Clarendon Press, Oxford [Oxfordshire], 1986.
- [90] W.H. Sutton, J. Chorne, *Potential of oxide-fiber reinforced metals*, General Electric, Missile and Space Division, 1965.
- [91] C.A. Calow, A. Moore, No hope for ceramic whiskers or fibres as reinforcement of metal matrices at high temperature, *J. Mater. Sci.* 7 (1972) 543–558. doi:10.1007/BF00761953.
- [92] R.R. Bowman, A.K. Misra, S.M. Arnold, Processing and mechanical properties of Al<sub>2</sub>O<sub>3</sub> fiber-reinforced NiAl composites, *Metall. Mater. Trans. A.* 26 (1995) 615–628. doi:10.1007/BF02663910.
- [93] V. Valcárcel, C. Cerecedo, F. Guitián, Method for production of  $\alpha$ -alumina whiskers via vapor–liquid–solid deposition, *J. Am. Ceram. Soc.* 86 (2003) 1683–1690. doi:10.1111/j.1151-2916.2003.tb03540.x.
- [94] S.T. Mileiko, Composites reinforced with single crystalline oxide fibres: experiments and modelling, *J. Mater. Sci.* 41 (2006) 6708–6717. doi:10.1007/s10853-006-0184-7.
- [95] S.T. Mileiko, Single crystalline oxide fibres for heat-resistant composites, *Compos. Sci. Technol.* 65 (2005) 2500–2513. doi:10.1016/j.compscitech.2005.05.029.
- [96] S.T. Mileiko, V.I. Kazmin, Crystallization of fibres inside a matrix: a new way of fabrication of composites, *J. Mater. Sci.* 27 (1992) 2165–2172. doi:10.1007/BF01117932.
- [97] V.M. Kiiko, S.T. Mileiko, Evaluation of the room-temperature strength of oxide fibres produced by the internal-crystallization method, *Compos. Sci. Technol.* 59 (1999) 1977–1981. doi:10.1016/S0266-3538(99)00054-8.
- [98] V.N. Kurlov, V.M. Kiiko, A.A. Kolchin, S.T. Mileiko, Sapphire fibres grown by a modified internal crystallisation method, *J. Cryst. Growth.* 204 (1999) 499–504. doi:10.1016/S0022-0248(99)00213-4.
- [99] P.E. Cantonwine, Strength of thermally exposed alumina fibers Part I Single filament behavior, *J. Mater. Sci.* 38 (2003) 461–470.
- [100] D.M. Wilson, L.R. Visser, High performance oxide fibers for metal and ceramic composites, *Compos. Part Appl. Sci. Manuf.* 32 (2001) 1143–1153. doi:10.1016/S1359-835X(00)00176-7.

- [101] J. He, D.R. Clarke, Determination of fibre strength distributions from bundle tests using optical luminescence spectroscopy, *Proc. R. Soc. Lond. Math. Phys. Eng. Sci.* 453 (1997) 1881–1901. doi:10.1098/rspa.1997.0101.
- [102] R.S. Hay, G.E. Fair, T. Tidball, Fiber strength after grain growth in nextel™ 610 alumina fiber, *J. Am. Ceram. Soc.* 98 (2015) 1907–1914. doi:10.1111/jace.13523.
- [103] S. Ochiai, S. Kuboshima, K. Morishita, H. Okuda, T. Inoue, Fracture toughness of Al<sub>2</sub>O<sub>3</sub> fibers with an artificial notch introduced by a focused-ion-beam, *J. Eur. Ceram. Soc.* 30 (2010) 1659–1667. doi:10.1016/j.jeurceramsoc.2009.12.020.
- [104] V. Lavaste, M.H. Berger, A.R. Bunsell, J. Besson, Microstructure and mechanical characteristics of alpha-alumina-based fibres, *J. Mater. Sci.* 30 (1995) 4215–4225. doi:10.1007/BF00361500.
- [105] R. Komanduri, M.C. Shaw, Scanning electron microscope study of surface characteristics of abrasive materials, *J. Eng. Mater. Technol.* 96 (1974) 145–156. doi:10.1115/1.3443203.
- [106] H. Huang, X.H. Zhu, Q.K. Huang, X.Z. Hu, Weibull strength distributions and fracture characteristics of abrasive materials, *Eng. Fract. Mech.* 52 (1995) 15–24. doi:10.1016/0013-7944(95)00010-S.
- [107] P.T. Bertrand, S.E. Laurich-McIntyre, R.C. Bradt, Strengths of fused and tabular alumina refractory grains, *Am. Ceram. Soc. Bull.* 67 (1988) 1217–1222.
- [108] L.D. Hart, ed., *Alumina chemicals: science and technology handbook*, Esther Lense, assoc. ed.. - Westerville, Ohio : The American Ceramic Society, 1990.
- [109] W.H. Gitzen, ed., *Alumina as a ceramic material*, The American Ceramic Society, 1970.
- [110] Y. Uchida, Y. Sawabe, M. Mohri, Nearly monodispersed single crystal particles of alpha-alumina, in: *Sci. Technol. Appl. Colloidal Suspens.*, The American Ceramic Society, Indianapolis, IN (United States), 1995: pp. 159–165. <http://www.osti.gov/scitech/biblio/181787> (accessed November 21, 2016).
- [111] T. Laha, K. Balani, A. Agarwal, S. Patil, S. Seal, Synthesis of nanostructured spherical aluminum oxide powders by plasma engineering, *Metall. Mater. Trans. A.* 36 (2005) 301–309.
- [112] A. Rosenflanz, M. Frey, B. Endres, T. Anderson, E. Richards, C. Schardt, Bulk glasses and ultrahard nanoceramics based on alumina and rare-earth oxides, *Nature*. 430 (2004) 761–764. doi:10.1038/nature02729.
- [113] K. Nitta, T.M. Shau, J. Sugahara, Flaky aluminum oxide and pearlescent pigment, and production thereof, EP0763573 B1, 2001. <http://www.google.com/patents/EP0763573B1> (accessed May 30, 2017).
- [114] G. Pfaff, *Special effect pigments: Technical basics and applications*, Vincentz Network GmbH & Co KG, Hannover, Germany, 2008.
- [115] C. Bacciarini, V. Mathier, Aluminium AA6061 Matrix Composite Reinforced with Spherical Alumina Particles Produced by Infiltration: Perspective on Aerospace Applications, *J. Metall.* 2014 (2014) e248542. doi:10.1155/2014/248542.
- [116] M. Kouzeli, L. Weber, C. San Marchi, A. Mortensen, Influence of damage on the tensile behaviour of pure aluminium reinforced with  $\geq 40$  vol. pct alumina particles, *Acta Mater.* 49 (2001) 3699–3709. doi:10.1016/S1359-6454(01)00279-8.
- [117] J. Segurado, J. LLorca, Computational micromechanics of composites: The effect of particle spatial distribution, *Mech. Mater.* 38 (2006) 873–883. doi:10.1016/j.mechmat.2005.06.026.
- [118] L. Babout, E. Maire, R. Fougères, Damage initiation in model metallic materials: X-ray tomography and modelling, *Acta Mater.* 52 (2004) 2475–2487. doi:10.1016/j.actamat.2004.02.001.
- [119] Y. Brechet, J.D. Embury, S. Tao, L. Luo, Damage initiation in metal matrix composites, *Acta Metall. Mater.* 39 (1991) 1781–1786. doi:10.1016/0956-7151(91)90146-R.



- [120] J. Gammage, D. Wilkinson, Y. Brechet, D. Embury, A model for damage coalescence in heterogeneous multi-phase materials, *Acta Mater.* 52 (2004) 5255–5263. doi:10.1016/j.actamat.2004.07.009.
- [121] S. Ghosh, S. Moorthy, Particle fracture simulation in non-uniform microstructures of metal–matrix composites, *Acta Mater.* 46 (1998) 965–982. doi:10.1016/S1359-6454(97)00289-9.
- [122] M.T. Kiser, F.W. Zok, D.S. Wilkinson, Plastic flow and fracture of a particulate metal matrix composite, *Acta Mater.* 44 (1996) 3465–3476. doi:10.1016/1359-6454(96)00028-6.
- [123] M. Kouzeli, L. Weber, C. San Marchi, A. Mortensen, Quantification of microdamage phenomena during tensile straining of high volume fraction particle reinforced aluminium, *Acta Mater.* 49 (2001) 497–505. doi:10.1016/S1359-6454(00)00334-7.
- [124] J.J. Lewandowski, C. Liu, W.H. Hunt Jr., Effects of matrix microstructure and particle distribution on fracture of an aluminum metal matrix composite, *Mater. Sci. Eng. A.* 107 (1989) 241–255. doi:10.1016/0921-5093(89)90392-4.
- [125] J. Llorca, A. Martin, J. Ruiz, M. Elices, Particulate fracture during deformation of a Spray Formed Metal-Matrix Composite, *Metall. Trans. A.* 24 (1993) 1575–1588. doi:10.1007/BF02646597.
- [126] E. Maire, C.L. Bourlot, J. Adrien, A. Mortensen, R. Mokso, 20 Hz X-ray tomography during an in situ tensile test, *Int. J. Fract.* 200 (2016) 3–12. doi:10.1007/s10704-016-0077-y.
- [127] B.S. Majumdar, A.B. Pandey, Deformation and fracture of a particle-reinforced aluminum alloy composite: Part II. Modeling, *Metall. Mater. Trans. A.* 31 (2000) 937–950. doi:10.1007/s11661-000-0036-z.
- [128] R. Mueller, A. Rossoll, L. Weber, M.A.M. Bourke, D.C. Dunand, A. Mortensen, Tensile flow stress of ceramic particle-reinforced metal in the presence of particle cracking, *Acta Mater.* 56 (2008) 4402–4416. doi:10.1016/j.actamat.2008.05.004.
- [129] P.M. Mummery, B. Derby, C.B. Scruby, Acoustic emission from particulate-reinforced metal matrix composites, *Acta Metall. Mater.* 41 (1993) 1431–1445. doi:10.1016/0956-7151(93)90252-N.
- [130] P.M. Mummery, B. Derby, In situ scanning electron microscope studies of fracture in particulate-reinforced metal-matrix composites, *J. Mater. Sci.* 29 (1994) 5615–5624. doi:10.1007/BF00349956.
- [131] A.B. Pandey, B.S. Majumdar, D.B. Miracle, Deformation and fracture of a particle-reinforced aluminum alloy composite: Part I. Experiments, *Metall. Mater. Trans. A.* 31 (2000) 921–936.
- [132] W.L. Prater, Comparison of ceramic material effects on the flexural Weibull statistics and fracture of high volume fraction particle reinforced aluminum, *Mater. Sci. Eng. A.* 420 (2006) 187–198. doi:10.1016/j.msea.2006.01.057.
- [133] D.S. Wilkinson, W. Pompe, M. Oeschner, Modeling the mechanical behaviour of heterogeneous multi-phase materials, *Prog. Mater. Sci.* 46 (2001) 379–405. doi:10.1016/S0079-6425(00)00008-6.
- [134] L. Babout, Y. Brechet, E. Maire, R. Fougères, On the competition between particle fracture and particle decohesion in metal matrix composites, *Acta Mater.* 52 (2004) 4517–4525. doi:10.1016/j.actamat.2004.06.009.
- [135] A. Hauert, A. Rossoll, A. Mortensen, Particle fracture in high-volume-fraction ceramic-reinforced metals: Governing parameters and implications for composite failure, *J. Mech. Phys. Solids.* 57 (2009) 1781–1800. doi:10.1016/j.jmps.2009.08.005.
- [136] J.E. Spowart, D.B. Miracle, The influence of reinforcement morphology on the tensile response of 6061/SiC/25p discontinuously-reinforced aluminum, *Mater. Sci. Eng. A.* 357 (2003) 111–123. doi:10.1016/S0921-5093(03)00244-2.

- [137] C. San Marchi, F. Cao, M. Kouzeli, A. Mortensen, Quasistatic and dynamic compression of aluminum-oxide particle reinforced pure aluminum, *Mater. Sci. Eng. A.* 337 (2002) 202–211. doi:10.1016/S0921-5093(02)00035-7.
- [138] J.E. Spowart, The 3-D analysis of discontinuously reinforced aluminum composite microstructures, *JOM.* 58 (2006) 29–33. doi:10.1007/BF02748492.
- [139] B.Y. Zong, C.W. Lawrence, B. Derby, Acoustic emission from a SiC reinforced Al-2618 metal matrix composite during straining, *Scr. Mater.* 37 (1997) 1045–1052. doi:10.1016/S1359-6462(97)00211-X.
- [140] A. Madgwick, T. Mori, P.J. Withers, A neutron diffraction study of creep and damage occurrence in an A359/SiC composite, *Mater. Sci. Eng. A.* 333 (2002) 232–238. doi:10.1016/S0921-5093(01)01843-3.
- [141] E. Maire, P.J. Withers, Quantitative X-ray tomography, *Int. Mater. Rev.* 59 (2014) 1–43. doi:10.1179/1743280413Y.0000000023.
- [142] J.J. Williams, Z. Flom, A.A. Amell, N. Chawla, X. Xiao, F. De Carlo, Damage evolution in SiC particle reinforced Al alloy matrix composites by X-ray synchrotron tomography, *Acta Mater.* 58 (2010) 6194–6205. doi:10.1016/j.actamat.2010.07.039.
- [143] M.S. Hu, Some effects of particle size on the flow behavior of Al/SiCp composites, *Scr. Metall. Mater.* 25 (1991) 695–700. doi:10.1016/0956-716X(91)90117-J.
- [144] W.H. Hunt, J.R. Brockenbrough, P.E. Magnusen, An Al-Si-Mg composite model system: Microstructural effects on deformation and damage evolution, *Scr. Metall. Mater.* 25 (1991) 15–20. doi:10.1016/0956-716X(91)90346-3.
- [145] P.M. Mummery, P. Anderson, G.R. Davis, B. Derby, J.C. Elliott, Damage assessment in particle-reinforced metal matrix composites using x-ray microtomography, *Scr. Metall. Mater.* 29 (1993) 1457–1462. doi:10.1016/0956-716X(93)90336-Q.
- [146] P.M. Singh, J.J. Lewandowski, Effects of heat treatment and reinforcement size, *Metall. Trans. A.* 24 (1993) 2531–2543. doi:10.1007/BF02646532.
- [147] M. Li, S. Ghosh, O. Richmond, An experimental–computational approach to the investigation of damage evolution in discontinuously reinforced aluminum matrix composite, *Acta Mater.* 47 (1999) 3515–3532. doi:10.1016/S1359-6454(99)00148-2.
- [148] P. Mummery, B. Derby, The influence of microstructure on the fracture behaviour of particulate metal matrix composites, *Mater. Sci. Eng. A.* 135 (1991) 221–224. doi:10.1016/0921-5093(91)90566-6.
- [149] B.J. Weng, S.T. Chang, J.S. Shiau, Microfracture mechanisms of SiC-6061 aluminum composite after hiping, *Scr. Metall. Mater.* 27 (1992) 1127–1132. doi:10.1016/0956-716X(92)90586-4.
- [150] W.J. Poole, E.J. Dowdle, Experimental measurements of damage evolution in Al-Si eutectic alloys, *Scr. Mater.* 39 (1998) 1281–1287. doi:10.1016/S1359-6462(98)00326-1.
- [151] S.G. Song, N. Shi, G.T. Gray, J.A. Roberts, Reinforcement shape effects on the fracture behavior and ductility of particulate-reinforced 6061-Al matrix composites, *Metall. Mater. Trans. A.* 27 (1996) 3739–3746. doi:10.1007/BF02595465.
- [152] C.R. Chen, S.Y. Qin, S.X. Li, J.L. Wen, Finite element analysis about effects of particle morphology on mechanical response of composites, *Mater. Sci. Eng. A.* 278 (2000) 96–105. doi:10.1016/S0921-5093(99)00603-6.
- [153] S. Qin, C. Chen, G. Zhang, W. Wang, Z. Wang, The effect of particle shape on ductility of SiCp reinforced 6061 Al matrix composites, *Mater. Sci. Eng. A.* 272 (1999) 363–370. doi:10.1016/S0921-5093(99)00503-1.
- [154] C. Krüger, A. Mortensen, Infiltrated Cu8Al–Ti alumina composites, *Compos. Part Appl. Sci. Manuf.* 66 (2014) 1–15. doi:10.1016/j.compositesa.2014.06.019.



- [155] A. Miserez, A. Rossoll, A. Mortensen, Fracture of aluminium reinforced with densely packed ceramic particles: link between the local and the total work of fracture, *Acta Mater.* 52 (2004) 1337–1351. doi:10.1016/j.actamat.2003.11.019.
- [156] A. Miserez, R. Müller, A. Rossoll, L. Weber, A. Mortensen, Particle reinforced metals of high ceramic content, *Mater. Sci. Eng. A.* 387–389 (2004) 822–831. doi:10.1016/j.msea.2004.05.054.
- [157] A. Miserez, S. Stücklin, A. Rossoll, C. San Marchi, A. Mortensen, Influence of heat treatment and particle shape on mechanical properties of infiltrated Al<sub>2</sub>O<sub>3</sub> particle reinforced Al-2 wt-%Cu, *Mater. Sci. Technol.* 18 (2002) 1461–1470. doi:10.1179/026708302225007754.
- [158] C.A. Lewis, P.J. Withers, Weibull modelling of particle cracking in metal matrix composites, *Acta Metall. Mater.* 43 (1995) 3685–3699. doi:10.1016/0956-7151(95)90152-3.
- [159] J. Llorca, An analysis of the influence of reinforcement fracture on the strength of discontinuously-reinforced metal-matrix composites, *Acta Metall. Mater.* 43 (1995) 181–192. doi:10.1016/0956-7151(95)90273-2.
- [160] A. Ayyar, N. Chawla, Microstructure-based modeling of the influence of particle spatial distribution and fracture on crack growth in particle-reinforced composites, *Acta Mater.* 55 (2007) 6064–6073. doi:10.1016/j.actamat.2007.06.044.
- [161] S.F. Corbin, D.S. Wilkinson, Influence of matrix strength and damage accumulation on the mechanical response of a particulate metal matrix composite, *Acta Metall. Mater.* 42 (1994) 1329–1335. doi:10.1016/0956-7151(94)90149-X.
- [162] M. Kouzeli, C. San Marchi, A. Mortensen, Effect of reaction on the tensile behavior of infiltrated boron carbide–aluminum composites, *Mater. Sci. Eng. A.* 337 (2002) 264–273. doi:10.1016/S0921-5093(02)00039-4.
- [163] D.J. Lloyd, Aspects of fracture in particulate reinforced metal matrix composites, *Acta Metall. Mater.* 39 (1991) 59–71. doi:10.1016/0956-7151(91)90328-X.
- [164] T. Mochida, M. Taya, D.J. Lloyd, Fracture of particles in a particle/metal matrix composite under plastic straining and its effect on the Young's modulus of the composite, *Mater. Trans. JIM.* 32 (1991) 931–942. doi:10.2320/matertrans1989.32.931.
- [165] P.B. Prangnell, T. Downes, P.J. Withers, W.M. Stobbs, The deformation of discontinuously reinforced MMCs—II. The elastic response, *Acta Metall. Mater.* 42 (1994) 3437–3442. doi:10.1016/0956-7151(94)90476-6.
- [166] M. Vedani, E. Gariboldi, Damage and ductility of particulate and short-fibre Al/Al<sub>2</sub>O<sub>3</sub> composites, *Acta Mater.* 44 (1996) 3077–3088. doi:10.1016/1359-6454(95)00437-8.
- [167] B.Y. Zong, B. Derby, Characterization of microstructural damage during plastic strain of a particulate-reinforced metal matrix composite at elevated temperature, *J. Mater. Sci.* 31 (1996) 297–303. doi:10.1007/BF01139143.
- [168] J. Lemaitre, A continuous damage mechanics model for ductile fracture, *J. Eng. Mater. Technol.* 107 (1985) 83–89. doi:10.1115/1.3225775.
- [169] M. Manoharan, M. Gupta, M.O. Lai, D. Saravanaranganathan, Application of model for work hardening behaviour of SiC reinforced magnesium based metal matrix composites, *Mater. Sci. Technol.* 16 (2000) 670–674. doi:10.1179/026708300101508252.
- [170] M. Manoharan, M. Gupta, Effect of silicon carbide volume fraction on the work hardening behaviour of thermomechanically processed aluminium-based metal–matrix composites, *Compos. Part B Eng.* 30 (1999) 107–112. doi:10.1016/S1359-8368(98)00041-9.
- [171] A.R. Kennedy, S.M. Wyatt, The effect of processing on the mechanical properties and interfacial strength of aluminium/TiC MMCs, *Compos. Sci. Technol.* 60 (2000) 307–314. doi:10.1016/S0266-3538(99)00125-6.

- [172] D.J. Lahaie, J.D. Embury, F.W. Zok, Damage accumulation and mechanical properties of particle-reinforced metal–matrix composites during hydrostatic extrusion, *Compos. Sci. Technol.* 64 (2004) 1539–1549. doi:10.1016/j.compscitech.2003.11.006.
- [173] W.J. Poole, N. Charras, An experimental study on the effect of damage on the stress–strain behaviour for Al–Si model composites, *Mater. Sci. Eng. A.* 406 (2005) 300–308. doi:10.1016/j.msea.2005.06.041.
- [174] C. Tekoglu, T. Pardoën, A micromechanics based damage model for composite materials, *Int. J. Plast.* 26 (2010) 549–569. doi:10.1016/j.ijplas.2009.09.002.
- [175] R. Mueller, A. Mortensen, Simplified prediction of the monotonic uniaxial stress–strain curve of non-linear particulate composites, *Acta Mater.* 54 (2006) 2145–2155. doi:10.1016/j.actamat.2006.01.002.
- [176] S.B. Batdorf, Tensile Strength of Unidirectionally Reinforced Composites — I, *J. Reinf. Plast. Compos.* 1 (1982) 153–164. doi:10.1177/073168448200100206.
- [177] M.B. Bush, The Interaction between a Crack and a Particle Cluster, *Int. J. Fract.* 88 (1997) 215–232. doi:10.1023/A:1007469631883.
- [178] D.L. Davidson, Fatigue and fracture toughness of aluminium alloys reinforced with SiC and alumina particles, *Composites.* 24 (1993) 248–255. doi:10.1016/0010-4361(93)90171-4.
- [179] H.M. Hu, E.J. Lavernia, W.C. Harrigan, J. Kajuch, S.R. Nutt, Microstructural investigation on B4C/Al-7093 composite, *Mater. Sci. Eng. A.* 297 (2001) 94–104. doi:10.1016/S0921-5093(00)01254-5.
- [180] W.H. Hunt, T.M. Osman, J.J. Lewandowski, Micro- and macrostructural factors in DRA fracture resistance, *JOM.* 45 (1993) 30–35. doi:10.1007/BF03223363.
- [181] J.W. Leggoe, X.Z. Hu, M.B. Bush, Crack tip damage development and crack growth resistance in particulate reinforced metal matrix composites, *Eng. Fract. Mech.* 53 (1996) 873–895. doi:10.1016/0013-7944(95)00167-0.
- [182] M. Manoharan, S.V. Kamat, On the fracture toughness of particulate reinforced metal-matrix composites, *Scr. Metall. Mater.* 25 (1991) 2121–2125. doi:10.1016/0956-716X(91)90285-9.
- [183] Z. Dan, F.R. Tuler, Effect of particle size on fracture toughness in metal matrix composites, *Eng. Fract. Mech.* 47 (1994) 303–308. doi:10.1016/0013-7944(94)90230-5.
- [184] J.J. Stephens, J.P. Lucas, F.M. Hosking, Cast Al-7 Si composites: Effect of particle type and size on mechanical properties, *Scr. Metall.* 22 (1988) 1307–1312. doi:10.1016/S0036-9748(88)80152-2.
- [185] Z.H.A. Kassam, R.J. Zhang, Z. Wang, Finite element simulation to investigate interaction between crack and particulate reinforcements in metal-matrix composites, *Mater. Sci. Eng. A.* 203 (1995) 286–299. doi:10.1016/0921-5093(95)09828-3.
- [186] E.M. Patton, M.H. Santare, Crack path prediction near an elliptical inclusion, *Eng. Fract. Mech.* 44 (1993) 195–205. doi:10.1016/0013-7944(93)90044-S.
- [187] S.A. Ponnusami, S. Turteltaub, S. van der Zwaag, Cohesive-zone modelling of crack nucleation and propagation in particulate composites, *Eng. Fract. Mech.* 149 (2015) 170–190. doi:10.1016/j.engfracmech.2015.09.050.
- [188] A. Mortensen, J. Llorca, Metal matrix composites, *Annu. Rev. Mater. Res.* 40 (2010) 243–270. doi:10.1146/annurev-matsci-070909-104511.
- [189] K. Wallin, T. Saario, K. Törrönen, Fracture of brittle particles in a ductile matrix, *Int. J. Fract.* 32 (1986) 201–209. doi:10.1007/BF00018353.
- [190] C.H. Caceres, J.R. Griffiths, Damage by the cracking of silicon particles in an Al-7Si-0.4Mg casting alloy, *Acta Mater.* 44 (1996) 25–33. doi:10.1016/1359-6454(95)00172-8.
- [191] K. Derrien, D. Baptiste, D. Guedra-Degeorges, J. Foulquier, Multiscale modeling of the damaged plastic behavior and failure of Al/SiCp composites, *Int. J. Plast.* 15 (1999) 667–685. doi:10.1016/S0749-6419(99)00009-1.

- [192] J.D. Eshelby, The determination of the elastic field of an ellipsoidal inclusion, and related problems, *Proc. R. Soc. Lond. Math. Phys. Eng. Sci.* 241 (1957) 376–396. doi:10.1098/rspa.1957.0133.
- [193] T. Mori, K. Tanaka, Average stress in matrix and average elastic energy of materials with misfitting inclusions, *Acta Metall.* 21 (1973) 571–574. doi:10.1016/0001-6160(73)90064-3.
- [194] M. Taya, K.E. Lulay, D.J. Lloyd, Strengthening of a particulate metal matrix composite by quenching, *Acta Metall. Mater.* 39 (1991) 73–87. doi:10.1016/0956-7151(91)90329-Y.
- [195] J.R. Brockenbrough, F.W. Zok, On the role of particle cracking in flow and fracture of metal matrix composites, *Acta Metall. Mater.* 43 (1995) 11–20. doi:10.1016/0956-7151(95)90256-2.
- [196] C.W. Lawrence, P.M. Mummery, J.H. Tweed, Observations of extrusion-induced damage of metal-matrix composites, *J. Mater. Sci. Lett.* 12 (1993) 647–649. doi:10.1007/BF00465579.
- [197] M. Li, S. Ghosh, O. Richmond, H. Weiland, T.N. Rouns, Three dimensional characterization and modeling of particle reinforced metal matrix composites: part I: Quantitative description of microstructural morphology, *Mater. Sci. Eng. A.* 265 (1999) 153–173. doi:10.1016/S0921-5093(98)01132-0.
- [198] J.-Y. Buffiere, E. Maire, C. Verdu, P. Cloetens, M. Pateyron, G. Peix, J. Baruchel, Damage assessment in an Al/SiC composite during monotonic tensile tests using synchrotron X-ray microtomography, *Mater. Sci. Eng. A.* 234 (1997) 633–635. doi:10.1016/S0921-5093(97)00302-X.
- [199] E. Broch, J.A. Franklin, The point-load strength test, *Int. J. Rock Mech. Min. Sci. Geomech. Abstr.* 9 (1972) 669–676. doi:10.1016/0148-9062(72)90030-7.
- [200] R.H. Brzesowsky, C.J. Spiers, C.J. Peach, S.J.T. Hangx, Failure behavior of single sand grains: Theory versus experiment, *J. Geophys. Res.* 116 (2011). doi:10.1029/2010JB008120.
- [201] G.R. McDowell, M.D. Bolton, On the micromechanics of crushable aggregates, *Géotechnique.* 48 (1998) 667–679. doi:10.1680/geot.1998.48.5.667.
- [202] Y. Nakata, A.F.L. Hyde, M. Hyodo, H. Murata, A probabilistic approach to sand particle crushing in the triaxial test, *Géotechnique.* 49 (1999) 567–583. doi:10.1680/geot.1999.49.5.567.
- [203] S. Antonyuk, S. Heinrich, J. Tomas, N.G. Deen, M.S. van Buijtenen, J.A.M. Kuipers, Energy absorption during compression and impact of dry elastic-plastic spherical granules, *Granul. Matter.* 12 (2010) 15–47. doi:10.1007/s10035-009-0161-3.
- [204] S. Antonyuk, J. Tomas, S. Heinrich, L. Mörl, Breakage behaviour of spherical granulates by compression, *Chem. Eng. Sci.* 60 (2005) 4031–4044. doi:10.1016/j.ces.2005.02.038.
- [205] M. Khanal, W. Schubert, J. Tomas, Compression and impact loading experiments of high strength spherical composites, *Int. J. Miner. Process.* 86 (2008) 104–113. doi:10.1016/j.minpro.2007.12.001.
- [206] S.F. Yap, M.J. Adams, J.P.K. Seville, Z. Zhang, Single and bulk compression of pharmaceutical excipients: Evaluation of mechanical properties, *Powder Technol.* 185 (2008) 1–10. doi:10.1016/j.powtec.2007.09.005.
- [207] S.F. Yap, M. Adams, J. Seville, Z. Zhang, Understanding the mechanical properties of single micro-particles and their compaction behaviour, *China Particuology.* 4 (2006) 35–40. doi:10.1016/S1672-2515(07)60231-0.
- [208] S. Lobo-Guerrero, L.E. Vallejo, Application of Weibull statistics to the tensile strength of rock aggregates, *J. Geotech. Geoenvironmental Eng.* 132 (2006) 786–790. doi:10.1061/(ASCE)1090-0241(2006)132:6(786).
- [209] L.M. Tavares, Chapter 1 Breakage of single particles: Quasi-static, in: A.D. Salman, M. Ghadiri, M.J. Hounslow (Eds.), *Handb. Powder Technol.*, Elsevier Science B.V., 2007: pp. 3–68. <http://www.sciencedirect.com/science/article/pii/S0167378507120042> (accessed July 17, 2013).

- [210] G. Ledergerber, Z. Kopajtic, F. Ingold, R.W. Stratton, Preparation of uranium nitride in the form of microspheres, *J. Nucl. Mater.* 188 (1992) 28–35. doi:10.1016/0022-3115(92)90450-Y.
- [211] S. Zhao, Y. Gan, M. Kamlah, T. Kennerknecht, R. Rolli, Influence of plate material on the contact strength of  $\text{Li}_4\text{SiO}_4$  pebbles in crush tests and evaluation of the contact strength in pebble–pebble contact, *Eng. Fract. Mech.* 100 (2013) 28–37. doi:10.1016/j.engfrac-mech.2012.05.011.
- [212] Y. Hiramatsu, Y. Oka, Determination of the tensile strength of rock by a compression test of an irregular test piece, *Int. J. Rock Mech. Min. Sci. Geomech. Abstr.* 3 (1966) 89–99. doi:10.1016/0148-9062(66)90002-7.
- [213] B.W. Darvell, Uniaxial compression tests and the validity of indirect tensile strength, *J. Mater. Sci.* 25 (1990) 757–780.
- [214] Y. Hiramatsu, Y. Oka, Determination of the tensile strength of rock by a compression test of an irregular test piece: Authors’ reply to discussion by J. Salençon, *Int. J. Rock Mech. Min. Sci. Geomech. Abstr.* 4 (1967) 363–365. doi:10.1016/0148-9062(67)90017-4.
- [215] J. Salençon, Comments on “determination of the tensile strength of rock by a compression test of an irregular test piece,” *Int. J. Rock Mech. Min. Sci. Geomech. Abstr.* 3 (1966) 349–350.
- [216] G. Wijk, Some new theoretical aspects of indirect measurements of the tensile strength of rocks, *Int. J. Rock Mech. Min. Sci. Geomech. Abstr.* 15 (1978) 149–160. doi:10.1016/0148-9062(78)91221-4.
- [217] J.C. Jaeger, Failure of rocks under tensile conditions, *Int. J. Rock Mech. Min. Sci. Geomech. Abstr.* 4 (1967) 219–227. doi:10.1016/0148-9062(67)90046-0.
- [218] B.A. Kschinka, S. Perrella, H. Nguyen, R.C. Bradt, Strengths of glass spheres in compression, *J. Am. Ceram. Soc.* 69 (1986) 467–472. doi:10.1111/j.1151-2916.1986.tb07447.x.
- [219] G.R. McDowell, A. Amon, The application of Weibull statistics to the fracture of soil particles, *J. Jpn. Geotech. Soc. Soils Found.* 40 (2000) 133–141.
- [220] H. Ogiso, M. Yoshida, S. Nakano, J. Akedo, Effects of Al ion implantation on the strength of  $\text{Al}_2\text{O}_3$  particles, *Surf. Coat. Technol.* 201 (2007) 8180–8184. doi:10.1016/j.surf-coat.2006.01.093.
- [221] R. Pitchumani, O. Zhupanska, G.M.H. Meesters, B. Scarlett, Measurement and characterization of particle strength using a new robotic compression tester, *Powder Technol.* 143–144 (2004) 56–64. doi:10.1016/j.powtec.2004.04.007.
- [222] D. Portnikov, H. Kalman, S. Aman, J. Tomas, Investigating the testing procedure limits for measuring particle strength distribution, *Powder Technol.* 237 (2013) 489–496. doi:10.1016/j.powtec.2012.12.025.
- [223] L. Ribas, G.C. Cordeiro, R.D. Toledo Filho, L.M. Tavares, Measuring the strength of irregularly-shaped fine particles in a microcompression tester, *Miner. Eng.* 65 (2014) 149–155. doi:10.1016/j.mineng.2014.05.021.
- [224] Y. Rozenblat, D. Portnikov, A. Levy, H. Kalman, S. Aman, J. Tomas, Strength distribution of particles under compression, *Powder Technol.* 208 (2011) 215–224. doi:10.1016/j.powtec.2010.12.023.
- [225] R.J. Verrall, A sphere compression test for measuring the mechanical properties of dental composite materials, *J. Dent.* 4 (1976) 11–14. doi:10.1016/0300-5712(76)90064-6.
- [226] M. Yoshida, H. Ogiso, S. Nakano, J. Akedo, Compression test system for a single submicrometer particle, *Rev. Sci. Instrum.* 76 (2005) 093905. doi:10.1063/1.2038187.
- [227] D. Li, L.N.Y. Wong, The brazilian disc test for rock mechanics applications: Review and new insights, *Rock Mech. Rock Eng.* 46 (2013) 269–287. doi:10.1007/s00603-012-0257-7.
- [228] J.N. Brecker, The Fracture Strength of Abrasive Grains, *J. Eng. Ind.* 96 (1974) 1253–1257. doi:10.1115/1.3438503.
- [229] M. Geltink-Verspui, Modelling abrasive processes of glass, (1998).



- [230] H. Huang, Q.K. Huang, X.H. Zhu, X.Z. Hu, An experimental investigation of the strengths of individual brown corundum abrasive grains, *Scr. Metall. Mater.* 29 (1993) 299–304. doi:10.1016/0956-716X(93)90503-K.
- [231] J. Larsen-Basse, Effect of atmospheric humidity on the dynamic fracture strength of SiC abrasives, *Wear.* 166 (1993) 93–100. doi:10.1016/0043-1648(93)90283-R.
- [232] P.J. Slikkerveer, H. in't Veld, M. Verspui, B. de With, D. Reefman, Alumina particle degradation during solid particle impact on glass, *J. Am. Ceram. Soc.* 83 (2000) 2263–2266. doi:10.1111/j.1151-2916.2000.tb01545.x.
- [233] M.A. Verspui, G. de With, E.C.A. Dekkers, A crusher for single particle testing, *Rev. Sci. Instrum.* 68 (1997) 1553–1556. doi:10.1063/1.1147644.
- [234] E. Calvié, L. Joly-Pottuz, C. Esnouf, P. Clément, V. Garnier, J. Chevalier, Y. Jorand, A. Malchère, T. Epicier, K. Masenelli-Varlot, Real time TEM observation of alumina ceramic nanoparticles during compression, *J. Eur. Ceram. Soc.* 32 (2012) 2067–2071. doi:10.1016/j.jeurceramsoc.2012.02.029.
- [235] J.T. Hagan, Impossibility of fragmenting small particles: brittle—ductile transition, *J. Mater. Sci.* 16 (1981) 2909–2911. doi:10.1007/BF02402857.
- [236] A. Rosenflanz, J. Tangeman, T. Anderson, On processing and properties of liquid phase derived glass ceramics in Al<sub>2</sub>O<sub>3</sub>–La<sub>2</sub>O<sub>3</sub>–ZrO<sub>2</sub> system, *Adv. Appl. Ceram.* 111 (2012) 323–332. doi:10.1179/1743676112Y.0000000012.
- [237] E. Calvié, J. Réthoré, L. Joly-Pottuz, S. Meille, J. Chevalier, V. Garnier, Y. Jorand, C. Esnouf, T. Epicier, J.B. Quirk, K. Masenelli-Varlot, Mechanical behavior law of ceramic nanoparticles from transmission electron microscopy in situ nano-compression tests, *Mater. Lett.* 119 (2014) 107–110. doi:10.1016/j.matlet.2014.01.002.
- [238] S. Aman, J. Tomas, H. Kalman, Breakage probability of irregularly shaped particles, *Chem. Eng. Sci.* 65 (2010) 1503–1512. doi:10.1016/j.ces.2009.10.016.
- [239] C. O'Sullivan, I. Cavarretta, The mechanics of rigid irregular particles subject to uniaxial compression, *Géotechnique*. 62 (2012) 681–692. doi:10.1680/geot.10.P.102.
- [240] W. Wang, M.R. Coop, An investigation of breakage behaviour of single sand particles using a high-speed microscope camera, *Géotechnique*. 66 (2016) 984–998. doi:10.1680/jgeot.15.P.247.
- [241] J.A. Hudson, E.T. Brown, F. Rummel, The controlled failure of rock discs and rings loaded in diametral compression, *Int. J. Rock Mech. Min. Sci. Geomech. Abstr.* 9 (1972) 241–248. doi:10.1016/0148-9062(72)90025-3.
- [242] R. Majzoub, M.M. Chaudhri, High-speed photography of low-velocity impact cracking of solid spheres, *Philos. Mag. Lett.* 80 (2000) 387–393. doi:10.1080/095008300403521.
- [243] K. Schönert, Breakage of spheres and circular discs, *Powder Technol.* 143–144 (2004) 2–18. doi:10.1016/j.powtec.2004.04.004.
- [244] J.J. Swab, J. Yu, R. Gamble, S. Kilczewski, Analysis of the diametral compression method for determining the tensile strength of transparent magnesium aluminate spinel, *Int. J. Fract.* 172 (2011) 187–192. doi:10.1007/s10704-011-9655-1.
- [245] W.M. Mook, J.D. Nowak, C.R. Perrey, C.B. Carter, R. Mukherjee, S.L. Girshick, P.H. McMurry, W.W. Gerberich, Compressive stress effects on nanoparticle modulus and fracture, *Phys. Rev. B.* 75 (2007). doi:10.1103/PhysRevB.75.214112.
- [246] B.R. Lawn, *Fracture of brittle solids*, 2nd ed, Cambridge University Press, Cambridge ; New York, 1993.
- [247] A.A. Wereszczak, T.P. Kirkland, O.M. Jadaan, Strength measurement of ceramic spheres using a diametrically compressed “C-Sphere” specimen, *J. Am. Ceram. Soc.* 90 (2007) 1843–1849. doi:10.1111/j.1551-2916.2007.01639.x.

- [248] A.A. Wereszczak, W. Wang, O.M. Jadaan, M.J. Lance, H.-T. Lin, Strength of AC-sphere flexure specimen, in: R. Tandon, A. Wereszczak, E. Lara-Curzio (Eds.), *Mech. Prop. Perform. Eng. Ceram. II Ceram. Eng. Sci. Proc.*, John Wiley & Sons, Inc., 2006: pp. 281–293. <http://onlinelibrary.wiley.com/doi/10.1002/9780470291313.ch27/summary> (accessed May 19, 2017).
- [249] P. Supancic, R. Danzer, S. Witschnig, E. Polaczek, R. Morrell, A new test to determine the tensile strength of brittle balls—The notched ball test, *J. Eur. Ceram. Soc.* 29 (2009) 2447–2459. doi:10.1016/j.jeurceramsoc.2009.02.018.
- [250] S. Strobl, P. Supancic, O. Schöppl, R. Danzer, A new strength test for ceramic cylinders—The Notched Roller Test, *J. Eur. Ceram. Soc.* 34 (2014) 2575–2584. doi:10.1016/j.jeurceramsoc.2014.02.009.
- [251] Standard Test Method for Ultimate Strength of Advanced Ceramics with Diametrically Compressed C-Ring Specimens at Ambient Temperature, ASTM International, West Conshohocken, PA, 2016.
- [252] A.A. Wereszczak, O.M. Jadaan, H.-T. Lin, G.J. Champoux, D.P. Ryan, Hoop tensile strength testing of small diameter ceramic particles, *J. Nucl. Mater.* 361 (2007) 121–125. doi:10.1016/j.jnuclmat.2006.11.013.
- [253] S.S. Brenner, Tensile Strength of Whiskers, *J. Appl. Phys.* 27 (1956) 1484–1491. doi:10.1063/1.1722294.
- [254] C. Herring, J.K. Galt, Elastic and plastic properties of very small metal specimens, *Phys. Rev.* 85 (1952) 1060–1061. doi:10.1103/PhysRev.85.1060.2.
- [255] J.L. Loubet, J.M. Georges, O. Marchesini, G. Meille, Vickers indentation curves of magnesium oxide (MgO), *J. Tribol.* 106 (1984) 43–48. doi:10.1115/1.3260865.
- [256] D. Newey, M.A. Wilkins, H.M. Pollock, An ultra-low-load penetration hardness tester, *J. Phys. [E]*. 15 (1982) 119. doi:10.1088/0022-3735/15/1/023.
- [257] W. c. Oliver, G. m. Pharr, An improved technique for determining hardness and elastic modulus using load and displacement sensing indentation experiments, *J. Mater. Res.* 7 (1992) 1564–1583. doi:10.1557/JMR.1992.1564.
- [258] D. Stone, W.R. LaFontaine, P. Alexopoulos, T.-W. Wu, C.-Y. Li, An investigation of hardness and adhesion of sputter-deposited aluminum on silicon by utilizing a continuous indentation test, *J. Mater. Res.* 3 (1988) 141–147. doi:10.1557/JMR.1988.0141.
- [259] D. Kiener, C. Motz, G. Dehm, R. Pippan, Overview on established and novel FIB based miniaturized mechanical testing using in-situ SEM, *Int. J. Mater. Res.* 100 (2009) 1074–1087. doi:10.3139/146.110149.
- [260] C.A. Volkert, A.M. Minor, Focused ion beam microscopy and micromachining, *MRS Bull.* 32 (2007) 389–399. doi:10.1557/mrs2007.62.
- [261] N. Gane, The direct measurement of the strength of metals on a sub-micrometre scale, *Proc. R. Soc. Lond. Math. Phys. Eng. Sci.* 317 (1970) 367–391. doi:10.1098/rspa.1970.0122.
- [262] R. Kositski, D. Mordehai, Depinning-controlled plastic deformation during nanoindentation of BCC iron thin films and nanoparticles, *Acta Mater.* 90 (2015) 370–379. doi:10.1016/j.actamat.2015.03.010.
- [263] W.M. Mook, C. Niederberger, M. Bechelany, L. Philippe, J. Michler, Compression of free-standing gold nanostructures: from stochastic yield to predictable flow, *Nanotechnology.* 21 (2010) 055701. doi:10.1088/0957-4484/21/5/055701.
- [264] Z.-J. Wang, Z.-W. Shan, J. Li, J. Sun, E. Ma, Pristine-to-pristine regime of plastic deformation in submicron-sized single crystal gold particles, *Acta Mater.* 60 (2012) 1368–1377. doi:10.1016/j.actamat.2011.10.035.
- [265] N. Gane, The compressive strength of sub-micrometre diameter magnesium oxide crystals, *Philos. Mag.* 25 (1972) 25–34. doi:10.1080/14786437208229212.



- [266] J. Paul, S. Romeis, M. Mačković, V.R.R. Marthala, P. Herre, T. Przybilla, M. Hartmann, E. Spiecker, J. Schmidt, W. Peukert, In situ cracking of silica beads in the SEM and TEM — Effect of particle size on structure–property correlations, *Powder Technol.* 270, Part A (2015) 337–347. doi:10.1016/j.powtec.2014.10.026.
- [267] J. Paul, S. Romeis, J. Tomas, W. Peukert, A review of models for single particle compression and their application to silica microspheres, *Adv. Powder Technol.* 25 (2014) 136–153. doi:10.1016/j.apt.2013.09.009.
- [268] S. Romeis, J. Paul, M. Ziener, W. Peukert, A novel apparatus for in situ compression of sub-micron structures and particles in a high resolution SEM, *Rev. Sci. Instrum.* 83 (2012) 095105. doi:10.1063/1.4749256.
- [269] K. Zheng, C. Wang, Y.-Q. Cheng, Y. Yue, X. Han, Z. Zhang, Z. Shan, S.X. Mao, M. Ye, Y. Yin, E. Ma, Electron-beam-assisted superplastic shaping of nanoscale amorphous silica, *Nat. Commun.* 1 (2010) 24. doi:10.1038/ncomms1021.
- [270] J. Deneen, W.M. Mook, A. Minor, W.W. Gerberich, C.B. Carter, In situ deformation of silicon nanospheres, *J. Mater. Sci.* 41 (2006) 4477–4483. doi:10.1007/s10853-006-0085-9.
- [271] W.W. Gerberich, W.M. Mook, C.R. Perrey, C.B. Carter, M.I. Baskes, R. Mukherjee, A. Gidwani, J. Heberlein, P.H. McMurry, S.L. Girshick, Superhard silicon nanospheres, *J. Mech. Phys. Solids.* 51 (2003) 979–992. doi:10.1016/S0022-5096(03)00018-8.
- [272] J.D. Nowak, W.M. Mook, A.M. Minor, W.W. Gerberich, C.B. Carter, Fracturing a nanoparticle, *Philos. Mag.* 87 (2007) 29–37. doi:10.1080/14786430600876585.
- [273] M.D. Uchic, D.M. Dimiduk, J.N. Florando, W.D. Nix, Sample dimensions influence strength and crystal plasticity, *Science.* 305 (2004) 986–989. doi:10.1126/science.1098993.
- [274] A.T. Jennings, M.J. Burek, J.R. Greer, Microstructure versus size: mechanical properties of electroplated single crystalline Cu nanopillars, *Phys. Rev. Lett.* 104 (2010) 135503. doi:10.1103/PhysRevLett.104.135503.
- [275] J.-Y. Kim, J.R. Greer, Tensile and compressive behavior of gold and molybdenum single crystals at the nano-scale, *Acta Mater.* 57 (2009) 5245–5253. doi:10.1016/j.actamat.2009.07.027.
- [276] Q. Yu, S. Li, A.M. Minor, J. Sun, E. Ma, High-strength titanium alloy nanopillars with stacking faults and enhanced plastic flow, *Appl. Phys. Lett.* 100 (2012) 063109. doi:10.1063/1.3683489.
- [277] C. Niederberger, W.M. Mook, X. Maeder, J. Michler, In situ electron backscatter diffraction (EBSD) during the compression of micropillars, *Mater. Sci. Eng. A.* 527 (2010) 4306–4311. doi:10.1016/j.msea.2010.03.055.
- [278] R. Maaß, S. Van Petegem, J. Zimmermann, C.N. Borca, H. Van Swygenhoven, On the initial microstructure of metallic micropillars, *Scr. Mater.* 59 (2008) 471–474. doi:10.1016/j.scriptamat.2008.04.034.
- [279] R. Maaß, S. Van Petegem, H. Van Swygenhoven, P.M. Derlet, C.A. Volkert, D. Grolimund, Time-resolved laue diffraction of deforming micropillars, *Phys. Rev. Lett.* 99 (2007) 145505. doi:10.1103/PhysRevLett.99.145505.
- [280] D.M. Dimiduk, M.D. Uchic, T.A. Parthasarathy, Size-affected single-slip behavior of pure nickel microcrystals, *Acta Mater.* 53 (2005) 4065–4077. doi:10.1016/j.actamat.2005.05.023.
- [281] J.R. Greer, W.D. Nix, Nanoscale gold pillars strengthened through dislocation starvation, *Phys. Rev. B.* 73 (2006) 245410. doi:10.1103/PhysRevB.73.245410.
- [282] D. Kiener, C. Motz, T. Schöberl, M. Jenko, G. Dehm, Determination of mechanical properties of copper at the micron scale, *Adv. Eng. Mater.* 8 (2006) 1119–1125. doi:10.1002/adem.200600129.
- [283] A. Kunz, S. Pathak, J.R. Greer, Size effects in Al nanopillars: Single crystalline vs. bicrystalline, *Acta Mater.* 59 (2011) 4416–4424. doi:10.1016/j.actamat.2011.03.065.

- [284] J.-Y. Kim, D. Jang, J.R. Greer, Tensile and compressive behavior of tungsten, molybdenum, tantalum and niobium at the nanoscale, *Acta Mater.* 58 (2010) 2355–2363. doi:10.1016/j.actamat.2009.12.022.
- [285] C.M. Byer, B. Li, B. Cao, K.T. Ramesh, Microcompression of single-crystal magnesium, *Scr. Mater.* 62 (2010) 536–539. doi:10.1016/j.scriptamat.2009.12.017.
- [286] B. Girault, A.S. Schneider, C.P. Frick, E. Arzt, Strength effects in micropillars of a dispersion strengthened superalloy, *Adv. Eng. Mater.* 12 (2010) 385–388. doi:10.1002/adem.201000089.
- [287] B.E. Schuster, L.S. Magness, L.J. Kecskes, Q. Wei, M.K. Miller, M.F. Ervin, S. Hruszkewycz, T.C. Minagel, K.T. Ramesh, Microcompression of bulk metallic glass and tungsten-bulk metallic glass composites, U.S. Army Research Laboratory, Aberdeen Proving Ground, MD, USA, 2007. <http://oai.dtic.mil/oai/oai?verb=getRecord&metadataPrefix=html&identifier=ADA469175> (accessed May 23, 2017).
- [288] E.L. Huskins, Z.C. Cordero, C.A. Schuh, B.E. Schuster, Micropillar compression testing of powders, *J. Mater. Sci.* 50 (2015) 7058–7063. doi:10.1007/s10853-015-9260-1.
- [289] D.R.P. Singh, N. Chawla, G. Tang, Y.-L. Shen, Micropillar compression of Al/SiC nanolaminates, *Acta Mater.* 58 (2010) 6628–6636. doi:10.1016/j.actamat.2010.08.025.
- [290] L.-Y. Chen, J.-Q. Xu, H. Choi, M. Pozuelo, X. Ma, S. Bhowmick, J.-M. Yang, S. Mathaudhu, X.-C. Li, Processing and properties of magnesium containing a dense uniform dispersion of nanoparticles, *Nature*. 528 (2015) 539–543. doi:10.1038/nature16445.
- [291] J. Schwiedrzik, R. Raghavan, A. Bürki, V. LeNader, U. Wolfram, J. Michler, P. Zysset, In situ micropillar compression reveals superior strength and ductility but an absence of damage in lamellar bone, *Nat. Mater.* 13 (2014) 740–747. doi:10.1038/nmat3959.
- [292] S. Korte, W.J. Clegg, Micropillar compression of ceramics at elevated temperatures, *Scr. Mater.* 60 (2009) 807–810. doi:10.1016/j.scriptamat.2009.01.029.
- [293] P.R. Howie, S. Korte, W.J. Clegg, Fracture modes in micropillar compression of brittle crystals, *J. Mater. Res.* 27 (2012) 141–151. doi:10.1557/jmr.2011.256.
- [294] J.M. Wheeler, R. Raghavan, J. Wehrs, Y. Zhang, R. Erni, J. Michler, Approaching the limits of strength: Measuring the uniaxial compressive strength of diamond at small scales, *Nano Lett.* 16 (2016) 812–816. doi:10.1021/acs.nanolett.5b04989.
- [295] D. Kiener, W. Grosinger, G. Dehm, R. Pippan, A further step towards an understanding of size-dependent crystal plasticity: In situ tension experiments of miniaturized single-crystal copper samples, *Acta Mater.* 56 (2008) 580–592. doi:10.1016/j.actamat.2007.10.015.
- [296] Y. Kihara, T. Nagoshi, T.-F.M. Chang, H. Hosoda, S. Tatsuo, M. Sone, Tensile behavior of micro-sized specimen made of single crystalline nickel, *Mater. Lett.* 153 (2015) 36–39. doi:10.1016/j.matlet.2015.03.119.
- [297] S. Yanagida, A. Araki, T.-F.M. Chang, C.-Y. Chen, T. Nagoshi, E. Kobayashi, H. Hosoda, T. Sato, M. Sone, Deformation behavior of pure Cu and Cu-Ni-Si alloy evaluated by micro-tensile testing, *Mater. Trans.* 57 (2016) 1897–1901. doi:10.2320/matertrans.M2016188.
- [298] C. Motz, T. Schöberl, R. Pippan, Mechanical properties of micro-sized copper bending beams machined by the focused ion beam technique, *Acta Mater.* 53 (2005) 4269–4279. doi:10.1016/j.actamat.2005.05.036.
- [299] S. Massl, W. Thomma, J. Keckes, R. Pippan, Investigation of fracture properties of magnetron-sputtered TiN films by means of a FIB-based cantilever bending technique, *Acta Mater.* 57 (2009) 1768–1776. doi:10.1016/j.actamat.2008.12.018.
- [300] M.G. Mueller, M. Fornabaio, G. Žagar, A. Mortensen, Microscopic strength of silicon particles in an aluminium–silicon alloy, *Acta Mater.* 105 (2016) 165–175. doi:10.1016/j.actamat.2015.12.006.
- [301] E. Feilden, T. Giovannini, N. Ni, C. Ferraro, E. Saiz, L. Vandeperre, F. Giuliani, Micromechanical strength of individual Al<sub>2</sub>O<sub>3</sub> platelets, *Scr. Mater.* 131 (2017) 55–58. doi:10.1016/j.scriptamat.2017.01.008.

- [302] D.K. Shukla, V. Parameswaran, Epoxy composites with 200 nm thick alumina platelets as reinforcements, *J. Mater. Sci.* 42 (2007) 5964–5972. doi:10.1007/s10853-006-1110-8.
- [303] R.M. Erb, R. Libanori, N. Rothfuchs, A.R. Studart, Composites reinforced in three dimensions by using low magnetic fields, *Science*. 335 (2012) 199–204. doi:10.1126/science.1210822.
- [304] D. Kiener, C. Motz, M. Rester, M. Jenko, G. Dehm, FIB damage of Cu and possible consequences for miniaturized mechanical tests, *Mater. Sci. Eng. A*. 459 (2007) 262–272. doi:10.1016/j.msea.2007.01.046.
- [305] R.W. Rice, Machining flaws and the strength grain size behavior of ceramics., in: *Sci. Ceram. Mach. Surf. Finish. II*, National Bureau of Standards Special Publication, Gaithersburg, Maryland, 1979: pp. 429–454.
- [306] S. Shim, H. Bei, M.K. Miller, G.M. Pharr, E.P. George, Effects of focused ion beam milling on the compressive behavior of directionally solidified micropillars and the nanoindentation response of an electropolished surface, *Acta Mater.* 57 (2009) 503–510. doi:10.1016/j.actamat.2008.09.033.
- [307] B. Basnar, A. Lugstein, H. Wanzenboeck, H. Langfischer, E. Bertagnolli, E. Gornik, Focused ion beam induced surface amorphization and sputter processes, *J. Vac. Sci. Technol. B Microelectron. Nanometer Struct. Process. Meas. Phenom.* 21 (2003) 927–930. doi:10.1116/1.1565345.
- [308] S. Rubanov, P.R. Munroe, FIB-induced damage in silicon, *J. Microsc.* 214 (2004) 213–221. doi:10.1111/j.0022-2720.2004.01327.x.
- [309] Z. Wang, T. Kato, T. Hirayama, N. Kato, K. Sasaki, H. Saka, Surface damage induced by focused-ion-beam milling in a Si/Si p–n junction cross-sectional specimen, *Appl. Surf. Sci.* 241 (2005) 80–86. doi:10.1016/j.apsusc.2004.09.092.
- [310] S. Rubanov, P.R. Munroe, Investigation of the structure of damage layers in TEM samples prepared using a focused ion beam, *J. Mater. Sci. Lett.* 20 (2001) 1181–1183. doi:10.1023/A:1010950201525.
- [311] J. Mayer, L.A. Giannuzzi, T. Kamino, J. Michael, TEM sample preparation and FIB-induced damage, *MRS Bull.* 32 (2007) 400–407. doi:10.1557/mrs2007.63.
- [312] D. a. M. de Winter, J.J.L. Mulders, Redeposition characteristics of focused ion beam milling for nanofabrication, *J. Vac. Sci. Technol. B Microelectron. Nanometer Struct. Process. Meas. Phenom.* 25 (2007) 2215–2218. doi:10.1116/1.2806973.
- [313] B.I. Prenitzer, C.A. Urbanik-Shannon, L.A. Giannuzzi, S.R. Brown, R.B. Irwin, T.L. Shofner, F.A. Stevie, The correlation between ion beam/material interactions and practical FIB specimen preparation, *Microsc. Microanal.* 9 (2003) 216–236. doi:10.1017/S1431927603030034.
- [314] T. Ishitani, T. Yaguchi, Cross-sectional sample preparation by focused ion beam: A review of ion-sample interaction, *Microsc. Res. Tech.* 35 (1996) 320–333. doi:10.1002/(SICI)1097-0029(19961101)35:4<320::AID-JEMT3>3.0.CO;2-Q.
- [315] A.D. Norton, S. Falco, N. Young, J. Severs, R.I. Todd, Microcantilever investigation of fracture toughness and subcritical crack growth on the scale of the microstructure in Al<sub>2</sub>O<sub>3</sub>, *J. Eur. Ceram. Soc.* 35 (2015) 4521–4533. doi:10.1016/j.jeurceramsoc.2015.08.023.
- [316] D. Tabor, *The Hardness of Metals*, Clarendon Press, Oxford, 1951.
- [317] G.E. Dieter, *Mechanical metallurgy*, 3rd ed, McGraw-Hill, New York, 1986.
- [318] E.G. Kelly, D.J. Spottiswood, The breakage function; What is it really?, *Miner. Eng.* 3 (1990) 405–414. doi:10.1016/0892-6875(90)90034-9.
- [319] M.M. Chaudhri, Impact breakage of semi-brittle spheres, *Powder Technol.* 143–144 (2004) 31–40. doi:10.1016/j.powtec.2004.04.006.
- [320] J.P. Klein, M.L. Moeschberger, *Survival analysis: techniques for censored and truncated data*, 2nd ed., Springer, New York, 2003.

- [321] E.L. Kaplan, P. Meier, Nonparametric estimation from incomplete observations, *J. Am. Stat. Assoc.* 53 (1958) 457. doi:10.2307/2281868.
- [322] N. Balakrishnan, D. Mitra, Left truncated and right censored Weibull data and likelihood inference with an illustration, *Comput. Stat. Data Anal.* 56 (2012) 4011–4025. doi:10.1016/j.csda.2012.05.004.
- [323] G. Žagar, V. Pejchal, M.G. Mueller, L. Michelet, A. Mortensen, Fracture toughness measurement in fused quartz using triangular chevron-notched micro-cantilevers, *Scr. Mater.* 112 (2016) 132–135. doi:10.1016/j.scriptamat.2015.09.032.
- [324] G. Žagar, V. Pejchal, M.G. Mueller, A. Rossoll, M. Cantoni, A. Mortensen, The local strength of microscopic alumina reinforcements, *Acta Mater.* 100 (2015) 215–223. doi:10.1016/j.actamat.2015.08.026.
- [325] J.L. Armstrong, M.J. Matthewson, C.R. Kurkjian, Humidity Dependence of the Fatigue of High-Strength Fused Silica Optical Fibers, *J. Am. Ceram. Soc.* 83 (2000) 3100–3109. doi:10.1111/j.1151-2916.2000.tb01689.x.
- [326] B.A. Proctor, I. Whitney, J.W. Johnson, The strength of fused silica, *Proc. R. Soc. Lond. Math. Phys. Eng. Sci.* 297 (1967) 534–557. doi:10.1098/rspa.1967.0085.
- [327] J. Huang, S. Xu, H. Yi, S. Hu, Size effect on the compression breakage strengths of glass particles, *Powder Technol.* 268 (2014) 86–94. doi:10.1016/j.powtec.2014.08.037.
- [328] J.A. Salem, Transparent armor ceramics as spacecraft windows, *J. Am. Ceram. Soc.* 96 (2013) 281–289. doi:10.1111/jace.12089.
- [329] T.I. Suratwala, R.A. Steele, Anomalous temperature dependence of sub-critical crack growth in silica glass, *J. Non-Cryst. Solids.* 316 (2003) 174–182. doi:10.1016/S0022-3093(02)01799-4.
- [330] S.M. Wiederhorn, L.H. Bolz, Stress corrosion and static fatigue of glass, *J. Am. Ceram. Soc.* 53 (1970) 543–548.
- [331] G. Žagar, A. Singh, V. Pejchal, M.G. Mueller, A. Mortensen, On measuring fracture toughness under load control in the presence of slow crack growth, *J. Eur. Ceram. Soc.* 35 (2015) 3155–3166. doi:10.1016/j.jeurceramsoc.2015.04.004.
- [332] M.G. Mueller, V. Pejchal, G. Žagar, A. Singh, M. Cantoni, A. Mortensen, Fracture toughness testing of nanocrystalline alumina and fused quartz using chevron-notched microbeams, *Acta Mater.* 86 (2015) 385–395. doi:10.1016/j.actamat.2014.12.016.
- [333] Y. Oka, H. Majima, A theory of size reduction involving fracture mechanics, *Can. Metall. Q. Can. J. Metall. Mater. Sci.* 9 (1970) 429–439. doi:10.1179/cm.1970.9.2.429 Y.
- [334] D. Louapre, K. Breder, Hertzian indentation stress field equations, *Int. J. Appl. Ceram. Technol.* 12 (2015) 1071–1079. doi:10.1111/ijac.12317.
- [335] D.M. Wilson, Statistical tensile strength of Nextel™ 610 and Nextel™ 720 fibres, *J. Mater. Sci.* 32 (1997) 2535–2542. doi:10.1023/A:1018538030985.
- [336] K. Niihara, New Design Concept of Structural Ceramics, *J. Ceram. Soc. Jpn.* 99 (1991) 974–982. doi:10.2109/jcersj.99.974.
- [337] J.D. Kuntz, G.-D. Zhan, A.K. Mukherjee, Nanocrystalline-Matrix Ceramic Composites for Improved Fracture Toughness, *MRS Bull.* 29 (2004) 22–27. doi:10.1557/mrs2004.12.
- [338] I.A. Ovid'ko, Micromechanics of fracturing in nanoceramics, *Phil Trans R Soc A.* 373 (2015) 20140129. doi:10.1098/rsta.2014.0129.
- [339] I. Szlufarska, A. Nakano, P. Vashishta, A Crossover in the Mechanical Response of Nanocrystalline Ceramics, *Science.* 309 (2005) 911–914. doi:10.1126/science.1114411.
- [340] Y. Zhao, J. Qian, L.L. Daemen, C. Pantea, J. Zhang, G.A. Voronin, T.W. Zerda, Enhancement of fracture toughness in nanostructured diamond–SiC composites, *Appl. Phys. Lett.* 84 (2004) 1356–1358. doi:10.1063/1.1650556.



- [341] T. Chraska, K. Neufuss, J. Dubsky, P. Ctibor, M. Klementova, Fabrication of Bulk Nanocrystalline Ceramic Materials, *J. Therm. Spray Technol.* 17 (2008) 872. doi:10.1007/s11666-008-9241-x.
- [342] H.-J. Kim, Y.J. Kim, Amorphous phase formation of the pseudo-binary  $\text{Al}_2\text{O}_3\text{-ZrO}_2$  alloy during plasma spray processing, *J. Mater. Sci.* 34 (1999) 29–33. doi:10.1023/A:1004492919174.
- [343] A.F. Gualtieri, Accuracy of XRPD QPA using the combined Rietveld–RIR method, *J. Appl. Crystallogr.* 33 (2000) 267–278. doi:10.1107/S002188989901643X.
- [344] V. Pejchal, G. Žagar, R. Charvet, C. Dénéreaz, A. Mortensen, Compression testing spherical particles for strength: Theory of the meridian crack test and implementation for microscopic fused quartz, *J. Mech. Phys. Solids.* 99 (2017) 70–92. doi:10.1016/j.jmps.2016.11.009.
- [345] T. Chraska, Z. Pala, R. Mušálek, J. Medřický, M. Vilémová, Post-treatment of Plasma-Sprayed Amorphous Ceramic Coatings by Spark Plasma Sintering, *J. Therm. Spray Technol.* 24 (2015) 637–643. doi:10.1007/s11666-015-0225-3.
- [346] G. Žagar, V. Pejchal, M. Kissling, A. Mortensen, On the diametric compression strength test of brittle spherical particles, *Prep.* (2017).
- [347] J.J. Mecholsky, R.W. Rice, S.W. Freiman, Prediction of Fracture Energy and Flaw Size in Glasses from Measurements of Mirror Size, *J. Am. Ceram. Soc.* 57 (1974) 440–443. doi:10.1111/j.1151-2916.1974.tb11377.x.
- [348] G.K. Bansal, W.H. Duckworth, Fracture stress as related to flaw and fracture mirror sizes, *J. Am. Ceram. Soc.* 60 (1977) 304–310.
- [349] S.R. Choi, J.P. Gyekenyesi, Crack branching and fracture mirror data of glasses and advanced ceramics, National Aeronautics and Space Administration, Lewis Research Center, Cleveland, Ohio, 1998. <https://ntrs.nasa.gov/search.jsp?R=19980137602> (accessed April 12, 2017).
- [350] F.Y. Cui, R.P. Vinci, A chevron-notched bowtie micro-beam bend test for fracture toughness measurement of brittle materials, *Scr. Mater.* 132 (2017) 53–57. doi:10.1016/j.scrip-tamat.2017.01.031.
- [351] R.W. Rice, Pores as fracture origins in ceramics, *J. Mater. Sci.* 19 (1984) 895–914. doi:10.1007/BF00540460.
- [352] H. Schneider, R.X. Fischer, J. Schreuer, Mullite: Crystal Structure and Related Properties, *J. Am. Ceram. Soc.* 98 (2015) 2948–2967. doi:10.1111/jace.13817.
- [353] I.A. Aksay, D.M. Dabbs, M. Sarikaya, Mullite for Structural, Electronic, and Optical Applications, *J. Am. Ceram. Soc.* 74 (1991) 2343–2358. doi:10.1111/j.1151-2916.1991.tb06768.x.
- [354] H. Schneider, J. Schreuer, B. Hildmann, Structure and properties of mullite—A review, *J. Eur. Ceram. Soc.* 28 (2008) 329–344. doi:10.1016/j.jeurceramsoc.2007.03.017.
- [355] E. Rocha-Rangel, S. Díaz-de-la-Torre, M. Umemoto, H. Miyamoto, H. Balmori-Ramírez, Zirconia–Mullite Composites Consolidated by Spark Plasma Reaction Sintering from Zircon and Alumina, *J. Am. Ceram. Soc.* 88 (2005) 1150–1157. doi:10.1111/j.1551-2916.2005.00234.x.
- [356] P. Kumar, M. Nath, A. Ghosh, H.S. Tripathi, Synthesis and characterization of mullite–zirconia composites by reaction sintering of zircon flour and sillimanite beach sand, *Bull. Mater. Sci.* 38 (2015) 1539–1544.
- [357] Q.-M. Yuan, J.-Q. Tan, Z.-G. Jin, Preparation and Properties of Zirconia-Toughened Mullite Ceramics, *J. Am. Ceram. Soc.* 69 (1986) 265–267. doi:10.1111/j.1151-2916.1986.tb07422.x.
- [358] F. Deléglise, M.H. Berger, A.R. Bunsell, Microstructural evolution under load and high temperature deformation mechanisms of a mullite/alumina fibre, *J. Eur. Ceram. Soc.* 22 (2002) 1501–1512. doi:10.1016/S0955-2219(01)00461-7.
- [359] T. Rouxel, Elastic Properties and Short-to Medium-Range Order in Glasses, *J. Am. Ceram. Soc.* 90 (2007) 3019–3039. doi:10.1111/j.1551-2916.2007.01945.x.

- [360] G.N. Greaves, A.L. Greer, R.S. Lakes, T. Rouxel, Poisson's ratio and modern materials, *Nat. Mater.* 10 (2011) 823–837. doi:10.1038/nmat3134.
- [361] G.A. Rosales-Sosa, A. Masuno, Y. Higo, H. Inoue, Crack-resistant Al<sub>2</sub>O<sub>3</sub>–SiO<sub>2</sub> glasses, *Sci. Rep.* 6 (2016) 23620. doi:10.1038/srep23620.
- [362] A. Makishima, J.D. Mackenzie, Direct calculation of Young's modulus of glass, *J. Non-Cryst. Solids.* 12 (1973) 35–45. doi:10.1016/0022-3093(73)90053-7.
- [363] A. Makishima, J.D. Mackenzie, Calculation of bulk modulus, shear modulus and Poisson's ratio of glass, *J. Non-Cryst. Solids.* 17 (1975) 147–157. doi:10.1016/0022-3093(75)90047-2.
- [364] J. Rocherulle, C. Ecolivet, M. Poulain, P. Verdier, Y. Laurent, Elastic moduli of oxynitride glasses, *J. Non-Cryst. Solids.* 108 (1989) 187–193. doi:10.1016/0022-3093(89)90582-6.
- [365] H. Ledbetter, S. Kim, D. Balzar, S. Crudele, W. Kriven, Elastic Properties of Mullite, *J. Am. Ceram. Soc.* 81 (1998) 1025–1028. doi:10.1111/j.1151-2916.1998.tb02441.x.
- [366] W. Pabst, E. Gregorová, T. Uhlířová, A. Musilová, ELASTIC PROPERTIES OF MULLITE AND MULLITE-CONTAINING CERAMICS PART 1: THEORETICAL ASPECTS AND REVIEW OF MONOCRYSTAL DATA, *Ceram Silik.* 57 (2013) 265–274.
- [367] I.N. Sneddon, The Distribution of Stress in the Neighbourhood of a Crack in an Elastic Solid, *Proc. R. Soc. Lond. Math. Phys. Eng. Sci.* 187 (1946) 229–260. doi:10.1098/rspa.1946.0077.
- [368] A.L. Yurkov, V.N. Skvortsov, I.A. Buyanovsky, R.M. Matvievsky, Sliding friction of diamond on steel, sapphire, alumina and fused silica with and without lubricants, *J. Mater. Sci. Lett.* 16 (1997) 1370–1374. doi:10.1023/A:1018536621995.
- [369] A. Jayatilaka, K. Trustrum, Statistical approach to brittle fracture, *J. Mater. Sci.* 12 (1977) 1426–1430.
- [370] R.H. Doremus, Fracture statistics: A comparison of the normal, Weibull, and Type I extreme value distributions, *J. Appl. Phys.* 54 (1983) 193. doi:10.1063/1.331731.
- [371] C. Lu, R. Danzer, F. Fischer, Fracture statistics of brittle materials: Weibull or normal distribution, *Phys. Rev. E.* 65 (2002) 1–4. doi:10.1103/PhysRevE.65.067102.
- [372] S. van der Zwaag, The concept of filament strength and the Weibull modulus, *ASTM J Test Eval.* 17 (1989) 292–298.
- [373] W. Weibull, A statistical theory of the strength of materials, *Lngeniors Vetensk. Akad. Handl.* 151 (1939) 45.
- [374] B. Moser, A. Rossoll, L. Weber, O. Beffort, A. Mortensen, Damage evolution of Nextel 610TM alumina fibre reinforced aluminium, *Acta Mater.* 52 (2004) 573–581. doi:10.1016/j.actamat.2003.09.040.
- [375] A. Rossoll, B. Moser, A. Mortensen, Tensile strength of axially loaded unidirectional Nextel 610<sup>TM</sup> reinforced aluminium: A case study in local load sharing between randomly distributed fibres, *Compos. Part Appl. Sci. Manuf.* 43 (2012) 129. doi:10.1016/j.compositesa.2011.09.027.
- [376] A. Rossoll, C. Otto, B. Moser, L. Weber, A. Wanner, A. Mortensen, Measurement of damage evolution in continuous ceramic fibre-reinforced metals by acoustic emission, *Scr. Mater.* 59 (2008) 842. doi:10.1016/j.scriptamat.2008.06.027.
- [377] R. Danzer, Some notes on the correlation between fracture and defect statistics: Are Weibull statistics valid for very small specimens?, *J. Eur. Ceram. Soc.* 26 (2006) 3043–3049. doi:10.1016/j.jeurceramsoc.2005.08.021.
- [378] R. Danzer, P. Supancic, J. Pascual, T. Lube, Fracture statistics of ceramics – Weibull statistics and deviations from Weibull statistics, *Eng. Fract. Mech.* 74 (2007) 2919–2932. doi:10.1016/j.engfracmech.2006.05.028.
- [379] A. Rossoll, B. Moser, L. Weber, A. Mortensen, In situ flow stress of pure aluminium constrained by tightly packed alumina fibres, *Acta Mater.* 57 (2009) 1795–1812. doi:10.1016/j.actamat.2008.12.024.



- [380] M. Asmani, C. Kermel, A. Leriche, M. Ourak, Influence of porosity on Young's modulus and Poisson's ratio in alumina ceramics, *J. Eur. Ceram. Soc.* 21 (2001) 1081–1086. doi:10.1016/S0955-2219(00)00314-9.
- [381] M.M. Choy, K.-H. Hellwege, H. Landolt, R. Börnstein, O. Madelung, eds., *Elastic, piezoelectric, pyroelectric, piezooptic, electrooptic constant, and nonlinear dielectric susceptibilities of crystals: revised and expanded edition of volumes III/1 and III/2*, Springer, Berlin, 1979.
- [382] G. Simmons, H. Wang, *Single crystal elastic constants and calculated aggregate properties: a handbook*, 2d ed, M.I.T. Press, Cambridge, Mass, 1971.
- [383] S. Van Der Zwaag, The Concept of Filament Strength and the Weibull Modulus  $i$  L, *J. Test. Eval.* 17 (1989) 292–298.
- [384] A.R. Bunsell, M.-H. Berger, Fine diameter ceramic fibres, *J. Eur. Ceram. Soc.* 20 (2000) 2249–2260. doi:10.1016/S0955-2219(00)00090-X.
- [385] F.M. Beremin, A. Pineau, F. Mudry, J.-C. Devaux, Y. D'Escatha, P. Ledermann, A local criterion for cleavage fracture of a nuclear pressure vessel steel, *Metall. Trans. A.* 14 (1983) 2277–2287. doi:10.1007/BF02663302.
- [386] A. Miserez, R. Müller, A. Mortensen, Increasing the strength/toughness combination of high volume fraction particulate metal matrix composites using an Al-Ag matrix alloy, *Adv. Eng. Mater.* 8 (2006) 56–62. doi:10.1002/adem.200500185.
- [387] M.G. Mueller, G. Žagar, A. Mortensen, In-situ strength of individual silicon particles within an aluminium casting alloy, *Acta Mater.* submitted (2017).
- [388] Z. Xu, W. Wen, T. Zhai, Effects of pore position in depth on stress/strain concentration and fatigue crack initiation, *Metall. Mater. Trans. A.* 43 (2012) 2763–2770. doi:10.1007/s11661-011-0947-x.
- [389] W.D. Pilkey, D.F. Pilkey, *Peterson's stress concentration factors*, 3rd ed., John Wiley & Sons, 2008.
- [390] P. Peralta, A. Schober, C. Laird, Elastic stresses in anisotropic bicrystals, *Mater. Sci. Eng. A.* 169 (1993) 43–51. doi:10.1016/0921-5093(93)90597-8.
- [391] J.E. Gagorik, R.A. Queeney, H.A. McKinstry, Stress distributions in Al<sub>2</sub>O<sub>3</sub> bicrystal tensile specimens, *J. Am. Ceram. Soc.* 54 (1971) 625–627. doi:10.1111/j.1151-2916.1971.tb16018.x.
- [392] H.Y.B. Mar, W.D. Scott, Fracture induced in Al<sub>2</sub>O<sub>3</sub> bicrystals by anisotropic thermal expansion, *J. Am. Ceram. Soc.* 53 (1970) 555–558. doi:10.1111/j.1151-2916.1970.tb15965.x.
- [393] Y. Lifshitz, Diamond-like carbon — present status, *Diam. Relat. Mater.* 8 (1999) 1659–1676. doi:10.1016/S0925-9635(99)00087-4.
- [394] J. Robertson, Hard amorphous (diamond-like) carbons, *Prog. Solid State Chem.* 21 (1991) 199–333. doi:10.1016/0079-6786(91)90002-H.
- [395] J. Robertson, E.P. O'Reilly, Electronic and atomic structure of amorphous carbon, *Phys. Rev. B.* 35 (1987) 2946–2957. doi:10.1103/PhysRevB.35.2946.
- [396] I.M. Watt, *The principles and practice of electron microscopy*, Cambridge University Press, Cambridge [Cambridgeshire] ; New York, 1985.
- [397] M. Holmes, J. Keeley, K. Hurd, H. Schmidt, A. Hawkins, Optimized piranha etching process for SU8-based MEMS and MOEMS construction, *J. Micromechanics Microengineering Struct. Devices Syst.* 20 (2010) 1–8. doi:10.1088/0960-1317/20/11/115008.
- [398] J.-H. Pyun, T.-B. Shin, J.-H. Lee, K.-M. Ahn, T.-H. Kim, H.-S. Cha, Effects of hydrogen peroxide pretreatment and heat activation of silane on the shear bond strength of fiber-reinforced composite posts to resin cement, *J. Adv. Prosthodont.* 8 (2016) 94–100. doi:10.4047/jap.2016.8.2.94.
- [399] H. Poulsen, *Three-Dimensional X-Ray Diffraction Microscopy Mapping Polycrystals and their Dynamics*, Springer-Verlag Berlin/Heidelberg : Springer e-books, Berlin, Heidelberg, 2004.

- [400] P. Sedmák, J. Pilch, L. Heller, J. Kopeček, J. Wright, P. Sedlák, M. Frost, P. Šittner, Grain-resolved analysis of localized deformation in nickel-titanium wire under tensile load, *Science*. 353 (2016) 559–562. doi:10.1126/science.aad6700.

**Václav Pejchal**

Avenue du Moulin 14  
 1110 Morges, Switzerland  
 vaclav.pejchal@gmail.com  
 Slovak nationality, married



## EDUCATION

<b>École Polytechnique Fédérale de Lausanne (EPFL)</b> Doctor of Science in Materials Science and Engineering	<b>2017</b>
<b>Czech Technical University in Prague, Faculty of Nuclear Sciences and Physical Engineering</b> Master in Physical Engineering (with honours) – Academic exchange year at Peter the Great St. Petersburg Polytechnic University	<b>2012</b>
<b>Czech Technical University in Prague, Faculty of Nuclear Sciences and Physical Engineering</b> Bachelor in Physical Engineering	<b>2009</b>

## PROFESSIONAL EXPERIENCE

<b>Laboratory of Mechanical Metallurgy, EPFL</b> <i>European Research Council (ERC) project: Probing at the Nanoscale the Structure and Properties of Hard Second Phases in Alloys and Composites</i>	<b>2012 – 2017</b> (research & teaching assistant)
--	---

- Design and development of new strategies to measure mechanical properties of materials at micro- and nano-scale in a team of five researchers.
- Implementation of new methods combining Focused Ion Beam (FIB) machining, nanoindentation, and bespoke finite element (FE) simulations.
- Application of new methods to investigate the structure-property relationship of microscopic ceramic reinforcements used in metal matrix composites.
- Development of stress and statistical analysis methods implemented using *Mathematica* program.
- Extensive use of electron microscopy for material characterization and defects identification.
- Outcomes of the work show prospective pathways towards production of stronger and tougher particle reinforced composites.

<b>European Space Research and Technology Centre (ESTEC), European Space Agency (ESA)</b> <i>Hydrogen embrittlement of Ti6Al4V alloy</i>	<b>2011</b> (research fellow, 3 months)
---	--

- Implementation of an experimental procedure for evaluating hydrogen embrittlement of the titanium alloy Ti6Al4V to determine maximum permissible hydrogen concentrations.
- Successfully set up an electrochemical hydrogen charging experiment of the titanium alloy specimens in less than 3 months.
- Measurement of fracture toughness and strength of the titanium alloy according to ASTM standards.
- Responsibility to acquire the necessary equipment, design of specimens and of a fixture to grip specimens mechanically in the testing device.

<b>Institute of Plasma Physics of the Czech Academy of Sciences</b> <i>Mechanical properties of thermal spray coatings</i>	<b>2011-2012</b> (research assistant p/t 20%)
---	--

- Implemented three different methods to evaluate the adhesive and cohesive strength of thermal spray coatings at the Institute's materials department.
- Successful validation of the methods on plasma sprayed ceramic and metallic coatings prepared at the Institute.
- Application of the methods on industrial Nickel based alloy prepared by high-velocity oxy-fuel (HVOF) technique in collaboration with a local company.
- Microstructural characterization of coatings using electron microscopy including energy dispersive X-ray spectroscopy (EDS). Analysis of deformation and failure mechanisms.
- The implemented methods are now used in the development of new coating systems at the Institute.

## TECHNICAL SKILLS

**Characterization techniques:** Focused Ion Beam (FIB) machining, Scanning Electron Microscopy (SEM), Energy Dispersive X-ray Spectroscopy (EDS), fractography, metallography, micro and nano-indentation, Finite Element Analysis (FEA), mechanical characterization using universal testing machine and *in-situ* SEM nanomechanical testing apparatus (FemtoTools).

**Synthesis and materials treatment:** thermal spraying, casting, powder metallurgy, liquid metal infiltration, and experience in electrochemistry.

**IT:** Abaqus (FEA), MSC Marc (FEA), Mathematica, Solid Edge, image analysis and processing (Photoshop, ImageJ, DraftSight etc.), MS Office (PC&Mac), basics in Matlab, LabView and Python.

## LANGUAGES

Slovak	native
English	C2 written & spoken (working language for the last 4 years)
French	B2 written & spoken (teaching assistant of courses in French at EPFL)
Russian	B2 written & spoken (one year exchange in St. Petersburg)
Czech	C2 written & spoken (studying 5 years in Czech Republic)
German	A2 written & spoken

## EXTRACURRICULAR ACTIVITIES

- *EPFL Materials Science Doctoral School Research Day 2015* – Organization committee member.
- *JuveMatter 2011: Student research conference in materials science* – Chair of the organization committee.
- *Slovak Organization for Space Activities (SOSA)* – Member.
- *International Student Club at Czech Technical University in Prague* – Activities manager (2010/11).
- *Faculty of Nuclear Sciences and Physical Engineering Sports Team* – Committee member (2008/12).

## LIST OF SCIENTIFIC PUBLICATIONS IN PEER-REVIEWED JOURNALS

Žagar, G. – Pejchal, V. – Kissling, M. – Mortensen, A.: On the diametric compression strength test of brittle spherical particles. *in preparation*.

Pejchal, V. – Fornabaio, M. – Žagar, G. – Riesen, G. – Martin, R. G. – Medřický, J. – Chráska, T. – Mortensen, A.: Meridian crack test strength of plasma-sprayed amorphous and nanocrystalline ceramic microparticles. Submitted to *Acta Materialia*, 2017.

Pejchal, V. – Žagar, G. – Fornabaio, M. – Mortensen, A.: The local strength of individual alumina particles. *Journal of the Mechanics and Physics of Solids*, 2017, vol. 109, pp. 34-49.

Pejchal, V. – Žagar, G. – Charvet, R. – Dénéréaz, C. – Mortensen, A.: Compression testing spherical particles for strength: Theory of the meridian crack test and implementation for microscopic fused quartz. *Journal of the Mechanics and Physics of Solids*, 2017, vol. 99, pp. 70-92.

Žagar, G. – Pejchal, V. – Mueller, M. – Michelet, L. – Mortensen, A.: Fracture toughness measurement in fused quartz using triangular chevron-notched micro-cantilevers. *Scripta Materialia*, 2016, vol. 112, pp. 132-135.

Žagar, G. – Pejchal, V. – Mueller, M. – Cantoni, M. – Rossoll, A. – Mortensen, A.: The local strength of microscopic alumina reinforcements. *Acta Materialia*, 2015, vol. 100, pp. 215-223.

Mueller, M. – Pejchal, V. – Žagar, G. – Singh, A. – Cantoni, M. – Mortensen, A.: Fracture toughness testing of nanocrystalline alumina and fused quartz using chevron-notched microbeams. *Acta Materialia*, 2015, vol. 86, pp. 385-395.

Žagar, G. – Singh, A. – Pejchal, V. – Mueller, M. – Mortensen, A.: On measuring fracture toughness in the presence of slow crack growth. *Journal of the European Ceramic Society*, 2015, vol. 35, pp. 3155-3166.

Mušálek, R. – Pejchal, V. – Vilémová, M. – Matějíček, J.: Multiple-approach evaluation of WSP coatings adhesion/cohesion strength, *Journal of Thermal Spray Technology*, 2013, vol. 22, pp. 221-232.

